Superconductivity of Potassium-Intercalated Epitaxial Graphene

Dissertation

zur Erlangung des akademischen Grades

doctor rerum naturalium (Dr. rer. nat.)

FRIEDRICH-SCHILLER-
UNIVERSITÄT
JENA

vorgelegt dem Rat der Physikalisch-Astronomischen Fakultät

der Friedrich-Schiller-Universität Jena

von M.Sc. Tobias Dominik Hümpfner

geboren am 21.05.1987 in Haßfurt

1. Gutachter: Prof. Dr. Torsten Fritz *(Friedrich-Schiller-Universität Jena)*

2. Gutachter: Prof. Dr. Jörg Fink *(Technische Universität Dresden)*

3. Gutachter: Prof. Dr. Reinhold Kleiner *(Eberhard Karls Universität Tübingen)*

Tag der Disputation: 08. März 2021

Für Sophia

Abstract

The properties related to superconductivity of metal-intercalated, graphene-based, layered systems exhibit a clear dependence on the number of adjacent graphene layers and the intercalant species. To the best of my knowledge, however, there are no experimental studies that enable deeper insights into the physical mechanisms responsible for superconductivity among this material class. In particular, superconductivity of potassium-intercalated mono- and bilayer graphene has not been proven yet. This work provides a detailed investigation of the evolution of structural and electronic properties of epitaxial monolayer graphene on SiC(0001) upon K intercalation. It is shown that the well-known (2×2) superstructure of the K atoms with respect to the graphene lattice forms below the topmost layer. Moreover, the intercalants accumulate as well below the buffer layer and induce its effective decoupling from the underlying SiC substrate, enabling the sample to behave like K-intercalated, quasi-freestanding epitaxial bilayer graphene. Via local and area-averaging experimental methods, it is determined that the presence of K atoms causes not only a filling of the Dirac bands of graphene, but also an occupation of two parabolic interlayer bands. Nevertheless, this highly n-doped phase appears to be stable at low temperatures only. By means of tunneling spectroscopy measurements of an emerging temperature-dependent energy gap around the Fermi level, it is shown that K-intercalated quasi-freestanding epitaxial bilayer graphene is a superconductor below a critical temperature of $T_c = 3.65(2)\,\mathrm{K}$, which is also verified by determination of the average electron-phonon coupling strength on the Dirac bands using angle-resolved photoelectron spectroscopy. Due to several peculiarities in the temperature-dependent data, the findings are also discussed in terms of gap anisotropy and the possible existence of multiple gaps. Although a strongly elevated gap ratio of $2\Delta_0/k_B T_c = 6.19(7)$ compared to conventional superconductors is determined, strong-coupling mechanisms appear to be unlikely considering the related electron-phonon coupling strength. Hence, the unconventional behavior is most likely a consequence of low-dimensional effects. In particular, this study provides the first investigation of the temperature dependence of the energy gap related to superconductivity among metal-intercalated thin films of graphene-based, layered systems.

Kurzfassung

Die supraleitenden Eigenschaften von Metall-interkalierten, Graphen-basierten Schichtsystemen sind abhängig von der Anzahl gestapelter Graphenschichten und dem jeweiligen Element, mit dem die Probe modifiziert wird. Nach meinem Kenntnisstand fehlen jedoch generell experimentelle Studien in der einschlägigen Fachliteratur, welche einen tieferen Einblick in die physikalischen Mechanismen erlauben, die zur Supraleitung in dieser Materialklasse führen. Speziell wurde Supraleitung in Kalium-interkalierten Mono- und Bilagengraphen bisher noch nicht nachgewiesen. In dieser Arbeit werden die Auswirkungen der K-Interkalation auf die strukturellen und elektronischen Eigenschaften von epitaktischen Graphenmonolagen auf SiC(0001) untersucht. Es wird gezeigt, dass sich die bekannte (2×2) Überstruktur der Kaliumatome bezüglich des Graphengitters unterhalb der obersten Graphenschicht ausbildet. Die eingebrachten Fremdatome sammeln sich allerdings auch unterhalb der Pufferschicht an und entkoppeln diese effektiv vom darunterliegenden Substrat, was dazu führt, dass sich die Probe wie Kalium-interkaliertes quasi freistehendes epitaktisches Bilagengraphen verhält. Es wird mittels lokaler und flächenmittelnder experimenteller Methoden gezeigt, dass das Einbringen von K-Atomen nicht nur eine Füllung der Dirac-Bänder zur Folge hat, sondern auch zwei parabolische Bänder mit Elektronen besetzt werden. Diese stark n-dotierte Phase ist jedoch nur bei tiefen Temperaturen stabil. Durch Tunnelspektroskopie-Untersuchungen einer temperaturabhängigen Energielücke, die um das Fermi Niveau auftritt, kann gezeigt werden, dass es sich bei der Kalium-interkalierten Probe tatsächlich um einen Supraleiter handelt, der eine kritische Temperatur von $T_c = 3.65(2)\,\mathrm{K}$ aufweist. Diese kann durch die Bestimmung der mittleren Elektronen-Phonon-Kopplungsstärke mit Hilfe von winkelaufgelöster Photoelektronenspektroskopie verifiziert werden. Da die temperaturabhängigen Daten teilweise unerwartetes Verhalten zeigen, wird auch die Möglichkeit von Anisotropie und das Auftreten mehrerer Energielücken diskutiert. Obwohl verglichen mit konventionellen Supraleitern ein sehr hoher Wert für $2\Delta_0/k_BT_c = 6.19(7)$ ermittelt wird, kann starke Kopplung in diesem Material nahezu ausgeschlossen werden, wenn man die zuvor bestimmte Elektronen-Phononen-Kopplungsstärke berücksichtigt. Vielmehr ist das unkonventionelle Verhalten eher ein Effekt, der auf die Niederdimensionalität der Probe zurückzuführen ist. Insbesondere ist dies die erste Studie in der die Temperaturabhängigkeit der Energielücke untersucht wird, die für die Supraleitung in Metall-interkalierten, Graphen-basierten Dünnschichtsystemen verantwortlich ist.

Contents

1 Introduction

Superconductivity of graphene-based materials regained scientific interest due to the recent discovery of this property in twisted bilayer graphene. Critical temperatures up to $T_c = 1.7\,\mathrm{K}$ were reported by simply twisting adjacent layers by a “magic angle“ of 1.1° [1, 2]. Superconductivity has also been reported for layered, graphene-based systems upon chemical doping via metal intercalation, with even higher transition temperatures up to 11.5 K for Ca-intercalated graphite [3,4]. Since the number of adjacent graphene layers can be controlled experimentally, this material class represents a model system for studying the influence of dimensionality on superconductivity from the three-dimensional (3D) bulk counterpart graphite of stacked graphene layers down to the quasi two-dimensional (2D) thin film limit. In the case of Ca-intercalated compounds, the reported transition temperatures decrease significantly upon reducing the number of adjacent layers, e.g., $T_c = 7\,\mathrm{K}$ is found for few-layer graphene [5] and 4 K for the bilayer [6]. Surprisingly, Li-intercalated bulk graphite is not a superconductor [7], but the few-layer counterpart exhibits a remarkably high critical temperature of 7.4 K [8]. Contrary, K-intercalated graphite exhibits superconductivity up to $T_c = 0.55\,\mathrm{K}$ [9], while the critical temperature of the related few-layer equivalent (mainly four sheets) is elevated to 4.5 K [10]. This brief comparison reveals that upon Li and especially K intercalation the relation between the number of adjacent graphene layers and the critical temperature is reversed to the case of Ca intercalation. Consequently, the properties of the superconducting state among metal-intercalated, layered, graphene-based systems show a clear dependence on the number of adjacent layers and the choice of the atomic species used as intercalants.

Especially in the bulk case of metal-intercalated graphite, superconductivity is believed to originate from electron-phonon coupling (EPC) of electrons located in the energetically shifted π^* bands of graphene and parabolic interlayer (IL) states, which are occupied upon chemical doping, with vibrations of the graphene lattice and the metal intercalants, whereas low-energy modes are of particular importance [11–17]. Accordingly, the deviating properties observed for finite numbers of adjacent graphene layers are attributed to low-dimensional effects that might alter the EPC strength and the IL state [8, 10]. However, to the best of my knowledge there are no reports in the literature which would corroborate this interpretation. In particular, the temperature dependence of the energy gap, which is unavoidably related to the existence of superconductivity, has only been reported for Ca-intercalated bulk graphite so far, albeit with contradicting results [18, 19]. Comparable studies regarding a finite number of intercalated graphene layers have not come to my attention yet. The understanding of the pairing mechanism leading to superconductivity in this material class thus remains fragmentary. Moreover, K-intercalated, graphene-based, layered systems of less than four adjacent carbon layers have not yet been proven to be superconducting.

Consequently, this study aims at proving superconductivity among K-intercalated, graphene-based, layered systems for a thickness below four layers, accompanied by a detailed analysis of essential physical properties to understand its origin. Therefore, samples of epitaxial monolayer graphene (EMLG) on SiC(0001) are produced and scrutinized, since the superconducting properties are closely related to the exact number of adjacent graphene layers. Subsequently, dynamics of the intercalation process are investigated and the final products are characterized regarding their structural and electronic properties. In particular, superconductivity shall be proven by examining the existence and temperature dependence of an energy gap via tunneling spectroscopy, combined with the determination of the EPC strength via angle-resolved photoelectron spectroscopy (ARPES) to shed light on the responsible pairing mechanism. In order to avoid misleading interpretations, all experiments on (K-intercalated) EMLG discussed in the main text are performed not just with similar, but with the very same sample.

2 Fundamentals

2.1 Freestanding Graphene

Graphene consists of a single sheet of sp^2-hybridized carbon atoms arranged in a honeycomb lattice. Each C atom is bound to the three nearest-neighbor atoms[a] by forming in-plane σ bonds. The remaining half-filled p$_z$ orbitals are localized above and below the sheet. Their overlap leads to the formation of a delocalized electron system that results in the well-known π bands of graphene [21].

The unit cell of the hexagonal lattice of graphene, with a lattice constant of $a_G = 2.461$ Å [20], is composed of two equivalent carbon atoms (A and B) as shown in fig. 2.1(a). The corresponding Brillouin zone (BZ) is shown in fig. 2.1(b). It contains two inequivalent K points (labeled K and K′) at the corners of the BZ. The K points are of particular importance for the physical properties of graphene [21, 22]. Further, the BZ includes three M points.

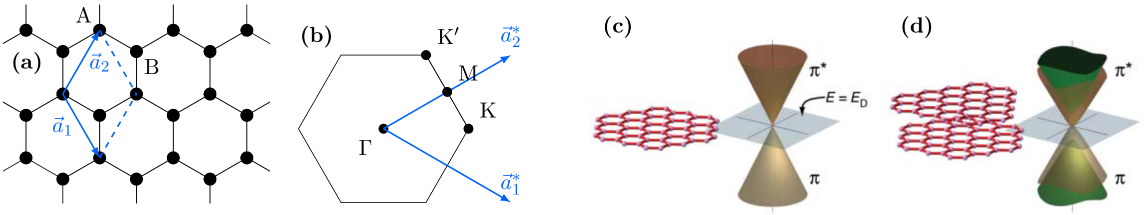

Figure 2.1: (a) Real-space structure of graphene. The black circles depict different species of carbon atoms A and B in the unit cell, which itself is defined by the lattice vectors $\vec{a}_1$ and $\vec{a}_2$. (b) BZ of the graphene lattice. Blue arrows depict the reciprocal lattice vectors. The electronic structure of freestanding (c) single-layer and (d) bilayer graphene at the K and K′ points of the BZ is reprinted from ref. [23].

The electronic band structure of (single-layer) graphene in the environment of the K points is shown in fig. 2.1(c) and can be calculated from a tight-binding (TB) approach [21]. The point of contact between the anti-bonding π^* bands and the bonding π bands is called Dirac point. It is situated at every K and K′ point of the BZ. The energy E_D of the crossing point coincides with the Fermi energy, which means that the π^* bands are unoccupied and the π bands are fully occupied without a gap between those bands. Therefore, graphene is often referred to as zero-gap semiconductor or zero-overlap semimetal. The key to the outstanding electronic

---

[a] Distance between two neighboring C atoms: $a_{nn} = a_G/\sqrt{3} = 1.421$ Å [20].

properties of graphene is the linear dispersion relation close to the Dirac point that was first predicted by Wallace [24]. Accordingly, electrons need to be treated as Dirac fermions giving rise to the naming of the crossing point.

As already mentioned above, graphene is strictly speaking one atomic layer of graphite. Yet, the term graphene is also frequently used for bilayers and also few-layer stacks up to ten layers [22]. In this work, monolayer graphene (MLG) and bilayer graphene (BLG) will be of particular interest.

The electronic structure of BLG can be calculated from a TB approach as well [21, 25]. For this purpose, Bernal stacking [26] like in 3D graphite is considered. The resulting band structure at the K point of an ideal bilayer (fig. 2.1(d)) shows two unoccupied parabolic π^* bands and two occupied parabolic π bands. The inner bands also come into contact at the Fermi energy E_F without any gap (ideal BLG). The presence of two shifted bands at either side of E_F is a result of the interlayer interaction of the two graphene sheets [21]. Moreover, the number of emerging π bands directly correlates with the number of stacked graphene layers [22].

Freestanding graphene is thermodynamically not stable, which has been predicted theoretically [27, 28] and later determined experimentally [29]. However, it is possible to produce stable graphene sheets (and also multilayer graphene) on various substrates by a variety of different methods [30]. In particular, quasi-freestanding graphene sheets can be achieved that are stabilized by van der Waals bonding to an underlying substrate [22, 31]. Hereby, the electronic interaction between graphene and the substrate are sufficiently weak, so that the intrinsic electronic properties of a hypothetically freestanding graphene sheet are largely preserved.

2.2 Epitaxial Graphene on SiC

A widely used method for producing large area quasi-freestanding graphene is the thermal desorption method from a silicon carbide (SiC) crystal. Annealing of the SiC crystal at $T >$ 1100 °C leads to desorption of Si atoms from the topmost surface layers. The remaining carbon atoms rearrange in the hexagonal graphene lattice [32]. SiC crystallizes in different polytypes [33], where 4H- and 6H-SiC are commonly used for the production of epitaxial graphene. The SiC(0001) surface forms a hexagonal lattice with a lattice constant of 3.0806 Å at 297 K [34], which is independent of the polytype.

Graphene can be grown on both, the C-terminated SiC(000$\bar{1}$) and Si-terminated SiC(0001) surface. While the number of graphene layers is difficult to control on the C face [22], the graphene samples used in this work are grown on the Si-terminated surface. The homogeneity of graphene grown in ultra-high vacuum (UHV) conditions is limited on both faces [22]. Better results for monolayer and few-layer graphene systems can be achieved by heating the samples in

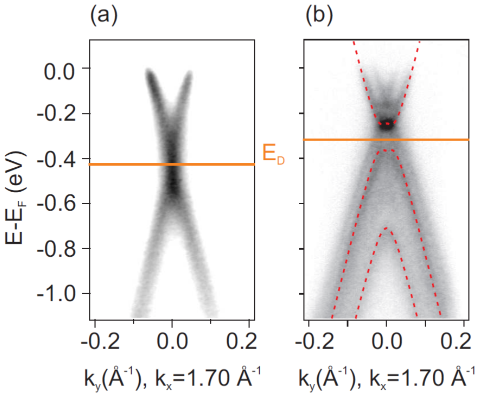

Figure 2.2: ARPES of the valence band structure at the K point of the SBZ of epitaxial (a) mono- and (b) bilayer graphene on SiC(0001). Orange lines depict the Dirac energy E_D. Red dashed lines show fitted spectral functions from TB calculations. Reprinted from ref. [22].

an Ar atmosphere at 1600 °C [32, 35], where the number of layers can be controlled by variation of the annealing time. Details on the exact procedure used for the sample preparation in this work are given in sec. 3.3.

The sublimation of Si atoms from the Si-terminated face leads to the formation of a carbon-rich SiC layer on top of the sample. This layer is still covalently bound to the SiC substrate [36–38]. Further annealing results in a new deeper lying carbon-rich layer, which allows the uppermost C atoms to rearrange in the desired sp^2-hybridized graphene structure. The carbon-rich SiC layer is therefore often referred to as buffer or interface layer.

The buffer layer exhibits a $(6\sqrt{3} \times 6\sqrt{3})$R30° surface reconstruction in relation to the SiC lattice that results from the lattice mismatch between SiC and graphene layers [39]. The origin of this reconstruction has been debated for a long time [22], because some experimental techniques, especially scanning tunneling microscopy (STM), suggested that a description considering a smaller (6×6) superstructure with respect to the SiC lattice should be sufficient [38, 40]. Electronically, this buffer layer does not exhibit any evidence of graphene-like π bands at the K point according to ARPES measurements [22, 31]. Even though the C atoms of the buffer layer are arranged in a graphene-like manner, the covalent bond to Si atoms hinders the formation of a delocalized hexagonal π-electron system, while the σ bonds are preserved [22]. For this reason, the buffer layer is also referred to as “zero-layer graphene (ZLG)“ [41, 42]. The counting of graphene layers starts with carbon layers placed on top of the buffer layer.

In fig. 2.2(a) the band crossing at the K point of the surface Brillouin zone (SBZ) of the first monolayer of graphene above the buffer layer, as measured via ARPES, is shown. The crossing point, however, is shifted below the Fermi level to $E_D = -420\,\text{meV}$. This is a result of a non-negligible charge transfer from the SiC substrate to the graphene layer [43]. Thus, epitaxial graphene on SiC(0001) is intrinsically n-doped by an additional charge carrier density of $n \approx 1 \times 10^{13}\,\text{cm}^{-2}$ that is independent of the preparation procedure, the polytype, and the doping level of the substrate [22].

In an epitaxially grown bilayer system on SiC, the resulting band structure is not explainable by a simple shift of the Dirac point below the Fermi level. In fact, the charge donated from the

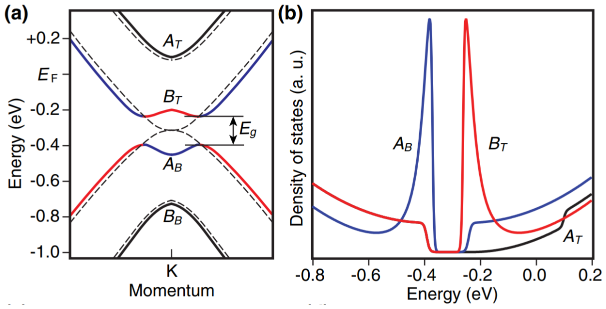

Figure 2.3: (a) Band structure of epitaxial BLG near the K point with (solid lines) and without (dashed lines) a band gap. Colors are related to contributions of different carbon atoms A and B to the electronic structure that are located in the top (T) or bottom graphene (B) layer. (b) Site-resolved density of states (DOS) of epitaxial BLG that exhibits a band gap at the K point. Reprinted from ref. [45].

substrate causes a shift of E_D as can be seen in fig. 2.2(b); at the same time a gap is opening between the two inner bands. This is a consequence of a dipole field induced between the depletion layer of the SiC substrate and the charge predominantly located in the first layer above the buffer layer. Hence, the two graphene layers are inequivalent in terms of charge and electrostatic potential, which results in the observed gap [23]. Nonetheless, the total amount of charge, donated from the substrate to the bilayer system,[b] remains equal to the case of EMLG [41]. Thus, the Dirac point is located closer to the Fermi level ($E_D \approx -300\,\text{meV}$) compared to the monolayer case [22].

There are many theoretical and experimental studies claiming that epitaxial bilayer graphene (EBLG) on 6H-SiC(0001) shows Bernal (AB) stacking, where two adjacent layers are laterally displaced like in bulk graphite, rather than AA stacking, where the carbon atoms of adjacent layers are placed at the exact same lateral position. However, the experimental proof was recently provided by Razado-Colambo *et al.* [44], who also report that the distance between the first graphene layer and the buffer layer is smaller while the interlayer spacing of the adjacent graphene layers is larger than the interlayer distance of bulk graphite (3.35 Å) [44].

The band structure close to the K point of EBLG can be calculated from a TB approach by applying a potential energy difference across the films [41]. As presented in fig. 2.3(a), an electronic gap is apparent in the calculated band structure (solid lines) that is not expected for freestanding bilayer graphene (dashed lines). The former touching bands develop a Mexican-hat-like dispersion near the band edges [25, 45]. A recent ARPES study investigating 1.2 monolayers graphene on SiC(0001) revealed that this dispersion is overestimated. The band is rather flat (dispersion $< 2\,\text{meV}$ for $\pm 0.017\,\text{Å}^{-1}$) and intense in the ARPES data near the K point [42]. This observation will become important later in this work.

As already mentioned above, the graphene lattice is describable by two different sublattices of A and B atoms (cf. fig. 2.1). In Bernal stacked bilayer graphene an A atom of the top layer (A_T) is located above a B atom of the bottom layer (B_B), while the A atom of the bottom layer (A_B) is located at a hollow site of the top hexagonal lattice. The band structure shown in fig. 2.3(a) also indicates where the respective bands are located in real space [46]. The flat dispersion in the band structure leads to van Hove singularities that strongly increase the density of states

---

[b] also for higher numbers of graphene layers

(DOS) at the gap edges [47], as shown in 2.3(b). The locally resolved contributions to the total DOS will be of particular importance for the interpretation of tunneling spectra in this work.

SiC is a semiconductor with a relatively large band gap of about 3 eV [48, 49].[c] Its conduction and valence bands are energetically well separated from E_F and E_D of epitaxial bilayer graphene [23, 50].[d] Therefore, Ohta *et al.* conclude that EBLG on SiC(0001) can be treated as a two-dimensional semimetal, because the bilayer graphene states are practically decoupled from the substrate [23].

2.3 Doping of Graphene Compounds

The electronic properties of graphene, bilayer (few-layer) graphene, and also graphite can be modified. For instance, the band gap of epitaxially grown bilayer graphene on SiC(0001) is tunable by gating [51] or chemical doping [23]. In this thesis, particular attention is placed on chemical doping methods. For example, *p*-doping can be realized by deposition of the acceptor molecule F_4TCNQ[e] on epitaxial mono- and bilayer graphene to compensate for the intrinsic doping induced by the SiC substrate, such that charge neutrality can be achieved for graphene [52, 53]. The latter can also be realized by hydrogen intercalation, where the dangling Si bonds that are covalently bound to C atoms of the buffer layer are saturated with hydrogen. Consequently, the C atoms of the buffer layer are detached and create an additional graphene layer [54].

In this work, the main focus is placed on *n*-doping methods upon intercalation of alkali metal and alkaline earth metal atoms that potentially promote the appearance of superconductivity of graphene. In particular, the properties upon potassium (K) intercalation shall be discussed in comparison to lithium (Li), calcium (Ca), and rubidium (Rb) intercalation as well as in dependence of the number of graphene sheets. The first part of this section focuses on the discussion of highly ordered structures of the intercalants that are reported to appear for different numbers of carbon sheets ranging from BLG up to the bulk limit (graphite). The second part deals with the particular intercalation dynamics of thinner epitaxial graphene films on SiC(0001), where the comparison to further atomic species of intercalants is necessary.

Graphite intercalation compounds (GICs) have been extensively studied in the past. The K atoms (also Rb) form of a lateral (2×2) structure with respect to the graphene lattice [55] as depicted in fig. 2.4(a). By contrast, the intercalation of Ca and Li leads to a different, more densely packed, $(\sqrt{3} \times \sqrt{3})\mathrm{R}30^\circ$ superstructure with respect to the graphene lattice [3, 55]. The same lateral structures are observed for intercalated (epitaxial) few- and bilayer graphene (K [56], Rb [57], Li [58], Ca [58]). However, the metal atoms intercalating graphene monolayers on various substrates did in most cases not exhibit any highly ordered lateral structure [59–61]. Only one

---

[c] Slight variations occur for different polytypes.

[d] The SiC valence band is located about 2.6 eV below E_F and the conduction band about 0.4 eV above [23, 50].

[e] tetrafluoro-tetracyanoquinodimethane

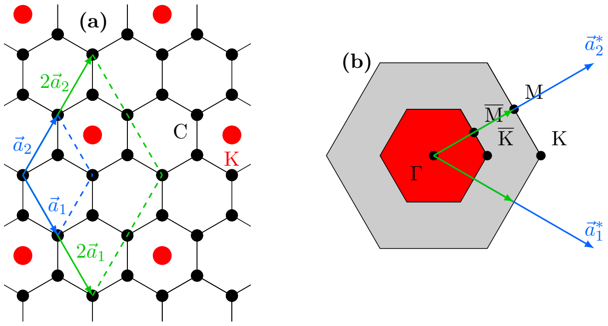

Figure 2.4: (a) Top view of the real space of K-intercalated graphene. K atoms (red circles) are located at hollow sites of the graphene lattice (black). The unit cell that describes the entire lattice is defined by the vectors $2\vec{a}_1$ and $2\vec{a}_2$ (green) which are twice as large compared to the graphene unit cell (blue). (b) The SBZ of the K-intercalated graphene lattice (red) shrinks compared to the BZ of the graphene lattice (gray) due to the reduction of the reciprocal lattice vectors (green) compared to the graphene lattice (blue).

recent study achieved a (2×2) superstructure of Rb atoms deposited on a monolayer graphene sample on SiC(0001) produced by prior hydrogen intercalation of the buffer layer [62].

The carbon sheets of bulk graphite crystals are usually stacked in an AB (Bernal) manner [55] and bound by weak van der Waals forces, with a layer separation of ≈ 3.35 Å [63]. Upon intercalation, where the metal atoms penetrate between the single graphene sheets, the distance of two adjacent graphene layers increases. Due to the different size of the metal ions, the interlayer spacing takes different values, e.g., 5.4 Å for K [64] and 4.5 Å for Ca [65]. Furthermore, it was reported that intercalation causes a change from AB to AA stacking [4], allowing the metal atoms to be attached to the hollow sites of the honeycomb lattice of both neighboring sheets. In so-called stage-1 GICs every interspace between adjacent graphene sheets is populated with intercalants. Due to the consequential stoichiometry, the (2×2) superstructure is mostly referred to as MC_8 (here: M=K, Rb) in the literature, while the $(\sqrt{3} \times \sqrt{3})R30°$ superstructure is referred to as MC_6 (here: M=Li, Ca). According to Emery *et al.*, the type of arrangement of the metal atoms is closely related to the interlayer distance. In particular, MC_8 is formed for interlayer distances $d > 5.3$ Å, while the more densely packed MC_6 arrangement emerges for smaller distances [65].

Theoretical calculations of metal intercalants between two carbon sheets of freestanding bilayer graphene suggest that AA stacking is always more stable than AB stacking, with slightly modified interlayer distances compared to GICs [66]. Additional consideration of a SiC substrate in the theoretical models causes a notable decrease of the interlayer distance, as shown for the particular case of K-intercalated epitaxial graphene [67].[f] The fact that there is only one layer of metal intercalants between two graphene sheets leads to a modified stoichiometry of 16 and 12

---

[f] Note that in the work of Kaloni *et al.* a different nomenclature is used. There, the term bilayer graphene on SiC refers to two carbon layers, where the lower C sheet is covalently bound to the SiC substrate (denoted as buffer layer in this work). Therefore, the case of epitaxial bilayer graphene in this thesis needs to be compared to trilayer graphene of the calculations in ref. [67].

carbon atoms per metal atom in the highly ordered (2 × 2) and ($\sqrt{3} \times \sqrt{3}$)R30° superstructure, respectively. Therefore, metal-intercalated bilayer graphene is referred to as C_8MC_8 and C_6MC_6, respectively.

While theoretical approaches presume that the M atoms are trapped between both graphene sheets of BLG, it is still under debate where the intercalated atoms actually reside, namely, on top of the graphene bilayer, in the graphene-graphene interlayer, or even in the graphene-buffer interlayer. For Li-intercalated BLG on SiC(0001), where a change from Bernal to AA stacking was observed [68], intercalants are assumed to accumulate between the graphene sheets, which was concluded from the absence of an ordered structure of Li-intercalated EMLG on SiC(0001), however, under the assumption that M atoms could only adsorb on top or between buffer and graphene layer [7, 58, 69]. Kanetani *et al.* assume that C_6CaC_6 fabricated by substitution of the highly ordered Li-intercalated structure exhibits the same adsorption sites [58]. On the contrary, in a recent study, in which Ca was directly intercalated (without substitution of Li) into the epitaxial BLG, Endo *et al.* revealed that there is no stacking shift and the Ca atoms are placed in the graphene-buffer interlayer [70]. Thus, the location of the metal intercalants is still under debate. Moreover, it is still unclear how atoms can pass the impermeable graphene layer during the intercalation process. It was suggested that they pass at boundaries of different domains since the films consist of areas with variable thickness [71].

Besides structural modifications, the intercalation of alkali metal and alkaline earth metal atoms into graphene-based systems causes significant changes of the electronic structure. The donation of additional charges to the graphene sheets leads to an occupation of formerly unoccupied electronic levels. Consequently, the Dirac point at E_D shifts to higher binding energies away from the Fermi level E_F. As presented in tab. 2.1 (first row), the experimentally determined values of E_D for the highly ordered superstructures of GICs exhibit a clear dependency on the intercalant atom species used. This is a direct consequence of the ionization potential of the respective metal, but does also depend on the particular atomic size, the consequential layer separation and, thus, the superstructure. The reported shifts of the Dirac point seem to be even more pronounced in the case of EBLG as shown in the second row of tab. 2.1, although the ratio of metal intercalants to carbon atoms is smaller in this case. This implies that other effects besides sole charge donation play a crucial role in the intercalation process. In particular, no value for the highly ordered superstructure of K-intercalated EBLG has been reported thus far.

Table 2.1: Comparison of experimentally determined Dirac energies E_D reported in the literature for highly ordered structures of different atomic species between graphite and bilayer graphene. References are provided for each value.

	E_D(Li)	E_D(Ca)	E_D(K)	E_D(Rb)
GIC	0.825 eV [72]	1.0 – 1.5 eV [17]	1.35 eV [72]	n/a
BLG	1.4 eV [58, 69]	≈ 2.0 eV [58]	n/a	1.0 eV [57, 73]

Ohta *et al.* reported a gradual shift of the Dirac point of EBLG to higher binding energies upon increasing potassium concentrations [23]. Interestingly, the energy gap of pristine EBLG (0.005 electrons per unit cell), already mentioned above, closes for higher potassium concentrations (0.0125 electrons per unit cell) and reopens upon additional increase (0.035 electrons per unit cell). This phenomenon can be explained by different charge carrier concentrations in the adjacent graphene layers and the consequentially induced electrostatic field [43]. At the highest reported electron concentration, the Dirac point is located at about 0.6 eV below the Fermi level, while no structural order of the intercalants is mentioned. Additionally, Ohta *et al.* propose an increased overlap of the π bands of adjacent graphene layers for higher electron densities [23].

Besides the shift of the Dirac point, an additional filling of IL bands is reported for some intercalation compounds. Those bands develop from originally unoccupied bands of (stacked) graphene or graphite that originate from wave functions that are localized between adjacent graphene layers. Moreover, IL bands exhibit a parabolic dispersion located at the Γ point with a circular Fermi surface [7]. Those bands were reported for C_8RbC_8 [57] and C_6CaC_6 [74], while in the latter case a dispersion along $k_\perp$ was determined via ARPES, which depicts that IL bands exhibit a 3D character.

If compounds exhibit an ordered lateral superstructure upon intercalation, an additional effect occurs that modifies the electronic structure, especially when monitored via ARPES. As shown in fig. 2.4(b) at the example of a (2×2) superstructure, the enlarged unit cell in real space causes a reduction of the SBZ size in momentum space. Consequentially, the electronic bands are folded back into the smaller SBZ. Upon symmetry considerations that will be given in detail in sec. 4.2, in the case of an additional (2×2) superstructure the K point of the former SBZ is folded back to the $\overline{\mathrm{K}}$ point of the smaller SBZ. Additionally, for this superstructure the M point appears also at the Γ point of the SBZ. This effect has been shown experimentally for Rb-intercalated mono- [62] and bilayer graphene [57]. The $(\sqrt{3} \times \sqrt{3})\mathrm{R}30^\circ$ superstructure with respect to the graphene lattice of Ca and Li intercalation compounds causes similar effects. Due to the different symmetry, however, the K point is folded back to the center of the SBZ as shown via ARPES measurements for Ca and Li [58, 69].

For Li [75, 76] and Cs [77] intercalation of EMLG (without annealing), ARPES data recorded near the K point of the SBZ shows two occupied π bands with its Dirac points both shifted to higher binding energies compared to the pristine sample. This is unexpected, because EMLG samples possess only one graphene sheet that can be doped by the intercalant atoms and, accordingly, only one π band should be observed. Upon intercalation of EMLG with atoms other than Li and Cs, indeed only one π band is observed with E_D shifted to higher binding energies (Na [78], Rb [77], Eu[g] [79]) or even no modifications compared to the pristine sample (Al [80], Yb [81, 82]). Upon mild annealing ($T \lesssim 500\,^\circ\mathrm{C}$), however, the electronic structure appears qualitatively similar for all mentioned intercalants. Two π^* bands are observed in all

---

[g] Gap observed in as-deposited and slightly annealed sample.

cases, one located at the position comparable to the pristine sample and one at significantly higher binding energies, whereas the absolute values of E_D of the high-binding-energy band differ for different intercalants. Further annealing at $T \gtrsim 500\,°\mathrm{C}$ is reported to result in an electronic structure comparable to the pristine sample with only one observed π^* band, but in some cases slightly shifted to even lower binding energies [80].

Especially the observed electronic structure that emerges upon mild annealing is in most studies explained by penetration of metal atoms into the interlayer between the SiC substrate and the buffer layer. Consequently, the buffer layer is effectively decoupled from the SiC substrate and, thus, develops graphene-like π bands [78, 81, 83] similar to hydrogen intercalation [31], but strongly n-doped. This argument is often supported by vanishing diffraction features that are usually assigned to the structure of the buffer layer of in the pristine sample. Additional features that suggest a highly ordered structure of the intercalants are not observed at this stage [80, 81]. In several cases this is accompanied by a shift of the C 1s core level component assigned to carbon atoms of SiC to lower binding energies (e.g., Cs [77], Na [78], Al [80]), but is not always apparent (e.g., Rb [77]).

The buffer layer decoupling was proven experimentally via intercalation of ZLG with ytterbium (Yb) [84] and terbium (Tb) [82]. There, a single π band is observed with a Dirac point at binding energies comparable to high-binding-energy band in the mildly annealed samples. In the case of Yb intercalation of ZLG, the diffraction features assigned to the buffer layer do not vanish, but appear severely weakened. Upon further annealing, a $(\sqrt{3}\times\sqrt{3})\mathrm{R}30°$ superstructure with regard to the graphene lattice appeared in the diffraction pattern [84].

Theoretical calculations further substantiate the experimental observations using the example of Yb-intercalated EMLG [85]. In particular, the electronic structure of the mildly annealed sample can be assigned to a configuration, where Yb atoms are solely located between the SiC and the former buffer layer. If the atoms also populate the interspace between both graphene layers, the π band at low binding energies is shifted to higher values, so that the energy difference between the Dirac points of both π bands is small. Similar results are also achieved with density functional theory (DFT) calculations of Li-intercalated EMLG [76].

It is likely that decoupling of the buffer layer might also occur in EBLG samples when the dopant concentration is large enough. The effect of buffer layer decoupling upon K intercalation of EMLG has not been observed yet. Bostwick *et al.* determined a rigid shift of the Dirac point to higher binding energies that scales with the K content [86, 87]. Yet, in this study the K atoms were deposited at low temperatures of about 20 K [86, 87].

In summary, the number of adjacent graphene layers, the substrate, the intercalant species, and annealing of the sample all have a significant impact on the resulting electronic structure of the graphene-based systems upon metal intercalation. Therefore, a thorough consideration and characterization of all influencing factors is mandatory for a comparison of similar systems.

Some metal-intercalated graphene-based materials are reported to be superconductors. Thus, relevant general aspects of superconductivity are reviewed in the following, before the specific properties of graphene-based superconductors are discussed.

2.4 Superconductivity

Superconductivity is a quantum mechanical phenomenon characterized by two macroscopically traceable effects. Firstly, the electrical resistance of superconducting materials drops down to zero at a certain temperature [88]. Below this critical temperature T_c, the resistance remains unmeasurable and the specimen behaves like an ideal conductor [89]. Secondly, in 1933 Meissner and Ochsenfeld discovered that the magnetic field within a superconductor is always zero, independent of the applied cooling procedure [90]. Superconductors therefore act like perfect diamagnets which is not to be confused with merely ideal conductivity. If an external magnetic field is applied to a hypothetical ideal conductor (but not a superconductor) below T_c, according to Lenz's law a current is induced that generates a magnetic field of opposed direction. Hence, the effective field within the ideal conductor is zero. The situation changes if the magnetic field is applied at $T > T_c$. Due to the finite resistivity, the magnetic field penetrates into the ideal conductor. Upon subsequent cooling below T_c, the magnetic field remains in the specimen [89].

2.4.1 Microscopic Theory of Classical Superconductors

The statements provided in this section are adapted from refs. [89, 91], if not referenced otherwise.

The first theory of superconductivity based on microscopic mechanisms was presented by Bardeen, Cooper, and Schrieffer and is therefore called BCS theory [92, 93]. It is based on an attractive interaction of two electrons via phonon coupling within a solid.

Below the critical temperature, an electron with wave vector $\vec{k}_1$ moving through the solid is able to excite a lattice vibration (phonon) with a wave vector $\vec{q}$ that did not exist before. Consequently, the electron occupies a new state with the wave vector $\vec{k}_1^{\prime} = \vec{k}_1 - \vec{q}$. A second electron with $\vec{k}_2$ can absorb the phonon $\vec{q}$ almost instantly and it follows that $\vec{k}_2^{\prime} = \vec{k}_2 + \vec{q}$ due to momentum conservation. The total momentum adds up to

$$\vec{k}_1 + \vec{k}_2 = \vec{k}_1^{\prime} + \vec{k}_2^{\prime}. \tag{2.1}$$

This mechanism is only possible if the electronic state with the wave vector $\vec{k}_1^{\prime}$ is unoccupied. Therefore, this process can only occur in a small region of the k space around the Fermi surface. The thickness $2\Delta k$ of the spherical layer in k space, where an attractive interaction of two electrons is possible (cf. fig. 2.5(a)) is directly related to the Debye frequency ω_{D}. The attractive

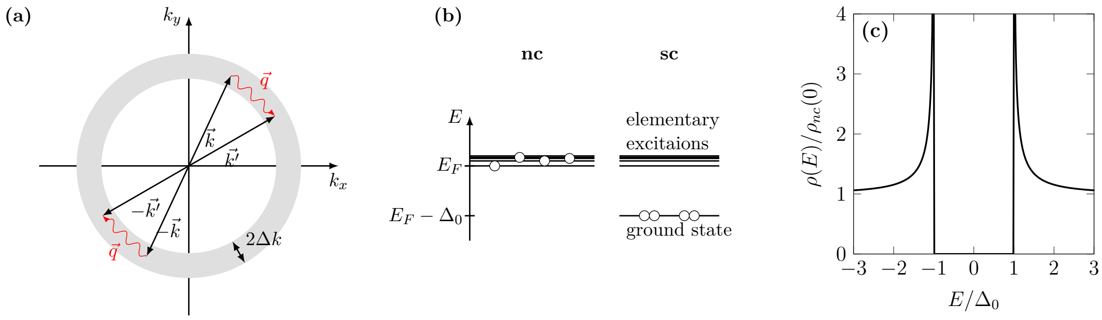

Figure 2.5: (a) Electron pairing mechanism according to the BCS theory. Attractive interactions are possible within a spherical layer with a thickness of $2\Delta k$ near the Fermi surface by virtue of a phonon $\vec{q}$. (b) Population of electronic states in the normal conducting (nc) state (left) and formation of electron pairs in the BCS ground state leading to the superconducting (sc) state (right). (c) DOS of a superconductor near the Fermi level. Adapted from ref. [89].

interaction of two fermions is enhanced with increasing overlap of the spheres of each electron in momentum space and reaches its maximum when those spheres perfectly coincide. This is the case when the total momentum is zero and thus the electron pair $(\vec{k}, -\vec{k})$ scatters to a state $(\vec{k}', -\vec{k}')$ via phonons.[h] Those attractively interacting electron pairs $(\vec{k}, -\vec{k})$ are called Cooper pairs. Upon pairing, the electrons condensate in an energetically more favorable ground state. Due to the boson character of the Cooper pairs (composed of two fermions), all paired electrons are able to occupy the same state as illustrated in fig. 2.5(b). Electronic single-particle excitations have to be provided by Cooper-pair breakup, i.e., an energy of at least $2\Delta_0$ is required. Consequently, superconductors exhibit a symmetric energy gap of $2\Delta_0$ around the Fermi level. The general expression for the DOS $\rho_{sc}(E)$ of a superconductor can be deduced from the requirement that during the transition from the normal-conducting to the superconducting state the total number of states has to be conserved. In consideration of the single-particle kinetic energy ξ (with regard to the Fermi level) that is defined by $E = \sqrt{\xi^2 + \Delta_0^2}$ the DOS in the superconducting state at $T = 0$ can be expressed via [91]

$$\rho_{sc}(E) = \rho_{nc}(\xi) \cdot \frac{d\xi}{dE} = \rho_{nc}\left(\pm\mathrm{Re}\left[\sqrt{E^2 - \Delta_0^2}\right]\right) \cdot \mathrm{Re}\left[\frac{|E|}{\sqrt{E^2 - \Delta_0^2}}\right], \tag{2.2}$$

where ± accounts for the occupied and unoccupied branches of the DOS. Usually, $\rho_{nc}(E)$ is assumed sufficiently flat in the region of the Fermi level ($\rho_{nc}(\xi) \approx \rho_{nc}(E_F = 0) = \text{const.}$). On that basis, $\rho_{sc}(E)$ simplifies to [89, 91]

$$\rho_{sc}(E) = \rho_{nc}(0) \cdot \mathrm{Re}\left[\frac{|E|}{\sqrt{E^2 - \Delta_0^2}}\right]. \tag{2.3}$$

The resulting DOS is presented in fig. 2.5(c). There are no contributions to the DOS within the energy gap and further two sharp singularities (coherence peaks) located at $\pm\Delta_0$.

---

[h] Note that the interacting electrons carry opposite spin directions.

While the gap parameter Δ_0 refers to $T = 0\,\mathrm{K}$, the actual gap $\Delta(T)$ exhibits a dependency on the respective temperature which is implicitly given by the gap equation [89]:

$$\frac{1}{\rho_{nc}(0)V} = \int_0^{\hbar\omega_\mathrm{D}} \frac{d\varepsilon}{\sqrt{\varepsilon^2 + \Delta^2(T)}} \tanh\left[\frac{\sqrt{\varepsilon^2 + \Delta^2(T)}}{2k_\mathrm{B}T}\right], \tag{2.4}$$

where V is the interaction potential of pairing electrons and k_B is the Boltzmann constant. Instead of solving this implicit formula numerically, an approximative relation is used in this work that is sufficient to satisfy the gap equation with regard to experimental errors [94]:

$$\Delta(T) = \Delta_0 \tanh\left[1.82\left(1.018\left(\frac{T_c}{T} - 1\right)\right)^{0.51}\right]. \tag{2.5}$$

For $T \to 0\,\mathrm{K}$ the gap parameter tends towards Δ_0, while the size decreases with increasing temperature and vanishes entirely for $T \geq T_c$. Within the limitations of the BCS theory there is a well-defined relation between Δ_0 and T_c that is commonly referred to as gap ratio [89]:

$$\frac{2\Delta_0}{k_\mathrm{B}T_c} = 3.52. \tag{2.6}$$

The BCS theory considers isotropic interactions with spherical wave functions of the Cooper pairs (angular momentum equals zero). The pairing mechanism is therefore referred to as s-wave pairing in the literature. However, some superconductors exhibit different pairing symmetries. For instance, d-wave pairing leads to an anisotropically altered DOS around the Fermi level with electronic states even within the gap [95] and further a modified gap ratio of 4.28 [96].

2.4.2 Eliashberg Theory

The statements given in this section are adapted from ref. [97], if not referenced otherwise.

Even if the BCS theory provides a qualitative explanation for superconductivity on a microscopic basis, its quantitative predictions deviate for actual superconductors. This stems from the fact that the characteristic phonon energy $\hbar\omega$ considered in this model is much higher than the typical superconducting energy $k_\mathrm{B}T_c$. To overcome those deviations, Eliashberg introduced an enhanced theoretical model in 1960 by using a formal Green's function approach that takes strong electron-phonon interactions into account [98]. A detailed discussion of this theory is beyond the scope of this thesis. Nevertheless, some assumptions and conclusions will be discussed in the following.

The main idea of the Eliashberg approach is to apply a spectral function $\alpha^2F(\omega)$ that includes the interaction between electrons and phonons. Thereby, $\alpha^2(\omega)$ describes electron-phonon coupling (squared because two electrons are coupled) and $F(\omega)$ the phonon distribution. In general, $\alpha^2F(\omega)$ can also exhibit an explicit $\vec{k}$ dependence in materials with anisotropic phonon dispersions. As a dimensionless measure of the coupling strength, the so-called mass enhancement factor λ is given by [99]:

$$\lambda_{\vec{k}}(\omega) = 2\int_0^{\omega} d\omega' \frac{\alpha^2 F(\vec{k},\omega')}{\omega'}, \tag{2.7}$$

with $\lambda_{\vec{k}} \equiv \lambda_{\vec{k}}(\omega \to \infty)$ at a given $\vec{k}$, which is also referred to as EPC constant in the literature. To additionally account for the effective electrostatic repulsion between coupled electrons, the dimensionless Coulomb pseudopotential μ^* is introduced. The improved theory predicts that the energy gap shows a frequency dependence $\Delta = \Delta(\omega)$. This modifies the shape of the DOS compared to BCS theory. However, the DOS within the gap remains zero, whereas the appearance outside the energy gap alters slightly.

The mass enhancement factor and the Coulomb pseudopotential are related to the critical temperature by the McMillan formula [100]:

$$T_c = \frac{\langle\Theta\rangle}{1.45} \exp\left(-\frac{1.04(\lambda+1)}{\lambda-(0.62\lambda+1)\mu^*}\right), \tag{2.8}$$

where $\langle\Theta\rangle$ is the Debye temperature that is defined by

$$\langle\Theta\rangle = \frac{2}{k_B}\int_0^{\infty} d\omega \frac{\alpha^2 F(\omega)}{\lambda}. \tag{2.9}$$

Values of μ^* typically range from 0.10 to 0.15 [101]. The McMillan formula is also valid in the BCS limit of weak electron-phonon coupling, but the stronger the coupling gets, the larger are the deviations from the BCS theory. Therefore, the Eliashberg theory is often referred to as strong-coupling theory, where the term „strong coupling“ implies that the phonon energies are in the same order of magnitude as $k_\mathrm{B}T_c$. Allen and Dynes introduced a logarithmically weighted phonon frequency [102]:

$$\omega_\mathrm{ln} = \exp\left(\frac{2}{\lambda}\int_0^{\infty}\frac{d\omega}{\omega}\alpha^2 F(\omega)\ln\omega\right) \tag{2.10}$$

that additionally modifies the McMillan formula for better results in the strong-coupling limit [103]:

$$k_B T_c = \frac{\hbar\omega_\mathrm{ln}}{1.2}\exp\left(-\frac{1.04(\lambda+1)}{\lambda-(0.62\lambda+1)\mu^*}\right). \tag{2.11}$$

Moreover, the fixed gap ratio of the BCS theory in eq. (2.6) is also modified by strong coupling in the following way [104]:

$$\frac{2\Delta_0}{k_B T_c} = 3.53\left[1 + 12.5\left(\frac{k_B T_c}{\hbar\omega_\mathrm{ln}}\right)^2 \ln\left(\frac{\hbar\omega_\mathrm{ln}}{2k_B T_c}\right)\right]. \tag{2.12}$$

For the quantitative analyses presented in this thesis, equations (2.7), (2.8), and (2.12) are of particular importance.

2.5 Phonons of Graphene

Since quantized lattice vibrations (phonons) of a solid mediate superconductivity, the phonon properties of graphene shall be reviewed here. The calculated phonon dispersion of a single freestanding graphene sheet is presented in fig. 2.6(a). Various phonon modes are apparent up to a maximal energy of about 200 meV [105]. In-plane longitudinal and transverse modes are labeled with L and T, respectively, out-of-plane modes with Z, while A and O denote acoustic and optical phonons. Particularly, it is worth mentioning that ZA modes exhibit a parabolic dispersion relation near the Γ point, and calculations predict a crossing of ZA and ZO modes at the K point reminiscent of the crossing in the electronic band structure. The associated phonon density of states (PhDOS) (black curve in fig. 2.6(b)) exhibits pronounced peaks at energies, where the phonon dispersion is considerably flat. For freestanding bilayer graphene (red curve in fig. 2.6(b)) the intensity of the complete spectrum, besides ZA modes, is doubled compared to MLG. Those phonon modes occur in both adjacent graphene layers of the AB-stacked BLG system and, thus, are nearly two-fold degenerate [106]. The low-energy mode at about 12 meV is only observed in the PhDOS of BLG and stems from vibrations that are enabled by the presence of both sheets (additional ZA mode) [106]. Upon intercalation of BLG, especially those out-of-plane modes are expected to change, due to the modified interlayer distance mentioned above. However, theoretical studies predict low-energy phonon modes also in metal-intercalated BLG (AA-stacked). In particular, an out-of-plane vibration at about 9 meV of C_8KC_8 is expected [66]. The mentioned phonon modes are of major relevance for the analyses of tunneling spectra of pristine and K-intercalated graphene presented in sections 4.1 and 4.3, respectively, as well as for the determination of the EPC strength in sec. 5.2.

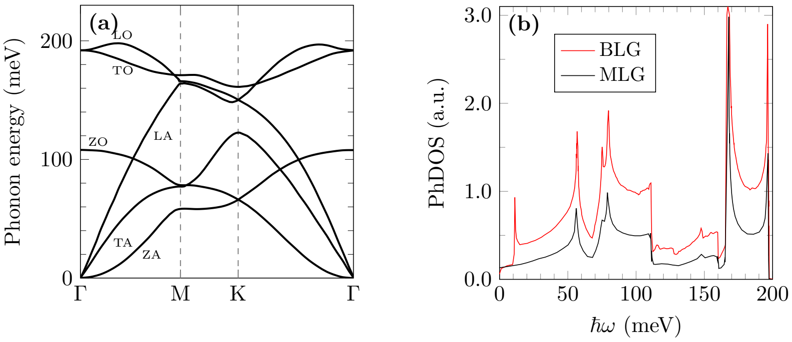

Figure 2.6: (a) Phonon dispersion of freestanding graphene. Digitized and reprinted from ref. [105]. (b) PhDOS of freestanding MLG and AB-stacked BLG. Digitized and reprinted from refs. [106, 107].

2.6 Experimental Proof of Superconductivity

Experimentally, there are three commonly used direct ways of proving a sample to be a superconductor. Firstly, the behavior of the magnetization of a specimen is tracked while it is cooled in an external magnetic field (field cooling) and without the magnetic field (zero field cooling). According to the Meissner-Ochsenfeld effect, the magnetization of the sample must exhibit a sharp drop at the critical temperature in both cases. Secondly, if the resistance of a sample can be assessed (which is not always trivial) then it must vanish upon cooling below the critical temperature. Thirdly, it is possible to prove the existence of a superconducting gap that develops according to eq. (2.5) upon cooling. For this purpose, high-resolution scanning tunneling spectroscopy (STS) or photoelectron spectroscopy (PES) are appropriate experimental methods. Note that the mere determination of the mass enhancement factor λ (see eq. (2.7)) can only indicate the possibility of superconductivity, but does not prove it.

2.7 Superconductivity of Graphene Compounds

Monolayer and multilayer graphene exhibit superconductivity upon modification of its intrinsic electronic structure in various ways. A recently discovered opportunity for creating a superconducting state is to twist the adjacent layers of BLG by a “magic angle“ of 1.1°. This induces the formation of flat half-filled bands near the Fermi level. Additional electrostatic doping leads to observations of zero-resistance with critical temperatures up to 1.7 K [1, 2]. However, the electronic structure of twisted BLG strongly deviates from intercalation compounds (cf. sec. 2.3). Thus, the mechanism responsible for superconductivity of twisted BLG is most likely different and is therefore not further discussed here. Superconductivity induced via the proximity effect by placing multilayer graphene on a superconducting substrate [108] is also irrelevant in this thesis for the same reason.

The modification of graphene stacks with different thickness upon alkali metal and alkaline earth metal intercalation supports the development of a superconducting state for some combinations. Table 2.2 summarizes the highest reported critical temperatures for different intercalant and graphene thickness combinations. The highest transition temperature so far has been reported for Ca-intercalated graphite. However, Ca intercalation compounds show a clear trend of decreasing critical temperatures by reducing the number of adjacent graphene layers[i] [3–6, 109]. Reliable data concerning superconductivity of Ca-intercalated MLG is not available yet. Upon Li decoration, however, a transition to the superconducting state was reported at the monolayer limit [99]. Despite this, the bulk counterpart does not show any evidence of superconductivity [72]. For K-intercalated graphite the reported critical temperatures vary slightly, e.g., 550 mK [9], 390 mK [72], $128 - 198$ mK [64], but all are markedly lower than the Ca-intercalated counterpart. Surprisingly, Xue *et al.* determined a transition temperature of 4.5 K for K-intercalated few-layer graphene [10]. Accordingly, the relation between number of layers and critical temperature is seemingly reversed in comparison to Ca-intercalated compounds.

---

[i] Note that the number of adjacent graphene layers is not well defined for few-layer graphene and not determined in several studies. Broadly speaking, the term few-layer graphene corresponds to samples with three to ten adjacent graphene layers.

Table 2.2: Highest reported, experimentally determined critical temperatures T_c for different graphene-based materials upon intercalation with different metals. References are provided with each value.

Metal	Monolayer	Bilayer	Few-layer	Bulk
Ca	n/a	4 K*** [6]	7 K* [5]	11.5 K* [3, 4]
Li	5.9 K** [99]	n/a	7.4 K* [8]	ns [7]
K	n/a	n/a	4.5 K* [10]	0.55 K* [9]
Rb	n/a	n/a	n/a	0.15 K* [9]

Techniques: *Magnetization, **ARPES, ***Magnetization and resistance
ns = not superconducting

The mechanisms leading to superconductivity in all types of metal-intercalated graphene-based compounds are still not fully understood and are a matter of ongoing debate in the literature. Since superconductivity is neither an intrinsic property of (few-layer) graphene or graphite nor of the bulk counterparts of the intercalation metals (at least not under ambient pressure [91]), the interplay of both materials is responsible for this effect. It is further widely believed that the superconductivity is driven by the carbon layers, while the intercalants donate the necessary charge to the π^* states [67, 72, 110]. Moreover, in the special case of CaC_6 the existence of an IL band is claimed to be mandatory for the superconductivity [17], while electron-phonon pairing on both, IL and π^* bands is essential to explain its high critical temperature [74]. The discovery of higher T_c's of Li- and K-intercalated few-layer graphene compared to the bulk counterparts was explained by low-dimensional effects [8, 10]. Due to the usually smaller separation of adjacent graphene layers in bulk GICs, the electron-phonon coupling in bulk samples is enhanced, which suggests higher critical temperatures. When the distance, however, is too small, confinement of the interlayer state shifts the related bands above the Fermi level. As a result superconductivity is suppressed (LiC_6) [7, 72]. In the case of Li-intercalated MLG this confinement is removed and superconductivity is apparent [7, 99]. In summary, the superconductivity of layered, graphene-based compounds is supposed to depend on the existence of an IL band as well as the layer separation, and, therefore, on the intercalant atom and number of adjacent graphene layers.

For all graphene-based intercalation compounds that show superconducting properties, theoretical studies predict the existence of intercalant-induced low-energy out-of-plane phonon modes [11, 12, 110–113]. Since low-energy modes contribute strongest to the electron-phonon coupling (cf. eq. (2.7)), they are supposed to be crucial for the explanation.

Electron-phonon coupling can be determined experimentally via ARPES, which will be addressed in detail later. Many studies regarding various combinations of metal intercalants and graphene-based systems are available [12, 14, 16, 59, 61, 62, 73, 74, 99]. While some studies verify the known critical temperatures, others predict deviating values. This stems from the fact that the analysis of the measured data is rather complex and the results deviate upon the used method and assumptions applied. Moreover, the exact measured position in k space is of relevance since some studies report strong anisotropy of the electron-phonon coupling on the Dirac cone [12, 14, 16, 61, 62, 73, 74].

Besides anisotropic electron-phonon coupling the existence of multiple band gaps is suggested that originate from pairing on different Fermi surfaces [111]. Moreover, there are many possible pairing mechanisms that have been considered besides conventional s-wave pairing [114], for instance, p+ip [114], d [115], d+id [116], and f-wave pairing [116]. Among the intercalation compounds considered here, studies that prove the existence of a temperature-dependent energy gap via tunneling spectroscopy are only available for bulk CaC_6. Both studies do not find significant evidence of anisotropy, multiple gaps, or deviations from s-wave symmetry that would lead to the conclusion of an alternative pairing mechanism. However, the determined energy gaps deviate in size ($\Delta(0) = 1.6\,\text{meV}$ [18] and $\Delta(0) = 2.3\,\text{meV}$ [19]). Consequently, the authors of ref. [18] report on a gap ratio of 3.7 that suggests electron-pairing in almost weak-coupling limit. Contrary, in ref. [19] an enlarged gap ratio of about 4.6 is determined, which leads to the conclusion that CaC_6 is a strongly coupled superconductor. Therefore, further scrutiny is required to sort out such seemingly contradicting results.

3 Experimental Methods

3.1 Photoelectron Spectroscopy

3.1.1 Single-Particle Picture

Photoelectron spectroscopy (PES) is a commonly used experimental technique that allows conclusions about the electronic and chemical properties of a specimen. The working principle is based on the external photoelectric effect, stating that an electron can be emitted from gases or solid surfaces upon absorption of a photon with the energy $h\nu$. The energy balance of this process is given by the Einstein equation [117]:

$$E_{\text{kin}} = h\nu - \Phi_s - E_B, \tag{3.1}$$

where Φ_s is the work function of the specimen, E_B the binding energy of the electron, and E_{kin} the kinetic energy of the emitted electron analyzed in the detector.

Besides the energy dependence, it is further possible to analyze the emitted photoelectrons with angular resolution. Therefore, the photoelectron current is determined as a function of the polar θ and azimuth angle ϕ between detector and sample surface. This can be achieved by variation of the tilt and rotation of the specimen with respect to the electron analyzer. The polar angle is directly related to the modulus of the electron momentum $\hbar\vec{k}$ in the sample. The perpendicular component

$$|\vec{k}_\perp| = \sqrt{\frac{2m^*}{\hbar^2}}\sqrt{E_{\text{kin}}\cos^2\theta + V_0} \tag{3.2}$$

is affected by the unknown inner potential V_0 and effective mass m^*, and is generally not conserved at the sample-vacuum interface. Otherwise, the parallel component

$$|\vec{k}_\parallel| = \sqrt{\frac{2m_e}{\hbar^2}}\sqrt{E_{kin}}\sin\theta \tag{3.3}$$

is conserved and does only depend on known quantities [118]. Splitting $\vec{k}_{\parallel}$ into Cartesian components yields [119]:

$$\begin{aligned}|\vec{k}_x| &= \sqrt{\frac{2m_e}{\hbar^2}}\sqrt{E_{kin}}\sin\theta\cos\phi,\\ |\vec{k}_y| &= \sqrt{\frac{2m_e}{\hbar^2}}\sqrt{E_{kin}}\sin\theta\sin\phi.\end{aligned} \tag{3.4}$$

Different types of PES are distinguished based on the energy of the incident photons. For ultra-violet photoelectron spectroscopy (UPS) electromagnetic radiation in an energy range between 10 and 100 eV is used. This range enables photoemission from the valence band region. Upon variation of the polar angle, mostly used along a high-symmetry direction of the BZ, the dispersion of an electronic band can be tracked, called angle-resolved ultra-violet photoelectron spectroscopy (ARUPS). Additional variation of the azimuth angle results in a three-dimensional data stack that provides energy-resolved information about of the electronic band structure in the BZ. A constant-energy cut is referred to as photoelectron momentum map (PMM) in this work (cf. ref. [A2]). For x-ray photoelectron spectroscopy (XPS) higher photon energies are used, which additionally enable the excitation of electrons from atomic core levels. This method provides information about the chemical composition of a sample. Besides the assignment of spectral features to specific elements, it is also possible to determine the nature of the bonding within the sample upon the chemical shift.

3.1.2 Many-Body Effects

The single-particle picture neglects two important effects that modify the measured signal. Firstly, the exited photoelectrons interact strongly with the solid during their propagation to and out of the surface. The so-called mean free path of a charged particle in a solid is mainly restricted by inelastic processes and can be estimated by the universal curve given in ref. [120]. It shows that for typical kinetic energies of photoelectrons excited by UV light of about 20 eV (as used in this work) the mean free path is below 1 nm. Thus, the escape depth amounts to just a few monolayers. Consequently, the emitted photoelectrons carry information from the topmost layers of a specimen solely, making PES a surface-sensitive method. The exact value of the mean free path depends on the specific material and energy range. Secondly, upon emission of an electron, a photohole is created that represents a missing charge in the electron system of the solid. In particular, the former N-electron system turns into an $(N-1)$-electron system that responds to the modified electronic environment. This leads to the following modified energy balance:

$$E(N) + h\nu = E(N-1) + E_{\text{kin}} \qquad \text{or} \qquad E_{\text{kin}} = h\nu - [E(N-1) - E(N)]\,. \tag{3.5}$$

The resulting kinetic energy does therefore not only depend on the energy of an electron in the initial state of the undisturbed electronic structure, but likewise on the total energy of the disturbed electron system (final state). In several materials, the missing charge is effectively screened by the many-body system. As a result, the determined binding energy E_B can be interpreted as the energy of the electron in the initial state (cf. Koopman's theorem [121]). In general, the many-body system responds to the missing electron by more or less severe charge redistributions upon scattering events. Based on Fermi's golden rule, the spectral line shape in consideration of the complex self-energy $\Sigma = \Sigma' + i\Sigma''$ of the many-body system can be derived:

$$A(\vec{k}, E) = \frac{1}{\pi} \frac{\Sigma''(\vec{k}, E)}{\left(E - \varepsilon^b(\vec{k}) - \Sigma'(\vec{k}, E)\right)^2 + \left(\Sigma''(\vec{k}, E)\right)^2}, \tag{3.6}$$

where $\varepsilon^b(\vec{k})$ are the single-particle energies of the undisturbed electronic band that is not renormalized by many-body interaction (bare band) [122]. For slowly varying bands, the momentum distribution curves (MDCs) of the spectral function at constant energies show Lorentzian line shapes, whereas their width and height depend on the imaginary part of the self-energy, and their position is influenced by the undisturbed band and the real part of the self-energy. Thus, bands determined via ARPES are in general renormalized due to the influence of the self-energy of the many-body electron system. There are different scattering events that contribute additively to the total self-energy [122]:

$$\Sigma(\vec{k}, E) = \Sigma_{\text{e-e}}(\vec{k}, E) + \Sigma_{\text{e-ph}}(\vec{k}, E) + \Sigma_{\text{e-def}}(\vec{k}, E). \tag{3.7}$$

Besides contributions from electron-electron (e-e) and electron-defect (e-def) scattering, the electron system strongly interacts with phonons (e-ph) of the solid. Due to differing spectral evolutions of the respective processes, a deconvolution of the self-energy contribution caused by electron-phonon processes is feasible. Accordingly, it is possible to estimate the EPC constant that has a crucial impact on the superconducting properties (if any) of a solid. For the sake of consistency, all formulas and assumptions necessary for a proper interpretation will be given in sec. 5.2, where the measured data are analyzed and discussed.

3.1.3 Data Acquisition and Processing

The PES experiments shown in this work were all performed with a surface analysis system purchased from *SPECS Surface Nano Analysis*. UV light is provided by a microwave-heated light source using the He(I)α excitation (21.2182 eV) in combination with a toroidal mirror monochromator (line width < 1 meV adjusted for p polarization). For the XPS experiments, x-ray radiation from the Al K_α line (1486.71 eV) was used. The emitted photoelectrons are analyzed with a hemispherical electron energy analyzer (PHOIBOS150) equipped with a delay line detector (3D-DLD4040-150). The detector provides two relevant acquisition modes that are used in this work: (i) In the 1D mode electrons are analyzed by their kinetic energy solely. Different positions in k space are achieved by variation of the polar and azimuth angle as already described above. Here, the polar angle resolution of the recorded 1D data is 1°. (ii) With the 2D mode it is possible to simultaneously obtain data from different sections in k space. For a constant polar angle, those sections approximately coincide with small variations of the azimuth angle. The exact relations are provided in appendix A.1. Electron optics in front of the analyzer enable a customization of the data resolution to fulfill certain requirements of the experiment. The advantage of this mode is that PMM data stacks can be acquired relatively fast. Here PMMs are taken in the 2D mode by varying the azimuth angle from $60°$ to $-60°$ in steps of $12°$ and the polar angle from $-2°$ to $70°$ in steps of $2°$. The PMMs presented in sec. 4.2 are extracted from this data stack by cutting through data points at fixed binding energy with an integration range of 44 meV (± 22 meV of the given binding energy). Those methods are already described in ref. [A2]. During the measurement, the sample is mounted to a five-axis manipulator. The temperature of the sample has already been calibrated in a previous work and amounts to about 35 K at a constant liquid helium flux [123]. Since there is no additional shielding of the sample, lower temperatures cannot be achieved due to thermal radiation from the environment.

The presented PES measurements were carried out by Felix Otto[a] in close collaboration with me. He also converted the raw data into a readable format using a home-built software originally developed by Christian Udhardt[a] and further modified by himself. Herein, the conversion of angles to momentum and kinetic energy to binding energy is already included. Dr. Falko Sojka[a] developed a *MATLAB* tool particular for this work that displays PMM and ARUPS data with unequal step sizes of $k_{\|}$ at different binding energies correctly without using artificial averaging like standard software does. The remaining analysis, in particular, the determination of the electron-phonon coupling strength from ARUPS data, was performed with a home-built *MATLAB* software tool developed by the author of this thesis.

3.2 Scanning Tunneling Techniques

3.2.1 Elastic Electron Tunneling

Since the invention of the STM by Binnig and Rohrer [124, 125] in 1982, scanning tunneling techniques enable studying the surface topography of conducting samples even with atomic resolution. Moreover, compared to area-averaging methods like PES, it is possible to study electronic properties with respect to their lateral variations on the sample surface. Another substantial advantage is that, unlike PES, this method enables the investigation of unoccupied states as well.

A very sharp, in an ideal case atomically sharp, conductive tip is placed close to the surface of a conductive sample. At distances of typically a few Å, quantum mechanical electron tunneling

---

[a] Institute for Solid State Physics, FSU Jena, Germany

through the vacuum barrier occurs due to an overlap of the electronic wave functions of the tip apex and the sample. As a result, the Fermi levels of both electrodes are aligned and the total tunneling current amounts to zero. Applying a bias voltage V between both electrodes leads to a non-zero total tunneling current. By convention, positive bias voltages mean that electron tunneling is dominated from occupied states of the tip to unoccupied states of the sample; negative voltages mean that tunneling is dominated from occupied states of the sample to unoccupied states of the tip.

Tersoff and Hamann introduced a quantitative model of the tunneling current in STM geometry by assuming a flat surface and a spherical tip with atomic s-orbital symmetry, based on the general treatment of the tunneling process provided by Bardeen [126]. The total tunneling current within the Tersoff-Hamann model [127,128] is given by

$$I(d,V,T) = \kappa \int_{-\infty}^{\infty} T(d,V,E)\rho_t(E)\rho_s(E+eV)\left[f_t(E,T) - f_s(E+eV,T)\right] dE, \tag{3.8}$$

where ρ_t and ρ_s are the energy-dependent DOS of the tip and the sample, respectively. The energy-dependent transmission function T is a specific form of the general tunneling matrix elements used in the Bardeen formalism, and T further depends on the tip-sample distance d and the applied bias voltage V. The temperature dependence of the tunneling current is considered by the Fermi functions of the tip f_t and the sample f_s. In thermal equilibrium of tip and sample one has $f_t(E) = f_s(E) \equiv f(E)$. At $T > 0$ and a fixed sample bias, electron tunneling is possible in both directions (tip to sample and vice versa) due to the smearing of the Fermi levels, which is already accounted for in eq. (3.8). Consequently, the total tunneling current depends on the tip-sample distance, the applied bias voltage, and the temperature of the system.

In this picture of the tunneling current, the sample and tip DOS contribute only in their summed up form and the tunneling probability is given by the transmission function. Especially for materials that exhibit highly dispersive bands, such as graphene where, in the vicinity of the Fermi level, electronic bands are located only near the K/K′ points of the SBZ, the question of the k dependence of tunneling current arises. In general, scanning tunneling techniques are assumed to behave like angle-integrated PES, without the ability of resolving the wavevector of an electron in its initial state [129]. In the case of atomically sharp tips, the total electron momentum is only restricted by the Heisenberg uncertainty principle $|\vec{k}| \approx 1/a_t$, where a_t is the size of tip apex [130]. Thus, the provided momentum can be sufficiently large to enable tunneling into electronic bands even at the zone boundaries of the BZ. Other than that, this general relation is not capable of estimating the distribution of the total momentum into the components parallel ($k_\parallel$) and perpendicular ($k_\perp$) to the sample surface. To reach bands at the zone boundaries, high values of the in-plane crystal momentum $k_\parallel$ are necessary. As already mentioned above, however, an overlap of the orbitals of tip and sample through the vacuum barrier is essential to enable electron tunneling into/from those orbitals. States with low $k_\parallel$ values (located in the center of the SBZ) decay much slower into the vacuum compared to states with high $k_{\|}$ values [131]. The enhanced overlap leads to a stronger tunneling signal [129]. Therefore, the Tersoff-Hamann model considers the local density of states (LDOS) that resembles the value of the sample wave function at the center of the tip apex atom [128]. The dependency of the LDOS on the tip-sample distance z and the in-plane momentum $k_{\|}$ is given by the following relation [127, 128]:

$$\mathrm{LDOS}(z, k_{\|}) \propto e^{-z/\lambda}, \text{ with } \lambda^{-1} = 2\sqrt{\frac{2m\Phi}{\hbar^2} + k_{\|}^2}, \tag{3.9}$$

where m is the electron mass and Φ the sample work function. Thus, a reduction of the tip-sample distance leads to an enhancement of the contributions of states with high $k_{\|}$ values to the LDOS that results from an increased orbital overlap. Similarly, this behavior also applies for states with $k_{\|} \approx 0$. Further, due to the exponential z dependency, the apex atom of an atomically sharp tip channels the overwhelming part of the total tunneling current [132].

For a detailed interpretation of the k dependency of the tunneling current, knowledge about the sample wave functions and especially their decay into the vacuum is required [133]. These quantities are commonly not available, and furthermore the unknown exact tip shape has a drastic impact as well. This approach is not very practicable for the interpretation of tunneling data. Thus, in this work the tunneling junction will be described in the one-dimensional WKB (Wentzel-Kramers-Brillouin) approximation assuming a trapezoidal barrier. The momentum-independent transmission coefficient is given by the following quantity [133]:

$$T(d, V, E) = \exp\left[-2(d+R)\frac{2}{3}\sqrt{\frac{2m}{\hbar}}\left(\frac{(\Phi_t - E + eV)^{3/2} - (\Phi_s - E)^{3/2}}{\Phi_t - \Phi_s + eV}\right)\right], \tag{3.10}$$

where Φ_t and Φ_s are the work functions of the tip and the sample, respectively, d is the distance between the tip and sample surface, and R is the radius of the assumedly spherical tip apex. Since the exact tip shape is unknown, the transmission factor is calculated by the use of an effective tip-sample distance $z \approx d + R$. Within the Tersoff-Hamann model in 1D-WKB approximation the LDOS can be interpreted as [133]:

$$\mathrm{LDOS}(E) = T(z, V, E)\rho_s(E). \tag{3.11}$$

For all interpretations of the tunneling current, it is necessary to keep in mind that the k dependence is neglected within this approximation and, thus, ρ_t and ρ_s do not represent the k-integrated DOS of the tip and the sample, respectively. ρ_t and ρ_s shall rather be interpreted as effective DOS of the electronic states that contribute to the tunneling process. Moreover, their intensity is arbitrary, due to the generally unknown constant of proportionality κ in eq. (3.8), which is, for convenience, assumed as $\kappa = 1$ in this thesis. Nevertheless, the DOS contributions shall not be renamed here and can only be provided in arbitrary units.

The distance dependence of the tunneling current can be utilized for imaging techniques like scanning tunneling microscopy (STM). For this purpose, the tip is moved over the sample surface by piezo actuators. A feedback loop controls the distance between tip and sample to a specified tunneling current setpoint at given bias (constant current mode). The information about the lateral distribution of the energy-integrated electronic structure (cf. eq. (3.8)) at the sample surface is therefore provided by the z signal.

Scanning tunneling spectroscopy (STS) is the generic term for all methods that allow conclusions about the (L)DOS of the sample surface. Nonetheless, STS is mostly referred to point spectroscopy, where the tip is placed at a certain fixed location above the sample surface. Similar to STM, the tip height is first stabilized by the closed feedback loop to an adjusted current setpoint at a given bias. Subsequently, the feedback loop is opened and the tunneling current is recorded during a bias sweep in a prescribed range. As a crucial prerequisite, the system should be as stable as possible, since it is assumed that the tip-sample geometry remains unaltered. For an approximate interpretation of the spectroscopic data, it is useful to examine the first derivative of the tunneling current. Under several severe assumptions, it can be shown that

$$\frac{dI}{dV}(V) \propto \rho_t(0)\rho_s(eV). \tag{3.12}$$

This relation, which is widely used in many studies, is only valid under the assumption of a flat tip DOS, an energy-independent transmission function, and at temperatures low enough for the Fermi distribution to be satisfactorily approximated by a Heaviside function. Typically, the transmission function is only constant within a very small energy range (several meV) around the Fermi level [133]. Particularly in these narrow energy intervals the thermally broadened Fermi distribution contributes considerably to the measured spectral width. Even the assumption of a flat tip DOS is not valid in every case, as will be demonstrated in sec. 4.2. In order to avoid an unsubstantiated oversimplification by questionable assumptions, the complete tunneling current (eq. (3.8)) is taken into account by modeling and fitting the effective DOS of tip and sample including the transmission function and thermal broadening.

To gain lateral resolution, point spectroscopy can be performed at every coordinate in a specified grid. The result is similar to an STM image, but with additional energy resolution. This dI/dV signal exhibits information about the lateral distribution of electronic states at the sample surface. In practice, the tip is repeatedly stabilized prior to every bias sweep to a specified current setpoint. This is necessary for achieving appropriate signals, especially if the sample surface is not flat. For instance, also atomic corrugations lead to drastic weakening of the signal upon the exponential distance dependence. However, the constant current mode has one major disadvantage which is not particularly discussed in the literature yet:

For this purpose a sample surface with a laterally varying DOS is considered. In particular, at position A a spectrally constant DOS is assumed (black dashed line in fig. 3.1(a)), at position B a peak with a maximum at E_0 is introduced in addition to the same constant offset (red solid line). For simplicity, the transmission function and the tip DOS is assumed to be energy-independent

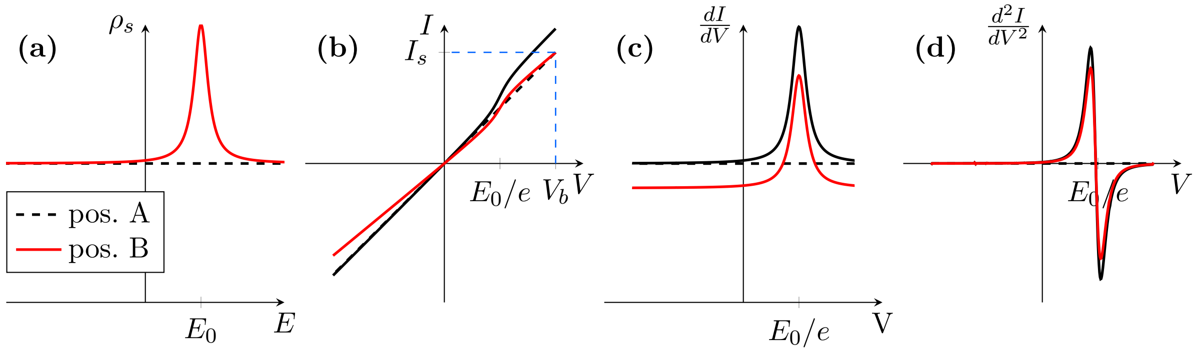

Figure 3.1: Stabilization problem of spatially resolved dI/dV mapping. Explanations are provided in the text.

in this discussion. The tunneling tip is moved to position A, and its height is stabilized with an applied bias V_b to a certain current I_s. According to eq. (3.8), the tunneling current determined from a bias sweep with opened feedback loop exhibits a linear characteristic (black dashed line in fig. 3.1(b)). Subsequently, the tip shall be moved to position B by assuming that the exact tip-sample distance could be retained (which is impossible to accomplish experimentally, in particular for non-flat surfaces). A recorded $I(V)$ curve under these conditions would result in an additional step-like feature at E_0/e caused by the peak in the sample DOS at position B (black solid line in fig. 3.1(b)). Consequently, the tunneling current at V_b exceeds the value I_s at which the tip was stabilized at position A. However, the slope of the $I(V)$ characteristic is preserved in the regions where both densities of states coincide. If the same procedure is repeated, but with prior current stabilization similar to position A, the maximum current is reduced to I_s (red solid line) by an increased tip-sample distance, mediated by the z dependency of the transmission function. Consequently, the slope is not preserved. This, of course, has a direct impact on the intensities of the dI/dV spectra. Even if both densities of states are prescribed to exhibit the same energy-independent offset, the existence of an additional feature at position B in combination with the indispensable current stabilization causes an overall lower intensity of the dI/dV spectrum at position B (fig. 3.1(c)). Even the peak height above the respective constant background is not conserved. Indeed, the tip-sample height variation Δz is usually known, but a subsequent correction of experimentally determined data is generally not possible, due to the non-trivial z dependency of the tunneling current that is mediated by the transmission function (cf. eqs. (3.8) and (3.10)). As a result, the intensity of dI/dV characteristics always depends on the current setpoint at which the tip is stabilized. This dependency influences the visibility of the spatial variation of certain states in laterally resolved dI/dV maps as will be shown sec. 4.2 and can generally be responsible for misinterpretations of the data.

3.2.2 Inelastic Electron Tunneling

Apart from elastic electron tunneling described above, there are additional inelastic processes that affect the current through the tunneling barrier. Basically, the charge transfer between tip and sample induces charge redistributions in the sample (and/or tip). Those temporary redistributions are able to relax through inelastic processes, which thus influence the tunneling current.

Inelastic electron tunneling spectroscopy (IETS) uses the same measurement principle as tunneling point spectroscopy discussed above. For the purpose of this work, the focus is placed on inelastic processes related to phonons. An electron that passes the tunneling barrier between a metallic tip and a metallic sample ($V_b > 0$) is able to excite a phonon of the sample lattice. However, the final state of the tunneling electron after the inelastic process must be unoccupied. Due to this requirement, the excitation of phonons with an energy $\hbar\omega$ is only possible for $eV_b \geq \hbar\omega$ (cf. fig. 3.2(a)). The inverted process is also possible for $V_b < 0$, where an electron within the sample is excited by a phonon and then tunnels to the tip. This process opens additional tunneling channels [134]. Therefore, the tunneling current and its derivatives (black lines in fig. 3.2(d-f)) are modified compared to the purely elastic contribution (gray dashed line). While the slope of the current changes at $\pm\hbar\omega/e$, this process causes additional steps in the first derivative and shows up as peaks (and dips) in the second derivative at these positions (cf. black lines in fig. 3.2(d-f)), whose energy separation corresponds to the vibrational energy [135]. The situation changes when the sample exhibits narrow-band energy levels (bands/states), e.g., semiconducting organic molecules (cf. fig. 3.2(b)). Due to the requirement of empty final (filled initial) states after (before) the inelastic process for $V_b > 0$ ($V_b < 0$), IETS features appear as slightly broadened replica of the electronic levels with lower intensity in the derivative of the tunneling current, shifted by $\pm\hbar\omega$ away from the Fermi level (blue solid line in fig. 3.2(e)) [136]. A third case that is of importance in this work is presented in fig. 3.2(c). The model DOS represents the case of a metal with a partially filled electronic band that is limited at the band edge E_E, e.g., the surface state of Au(111). Around the Fermi level, the resulting spectra are similar to a usual metal as discussed in fig. 3.2(a). At the step edge $eV_b \approx E_E$ the elastic contribution to the total tunneling current drops to zero. However, in the range $E_E \geq eV_b \geq E_E - \hbar\omega$ electrons at and near the band edge are still able to reach the tip via inelastic tunneling processes. As a result, the corresponding dI/dV characteristic shows a double-step feature in this energy range. A quantitative model of the inelastic tunneling current that covers all previously discussed situations is suggested in refs. [137–139]:

$$I_{\text{inel.},+}(V,T) = k\int_0^\infty d\omega D(\omega)\int_{-\infty}^{\infty} dE f(E,T)[1-f(E+eV-\hbar\omega,T)]\rho_t(E)\rho_s(E+eV-\hbar\omega). \tag{3.13}$$

Here, k is a constant of proportionality, and $D(\omega)$ is the spectral DOS of the inelastic contributions. All other quantities are similar to the elastic tunneling current (cf. eq. (3.8)). $D(\omega)$ is mainly

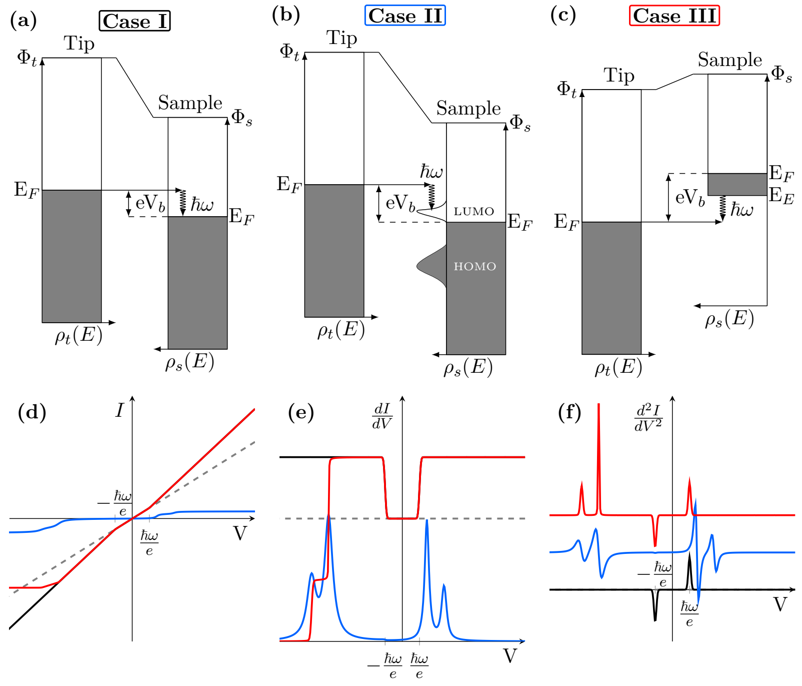

Figure 3.2: (a)-(c) Energy diagrams of selected cases for different sample densities of states with assumed possibility of additional inelastic tunneling processes. Respective (d) $I(V)$, (e) $dI/dV(V)$, and (f) $d^2I/dV^2(V)$ spectra (y-shifted) are assigned to the cases (a) (black), (b) (blue), and (c) (red). Further details are provided in the text.

influenced by contributions of the PhDOS $F(\omega)$ and can be modeled by a sum of peaks with Gaussian line shape [139]. Note that only positive frequencies ω are physically plausible. However, eq. (3.13) covers tunneling of electrons from the occupied tip states to unoccupied sample states solely, i.e., just the positive bias branch is considered (indicated by „+“sign in the subscript). Since for this work the negative bias branch will also be of major importance, a similar description for this case shall be introduced:

$$I_{\text{inel.},-}(V,T) = -k\int_0^\infty d\omega D(\omega)\int_{-\infty}^\infty dE[1-f(E,T)]f(E+eV+\hbar\omega,T)\rho_t(E)\rho_s(E+eV+\hbar\omega). \tag{3.14}$$

The total tunneling current can easily be calculated by summing up the elastic current and inelastic contributions of both branches:

$$I_{\text{total}} = I_{\text{el.}} + I_{\text{inel.},+} + I_{\text{inel.},-}. \tag{3.15}$$

Besides the commonly reviewed cases of IETS that are covered by this model (cf. fig. 3.2), different effects that are not usually discussed can occur. Therefore, tunneling between two metal electrodes is considered with an additional inelastic contribution to the total current expressed by a peak in $D(\omega)$ at ω_P as shown in fig. 3.3 (center). A peak in the sample DOS (cf. fig. 3.3(a)) at E_0 causes a feature at the same energy position in the dI/dV spectrum (elastic current). Besides the already discussed steps at $\hbar\omega_P$ (cf. fig. 3.2 (a),(e)), a replica of the peak in ρ_s appears at $\hbar\omega_P + E_0$ caused by inelastic effects. Generally, this means that every feature in the sample DOS is replicated by the inelastic channel. A similar peak in the tip DOS at $-E_0$ (occupied state) results in the very same dI/dV spectrum, if a flat sample DOS is considered as shown in fig. 3.3(b). Thus, it is generally not possible to distinguish if a feature in the measured

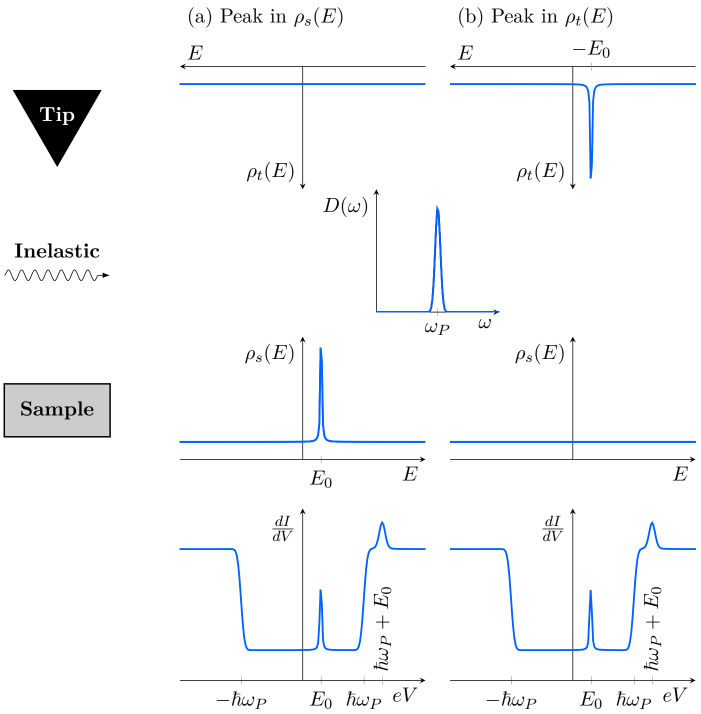

Figure 3.3: Inelastic tunneling spectra influenced by the existence of an additional sharp electronic feature in (a) the sample DOS (left column) and (b) the tip DOS (right column) in the unoccupied and occupied branch of the DOS, respectively. Both cases result in the same dI/dV spectra. Note that for a better visualization the energy axis of the tip DOS is drawn reversed here, since features in the negative branch of the tip DOS cause features in the positive bias branch of dI/dV spectra. The data in chapter 4 is illustrated similarly.

dI/dV signal originates from the sample or tip DOS. Both effects discussed here can easily result in misinterpretations of certain features in a qualitative discussion of measured data when the interplay of elastic and inelastic tunneling is neglected. Therefore, in this thesis a quantitative analysis will be performed by modeling the tip, sample, and inelastic DOS with subsequent fitting to the measured data.

The simple picture of opening tunneling channels is not accurate in some cases, because in this one-electron picture possible many-body interactions are not included [140]. This might have a drastic influence on the resulting tunneling spectra and needs to be kept in mind for the upcoming analysis. Moreover, the excitation probability of different inelastic processes and especially for different vibrational excitations at various energies is not equal. Therefore, the absolute heights of features in the $D(\omega)$ are not necessarily comparable to the PhDOS $F(\omega)$, for example (strong phonons can be absent in tunneling spectra). Additionally, it has already been observed that phonon excitation features indeed appear at same absolute bias, but with strongly deviating weight in the positive and negative bias branches [141].

To account for this, the positive and negative bias branches need to be treated separately. In this work, a new variable $\omega^* = \mathrm{sgn}(V_b) \cdot \omega$ is introduced that allows $D(\omega^*)$ to be well defined also at negative ω^*.[b] The negative bias branch of the inelastic tunneling current modifies to:[c]

$$\begin{aligned} I_{\text{inel.},-}(V,T) = -k \int_{-\infty}^{0} & d\omega^* D(\omega^*) \\ & \times \int_{-\infty}^{\infty} dE [1 - f(E,T)] f(E + eV - \hbar\omega^*, T) \rho_t(E) \rho_s(E + eV - \hbar\omega^*). \end{aligned} \tag{3.16}$$

---

[b] Note that only frequencies $\omega \geq 0$ are physically defined for inelastic processes.

[c] The positive bias branch does not change.

In this description, a transmission function similar to the elastic tunneling is not considered yet. The mechanisms that lead to an inelastic current are completely different from elastic tunneling. Therefore, the bias dependent transmission function might be different for inelastic processes compared to elastic tunneling, but is generally unknown. In this work the transmission function of the elastic tunneling is considered also for the inelastic contributions, keeping in mind that the absolute heights of peaks in $D(\omega^*)$ have no physical meaning. Accordingly, the constant of proportionality is defined as $k = \kappa = 1$ (cf. sec. 3.2.1).

Most commonly, inelastic processes are ascribed to phonon excitations (or vibrations of molecules) of the studied specimen. Electrons passing the tunneling barrier, however, can be influenced by all sorts of inelastic interactions. In this work it should be mentioned that especially features which can be assigned to plasmon excitations occur in measured spectra, as already shown for graphite [141].

3.2.3 Scattering Processes and FT-STM

Electrons that propagate through a material can scatter at surface point defects. In the simplest picture, the incident wave of a single electron interferes with its reflected wave and forms a standing wave pattern. These Friedel charge density oscillations, which are in general a consequence of defect screening by the electron system, cause modulations of the LDOS [142] that can be probed by STM (and STS). In the case of metal surfaces like Au(111) and Cu(111) that exhibit free electron-like[d] surface states, waves extending out from point defects become visible in the STM images as equidistantly spaced ring-shaped patterns surrounding the defect [143]. Accordingly, the 2D Fourier transform (FT) of such STM images exhibits a single ring-like pattern surrounding the FT image center that is related to the distance between adjacent ring patterns in the real-space STM image. In the special case of low bias voltages (typically a few meV), the circular-shaped pattern is directly related to the circular Fermi contour (radius k_F) of the surface state, but with twice the radius $2k_F$ [144], which stems from the fact that scattering between states $\vec{k}_F$ and $-\vec{k}_F$ are the most efficient processes [145]. In literature, this method is mostly referred to as Fourier-transform scanning tunneling microscopy (FT-STM). With spatially resolved STS it is further possible to determine different constant-energy contours (radius q_E) besides the 2D Fermi surface and thus gain information about the energy dispersion of the solid surface.

This simple picture is valid for free-electron-like states solely, since it does not consider the presence of bulk electrons and the particular electron energy dispersion, respectively. Therefore, possible scattering processes related to the unique band structure of graphene are discussed in the following. Since epitaxially grown graphene is slightly doped by the underlying SiC(0001)

---

[d] parabolic energy band at Γ point in reciprocal space

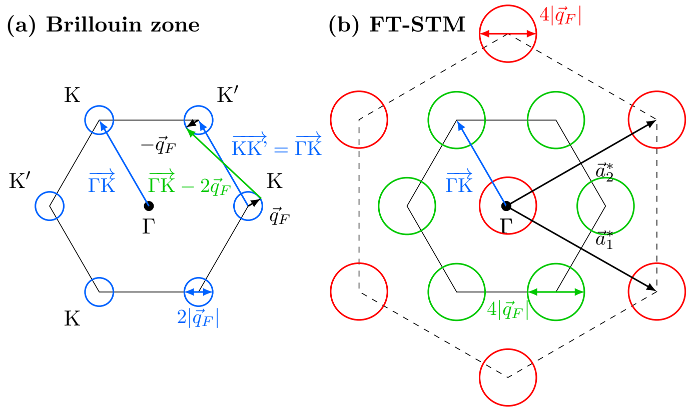

Figure 3.4: (a) SBZ and constant-energy contours at the Fermi level (blue circles) of epitaxial graphene on SiC(0001). (b) Schematic of expected FT-STM image using small bias upon elastic intravalley (red) and intervalley (green) scattering. Adapted from ref. [146].

substrate (cf. sec. 2.2), the Fermi surface consists of almost circular electron pockets[e] (cf. fig. 2.1) of radius q_F located at the K and K′ points of the SBZ as depicted by blue circles in fig. 3.4(a). Similar to the case of nearly free electrons, intravalley scattering processes connect states $\vec{q}_F$ and $-\vec{q}_F$ of the same electron pockets that are in this case of graphene located at the K and K′ points instead of the Γ point. This process is possible at every point of the circular Fermi surface with total momentum change of $2q_F$ (with $q_F = |\vec{q}_F|$). Thus, a ring with a diameter of $4q_F$ appears in the FT-STM image around the Γ point as result of respective contrast modulations in the real-space STM image. Because of translational symmetry, replicas of this feature appear also around the first-order spots of the reciprocal lattice, depicted as red circles in fig. 3.4(b). Moreover, in the particular case of graphene, processes that connect two inequivalent valleys located around the K and K′ point can occur upon scattering at defects, called intervalley scattering. Like intravalley scattering, this process is most efficient for opposing $\vec{q}_F$, due to the topology of the valleys. Since for hexagonal lattices $\overrightarrow{\mathrm{KK}'} = \overrightarrow{\Gamma\mathrm{K}}$, the total momentum change upon intervalley processes amounts to $\overrightarrow{\Gamma\mathrm{K}} - 2\vec{q}_F$ as depicted in fig. 3.4(a). Consequently, additional circular features with a diameter of $4q_F$ appear in the FT-STM image around the tip of the $\overrightarrow{\Gamma\mathrm{K}}$ vector (green circles in fig. 3.4(b)). Since $\overrightarrow{\Gamma\mathrm{K}}$ corresponds to a $(\sqrt{3} \times \sqrt{3})\mathrm{R}30^\circ$ superstructure in real space, those features stem from additional contrast modulations in the STM images of graphene caused by scattering processes that deviate just slightly from the mentioned superstructure [146]. Since electrons in graphene behave like massless Dirac quasiparticles [21], the discussed effect is often referred to as quasiparticle interference (QI) in the literature[f] [146, 148]. The simple picture of QI given in fig. 3.4 does not consider effects of the pseudospin[g] on the FT-STM patterns of graphene. Upon consideration of the electron pseudospin among MLG, the intravalley feature around the Γ point is absent in the FT-STM image, while the intravalley features around the first order spots remain unchanged [146]. Moreover, the intensity distribution of intervalley features are modified [146]. However, the pseudospin has no impact on the FT-STM image of BLG and thus the pattern as discussed in fig. 3.4(b) is expected [146]. A detailed discussion

---

[e] Also called „valleys“.

[f] Sometimes also called quantum interference [145, 147].

[g] Pseudospin is defined by the phase relation between the wave functions of electrons located on the different sublattices of graphene, which are available due to the presence of two different C atoms (A and B) in the unit cell (cf. fig. 2.1(a)) [146].

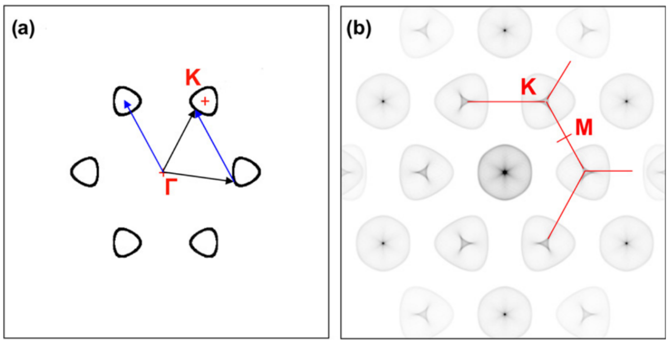

Figure 3.5: (a) Constant-energy contour of the π^* band of freestanding graphene several hundred millielectronvolts above the Fermi level. (b) Expected FT-STM image upon elastic scattering calculated within the JDOS approximation at the energy used in (a). Reprinted from ref. [150].

on the influence of pseudospin on FT-STM data is given in ref. [146]. QI patterns can also be recorded at energies besides E_F by LDOS imaging (dI/dV mapping). Therefore, spatially resolved STS data is Fourier transformed at a certain bias V_b (FT-STS). The diameter of the resulting pattern depends on q_E that resembles the size of the pockets of constant-energy contours at $E = eV_b$. The consideration of almost circular electron pockets is only a good approximation near the Dirac energy. For energies several hundred millielectronvolts above the Dirac point, the electron pockets exhibit a triangular shape [149], as depicted in fig. 3.5(a) for freestanding graphene. The resulting FT-STS image, which was calculated by Simon *et al.* within the JDOS[h] approximation [150], is shown in fig. 3.5(b). While the intravalley features still show an almost circular shape, the intervalley features exhibit a triangular shape that is flipped compared to the triangles that appear in constant-energy contours of the band structure. However, the extent of both, intra- and intervalley features, along high-symmetry directions remains twice the extent of the electron pockets in the same directions. Moreover, despite the triangular shape, the extent of the electron pockets can be interpreted as $2q_E$, which at the Fermi level corresponds to the Fermi wavevector q_F. The modulus of the Fermi wavevector q_F of graphene is directly related to the charge carrier density n via

$$n = g_s g_v \int_{|\vec{q}| \leq q_F} \frac{d\vec{q}}{(2\pi)^2} = g_s g_v \frac{q_F^2}{4\pi}, \tag{3.17}$$

where g_s and g_v are the spin and valley degeneracy, respectively [151]. Including the spin degeneracy ($g_s = 2$) and the contributions of both Dirac cones within the BZ ($g_v = 2$) of graphene [21] leads to

$$n = \frac{q_F^2}{\pi}. \tag{3.18}$$

Usually, the FT of recorded STM images and dI/dV maps is realized numerically. Thereby, a periodic structure with a periodicity a translates into features in the FT image. The distance of those features from the image center is then proportional to $1/a$. Standard software tools, e.g., *Gwyddion* [152] or *WSxM* [153], which are commonly used for STM data analysis, consider this distance in FT images as either $1/a$ or $2\pi/a$ regardless of the actual lattice symmetry. The $2\pi/a$ scaling is commonly used, but is only valid for lattices with a 90° angle between the lattice

---

[h] joint density of states

vectors. In the particular case of hexagonal lattices that are important in this thesis, the length of the reciprocal lattice vectors amounts to $\frac{4\pi}{\sqrt{3}a}$, due to the consideration of the 120° angle between the lattice vectors (e.g., ref. [91]). Therefore, the scaling of the reciprocal lattice differs among these dissimilar conventions. For hexagonal lattices the latter reciprocal dimensions shall be used here, i.e., the solid-state physics definition of the reciprocal lattice shall be applied [154]. As long as the FT images are just interpreted in terms of real-space periodicities, this error cancels upon backtransformation using the same convention as before. However, the length of the Fermi wavevector q_F, which is defined in reciprocal space, is directly related to the macroscopic quantity n via eq. (3.17). To achieve consistency, the particular scaling needs to be considered in the calculation of n. In this work, both values of the Fermi wavevector are given; $q_{F,\mathrm{1D}}$ using the one dimensional $2\pi/a$ scaling (1D scaling), and $q_{F,\mathrm{2D}}$ that considers the 2D hexagonal lattice (2D scaling). However, the FT-STM images presented in this work are scaled using the $\frac{4\pi}{\sqrt{3}a}$ convention to be comparable to the ARPES data.

3.2.4 Tunneling into Superconductors

As already mentioned in sec. 2.6, electron tunneling is not solely restricted to the case of two metals, but also possible between a metal and a superconducting electrode. Tunneling between two superconductors shall not be discussed here, since it is not relevant for this work. The total tunneling current is calculated in much the same way as already discussed above, but with a modified DOS of the superconducting electrode as introduced in sec. 2.4.1. Moreover, in real systems the ideal DOS provided in eq. (2.3) is broadened by various effects. Mathematically, the broadened energy gap in consideration of a flat (i.e., energy-independent) DOS in the normal-conducting state is described by the Dynes equation [155]:

$$\rho_{j,sc}(E,\Delta,\Gamma) = \rho_{j,nc}(0) \cdot \left| \mathrm{Re}\left[\frac{E - i\Gamma}{\sqrt{(E-i\Gamma)^2 - \Delta^2}} \right] \right|, \tag{3.19}$$

where $j = t, s$ for tip and sample, respectively. The broadening is characterized by the parameter Γ that is originally introduced to account for a finite lifetime τ of the quasiparticles (Cooper pairs) with $\Gamma = \frac{\hbar}{\tau}$. Nonetheless, other broadening mechanisms besides pure lifetime effects can also be described by this parameter. The temperature dependency of the superconducting gap is already given in eq. (2.4) and eq. (2.5), respectively. For strong-coupling superconductors the broadening parameter Γ exhibits a temperature dependency that is given by

$$\Gamma(T) = \Gamma_0 \left(\frac{k_B T}{\Delta_0} \right)^{1/2} e^{-\Delta_0/k_B T}, \tag{3.20}$$

where Γ_0 is related to the electron-phonon coupling strength. However, this equation is valid only for $T \ll T_c$ where $\Delta(T) \approx \Delta_0$ [155, 156]. Note that $\Gamma(T)$ increases with increasing T since

$\Gamma_0 > 0$. For weak-coupling superconductors like aluminum a temperature dependency was not observed and Γ remains constant [155].

STS data of superconductors are usually normalized in order to facilitate the interpretation. Therefore, the differential conductance spectra $G(V,T) = \frac{dI}{dV}(V,T)$ are divided by a spectrum that was determined above the critical temperature T_c. Assuming that in the vicinity of the Fermi level the tip and sample DOS are flat (i.e., energy independent) in the normal-conducting state and that the energy dependence of the transmission function is negligible, the normalized elastic differential conductance of a superconducting sample simplifies to (adapted from [157])

$$\frac{G(V,\Delta(T),\Gamma(T),T)}{G(V,T_{nc} \geq T_c)} \approx \int_{-\infty}^{\infty} \left| \mathrm{Re}\left[\frac{E - i\Gamma(T)}{\sqrt{(E - i\Gamma(T))^2 - (\Delta(T))^2}} \right] \right| \cdot \frac{d}{dV} f(E - eV, T) dE. \tag{3.21}$$

Thus, under these conditions, the normalized spectra can be directly interpreted as the thermally broadened superconducting DOS $\rho_{s,sc}$ of the sample. As an example, the numerically differentiated dI/dV spectra of a Pb(111) surface examined with a normal conducting tungsten tip at different temperatures are presented in fig. 3.6(a). The corresponding spectra that are normalized by the spectrum recorded at 7.0 K are presented in fig. 3.6(b). Note that the gap appears to be centered slightly below zero, which is caused by a small voltage offset (< 0.7 mV) of the measuring system. Equation (3.21) is sufficient for the description of normalized spectra with slowly varying densities of states in the normal conducting state.

The influence of the broadening mechanisms stemming from the broadening factor Γ and from the temperature T on the resulting normalized spectra are shown in fig. 3.7(a) and (b), respectively. At first glance, the evolution upon increasing Γ and increasing T seems very similar. A closer look, however, reveals that the spectral form of the resulting curves deviates, especially within the gap. Moreover, the coherence peaks remain at the same energy positions for different Γ values, while they shift away from the Fermi level upon increasing thermal broadening. Therefore, the different broadening mechanisms may be distinguishable in high-resolution STS data.

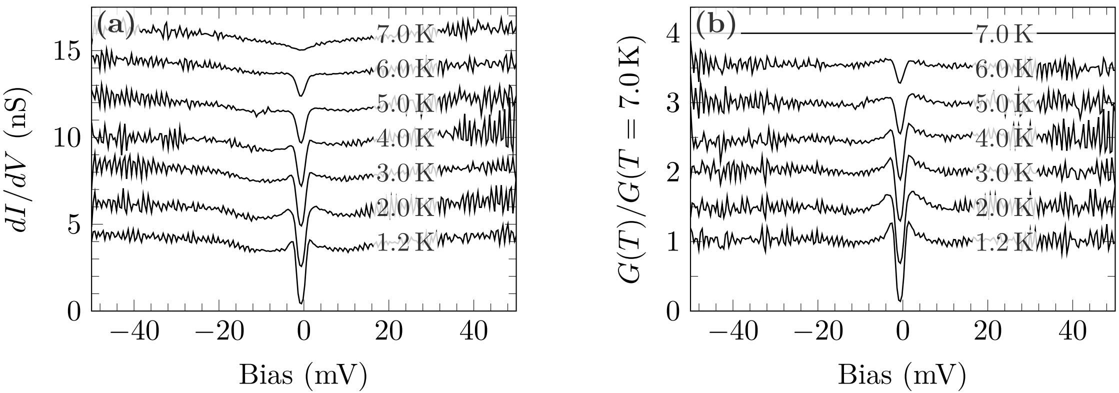

Figure 3.6: (a) Temperature-dependent dI/dV spectra taken with a tungsten tip on a Pb(111) surface (numerically differentiated, y-shifted 2 nS, $I_s = 200$ pA at $V_b = 50$ mV). (b) Spectra of (a) normalized by the spectrum recorded at 7.0 K (y-shifted 0.5). The gap appears to be centered slightly below 0 mV due to an uncorrected voltage offset of the employed STM electronics.

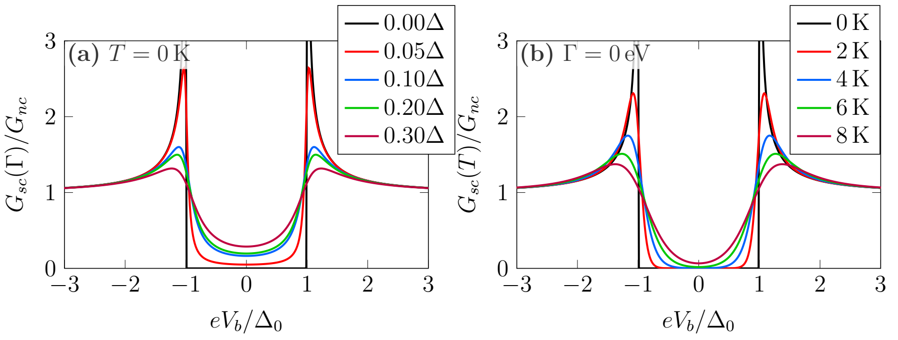

Figure 3.7: Analytically generated normalized conductance spectra that demonstrate the influence of (a) the broadening factor Γ at fixed $T = 0\,\mathrm{K}$ and (b) temperature-dependent thermal broadening at fixed $\Gamma = 0\,\mathrm{eV}$ on the shape of energy gap measurements based on eq. (3.21).

In this work, also non-flat densities of states in the normal-conducting state of a superconducting sample have to be considered according to eq. (2.2). To describe possible broadening mechanisms similar to the Dynes equation (3.19), the following description of the DOS in the superconducting state is suggested

$$\rho_{j,sc}(E,\Delta,\Gamma) = \rho_{j,nc}\left(\mathrm{sgn}(E)\cdot\mathrm{Re}\left[\sqrt{(E-i\Gamma)^2-\Delta^2}\right]\right)\cdot\left|\mathrm{Re}\left[\frac{E-i\Gamma}{\sqrt{(E-i\Gamma)^2-\Delta^2}}\right]\right|, \tag{3.22}$$

which conserves the total number of states also for broadened densities of states. Obviously, for the limiting case $\Gamma \to 0$ the non-broadened DOS of the superconducting state is reinstated (cf. eq. (2.2)), and for $\Delta \to 0$ the DOS of the normal-conducting state $\rho_{j,sc}(E,\Delta\to 0,\Gamma) = \rho_{j,nc}(E)$ is obtained.

3.2.5 Data Acquisition and Processing

STM setup

The presented tunneling experiments were performed with a JT-STM/AFM system purchased from *SPECS Surface Nano Analysis*. The cryoshield housing sample and tip during the measurement is cooled by liquid helium ($T \approx 4.2\,\mathrm{K}$) and an additional cooling stage based on the Joule-Thomson (JT) effect. With this setup a minimum temperature of 1.2 K is reachable. The exact temperatures are determined with *Cernox* sensors located close to the sample and a resistance bridge both purchased from *Lake Shore Cryotronics*. In thermal equilibrium, the temperature within the cryoshield can be determined with an accuracy of $\Delta T < 0.01\,\mathrm{K}$. The temperature of the STM core can be varied by an additional resistive heater located close to the sample. The piezo actuators of the STM setup are very sensitive even to small temperature variations. Accordingly, the piezo signals are susceptible to strong apparent drift. Therefore, the data acquisition is not started until especially the z actuator of the tip, which is furthest away from the heater, shows no further drift. From then on, tip and sample can be expected to be in thermal equilibrium. Since the (x, y) actuator also shows thermal drift, STS measurements of the very same sample position at different temperatures are not simply possible by moving the tip to the same (x, y) coordinate. Rather, the position has to be estimated from an STM scan prior to each point spectroscopy acquisition. The STM system is operated with a *Nanonis SPM controller* (Version 5) that provides an integrated lock-in amplifier for STS experiments.

All tunneling experiments of epitaxial graphene shown in this thesis were performed with the same self-made platinum/iridium tip (Pt/Ir tip). After manually cutting a Pt/Ir wire, the pinched off tip was additionally prepared in UHV by sputtering with Ar$^+$ ions ($p = 5 \cdot 10^{-6}\,\text{mbar}$, $E_\text{ion} = 2.5\,\text{keV}$, $t \approx 5\,\text{min}$), further conditioned by scanning a Au(111) surface and electronically checked by the appearance of the Au(111) surface state in tunneling spectra. The Pt/Ir alloy used here has a much higher concentration of Pt than of Ir and, accordingly, a work function of $\Phi_\text{Pt} = 5.6\,\text{eV}$ [158].

Lock-in Technique

Differential conductance spectra are commonly acquired using the lock-in technique to overcome the disadvantage of the numerical derivative that artificially amplifies noise in a measured $I(V)$ curve. To this end, a small sinusoidal voltage with an amplitude V_mod is modulated on the applied DC bias (V_b), which yields $V_\text{appl}(t) = V_b + V_\text{mod}\sin(\omega_\text{mod} t)$ with a frequency $f_\text{mod} = \frac{\omega_\text{mod}}{2\pi}$. The lock-in signal obtained from a deconvolution of all signals with ω_mod is directly related to the differential tunneling conductance via

$$\frac{dI}{dV}(V_b) = \frac{B}{V_\text{mod}} \cdot \text{lock-in signal}(V_b) \tag{3.23}$$

as shown in appendix A.2.1. The lock-in signal provided by the *Nanonis SPM controller* is given in ampere and the dimensionless parameter B is a constant that depends on the lock-in-specific parameters, e.g., sensitivity and amplification factors.

This treatment neglects possible broadening that is caused by the additional AC modulation voltage. To account for this experimental broadening mechanism, refs. [159, 160] suggest the following relation that is based on the working principle of the lock-in amplifier[i]

$$\left(\frac{dI}{dV}\right)_L (V_b) \propto \int_{-\pi/2}^{\pi/2} d\alpha \sin(\alpha) \cdot I\left(V_b + V_\text{mod}\sin(\alpha)\right). \tag{3.24}$$

In general, $\left(\frac{dI}{dV}\right)_L$ is related to the analytic derivative $\frac{dI}{dV}$, but broadened. In most cases, literature reports do not distinguish between these two quantities. Under the assumption of a linear $I(V)$ characteristic, the constant of proportionality in eq. (3.24) can be derived as shown in appendix A.2.2, which results in

---

[i] Note that V_mod is the amplitude and not the root mean square (RMS) voltage value as in refs. [159, 160], which is why the factor $\sqrt{2}$ is not necessary here.

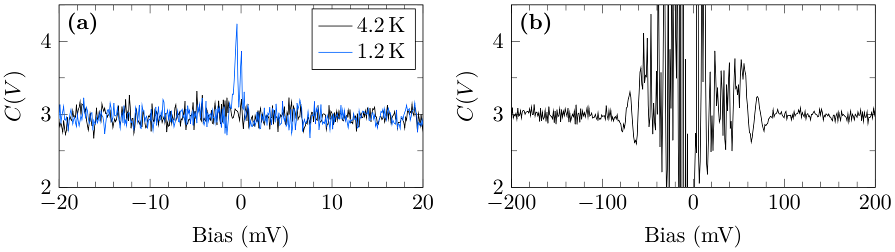

Figure 3.8: Bias dependency of the lock-in-specific scaling factor C defined in eq. (3.26) using data in (a) fig. 4.27 and (b) inset of fig. 4.6 as examples.

$$\left(\frac{dI}{dV}\right)_L (V_b) = \frac{2}{\pi V_\text{mod}} \int_{-\pi/2}^{\pi/2} d\alpha \sin(\alpha) \cdot I\left(V_b + V_\text{mod}\sin(\alpha)\right). \tag{3.25}$$

Since the integral in this equation represents the lock-in signal, it is useful to rewrite eq. (3.23) to

$$\left(\frac{dI}{dV}\right)_L (V_b) = C\frac{2}{\pi V_\text{mod}} \cdot \text{lock-in signal}(V_b), \tag{3.26}$$

where C is then a constant that includes lock-in-specific parameters solely. Rearrangement of this equation allows the determination of the parameter C from experimental data as shown for two measurements with different V_mod in fig. 3.8, where $\frac{dI}{dV}$ is calculated by numerical derivation of the tunneling current. The strong deviations from a constant value are the result of noise amplification, since in the low-voltage regions the signal is very small (cf. fig. 4.27 and inset of fig. 4.6(a)). Besides these deviations, the lock-in parameter is almost perfectly constant and can be estimated to $C \approx 3$. This allows rescaling of the measured lock-in signal, and the data can be given in units of siemens $S = A/V$. The result then corresponds to the analytical derivative of the tunneling current. Moreover, the absolute intensities of spectra recorded with different modulation voltages can be compared, which becomes necessary in sec. 4.2. To demonstrate the influence of lock-in broadening on the quantitative analysis, an STS spectrum acquired via the lock-in technique of a superconducting Nb tip above a metallic Au(111) surface is presented in fig. 3.9 (black solid line). Thereby, V_mod is intentionally exaggerated, so that its effect on the measured spectrum is visible to the naked eye. For fitting according to eq. (3.21), E needs to be replaced by $E - eV$ in the part that describes the broadened energy gap and the small voltage offset already mentioned above is considered by a shift of the Fermi level, which is treated as additional fit parameter. However, the result of the fitting procedure does not describe the measured signal accurately (blue solid line). Consequently, the extracted values $\Delta_t = 0.99(1)\,\text{meV}$ and $\Gamma_t = 0.31(1)\,\text{meV}$ strongly deviate from reported values in the literature, in this case $\Delta_t = 0.94\,\text{meV}$ and $\Gamma_t = 0.01\,\text{meV}$ [160,161]. In contrast, additional consideration of the lock-in broadening via eq. (3.25) results in a significantly improved agreement (red solid line). The extracted parameters $\Delta_t = 0.917(8)\,\text{meV}$ and $\Gamma_t = 0.067(7)\,\text{meV}$ are comparable to the above mentioned literature values, and the remaining small discrepancies can be explained considering that trace impurities of the Nb wire can have a significant influence on its superconducting

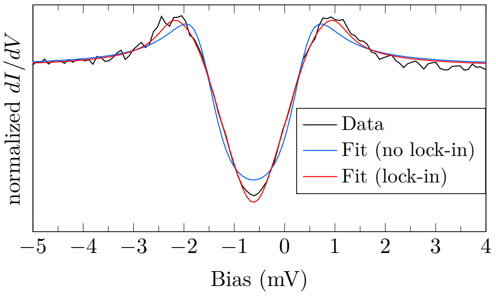

Figure 3.9: Normalized dI/dV spectrum acquired using a superconducting Nb tip on a Au(111) surface using the lock-in technique with inappropriate V_{mod} (black) ($T = 1.15\,\mathrm{K}$, $I_s = 200\,\mathrm{pA}$ at $V_b = 20\,\mathrm{mV}$, $f_{\mathrm{mod}} = 912\,\mathrm{Hz}$, $V_{\mathrm{mod}} = 0.8\,\mathrm{mV}$). Fit results using eq. (3.19) (blue) and in further consideration of the lock-in influence via eq. (3.25) (red).

properties. Therefore, it is essential to consider the broadening caused by the lock-in technique in quantitative analyses of electronic structures in the meV region like superconducting gaps.

Two experimental mechanisms have a major impact on the broadening of measured spectra, namely the temperature and the use of the lock-in technique. The total energy resolution can be estimated by $\Delta E \approx \sqrt{(3.3k_BT)^2 + (1.7eV_{\mathrm{mod}})^2}$ [162]. The influence of the temperature is already accounted for by considering the Fermi functions in the calculation of the tunneling current. For all measurements that are presented in this thesis, V_{mod} is chosen equal to the step size of two adjacent data points (V_b). Even if the resulting influence on the spectra is small, the broadening will be considered for all quantitative analyses. In all measurements presented hereafter a lock-in modulation frequency $f_{\mathrm{mod}} = 1612\,\mathrm{Hz}$ is used. All other parameters are given in the respective figures. The determined bias range of a particular measurement is scanned in both directions (forward and backward sweep) and averaged subsequently. To achieve additional noise reduction the recorded data of several successive bias sweeps (without interruption of the measurement) are averaged. The number of accumulations (acc.) is also given for every measurement presented below.

Numerical data analysis

As already mentioned above, the intensity of the measured data is rescaled according to eq. (3.26). Quantitative analysis of the rescaled data is performed by modeling the DOS of tip and sample as well as the inelastic contributions. Based on the model, the total tunneling current and, subsequently, the lock-in-broadened differential conductance are calculated without using any further approximations, and the latter is fitted to the measured STS data by variation of the model parameters. The particular models and fit parameters are provided later. This computationally expensive procedure is realized with a home-made software tool developed in *MATLAB* by the author. The error margins depicted in the following only account for statistical errors resulting from the numerical fitting procedure.

3.3 Auxiliary Methods

Differential Reflectance Spectroscopy (DRS)

Differential reflectance spectroscopy (DRS) is an optical method with the particular advantage that the reflectance R can be measured *in situ*, during the deposition of a material, as a function of time t and photon energy E. For this purpose, the light of a halogen lamp is focused on the sample at almost normal incidence and the reflected light is analyzed spectrally. Details of the setup can be found elsewhere [163, 164]. The DRS signal is defined as the relative change of the reflectance:

$$DRS(E,t) = \frac{R(E,t) - R(E,t_0)}{R(E,t_0)}, \tag{3.27}$$

where $R(E,t_0)$ is the spectrum of the pristine sample. To obtain one spectrum, reflectance spectra are accumulated for 30 s.

This method is commonly used to investigate the optical properties of adlayers deposited on clean substrates. However, it is also possible to monitor changes in the optical properties of an already present material by altering the electronic structure, for example, upon doping.

Low-Energy Electron Diffraction

Low-energy electron diffraction (LEED) probes the two-dimensional reciprocal lattice of the sample surface. It is a standard technique in surface science [165] and shall therefore not be discussed in detail here. The measurements in this work are performed with a dual microchannel plate LEED (MCP-LEED) device purchased from *OCI Vacuum Microengineering*. The images are calibrated and corrected for distortions and systematic errors by the freely available program *LEEDCal* [166,167] using the Si(111)-(7 × 7) superstructure as a reference sample [168]. Structural analyses are carried out using *LEEDLab* [169] as also described in refs. [A1, A2].

Sample preparation and handling

The graphene sheets used in this work were synthesized on 6H-SiC(0001) wafers with a similar procedure as described in ref. [32]. The wafers were etched in a hydrogen atmosphere at about 1600 °C for 20 min to remove surface polishing damages. Subsequently, the etched wafers were tempered in an Ar atmosphere also at about 1600 °C for 20 min. The samples used in this work were produced by Dr. Bernd Schröter[j] and his technical staff.

All experiments discussed in this work were performed in UHV conditions (base pressure $\approx 10^{-10}$ mbar). Prior to every experiment the sample was annealed (with electron bombardment

---

[j] Institute for Solid State Physics, FSU Jena, Germany

heating from the backside) at $T \lesssim 1200\,^\circ\mathrm{C}$ in UHV to remove possible contaminations. At these temperatures synthesis of additional graphene layers is not expected (cf. refs. [35, 36, 50]). The sample quality was checked via LEED prior to every experiment by inspecting the sharpness and intensity of distinct spots in the pattern (cf. sec. 4.1) in relation to the diffuse background.

Potassium deposition was performed by direct heating of a dispenser purchased from *SAES Getters* with an electric current, while the sample is mounted to the manipulator at room temperature (RT). Instead of estimating the K content by controlling the flux, the changes of the optical properties of the sample are monitored via DRS to achieve comparable and reproducible doping stages of the sample. This procedure does not require the assumption of constant material flux from the dispenser, which is in most cases not satisfied (not even during the same deposition cycle).

STM and PES measurements were performed in two different UHV chambers, located in two different buildings. Samples were transferred between both chambers in a portable UHV shuttle (base pressure $\approx 10^{-9}$ mbar), equipped with an ion-getter pump and a stand-alone battery power supply, without interrupting the UHV conditions.

4 Structural and Electronic Characterization of K-Intercalated Epitaxial Graphene

This chapter provides a thorough analysis of structural modifications and accompanied evolutions of the electronic structure upon K intercalation of epitaxial graphene on SiC(0001). As already discussed above, the initial composition of the pristine sample, in particular, the exact number of graphene layers, has a major impact on the final properties of the specimen resulting from K intercalation. Thus, key properties of the pristine sample are examined precisely from the outset. The aim is to determine physical and chemical properties of one specific sample. On several occasions a comparison to samples with different graphene layer thicknesses is mandatory. Since epitaxial graphene on SiC(0001) is well-studied in the literature, it further represents an appropriate system to evaluate the correctness of the modified data analysis methods, i.e., the enhanced numerical STS data analysis.

4.1 Pristine Epitaxial Graphene Samples

Apart from intensity variations, the LEED pattern obtained from the sample of interest (fig. 4.1(a)) agrees with the pattern reported numerous times in the literature, e.g., refs. [32, 35, 36], independent of the number of graphene layers[a] on SiC(0001). Besides features resulting from the graphene and SiC lattice, the pattern exhibits additional spots that are commonly ascribed to the $(6\sqrt{3} \times 6\sqrt{3})\mathrm{R}30^\circ$ reconstruction (in relation to the SiC lattice) of the buffer layer located between the substrate and the first graphene layer (e.g., ref. [170]). In particular, characteristic diamond-like spot groups occur that are highlighted in yellow. Further, consideration of a (6×6) superstructure with respect to the SiC lattice is sufficient to describe all features emerging in the LEED pattern. However, this simple approach is not capable of accounting for the observed intensity distribution of these features. For a detailed analysis of the spot intensities, kinematic LEED theory would be necessary. Instead, the observed features can also be described as a consequence of multiple scattering between graphene and the SiC lattice [171] as depicted by

---

[a] from one monolayer up to several monolayers

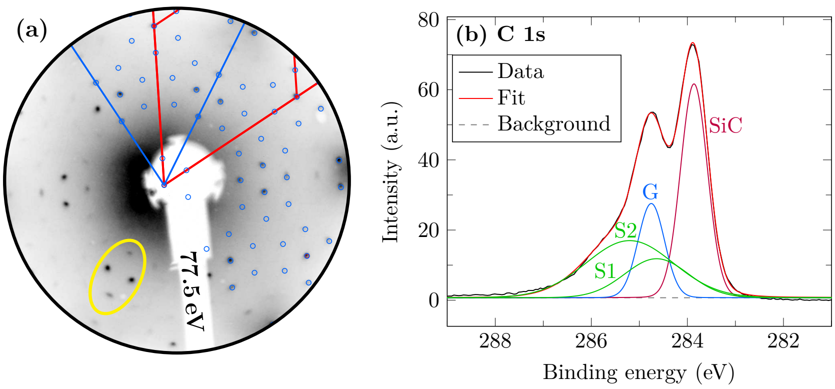

Figure 4.1: (a) Contrast-inverted, logarithmically scaled, distortion-corrected LEED image of 1.3 monolayer (ML) epitaxial graphene on SiC(0001). Lines depict the 2D reciprocal unit cell of the SiC (red) and graphene lattices (blue). Blue circles indicate spot positions of graphene and multiple scattering between graphene and SiC. (b) XPS spectrum of the C 1s core level (black) and respective fit function (red) comprising four components originating from SiC (magenta), graphene (blue), and S1 and S2 (green) from the buffer layer along with a Shirley background (gray dashed).

the blue circles in fig. 4.1(a) up to third order.[b] Noticeably, the spot intensity decreases with increasing order of the multiple scattering. For comparison, a LEED image of a different high-quality epitaxial graphene sample is shown in fig. A.15(a) of app. A.13, where also weak features are described by considering higher orders of the multiple scattering process. Consequently, the physical reconstruction of the buffer layer is not necessary to generate the observed (geometric) diffraction pattern. In the hypothetical case that non-interacting graphene could exist on a SiC(0001) surface, without the formation of a reconstructed buffer layer, the same LEED pattern would be expected, however, accompanied with an expectable weakening of the spot intensities.

To determine the number of graphene layers on this specific sample, the C 1s core level spectrum was measured via XPS (normal emission) and fitted by the sum of Voigt profiles as depicted in fig. 4.1(b). Accordingly, the spectrum comprises four components that are related to C atoms with different chemical bonds. The SiC component arises from C atoms bound within the SiC substrate, and the G component from carbon bound in the graphene layer. The components S1 and S2 both result from carbon located in the buffer layer, where S1 corresponds to C atoms covalently bound to Si atoms of the uppermost SiC layer, and S2 to carbon atoms bound to other carbon atoms. Since the stoichiometry within the buffer layer is known, the ratio of components is S2/S1= 2 [36], which is accounted for as constraint in the fitting procedure. In accordance to ref. [36], an effective graphene layer thickness can be determined from the intensity ratio of the G and SiC components, and amounts to 1.3(1) graphene layers above the buffer layer for this specific sample.[c] Noteworthily, samples with an effective graphene thickness of about 1 monolayer (ML) are usually composed of a mixture of domains with 0, 1 and 2 ML graphene [77, 174–176]. This results from the limited lateral domain size, caused by the formation of terraces, which are separated by grain boundaries due to the lattice mismatch in

---

[b] Faint features are described by considering higher diffraction orders.

[c] The modified expressions for normal emission spectra are provided in refs. [172, 173].

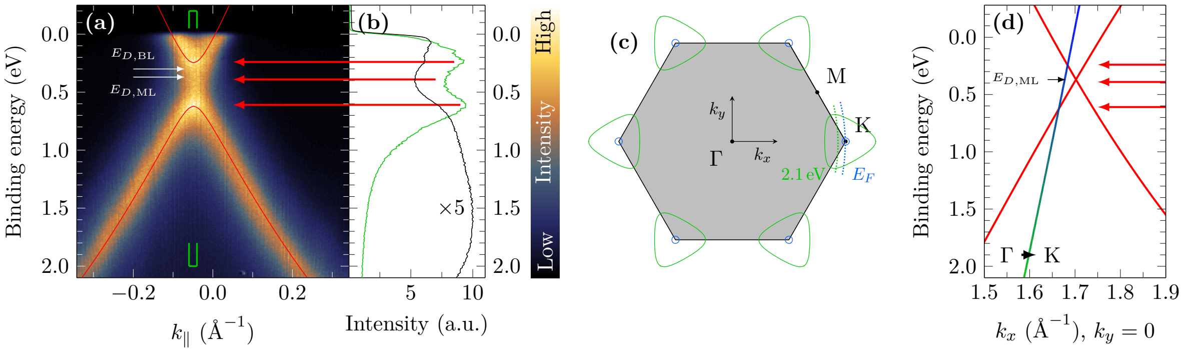

Figure 4.2: (a) ARUPS near the K point of 1.3 ML epitaxial graphene on SiC(0001) (cooled with liquid helium, $\theta = 53.4°$, $\phi = 1.65°$, resolution: 2.56 meV, 0.05° corresponding to $\approx 0.0018\,\text{Å}^{-1}$) and respective section from a 3NN TB calculation (red lines). (b) EDC of the ARUPS measurement in (a) integrated over all $k_\parallel$ values (black), and integrated in the selected range of the Dirac crossing (green) as indicated in (a) (normalized to number of data points, black curve five times enlarged). (c) SBZ of epitaxial graphene (gray); constant-energy contours at E_F (blue) and at 2.1 eV binding energy calculated via the 3NN TB approach. (d) Calculated band structure of the Dirac cone of EMLG (red) along the ΓK direction and the related energy-dependent position of the 2D detector (color gradient from blue to green, explanation in the text). Red arrows in (a) and (d) depict the position of extrema determined from the EDCs in (b).

that system [71]. Even if the effective graphene layer thickness is slightly higher than 1 ML, the determined band structure via ARUPS (2D detector) near the K point (fig. 4.2(a)) does not exhibit any evidence of a second band that would suggest a significant contribution of bilayer areas. This is also not the case for the σ band at the Γ point and the parabolic feature at the M point as shown in app. A.4.1, where two bands would be expected for bilayer graphene as well (cf. ref. [177]). Nevertheless, the momentum-integrated intensity (black) and an energy distribution curve (EDC) in the vicinity of the Dirac crossing (green) shown in fig. 4.2(b) both exhibit a minimum intensity at $E_{\mathrm{min}} = 0.391(1)\,\mathrm{eV}$ that is unexpected for EMLG. Rather, other studies investigating EMLG report on a maximum of the momentum-integrated intensity at the Dirac energy [41, 42]. Further, the existence of maxima in the EDC, obviously caused by the vertex of two parabolic bands, suggests the presence of an energy gap at the Dirac point, which is only expected for EBLG, but not for EMLG. At first glance, this finding apparently contradicts the observation of just a single π band, and a clear assignment of the measured band structure to either EMLG or EBLG seems not possible.

This seeming contradiction can be resolved by considering the $k_\parallel$ values that are actually probed by the 2D detector for the adjusted polar and azimuth angle during data acquisition. Those values can be determined by eq. (3.4) and the expressions in app. A.1. The sections at constant energy are slightly curved as illustrated as dotted lines in fig. 4.2(c), but comparable to sections almost perpendicular to the ΓK direction. Since the conversion of angles to $k_\parallel$ values explicitly depends on the kinetic energy of the emitted electron (cf. eq. (3.4)), the sections at which the 2D detector probes the band structure depend on the binding energy as depicted for two specific values by blue and green dotted lines. In particular, the energy dependence of the 2D detector section in ΓK direction is depicted in fig. 4.2(d) (color gradient line: blue to green). Thus, for higher binding energies smaller $k_{\|}$ values are probed. For demonstration purposes, the expected band structure $E(\vec{k})$ of MLG is calculated with the expressions shown in app. A.6, which describe a TB approach that considers interactions up to third-nearest-neighbor (3NN) atoms [24, 178]. The overlap of 2D detector sections with the calculated electronic structure reveals expectable bands in the measurement. Since the intercepts at a given binding energy cannot be analytically resolved for $k_{\|}$, the problem is solved numerically.[d]

For a qualitative description of the measured data, parameters for EMLG reported in ref. [179] are used as a first guess. Subsequently, the parameters E_{2p} and γ_0 are manually adjusted to qualitatively describe the measured data at given polar and azimuth angle (fig. 4.2(a)). The exact model parameters are provided in app. A.6. In this case, the section of the 2D detector, where the data is collected, does not coincide with the Dirac point (fig. 4.2(d)). Thus, conical sections of the Dirac cone are probed that result in parabolic bands in the measurement. Consequently, the maxima in the EDC are caused by the vertex of both resulting parabolic bands, where the 2D detector section intersects with the Dirac cone in ΓK direction as indicated by red arrows in fig. 4.2(a) and (d). Therefore, the apparent electronic gap is actually a consequence of the data collection method and not caused by the presence of bilayer areas on the specimen. According to this procedure, the Dirac crossing is located at $E_D \approx 0.37\,\mathrm{eV}$, which appears to be slightly shifted to lower binding energies compared to other reported values (e.g., $E_D = 0.42\,\mathrm{eV}$ [43]). However, the sample examined in fig. 4.2(a) was intercalated with K atoms prior to the shown measurement. Upon annealing, the specimen can be purged from intercalants as will be discussed in sec. 4.2. However, residual amounts of contaminations seem to remain on the sample and cause a slight shift of about $0.05\,\mathrm{eV}$ to lower binding energies. A similar behavior has already been reported for Al-intercalated EMLG with an observed shift of $0.10(2)\,\mathrm{eV}$ to lower binding energies [80].

As a result, the determined electronic structure of the 1.3 ML sample is fully consistent with EMLG solely, even if the nominal thickness is slightly higher. A similar measurement of a different sample with a smaller nominal thickness of 1.2 ML graphene, depicted in fig. A.4(a) (app. A.5), exhibits subtle evidence of additional bands related to EBLG. In particular, an extremely flat band of the upper Dirac cone is present that is directly related to 2 ML areas (cf. ref. [42]). Since the 1.3 ML sample of interest shows no evidence of those features, in spite of the higher nominal thickness, it can be concluded that the bilayer areas are of inferior structural quality as they do not contribute to the area-averaging signal of the electronic structure. However, it is also possible that the actual nominal thickness of the sample is lower than the determined value, since for the determination of its error margin only fitting errors are considered. Nevertheless, the 1.3 ML sample behaves like EMLG judging from ARUPS. Further, the electronic bands determined via ARUPS exhibit the expected polarization dependence in ΓK direction as shown

---

[d] Problem was solved numerically using `fsolve` as available in *MATLAB*.

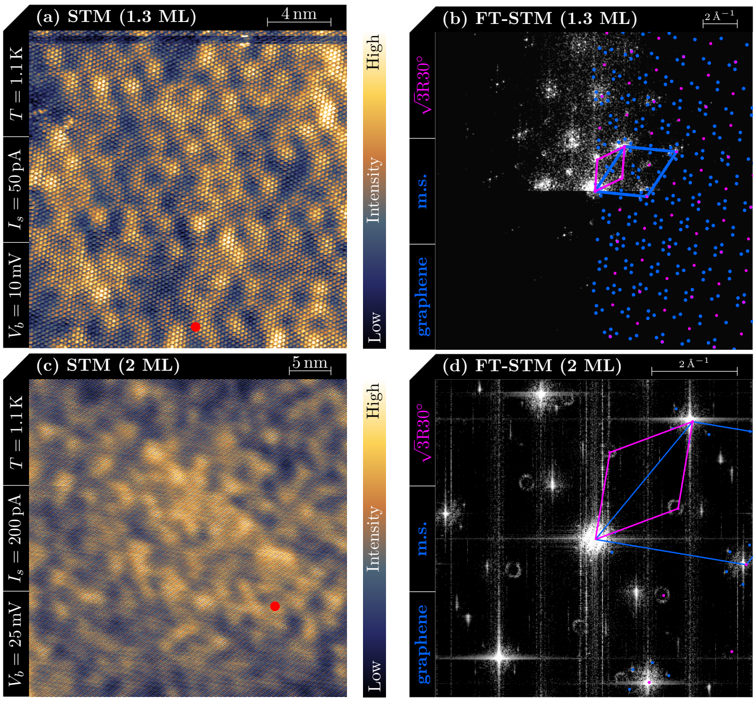

Figure 4.3: Low bias STM images of (a) 1.3 ML (Pt/Ir tip) and (c) 2 ML (W tip) epitaxial graphene samples as well as the associated FT-STM images shown in (b) and (d), respectively (upper part of (b) contrast-enhanced). Reciprocal unit cell of graphene (blue) along with simulation of expected features including multiple scattering (m.s.) with first order only (d) and higher orders in (b). Unit cell of a potential $(\sqrt{3} \times \sqrt{3})$R30° superstructure (magenta, short $\sqrt{3}$R30°) where dots indicate positions of possible features. Red dots in (a) and (c) indicate the tip positions for respective STS measurements.

in fig. A.2(b) that results from the anisotropy of the Dirac cone caused by the presence of two C atoms in the graphene unit cell [83]. Apart from sharpened features, the appearance of the electronic structure does not change upon cooling as shown in app. A.4.1 (fig. A.2(b) and (c)).

Figure 4.3(a) shows an STM image acquired from the 1.3 ML sample of interest at low temperature and bias. The corresponding FT-STM image in (b) exhibits features of the graphene lattice (reciprocal unit cell depicted in blue) and low orders of the (6×6) superstructure that are caused by the existence of the buffer layer below the graphene sheet. Additional features emerge in the FT-STM image suggesting a $(\sqrt{3} \times \sqrt{3})$R30° superstructure with respect to the graphene lattice (magenta). Those features are not described by the pattern determined via LEED (shown as blue dots) and not even by taking the larger $(6\sqrt{3} \times 6\sqrt{3})$R30° superstructure of the buffer layer into account. Those additional features, however, can be assigned to intervalley quasiparticle-scattering processes [147, 180]. For comparison, fig. 4.3(c) shows an STM image of an extended area recorded on a different sample with a nominal graphene thickness of 2.0(1) ML[e] (determined via XPS analysis of the C 1s core level emission as shown in app. A.12). The corresponding FT-STM image in fig. 4.3(d) clearly reveals that the positions where spots of a potential $(\sqrt{3} \times \sqrt{3})$R30° superstructure would be expected are surrounded by circular features that can also be attributed to quasiparticle-scattering processes, thus corroborating the assignment of the magenta spots.

The FT-STM images in fig. 4.3(b) and (d) are replotted in fig. 4.4(a) and (d), respectively, but with a color scheme that is specifically chosen to achieve a better visibility of low-intensity features. It can be discerned that QI features determined on the 1.3 ML graphene sample also exhibit an almost circular shape that is best visible in second order as depicted in fig. 4.4(b).

---

[e] This sample clearly also exhibits two π bands in ARUPS measurements (not shown).

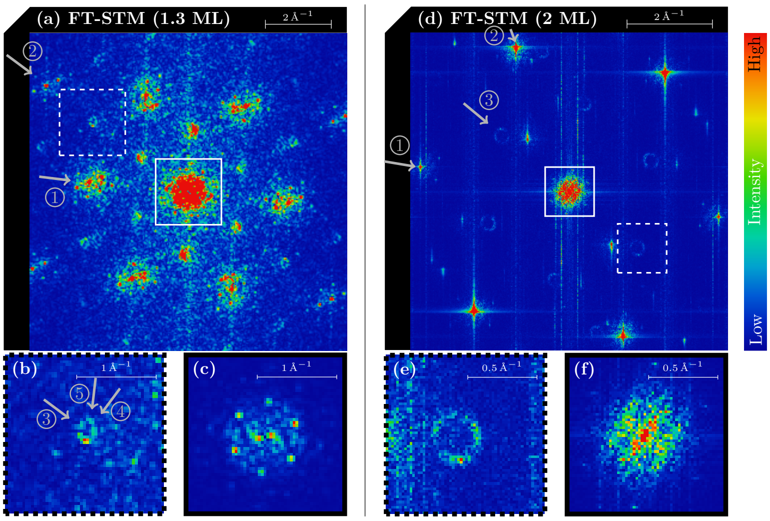

Figure 4.4: (a) and (d) show image sections of the FT-STM images in fig. 4.3(b) and (d), respectively, with a contrast-enhancing color scheme. White squares depict the area where particular zoom windows (b), (c) and (e), (f) are extracted from (a) and (d), respectively. In (c) and (f) the intensity scales are modified compared to (a) and (d), respectively. Gray arrows labeled by numbers depict the direction of different line scans shown in app. A.7.

The center of the FT-STM images, which is equivalent to the Γ point region of the SBZ, is shown in fig. 4.4(c) and (f) with adjusted contrast for the 1.3 ML and 2 ML sample, respectively. The comparison reveals that significant intensity is present in the case of 2 ML, but suppressed in the case of 1.3 ML. This behavior is a direct consequence of the pseudospin that affects the emergence of intravalley QI features in the Γ point region [146] as already discussed in sec. 3.2.3. Accordingly, it is evident that EMLG is probed via STM in the case of the 1.3 ML sample and EBLG in the case of the 2 ML sample. Since the 1.3 ML sample behaves like EMLG by applying local and area-averaging experimental methods, it is referred to as EMLG in the following and, correspondingly, the 2 ML sample as EBLG.

Table 4.1: Estimated values of the Fermi wave vector q_F from the FT-STM images in fig. 4.4 for different graphene layer thicknesses and scattering processes in 1D and 2D scaling (values in parentheses indicate the numerical error of the last significant digit).

Thickness	Scattering	$q_{F,\text{1D}}$ (nm^{-1})	$q_{F,\text{2D}}$ (nm^{-1})
1 ML	Intervalley	0.522(2)	0.603(2)
2 ML	Intervalley	0.544(4)	0.628(4)
2 ML	Intravalley	0.535(4)	0.618(5)

Since both STM measurements are performed at very low bias, the integration range contributing to the tunneling current is very low and the intervalley QI features in FT-STM can be interpreted as (slightly broadened) equivalent to the 2D Fermi surface, but with radius $2q_F$ (cf. sec. 3.2.3). For a quantitative analysis, line scans of the intensities along various directions depicted in fig. 4.4 are extracted and shown in app. A.7. The peaks stemming from (i) QI features and (ii) the lattice corrugation itself are fitted by Voigt profiles. STM images usually exhibit distortions that are caused by discrepancies in the length scale between slow and fast scan direction. To determine the reciprocal length between two features appropriately, the values are calibrated by the respective known lengths of the lattice in the specific directions (cf. app. A.7). The q_F values determined for different QI processes as a function of the graphene layer thickness are presented in tab. 4.1 considering 1D and 2D scaling (cf. sec. 3.2.3). In the case of EMLG, the

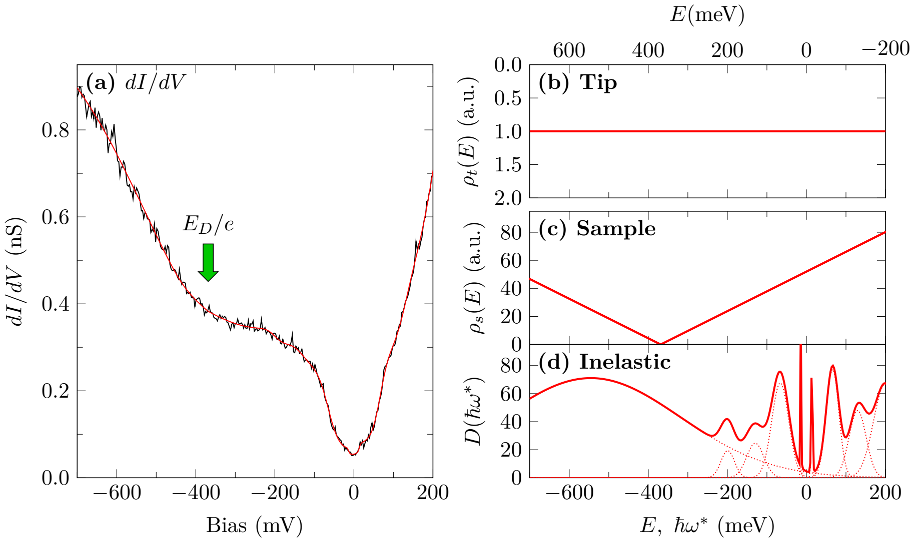

Figure 4.5: (a) Wide-range dI/dV spectrum acquired on EMLG sample (black solid line) ($T = 1.2\,\mathrm{K}$, $I_s = 500\,\mathrm{pA}$ at $V_b = 500\,\mathrm{mV}$, $V_{\mathrm{mod}} = 3\,\mathrm{mV}$, 5 acc.). Fit result (red solid line) containing contributions of the electronic DOS of (b) tip and (c) sample as well as (d) inelastic contributions (individual inelastic components depicted as red dotted lines).

intervalley QI feature exhibits an elliptical shape. Thus, only the value corresponding to the largest expansion (direction 5) is given. The values in the 1D scaling agree with the reported value $q_F = 0.53(6)\,\mathrm{nm}^{-1}$ for EMLG and EBLG within the error margin [146]. However, the 2D scaling is more appropriate for comparison to ARUPS data in sec. 4.3. Slight deviations of the absolute values of different processes are caused by the limited resolution of the STM images and the small shift of the Dirac energy of the EMLG sample to lower binding energies, as already discussed above, which causes a smaller elongation of the related Fermi surface. The resulting charge carrier concentration of 0.004 55(4) and 0.004 94(6) electrons per graphene unit cell, determined from the intervalley QI features of EMLG and EBLG, respectively, is induced by charge donation from the substrate and agrees well with the value of 0.005 reported for EBLG in refs. [23, 43]. In the case of EMLG, the electron concentration is slightly lower due to the tiny shift of the Dirac energy to lower binding energies upon prior K intercalation.

To prove the validity of the description of the total tunneling current provided in sec. 3.2.2 including elastic and inelastic contributions, tunneling spectroscopy data was acquired for EMLG and EBLG at the positions indicated by red dots in fig. 4.3. The wide-range dI/dV spectra of EMLG (fig. 4.5(a)) and EBLG (fig. 4.6(a)) exhibit a wide gap around the Fermi level. While the gap is smeared in the EMLG case, it is more pronounced in the EBLG case. The shape is qualitatively similar to spectra provided in ref. [181]. The origin of the gap, which is not of electronic nature, is still under debate. However, it is commonly attributed to inelastic tunneling effects based on phonon contributions [131, 182]. According to eq. (3.9), the elastic tunneling process is most efficient for electronic states of the sample with low $k_{\parallel}$ values. Yet, in the probed energy interval bands are available at the K point but not in the vicinity of the Γ point. Therefore, elastic tunneling into those bands with high $k_{\parallel}$ values is very ineffective. According to refs. [131, 182], virtual tunneling[f] processes are possible into unoccupied σ^* bands followed by

---

[f] A tunneling electron can populate electronic states of the sample that are usually not reachable due to its intrinsic energy within time uncertainty.

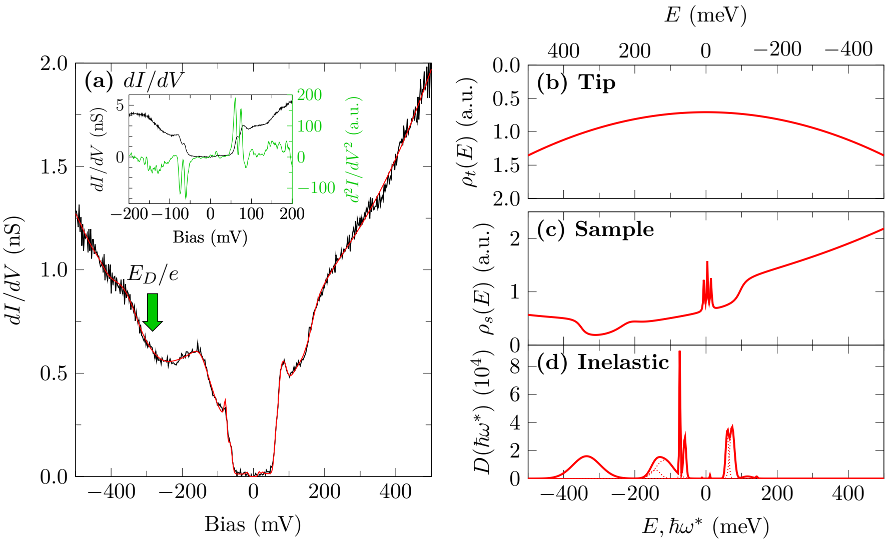

Figure 4.6: (a) Wide-range dI/dV spectrum acquired on the EBLG sample (black solid line) ($T = 1.2\,\mathrm{K}$, $I_s = 500\,\mathrm{pA}$ at $V_b = 500\,\mathrm{mV}$, $V_{\mathrm{mod}} = 0.35\,\mathrm{mV}$, 10 acc.). Fit result (red solid line) containing contributions of the electronic DOS of (b) tip and (c) sample as well as (d) inelastic contributions (individual inelastic components depicted as red dotted lines). Inset in (a): Smaller range, better resolved dI/dV spectrum at the same position (black line) and its numerical derivative (green) ($T = 1.2\,\mathrm{K}$, $I_s = 500\,\mathrm{pA}$ at $V_b = 200\,\mathrm{mV}$, $V_{\mathrm{mod}} = 1\,\mathrm{mV}$, 10 acc.).

an almost instant interaction with a sample phonon. Due to the momentum transfer provided by the phonon interaction, a tunneling electron can efficiently reach unoccupied states at high $k_{\|}$ values. Similar processes are also possible for the negative bias branch.

This phonon-mediated tunneling process, however, can only occur if the energy of the tunneling electron is high enough to excite (absorb) a phonon that provides a sufficient momentum transfer to reach unoccupied (occupied) electronic bands. Thus, an almost symmetric gap appears in the tunneling spectra around the Fermi level. The second derivative of the tunneling current acquired of the EBLG sample (inset in fig. 4.6(a)) exhibits pronounced peaks at about 60 and 75 mV (dips at negative bias branch) that can clearly be assigned to inelastic phonon processes. For the quantitative analysis of the tunneling spectra it is, thus, inevitable to include inelastic processes. The phonon contributions to the inelastic DOS $D(\hbar\omega)$ are described by the sum of several Gaussian profiles. Even though phonon contributions appear symmetric around the Fermi level, their intensities and widths might vary for the positive and negative bias branch as reported in ref. [141], which is accounted for in the fitting procedure. Also plasmon excitations can have an impact on the tunneling spectra [141]. According to ref. [86], in the case of epitaxial graphene those processes contribute most for $2E_D < eV_b < E_D$ and are included as a single peak in the inelastic DOS model.

The electronic DOS of EMLG is modeled by a simple V-shaped characteristic. This simple description, however, is not sufficient to account for the more complex DOS of EBLG. For that case a more advanced model needs to be considered that is sufficient to describe all possibilities of the site-resolved DOS [45,183] shown in fig. 2.3(b). Additionally, sharp electronic features near the Fermi level are further necessary in the case of EBLG to be able to describe the measured spectra. Those features stem from lateral LDOS variations that are caused by scattering processes and lead to the appearance of QI features. A more detailed discussion is given in sec. 4.3. For modeling of the electronic tip DOS, in each case the simplest model is chosen that is capable of describing the data along with physically reasonable models of the sample contributions. While for the EMLG data a constant tip DOS is sufficient (Pt/Ir tip), the description of the EBLG data requires a parabolic tip DOS (W tip). The exact equations of the applied models for EMLG and EBLG including all fitting parameters are provided in app. A.8.

For the quantitative analysis, the energy-dependent transmission coefficient needs to be estimated according to eq. (3.10). Therefore, the sample work function of 4.39(4) eV is determined from the secondary electron cut off (SECO) shown in app. A.3. To estimate an appropriate tip-sample distance the changes in height Δz for different applied biases during the stabilization at a given tunneling current are shown in app. A.9. The dependence $z(V)$ is non-trivial since it is affected by too many, generally unknown quantities (voltage part of transmission coefficient, electronic and inelastic DOS of sample and tip). From the progression of the curve, the z variation (normalized to $V_b = 200\,\mathrm{mV}$) is extrapolated to $V_b = 0$ visually. Hence, the tip-sample distance for a stabilization current $I_s = 500\,\mathrm{pA}$ at $V_b = 200\,\mathrm{mV}$ can be estimated to be about 2 Å. For measurements stabilized at a different V_b the particular distance is adjusted. The transmission coefficient is expected to be similar for elastic and inelastic contributions. Possible deviations would reflect in modified intensities, especially of inelastic contributions.

Upon numerical fitting, the respective models (red solid lines in fig. 4.5(a) and 4.6(a)) sufficiently describe the measured data with the contributions shown in (b)-(c) of the respective figure. The determined Dirac point of EMLG is located at $E_D = -0.37(1)\,\mathrm{eV}$, which perfectly agrees with the ARUPS result. Besides various phonon features that will be discussed below, a very broad plasmon feature is necessary to describe the measured data. In the case of EBLG, the Dirac point is located $E_D = -0.28(2)\,\mathrm{eV}$ with an electronic gap $E_g = 0.13(3)\,\mathrm{eV}$, which agrees with literature results (cf. sec. 2.2). Moreover, the sharp phonon features are sufficient to reproduce the sharply limited gap around the Fermi level. To further prove the inelastic nature of the gap, the tip was stabilized at $V_b = 50\,\mathrm{mV}$ ($I_s = 500\,\mathrm{pA}$ unchanged), which is obviously within the gap region of the EBLG. If the gap was purely of electronic nature, a tip crash with the sample surface would be expected by lowering the stabilization voltage to this value. However, it was possible to recored the dI/dV spectrum presented in fig. 4.7. Further, the low-bias STM images shown above could be acquired with an applied bias within the gap region. For this energy range, the graphene lattice does not exhibit phonons with sufficient momentum transfer to reach electronic bands (cf. fig. 2.6). On the basis of the $k_\parallel$ dependency of the LDOS within the Tersoff-Hamann model given in eq. (3.9), the tunneling probability for elastic tunneling to bands even with high $k_\parallel$ values can be increased upon decreasing the tip-sample distance. This is indeed achieved by lowering the bias setpoint at the same stabilization current. Accordingly, enough electrons exhibit sufficient momentum for an elastic tunneling process to electronic

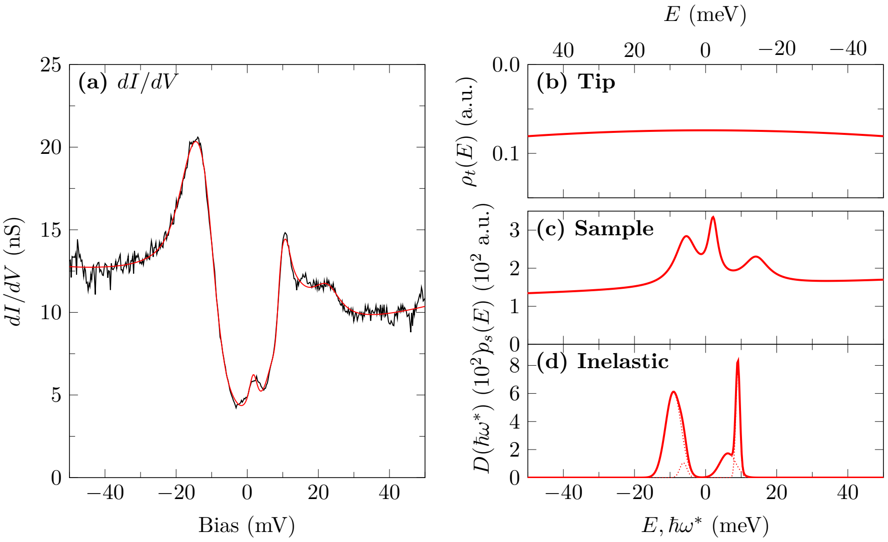

Figure 4.7: (a) dI/dV spectrum acquired within the gap range of the EBLG sample (black solid line) ($T = 1.2\,\mathrm{K}$, $I_s = 500\,\mathrm{pA}$ at $V_b = 50\,\mathrm{mV}$, $V_{\mathrm{mod}} = 0.35\,\mathrm{mV}$, 10 acc.). Fit result (red solid line) containing contributions of the electronic DOS of (b) tip and (c) sample as well as (d) inelastic contributions (individual inelastic components depicted as red dotted lines).

states located at the K point. However, the small range dI/dV spectrum also exhibits a gap that can only be explained quantitatively by the interplay of two phonon excitations with sharp scattering features (fig. 4.7(c) and (d)). The comparison with the phonon dispersion (cf. fig. 2.6) reveals that obviously also intravalley phonons with low momentum change significantly contribute to the total tunneling current, even if direct elastic tunneling to the K points is possible. Figure 4.8 compares the extracted PhDOS of each sample for the positive (upper panel) and negative (center panel) bias branch to the phonon dispersion (lower panel). In the case of EMLG (fig. 4.8(a)) the inelastic features are strongly broadened. The most prominent feature at 66 meV stems from high-momentum out-of-plane vibrations that enable inelastic tunneling to electronic bands at the K point. This is not possible for the low-energy feature since the momentum transfer is not sufficient. Thus, this feature stems from inelastic intravalley processes that seemingly open additional tunneling channels as well. The features at high energies are too broad to be clearly assigned to specific phonon modes. In the case of EBLG (fig. 4.8(b)), the determined features of the PhDOS are sharp enough to allow a clear assignment. Those features are more pronounced due to nearly two-fold degeneracy of phonon states compared to EMLG [106]. Similar to EMLG, the low-energy modes stem from acoustic phonons causing inelastic intravalley process. The maxima of all high-energy features coincide with the PhDOS at the very same phonon momentum close to the K point (red solid line in the lower panel of fig. 4.8(b)). The features at about 60 and 73 meV are usually assigned to M-point phonons [184]. However, the final (initial) state of an electron participating in the tunneling process has to be unoccupied (occupied). Since $k_{\|}$ at large tip-sample distances is small, the tunneling electrons are (virtually) located close to the Γ point. Thus, the momentum transfer from an M-point phonon is not sufficient to reach electronic bands. However, due to the finite reciprocal width of the electron pockets at the K point and the momentum distribution of tunneling electrons (cf.

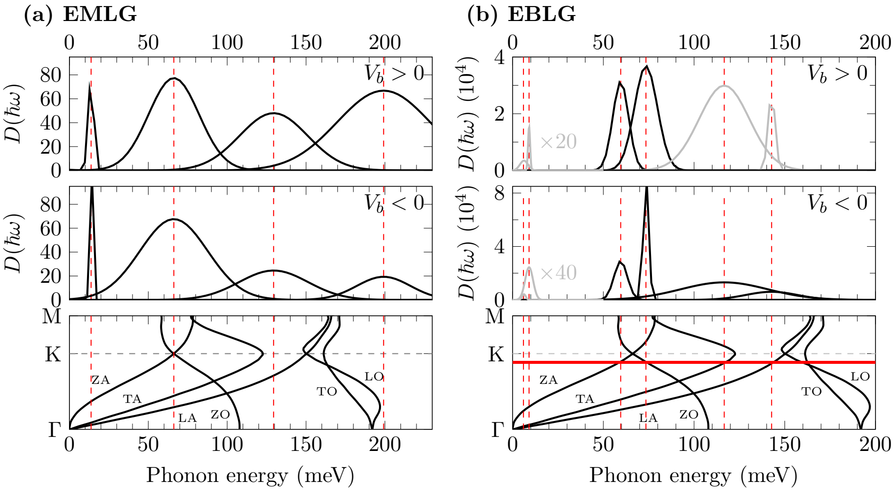

Figure 4.8: Comparison of phonon contributions extracted from dI/dV spectra of (a) EMLG and (b) EBLG (two lowest energy modes from gap range) with the graphene phonon dispersion from ref. [105] (lower panels). Positive (upper panel) and negative (center panels) bias branches are depicted separately. Red dashed lines indicate the maximum positions of the determined inelastic features. The red solid line depicts the momentum where the maximum positions of the high-energy features coincide with the PhDOS.

sec. 3.2.1), a momentum slightly smaller than that of K-point phonons is sufficient to relocate an electron with small parallel momentum into an available electronic state (same vice versa for the occupied sample branch). Thus, this interpretation is more likely than the participation of M-point phonons in the tunneling process. In conclusion, the developed procedure accounts for elastic and inelastic contributions to the total tunneling current and thereby enables a quantitative analysis of the experimentally determined dI/dV spectra with physically reasonable contributions that agree with previous studies.

Since tunneling within the inelastic gap region is possible, high-resolution dI/dV spectra of the Fermi level region can also be acquired. As shown in fig. 4.9, the intensities are increased compared to the data shown before, which is caused by the decreased tip-sample distance as a result of the lower stabilization voltage V_b (unchanged I_S). Obviously, there is no evidence of energy gaps in the meV range, neither for EMLG nor EBLG that would suggest superconductivity of the pristine samples.

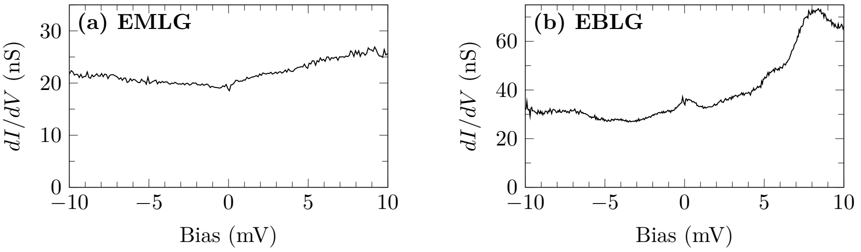

Figure 4.9: dI/dV spectra of the Fermi level region acquired at (a) EMLG and (b) EBLG ($T = 1.2\,\mathrm{K}$, (a) $I_s = 500\,\mathrm{pA}$ at $V_b = 20\,\mathrm{mV}$, $V_{\mathrm{mod}} = 0.15\,\mathrm{mV}$, 5 acc., (b) $I_s = 500\,\mathrm{pA}$ at $V_b = 10\,\mathrm{mV}$, $V_{\mathrm{mod}} = 0.1\,\mathrm{mV}$, 10 acc.).

4.2 Dynamics of the Intercalation Process

The intercalation process was monitored via DRS (cf. sec. 3.3) during the deposition of potassium as shown in fig. 4.10(a) and (b) for the EMLG and EBLG sample, respectively. Both measurements show a decreasing reflectivity on the low-energy side at first (black curve). Upon further deposition, this decrease moves toward higher energies (red curve). Subsequently, a broad dip is present in the visible range of the DRS spectrum (blue curve). The decreased reflectivity in the visible range has already been observed for fixed amounts of K intercalants in graphene laminates[g] [185] and for graphene on quartz[h], where the total signal change scales with the graphene layer thickness [186]. The predominant process leading to the observed decrease of the reflectance is the excitation of plasmons with an energy $\hbar\omega_P$ in the material [185]. Since ω_P scales with the total charge carrier density n [185], the continuous shift of the broad dip in the DRS spectra indicates an actual charge transfer from the intercalants to the sample, and the doping stage scales with the total number of K atoms embedded in the specimen. A quantitative analysis of the DRS data is not possible, because (i) the exact optical constants of SiC substrate and the graphene layer are not known for these specific samples and (ii) additional effects, like filling of IL bands as shown in ref. [185], would also have to be accounted for, which is beyond the scope of this thesis. Nevertheless, further potassium deposition on EBLG beyond 22 min (blue) leads to a significant change in the evolution of the DRS spectra. An additional, relatively sharp dip with a minimum at about 2.85 eV appears (orange curve), while the signal especially at low energies remains almost unchanged. The same behavior could be observed for the EMLG sample by changes in the differential DRS signal (not shown here), but the deposition

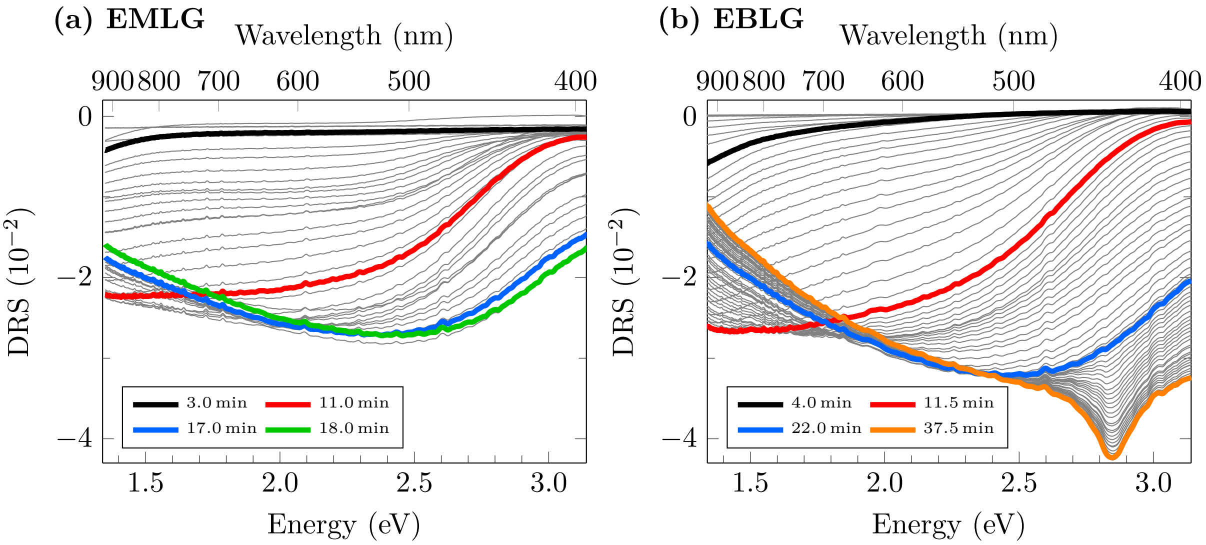

Figure 4.10: DRS signal evolution of (a) EMLG and (b) EBLG on SiC(0001) upon K deposition. Values in the legend correspond to different deposition times.

---

[g] Laminates were cleaved from highly oriented pyrolytic graphite (HOPG) in a solvent.

[h] Reflectivity measurements were carried out on a quartz substrate. The reported contrast is similar to the DRS signal, but refers to the bare substrate.

was always stopped at this point. The 2.85 eV feature cannot be assigned to a specific process yet, but indicates that the intercalation mechanism changes. Upon intercalation, both samples exhibit the same spectral evolution, though with slightly lower absolute signal of the EMLG sample. Thus, in the case of epitaxial graphene, DRS is a proper method for the fabrication of intercalated samples with reproducible K content, even for unsteady deposition rates.

If the deposition of potassium is stopped at the time when the 2.85 eV feature starts to develop in the DRS signal (blue curves in fig. 4.10), independent of the number of graphene layers the subsequently acquired LEED patterns exhibit an additional feature in the center of the diamond-like spot groups discussed in the previous section. The positions of these features are indicated by green circles in the LEED pattern of the K-intercalated EMLG sample shown in fig. 4.11(a) and correspond to the already reported (2×2) superstructure formed by the K intercalants with respect to the graphene lattice [56]. In contrast to previous studies, the typically observed features of pristine epitaxial graphene (already discussed in the previous section) do not vanish entirely. Indeed, those features appear strongly weakened compared to the pristine sample, but they are still discernible.[i] All data shown in the main text below were acquired using the EMLG (1.3 ML epitaxial graphene) on SiC(0001) sample.

Figure 4.11(b) shows a topographic STM image of the K-intercalated sample. The predominant part of the image shows a contrast modulation where every other honeycomb of the graphene lattice appears brighter. For clarification, an illustration of the graphene lattice is provided in the lower left part of the STM image. Accordingly, the FT-STM image (fig. 4.11(c)) exhibits additional bright features halfway between the Γ point and the first-order features of the graphene lattice (blue simulation) that arise from the (2×2) superstructure (green simulation) formed by the intercalants. However, a small area (left of center) is visible in the STM image that does not show the (2×2) superstructure. In this area a short bias pulse ($\approx 1\,\mathrm{ms}$) of 1.0 V was applied prior to the data acquisition. This approach is commonly used for tip conditioning, i.e., to get rid of contaminations of the tip or to change its geometry slightly. In the present case, it led to an alteration of the sample either by lifting the topmost graphene layer or by relocating the potassium atoms from their original positions in this area. Fortunately, due to the existence of this small area, tip-induced effects can be excluded since both lattices are resolved in the same lines in the fast (i.e., horizontal) scan direction. To the best of my knowledge, this is the first high resolution real space observation of the (2×2) superstructure formed by the K intercalants within epitaxial graphene on SiC(0001). STM measurements in the literature imaging the (2×2) superstructure of K-intercalated HOPG exhibit a completely different contrast for unknown reasons [187].

Figure 4.11(d) shows height profiles extracted along the lines depicted by the respective color in the STM image. The present corrugation clearly reveals the doubled lattice constant in the

---

[i] Faint features in the LEED image, which are not contained in the simulation, are explained by taking higher orders of multiple scattering into account as already discussed in the previous section.

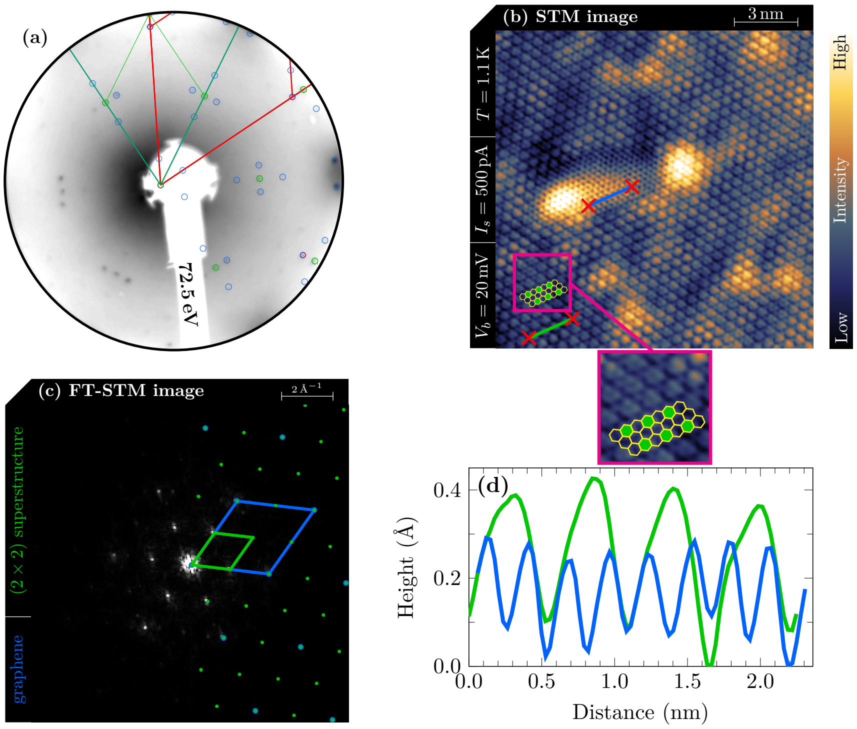

Figure 4.11: (a) Contrast-inverted, distortion-corrected LEED image of K-intercalated EMLG on SiC(0001). Lines depict the 2D reciprocal unit cell of the SiC (red) and the graphene lattice (blue) as well as the (2 × 2) superstructure (green). Circles indicate spot positions of multiple scattering between graphene and SiC lattice (blue) and of the (2 × 2) superstructure (green). (b) STM image of the sample surface. A structural model of both the graphene honeycomb lattice (yellow) and the superstructure (green) is depicted in the lower left corner and in the magenta-framed zoom window. (c) FT-STM image of (b) with respective reciprocal unit cells. (d) Height profiles along respective color lines in (a) (boundaries highlighted with red crosses).

intercalated area (green) compared to the pristine area (blue). The corrugation amplitude of the pristine area is about 0.2 Å (blue) which is significantly smaller than the reported average value 0.4 Å of pristine EMLG [38, 188], which itself is consistent with the average value estimated from the STM image of EMLG in this work (fig. 4.3(a)).[j] Compared to the small pristine area, the corrugation amplitude of the intercalated area is higher and amounts to about 0.3 Å (green). However, this value is significantly lower than the ionic radius of potassium (1.38 Å [190]), which suggests that the potassium atoms are located below the topmost graphene layer. Similar observations have been reported for STM images of Ca-intercalated EBLG (corrugation amplitude 0.1 Å [58], ionic radius of Ca 1.00 Å [190]) and upon Li intercalation [188].

To a much lesser extent the surface locally appears different as depicted in fig. 4.12(a).[k] The bright stripes can be attributed to wrinkles of the uppermost graphene sheet that are common for EMLG [191] even without being intercalated. The remaining surface is covered by bright, almost circular-shaped entities that do not show a particular structural order. This can be

---

[j] The corrugation amplitude of the sole buffer layer on SiC(0001) is reported to be about 1 Å [189] and, thus, even higher.

[k] The STM image was recorded on the same sample, but after a different preparation cycle of K deposition.

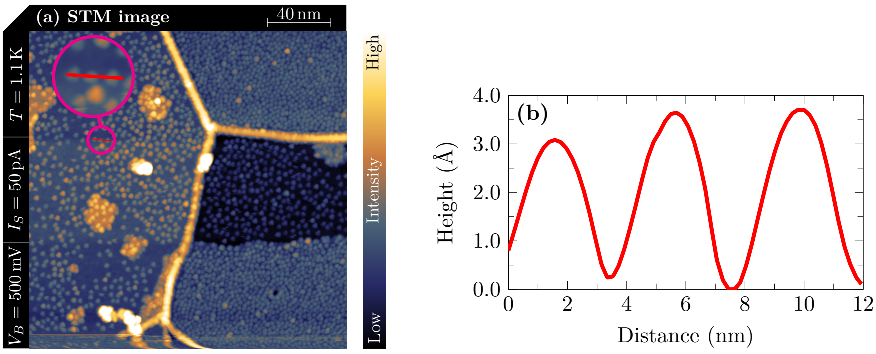

Figure 4.12: (a) STM image of the same sample as in fig. 4.11(b), but for a different area of the surface that is covered with clusters. The red line, which is better visible in the magenta-framed zoom window, depicts the section where the height profile in (b) is extracted.

concluded from the absence of defined features in the FT-STM image (not shown). The height profile in fig. 4.12(b), extracted along the red line in the STM image, shows that the amplitude of about 3.5 Å slightly exceeds the diameter of potassium ions (2.76 Å [190]), but is in the same order of magnitude. Therefore, it can be inferred that in this sample area potassium atoms (and even small clusters in the case of brighter features) are located on top of the uppermost graphene layer. In comparison to the lower corrugation amplitude of the (2×2) superstructure, this finding proves that the highly ordered structure is formed by K atoms below the topmost graphene layer. Further, the wave function of the metal layer penetrates into the uppermost graphene layer and changes the lateral contribution of the DOS, since it is visible via STM imaging.

Figure 4.13 shows PMMs of the K-intercalated EMLG sample at different binding energies. In the vicinity of the Fermi level (0.01 eV), triangular-shaped electron pockets appear near the K points ($k_{\parallel} \approx 1.7\,\text{Å}^{-1}$) with an extended size within the SBZ compared to pristine EMLG [41]. For higher binding energies, the width of the electron pockets decreases with a minimum size at about 1.5 eV (cf. full data set of PMMs in app. A.10). This indicates that the Dirac cone is rigidly shifted to higher binding energies and confirms a successful n-doping of the sample upon K intercalation. However, a second triangular shaped but mirrored electron pocket, located halfway between Γ and K point, is also present in the PMMs. Those features are a direct consequence of the presence of the (2×2) superstructure and emerge due to zone folding.

Folding of the band structure into the first BZ $E(\vec{k}) = E(\vec{k} + \vec{G})$ is a result of the translational symmetry of a crystalline solid and is described in standard textbooks on solid-state physics, e.g., ref. [91]. The resulting reduced zone scheme contains all information of the electronic band structure within the first BZ. In the case of (2×2) superstructures there is an additional periodicity $\vec{G}/2$ that alters the size of the first BZ. Instead of giving a mathematical approach to this phenomenon, a vivid visualization is provided in the following.

For reasons of symmetry all points of higher order BZs are equal to the first BZ. Thus, geometrically, a translation along a reciprocal lattice vector connects equal points as shown for Γ points in

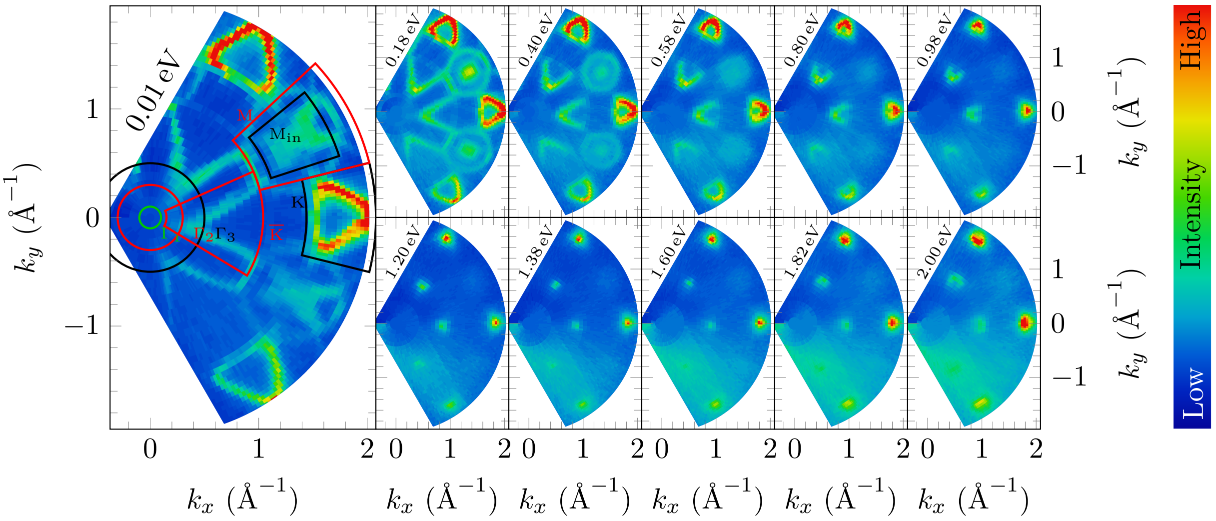

Figure 4.13: PMMs of K-intercalated EMLG on SiC(0001) at binding energies given in the upper left corners (energy integration range: ±22 meV, resolution: $\Delta\phi = 1°$, $\Delta\theta = 2°$). Differently labeled and colored areas depict integration regions for the EDCs in fig. 4.22.

fig. 4.14(a). Consequently, higher-order translations along $\vec{a}_1^* + \vec{a}_2^*$ are also possible. Introducing the (2×2) superstructure leads to a new BZ reduced in size by a factor of 2 (for reciprocal lengths). For the same reasons as before, translational invariance along $(2\vec{a}_i)^*$ and, thus, along $(2\vec{a}_1)^* + (2\vec{a}_2)^*$ as shown in fig. 4.14(b) needs to be fulfilled for the extended lattice. Therefore, as shown in fig. 4.14(c), the K′ point of the former BZ is translated via $(2\vec{a}_1)^* + 2(\vec{a}_2)^*$ to $\overline{\text{K}}$ of the new, smaller BZ. Accordingly, the triangular electron pocket appears mirrored compared to the K point as observed before. Moreover, the M point of the former BZ also appears at the Γ point due to translation along $2\vec{a}_i^*$ as shown in fig. 4.14(c). This is also visible in the PMMs, where additional circular-shaped electron pockets, occupied for low binding energies, appear most dominant at the M point, but are also present at the Γ point. Those circular features are addressed in detail in sec. 4.3.

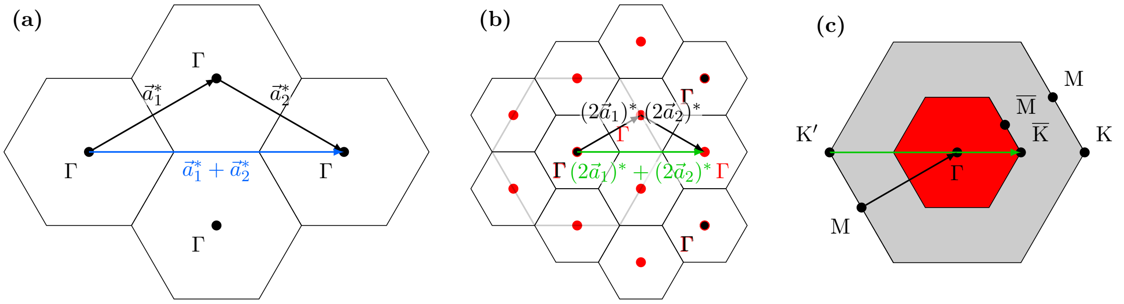

Figure 4.14: (a) BZs of a 2D hexagonal lattice with reciprocal lattice vectors $\vec{a}_i^*$ connecting equivalent points of neighboring zones (illustrated for Γ points here). (b) Reduced BZs upon consideration of an additional (2×2) superstructure (black) in relation to (a) (gray). Extra Γ points appear due to the superstructure (red) that are connected via reciprocal translational vectors $(2\vec{a}_i)^*$. (c) Examples of zone folding vectors of high symmetry points induced by a (2×2) superstructure.

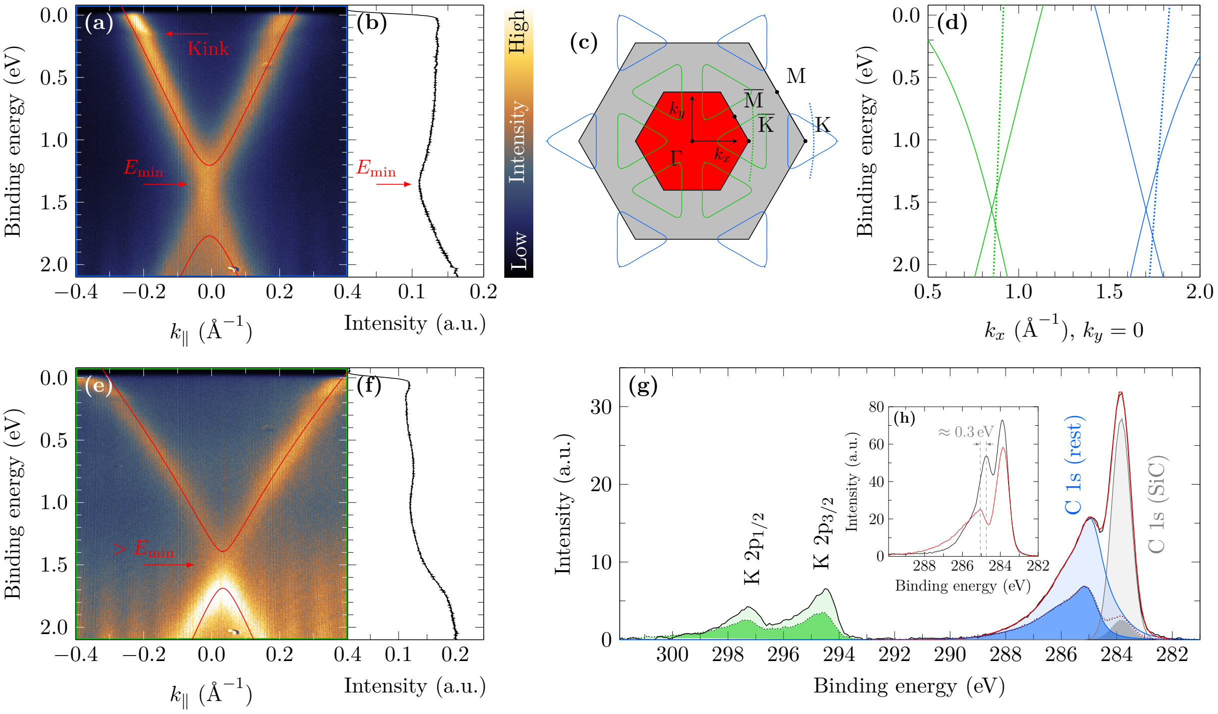

Figure 4.15: (a) ARUPS near the K point ($\theta = 56°$, $\phi = 0.22°$) and (e) near the $\overline{\text{K}}$ point ($\theta = 24.5°$, $\phi = -2.20°$) of K-intercalated EMLG on SiC(0001) (cooled with liquid helium, resolution: 2.56 meV, 0.05° corresponding to $\approx 0.0018\,\text{Å}^{-1}$) and respective sections from a 3NN TB calculation (red lines). (b) and (f) show the EDC of (a) and (e), respectively, integrated over all k values. (c) SBZ of epitaxial graphene (gray) and (2×2) superstructure with constant-energy contours at E_F calculated with a 3NN TB approach. Dotted lines depict the sections where the ARUPS data are acquired. (d) Related energy-dependent band structure and sections in ΓK direction. (g) XPS core level spectra of the C 1s and K 2p energy regions in normal (solid) and grazing (dotted) emission (0° and 70°). The spectral deconvolution is discussed in the text. (h) C 1s core level spectra, measured under normal emission, for the K-intercalated sample (red) in comparison to EMLG (black) as already shown in fig. 4.1(b).

Figure 4.15(a) shows an ARUPS section acquired with the 2D detector near the K point as depicted by the blue dotted line that refers to the section at the Fermi level. Seemingly, the data exhibits a single π band that presumably stems from a single Dirac cone that is rigidly shifted to higher binding energies (cf. fig. A.11(a,e)) upon K intercalation compared to the pristine sample. The related momentum-integrated intensity of this section shows a minimum at $E_{\text{min}} = 1.356(2)\,\text{eV}$ (fig. 4.15(b)).[1] This value agrees quite well with reported positions of the Dirac point of K-intercalated graphite ($E_D \approx 1.35\,\text{eV}$ [72, 192, 192]) and monolayer graphene on Au ($E_D \approx 1.3\,\text{eV}$ [16]). Due to folding, the π bands of graphene are also present in the ARUPS section acquired near the $\overline{\text{K}}$ point (green dotted line in fig. 4.15(c)) as shown in fig. 4.15(e). However, compared to the K point the Dirac point seems to appear at a slightly higher binding energy and the slope of the π^* band is seemingly lower which leads to an apparently wider opening of the cone at the Fermi level. Like in the previous section, this circumstance can be clarified by band modeling using the 3NN TB approach and a subsequent determination of the intersection with the 2D detector sections for the adjusted polar and azimuth angle. An

---

[1] E_{min} is determined by a parabolic fit in the vicinity of the minimum intensity.

appropriate qualitative description of the measured band structure (red lines in fig. 4.15(a) and (e)) is achieved based on parameters reported for K-intercalated graphite [192], but with modified E_{2p} and γ_0 (cf. app. A.6) and consideration of the folding process mediated by the (2×2) superstructure. As depicted in fig. 4.15(d), the 2D detector sections do not coincide with the Dirac point that is located at $E_D \approx 1.56\,\mathrm{eV}$ according to the model. Thus, instead of a linear dispersion the measured bands appear parabolic as a result of the conical sections of the Dirac cone. Moreover, the modeled band structure results in triangular-shaped electron pockets as depicted in the constant-energy cut at the Fermi level in fig. 4.15(c) that agree with the PMMs (cf. fig. 4.13). Since the ARUPS data near the K and $\overline{\mathrm{K}}$ point probe different positions of the triangular-shaped pockets, the measured dispersions obviously exhibit different slopes, but originate from equally shaped, even though folded, electronic bands. In the present case, a quantitative fitting of the 3NN TB model to the experimental data is not useful due to the strong renormalization effects upon electron-phonon and electron-electron (or electron-hole) many-body interactions that are especially pronounced for the π^* band [87]. Those interactions, which are not included in the simple 3NN TB model, affect the energy and intensity of the experimentally determined bands and result, e.g., in a kink at about 160 meV (cf. fig. 4.15(b)) that will be thoroughly discussed in sec. 5.2.

Figure 4.15(h) depicts XPS spectra of the C 1s core level of the pristine (black) and K-intercalated (red) sample in normal emission. Apart from a slight intensity decrease, the component originating from carbon atoms bound to Si atoms in the SiC crystal (at about $283 - 284\,\mathrm{eV}$) does not change significantly. However, the second maximum at 284.7 eV shifts about 0.3 eV toward higher binding energies upon K intercalation. This shift is accompanied with an asymmetric line shape that is most likely mediated by the emergence of at least one new component. Intriguingly, the components S1 and S2 originating from carbon atoms located in the buffer layer are no longer identifiable in the spectrum of the K-intercalated sample. A similar shift of about 0.8 eV accompanied with an asymmetric line shape upon K deposition has also been reported for 1 ML graphene on Au, where no buffer layer is present [16]. Moreover, the core level spectra of the K 2p doublet as shown in fig. 4.15(g) also exhibit an asymmetric line shape, which was neither observed for 1 ML graphene on Au [16] nor for K-intercalated graphite [193]. On the one hand, this asymmetry possibly originates from shake-up processes [194] that can additionally contribute to the XPS spectra at higher binding energies upon interactions with weakly bound electrons, e.g., in the conduction band. Then again, it would remain an open question why these shake-up processes seem to be absent in the measurements of K-intercalated graphite, for instance. On the other hand, this might indicate the presence of K atoms in a different chemical condition. In particular, this behavior is observed when the intercalants also penetrate into the interspace between buffer layer and SiC substrate, e.g., upon intercalation with Li [75], Au [195] or Yb [81], due to additional bonds to Si atoms of the topmost substrate layer. The angular dependence of the core level spectra reveals that the intensity in the entire range of the K 2p doublet is smaller for grazing emission (dotted line) than in normal emission (solid line). This finding suggests that the K atoms are located predominantly below the topmost graphene layer. Although the STM image in fig. 4.12(a) shows that K atoms can also adsorb on the surface, the sample areas where this occurs are small, since their contribution to the area-averaging XPS spectrum is negligible. Independent of the emission angle, no distinct features emerge in the XPS spectra of the K 2p doublet that would allow a deconvolution of different components contributing to the total signal. Therefore, the total intensity can only be estimated reliably by numerical integration over the entire K 2p doublet range.[m] For the estimation of the integrated intensity in the case of the C 1s core level spectra, four Voigt profiles are fitted to the data as shown in app. A.12. As already mentioned above, the buffer layer features can no longer be identified. Thus, only the origin of the C 1s (SiC) component is known to stem from C atoms that are bound in the SiC substrate. The remaining contributions stem from the graphene layer(s) and/or the (former) buffer layer that are influenced upon K intercalation. Thus, these features are cumulated to C 1s (rest) (blue shaded area) that shows a similar asymmetric line shape as for Yb-intercalated ZLG [84]. From the integrated intensities of the K 2p doublet and the C 1s (rest) feature a K:C_8 ratio of 0.9(3) can be estimated.[n] Considering that C 1s (rest) also includes contributions from the buffer layer of the pristine sample, the ratio indicates that almost twice the amount of potassium atoms that would be necessary for the formation of the (2 × 2) superstructure with the uppermost graphene layer, are situated on the sample. Since the amount of K atoms located on top of the sample is negligible, this finding strongly suggests that the K atoms also penetrate below the buffer layer. In most cases this is accompanied with a significant shift of the C 1s (SiC) component to lower binding energies (e.g., Cs [77], Na [78], Al [80]). However, fig. 4.15(h) reveals that this component does not shift upon K intercalation. The example of Rb intercalation (same lateral (2 × 2) structure) verifies that penetration below the buffer layer can, in fact, occur without an energetic shift of this component [77]. Furthermore, the momentum-integrated intensity the ARUPS data near the $\overline{\mathrm{K}}$ point in fig. 4.15(f) exhibits a weak maximum intensity at about 0.6 eV that is even more pronounced in the data acquired from a different preparation of the same sample with less potassium (K:C_8 ratio 0.7(2)), shown in app. A.11. Actually, this measurement exhibits the same electronic bands although the K concentration is lower (red lines from a 3NN TB calculation with identical parameters). The low signal-to-noise ratio (SNR) probably reveals a inferior structural quality of the (2 × 2) superstructure. Due to the low SNR, however, it becomes clear that the maximum in the momentum-integrated intensity originates from a non-dispersive band that can be most likely assigned to the still (partially) populated K 4s core level.[o] Similar non-dispersive bands have already been observed for metal-intercalated EMLG where the intercalants were assumed to penetrate below the buffer layer (e.g., Yb [81]).

---

[m] No error assumed for K 2p intensity integration

[n] For the determination the respective sensitivity factors [196] or cross sections [197] for each atomic species needs to be considered. The ratio provided in the text corresponds to the mean value of both methods.

[o] For pure K films the K 4s core level is located at a binding energy of 0.4(3) eV [198].

In particular, those bands were also observed upon Yb intercalation of ZLG [84], leading to the conclusion that these features originate from metal atoms located in the interspace between the SiC substrate and the former buffer layer.

Upon K intercalation the UPS spectra reveal two secondary electron backgrounds with distinct onsets (for both K concentrations) as shown in app. A.3. While this could be explained by lateral inhomogeneity of the sample, it might also indicate an effective decoupling of the former buffer layer based on the previous discussion. Since the SECO at higher kinetic energy is more pronounced, it represents the better estimate for the majority work function. Consequently, a value of 2.64(1) eV can be estimated that is strongly reduced compared to the pristine EMLG (4.20(2) eV), but slightly higher than the work function of pure potassium (2.3 eV [158]).

Having now established the possibility that decoupling of the buffer layer might proceed upon K penetration below the buffer layer, the structural properties are reanalyzed in the following. As discussed in sec. 4.1, the STM images of EMLG and EBLG both exhibit a long-range contrast modulation that results in the observation of defined features in the respective FT-STM images assignable to a (6×6) superstructure originating from the surface reconstruction of the buffer layer with respect to the SiC lattice (cf. sec. 2.2). However, there is no evidence of similar features in the FT-STM image of the K-intercalated sample (cf. fig. 4.3) that can be assigned to a (6×6) superstructure. Faint features surrounding the image center and the first-order features of the graphene lattice (i) appear in a different direction and (ii) describe a smaller lattice. Those features are addressed in the next section. In agreement to a study of Li-intercalated EMLG [188], the lack of a (6×6) contrast modulation in the STM image indicates that the buffer layer changes its surface reconstruction upon K intercalation, which gives an additional hint that the buffer layer is chemically detached form the substrate. Moreover, this behavior can only be achieved upon penetration of K atoms into the interspace between buffer layer and substrate. As a result, the K-intercalated EMLG sample behaves like K-intercalated quasi-freestanding EBLG.

However, the LEED pattern acquired of the K-intercalated sample (fig. 4.11(a)) still exhibits features that are commonly attributed to the surface reconstruction of the buffer layer. In several studies those features vanished upon metal intercalation (e.g., Li [188]). Nevertheless, in the case of Yb intercalation of ZLG, where the decoupling of the buffer layer has clearly been demonstrated, those features are still discernible but strongly weakened [84], similar to the observations upon K intercalation of EMLG here. As already discussed in sec. 4.1, this LEED pattern can also be expected without the presence of a reconstructed buffer layer because of multiple scattering processes, only with lower spot intensities. Since the penetration depth of LEED is capable to probe even the lattice of the SiC substrate, multiple scattering processes are possible. On the contrary, STM only probes the corrugation of the electronic structure at the surface with an expectedly smaller information depth compared to LEED, which confirms the experimental findings. Therefore, multiple scattering processes seem to play a major role in the LEED measurements. Under the assumption that the (2×2) superstructure in relation to the graphene lattice is formed by metal atoms above the buffer layer without modifying it, the intact buffer layer should still exhibit the (6×6) surface reconstruction with respect to the SiC lattice. Accordingly, one could expect at least first-order multiple scattering features of the (6×6) reconstruction surrounding the features of the (2×2) superstructure in the LEED pattern. This is not the case for the K-intercalated EMLG sample (cf. fig. 4.11(a)). On the other hand, as shown in fig. A.15(b) of app. A.13 those features were actually detected for low K concentrations in an EBLG sample alongside weak spots of the usual diamond-like pattern. Deposition of even more K atoms leads to the appearance of the very same LEED pattern as observed upon K intercalation of EMLG (cf. fig. A.15(c) of app. A.13). Therefore, it can be concluded that K atoms initially intercalate between the topmost layers of EBLG. For higher concentrations, they also penetrate between the uppermost SiC layer and the buffer layer by decoupling the latter from the underlying substrate. In retrospect, this finding supports the conclusion of an actual decoupling of the buffer layer from the substrate upon K intercalation of EMLG.

Figure 4.16(a) shows the LEED pattern of the K-intercalated EMLG sample acquired at RT after being stored in the STM setup at $T < 5\,\mathrm{K}$ for 20 days.[p] The determined LEED pattern did not change compared to the as-deposited sample (cf. fig. 4.11). At 300 K, however, the intensities of all features that originate from the (2×2) superstructure exponentially decay with a time constant of about 14 min as depicted in figs. 4.16(c)-(e). After about 20 min those features vanished entirely, which reveals that the (2×2) configuration of the K atoms is not stable at RT as opposed to low temperatures. Simultaneously to the vanishing of the (2×2) features new spots emerge, which can be assigned to a $(\sqrt{3} \times \sqrt{3})\mathrm{R}30^\circ$ superstructure with respect to the graphene lattice. This has already been reported for Yb-intercalated ZLG upon annealing at 450 °C, but without the prior existence of a highly ordered structure of the intercalants [84]. Obviously, for the K atoms this effect already occurs at RT. Further, the comparison suggests that the observed structural transition most likely takes place below the (former) buffer layer. Figure 4.17 depicts ARUPS data acquired near the K point of the graphene SBZ after the structural transition. The observed bands can clearly be identified as the superposition of two π bands, one with its Dirac point located at low binding energies similar to pristine EMLG (cf. fig. 4.2), and one at higher binding energies. This observation qualitatively agrees with experimental data in the literature acquired after annealing at temperatures, however, significantly above RT (Rb [77], Na [78], Eu [79], Al [80], Yb [81,82]). Earlier studies attribute this observation to a laterally inhomogeneous sample consisting of intercalated and pristine graphene areas [77]. However, recent calculations of Yb-intercalated EMLG, which also consider possible penetration of intercalants below the buffer layer, reveal that this observation can be attributed to a configuration in which intercalants are only located between the former buffer layer and the SiC substrate and no longer between both graphene sheets [85]. Thus, a smaller amount of K atoms effectively participates in

---

[p] The transfer from the STM setup until the first LEED image was acquired took about 3 min.

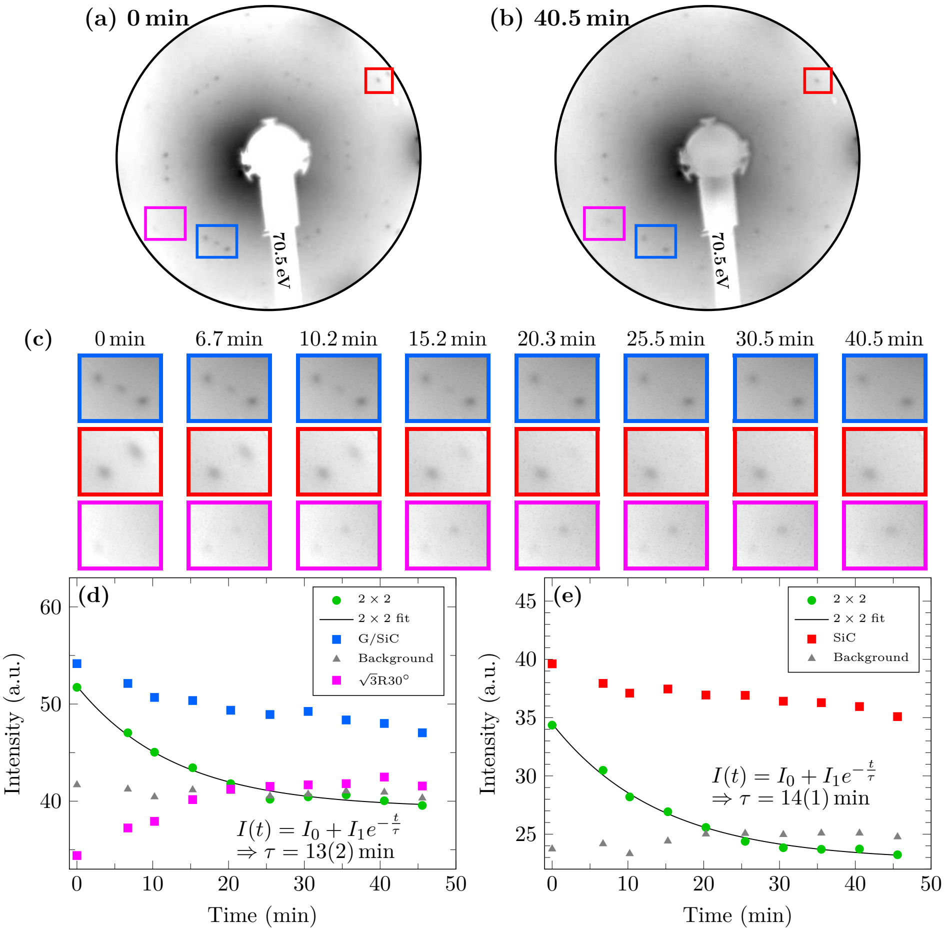

Figure 4.16: Time-dependent structural evolution of K-intercalated EMLG on SiC(0001) at RT. Contrast-inverted, logarithmically scaled LEED acquired (a) at the beginning of the measurement and (b) after 40.5 min. Colored rectangles depict the positions where the related image sections in (c) are extracted from. Spot and background intensities are given as a function of time in (d) determined from the image sections framed blue and magenta and (e) framed red. The decreasing intensities of features related to the (2×2) superstructure are fitted by an exponential decay function as depicted in each plot.

the doping process compared to the doping stage, where the (2×2) superstructure is present. In other words, the former buffer layer is doped by the K intercalants, while the topmost graphene layer is just slightly doped by the presence of the underlying substrate similar to pristine EMLG. The respective SECO shows only one onset (cf. app. A.3) that corresponds to a work function of 3.44 eV. This value is higher than the value before the transition, which suggests a lower effective doping concentration of the entire sample. To verify the possibility of buffer layer decoupling, ARUPS data acquired after K intercalation of a different 1.2 ML epitaxial graphene sample is shown in app. A.5. For low K concentrations (fig. A.4(b)), two π bands, which are comparable to fig. 4.17, are visible directly after the deposition. The data acquired of the same sample, but with higher K concentration (fig. A.4(c)), does only exhibit one π band at high binding energies similar to the highly doped stage of the EMLG sample. In summary, for low K concentrations as well as after the structural transition at RT the (former) buffer layer, which does not form π bands in the pristine sample, is effectively decoupled from the SiC substrate by penetration of

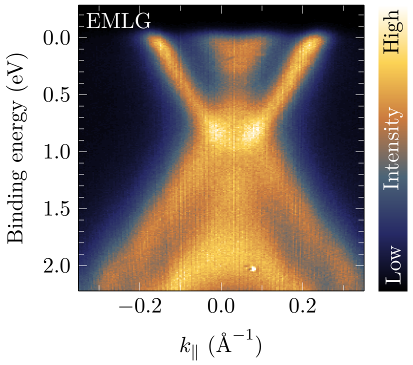

Figure 4.17: ARUPS acquired with the 2D detector near the K point of K-intercalated EMLG on SiC(0001) after the sample had been stored in UHV at RT for several days (resolution: 8.36 meV, 0.1° corresponding to $\approx 0.0034\,\text{Å}^{-1}$).

K atoms into the interspace, which can be concluded from the existence of additional π bands assignable to this layer.

Nevertheless, in the highly doped case, where the (2×2) superstructure is present, only one Dirac cone appears in the ARUPS data (fig. 4.15). Since K intercalation below the buffer layer most likely causes a decoupling of the latter, an effective bilayer is formed. Accordingly, the observation of two Dirac cones is expected just like in the case of pristine EBLG (cf. sec. 2.2). In fact, two slightly separated π bands were observed experimentally upon Li intercalation of EMLG [76], with both Dirac points located at higher binding energies compared to the pristine sample. This observation was confirmed by calculations that consider the intercalants located beneath the (former) buffer layer and also between the carbon layers (Li [76], and also Yb [85]). Surprisingly, the separation of the π bands is also correctly predicted for Li intercalation by a different theoretical study that was carried out for freestanding bilayer graphene intercalated with various metals between both graphene layers solely [66]. Indeed, this study predicted two π bands also in the case of K and Rb intercalation, albeit without energetic separation so that they overlap completely and appear as a single band. This prediction was confirmed experimentally in the case of Rb [77]. Thus, the experimental finding of just a single Dirac cone in the ARUPS data here is plausible and most likely originates from two overlapping, energetically degenerate π bands.

Considering all previous findings of the highly n-doped case, the intercalants are most likely located beneath the (former) buffer layer and also between the carbon layers, accompanied with an effective decoupling of the (former) buffer layer. Thereby, EMLG is transformed into K-intercalated quasi-freestanding EBLG. This configuration can also be referred to as the thinnest limit of a stage-1 GIC, but probably with an increased interlayer distance due to the missing binding partners at the surface. While the intercalants form a highly ordered superstructure beneath the uppermost layer (revealed via STM), the lateral structure of the intercalants below the buffer layer is not known. Since no distinct additional features appear in the LEED pattern, they might also arrange in a (2×2) superstructure or do not show any structural order. A (1×1) registry with the graphene or SiC lattice is not expected due to (i) the atomic radius of K and (ii) the low K concentration on the sample. The physical structure of potassium intercalants below the buffer layer remains an open question.

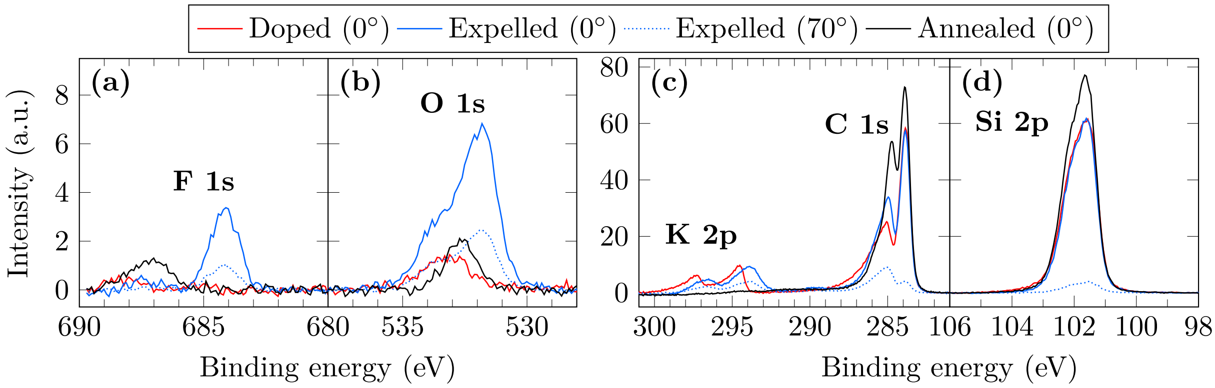

Figure 4.18: Comparison of XPS core level spectra of EMLG focusing on (a) F 1s, (b) O 1s, (c) K 2p and C 1s, and (d) Si 2p for optimally K-doped (red), expelled (blue) samples under normal (solid) and grazing (dotted) emission, and annealed (black) samples (Shirley background subtracted).

Since the effective concentration of K atoms participating in the doping process is found to be lower after the structural transition, and desorption of the K atoms from the sample at RT is unlikely, the question arises, where the expelled potassium atoms are located. The XPS core level spectra (fig. 4.18) reveal a significant amount of fluorine (F) and oxygen (O) on the sample (blue solid line), both of which were hardly detectable before the structural transition (red solid line). Those contaminations most likely stem from the residual gas in the UHV chamber. The C 1s core level is narrower for the sample after the structural transition at RT than for the doped sample, which possibly originates from the lower doping level. Further, the K 2p doublet is shifted to lower binding energies. That observation reveals a modified chemical bonding of the K atoms in the expelled sample by possible formation of KF [199] and KOH [200]. The other component of the O 1s peak most likely originates from water (H_2O), which often contaminates the sample surface even in UHV. The spectrum determined for grazing emission (blue dotted line) reveals that the contaminations are all located below the uppermost graphene layer. However, upon annealing the contaminations (and even the K atoms that were deposited on purpose) can be removed almost entirely (black solid line). The Dirac point of the annealed sample is slightly shifted towards the Fermi level compared to an as-grown pristine EMLG sample, as previously reported after Al deposition [80]. This small discrepancy can be attributed to remaining trace contaminations (KF, H_2O, KOH, etc.) that modify the interface between the substrate and BLG and/or MLG. Apart from these subtle differences, it can be concluded that the sample is largely reconditioned upon annealing.

Since the highly doped condition is not stable at RT, the sample handling turned out to be challenging. After K deposition at RT (monitored by DRS) the as-prepared samples were quickly checked for their structural quality via LEED and then immediately transferred to either the liquid helium-cooled manipulator for PES experiments or into the STM device (1.2 K). The susceptibility of the highly doped samples to rearrangements and/or disordering might be the reason why ARPES and STM data of the highly ordered structure of K-intercalated EMLG has not been reported yet.

4.3 Detailed Analysis of the Electronic Structure

In this section the electronic structure of the highly n-doped, as-deposited, former EMLG sample that exhibits the (2×2) superstructure is scrutinized by means of (i) area-averaging ARUPS and (ii) local tunneling techniques. In particular, the comparability of the acquired data in terms of the employed experimental method is discussed. Figure 4.19(a) shows the central part of the FT-STM image in fig. 4.11(c) of the K-intercalated EMLG sample with a color scheme specifically chosen for improved visibility of faint features.[q] Besides the already discussed high-intensity features that correspond to the reciprocal lattice of graphene and the (2×2) superstructure (cf. fig. 4.11(c)), faint triangular contours (cf. fig. 4.19(d)) are present surrounding the position of a potential $(\sqrt{3} \times \sqrt{3})$R30° structure that correlates with the K point of the SBZ of the graphene lattice. The extension of the graphene SBZ (blue solid line) is shown in fig. 4.11(b) along with hexagons connecting the first-order features of the graphene (blue dashed line) lattice and the superstructure (green dashed line) for comparison. The triangular contours can also be identified in second order, but mirrored at the second-order features of the (2×2) superstructure. Moreover, faint circular contours surround the first-order features of the reciprocal graphene lattice (fig. 4.19(c)). Based on the results in sec. 4.1 regarding the pristine sample, these faint contours most likely originate from QI effects. From this point of view, the triangular features are caused by intervalley scattering processes between two inequivalent K points. Compared to the triangular electron pockets apparent in the PMMs at the K point in the vicinity of the Fermi level (cf. 4.13), the triangles appear flipped in the FT-STM image and are wider in k space. However, this behavior qualitatively agrees with the expected FT-STM image calculated for freestanding graphene significantly above the Fermi level considering the triangular constant-energy contours of the π^* bands [150, 201, 202] already discussed in sec. 3.2.3. Accordingly, the circular features in the FT-STM image can be assigned to QI upon intravalley scattering processes. Compared to spots originating from the graphene lattice as well as the second-order spots of the (2×2) superstructure, the first-order features caused by the (2×2) superstructure appear strongly broadened (fig. 4.11(d)). As depicted in fig. 4.19(b) this position coincides with the M point of the graphene SBZ. Since circular electron pockets around the M point are observed in the PMMs, the broadening indicates additionally possible intervalley QI effects due to scattering between inequivalent M points. However, the quality of those features is not sufficient to allow a clear assignment. A circular feature, which would be expected around the center of the FT-STM image upon intervalley scattering especially in the case of EBLG, can neither be proven nor excluded as shown in fig. 4.19(f), owing to the limited size of the STM

---

[q] The lower part of the FT-STM image is artificially improved by upscaling of the resolution from 512 to 4096 data points (rounding of missing pixels) and extending the image by pasting it periodically to all sides (overall 4 times the size) to achieve an even better visibility of faint features. Quantitative analyses, however, are performed in the raw data (like in the upper part of the image).

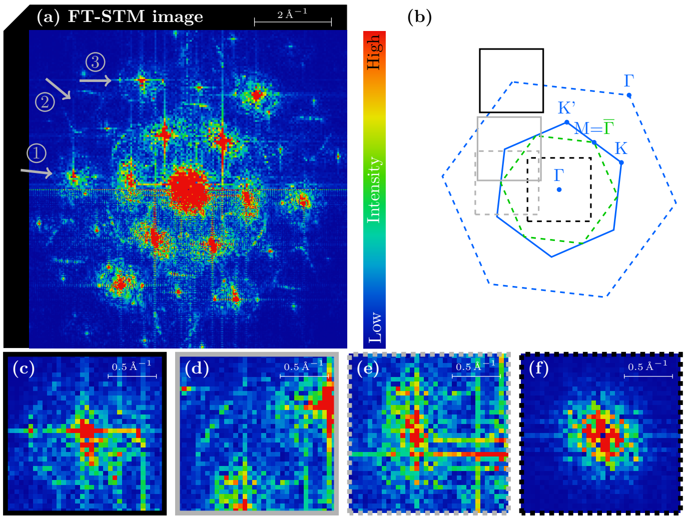

Figure 4.19: (a) Section of the FT-STM image in fig. 4.11(c) with contrast-enhancing color scheme. The lower half is further contrast-enhanced by using artificially augmented resolution and fast Fourier transform with Hann window function for better visibility. Gray arrows labeled by numbers depict the direction of different line scans shown in app. A.7. (b) Hexagons connecting the next-nearest Γ points of the graphene lattice (blue dashed) and of the (2×2) superstructure (green dashed). The blue solid hexagon indicates the extension of the SBZ of graphene (blue solid). Squares indicate the positions in k space where the close-up views in (c)-(f) are extracted, each with an individually adjusted intensity scale.

image. Contrary to the PMMs, the FT-STM image shows no evidence of contours originating from potential QI due to scattering between folded bands in the smaller SBZ, even if lattice features of the (2×2) superstructure are clearly present.

For a quantitative analysis of distinct QI contours, line scans along the directions depicted by gray arrows are analyzed to determine the diameter of the features (shown in app. A.7). To account for possible distortions of the STM image, the determined values are calibrated by a respective known length in the specific direction[r] just like in sec. 4.1 assuming the graphite lattice constant to be 2.461 Å [20]. Further, the bias applied during the acquisition of the respective STM image (20 mV) is low enough to correlate the QI contours with scattering processes at the Fermi level. The absolute values of the Fermi wave vectors $\vec{q}_F$ for different processes are estimated from the determined diameters. The results are shown in tab. 4.2 in 1D and 2D scaling (cf. sec. 3.2.3). Obviously, the determined values are about four times enlarged compared to pristine epitaxial graphene (cf. tab. 4.1). From the average value $q_{F,\mathrm{2D}} = 2.621(3)\,\mathrm{nm}^{-1}$, a charge carrier concentration of $n = 1.642(3) \cdot 10^{14}\,\mathrm{cm}^{-2}$ can be estimated by using eq. (3.18) (valley degeneracy of K point $g_v = 2$). This implies that, compared to freestanding pristine graphene, 0.3444(6) additional electrons are donated to the graphene layers per unit cell of the (2×2) superstructure. However, this approach underestimates the total charge carrier concentration, because it neglects the circular features observed in the PMMs at the M and Γ point of the graphene SBZ.

---

[r] The line scan in direction 2 is calibrated by second-order features of the (2×2) superstructure; the line scan in direction 3 with the graphene lattice features determined from line scan in direction 1.

Table 4.2: Estimated values of the Fermi wave vector q_F from the FT-STM images in fig. 4.19 for different scattering processes on the Dirac cone in 1D and 2D scaling (values in parentheses indicate the numerical error of the last significant digit, calibrated by respective factors in tab. A.7).

Direction	Scattering	$q_{F,\mathrm{1D}}$ (nm^{-1})	$q_{F,\mathrm{2D}}$ (nm^{-1})
2	Intervalley	2.192(2)	2.531(3)
3	Intravalley	2.348(2)	2.712(2)

Therefore, ARUPS data along the high symmetry ΓM and ΓK directions (cf. schematic inset at the top of fig. 4.20) are extracted from the PMM data stack (cf. fig. 4.13) and presented in fig. 4.20(a). In ΓK direction, the π and π^* band of the Dirac cone with a crossing point at the K point of the graphene SBZ ($k_\parallel \approx 1.7\,\text{Å}^{-1}$) are clearly visible. The apparent asymmetry between the left and the right branch of the π^* band is a result of the triangular shape of the electron pockets observed in the PMMs. Further, the intensities of both branches are markedly different, which is a consequence of using p polarized light for this experiment. The polarization dependence, which is similar to the pristine sample (cf. fig. A.2(c)), originates from the anisotropy caused by the two inequivalent carbon atoms in the graphene unit cell [83]. However, the left branch is still visible, because the incident light is not perfectly polarized (degree of polarization ≈ 90 %). Upon folding, the Dirac cone is also visible in the vicinity of the $\overline{\mathrm{K}}$ point ($k_\parallel \approx 0.85\,\text{Å}^{-1}$) that corresponds to the K point of the (2×2) superstructure SBZ. The mirrored asymmetry and intensity distribution of the left and the right branch compared to the Dirac cone at the K point verifies that it originates from the K′ point, i.e., the opposite side of the graphene SBZ.[s]

In the ΓM direction of the ARUPS data, two nearly parabolic bands centered at the M point of the graphene SBZ are apparent, which are responsible for the circular contours in the PMMs (cf. fig. 4.13). Upon folding (cf. sec. 4.2), those nearly free-electron-like bands are also present in the vicinity of the Γ point, better visible in the contrast-enhanced image section in fig. 4.20(e). In this region, however, the bands appear slightly different due to the presence of various bands in a smaller k-space volume for low $k_\parallel$ values. In particular, the folded π^* band overlaps with the parabolic bands in ΓK direction, but is also responsible for the high-intensity feature close to the Fermi level in ΓM direction (cf. fig. 4.13). None of those parabolic bands are present in ARUPS data recorded of the pristine sample as shown in fig. A.2(c), neither at the M, nor at the Γ point. In accordance with the literature, electronic bands of graphene with a parabolic dispersion at the Γ point exhibit interlayer character (cf. sec. 2.3) and are thus labeled as IL$_1$ and IL$_2$. Although filling of one interlayer state upon metal intercalation has already been determined experimentally (e.g., Rb-intercalated, H-passivated ZLG [62], Rb- [57] and Ca-intercalated EBLG [58]), this is (to my knowledge) the first observation of two IL bands below the Fermi level. Moreover, the ARUPS data exhibits significantly increased intensity at higher binding energies centered at the M and Γ point that becomes better visible in the contrast-enhanced image sections in 4.20(c) and (d), respectively. Since it is present at both high-symmetry points,

---

[s] The polarization dependence is responsible for the low SNR in the 2D-detector measurement near the $\overline{\mathrm{K}}$ point in fig. 4.15(e).

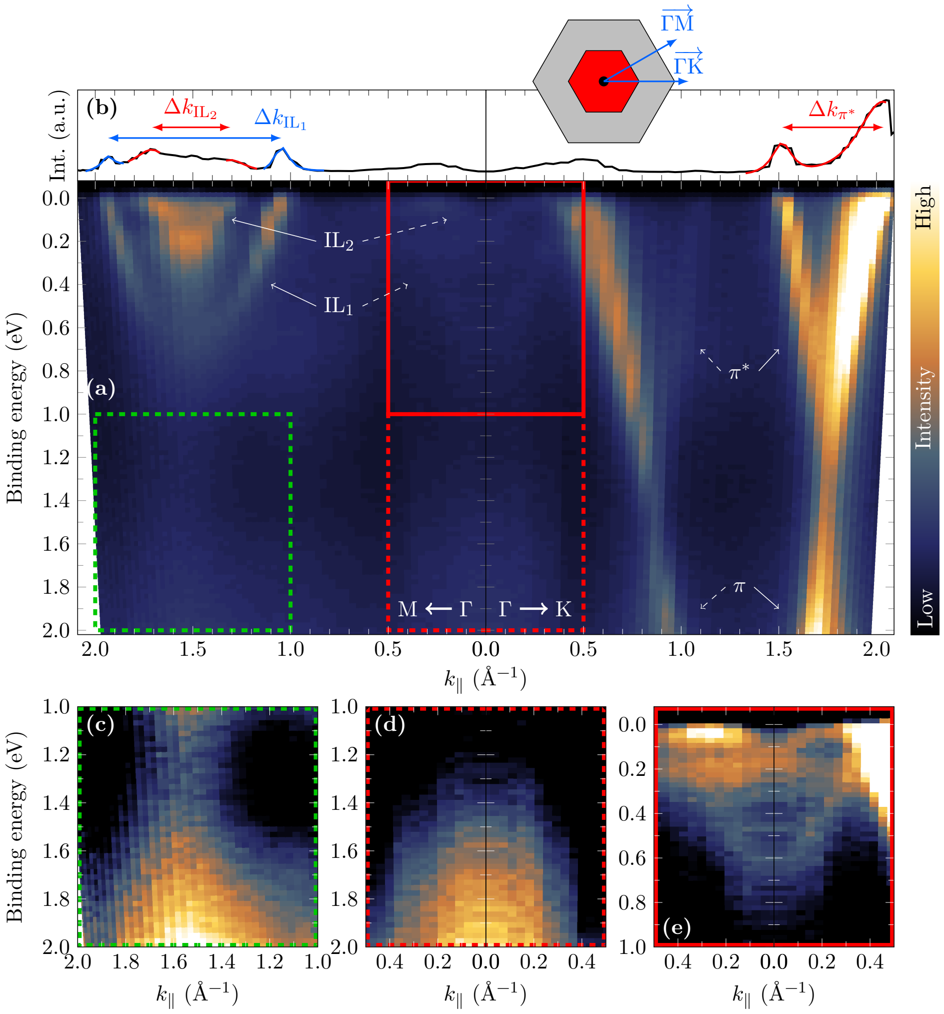

Figure 4.20: (a) ARUPS data extracted from PMMs along the high symmetry directions ΓM and ΓK as depicted by the schematic inset at the top. (10 azimuth slices averaged, resolution: $\Delta k_\parallel = 0.0375\,\text{Å}^{-1}$, $\Delta E = 22\,\text{meV}$). (b) MDC at the Fermi level. (c)-(e) Contrast-enhanced close-up views from areas framed with the respective line types and colors in (a).

this observation is most likely not an experimental artifact, and the presence of an additional downward opened parabolic band is assumed to be the cause. Since graphene does not exhibit electronic bands in the relevant energy region, those dispersive bands most likely originate from the metal intercalant layer. For comparison to the locally probed STM data, an MDC near the Fermi level is extracted from the ARUPS data in the high symmetry directions (fig. 4.20(b)). The intersection of every band with the Fermi level (numerically determined by peak fitting) allows the estimation of the respective Fermi wave vectors, separately for each band. The results are provided in tab. 4.3. The value determined for the π^* band matches the average q_F determined via FT-STM[t] ($q_{F,\mathrm{2D}} = 2.621(3)\,\mathrm{nm}^{-1}$) within the experimental uncertainty. This finding ensures that the same electronic structure is probed with both methods. To estimate the total charge carrier density of the K-intercalated sample, the reduced SBZ resulting from the (2×2) superstructure is considered. Since the K point of the SBZ of any hexagonal lattice is

---

[t] Direction 3 of the FT-STM analysis and the ΓK direction of the ARUPS data probe the same section through the triangular Fermi surface.

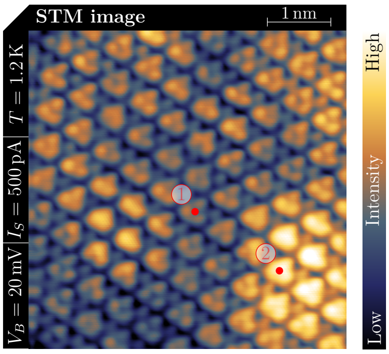

Figure 4.21: STM image of K-intercalated EMLG that was recorded in the lower right part of the area shown in fig. 4.11(b). Red dots indicate positions where the all following single STS spectra are recorded.

two-fold degenerate, the π bands contribute twice ($g_v = 2$). In contrast to the BZ of graphene, for the reduced BZ the three-fold degeneracy of the M point must not be included, since the parabolic bands are present at the Γ point solely and not at its M points. The determined contributions to the total charge carrier densities (tab. 4.3) demonstrate that the occupation of the IL_1 band upon K intercalation has the greatest impact on the total carrier concentration, followed by π^*.

Table 4.3: Estimation of the charge transfer to the graphene sheets based on the MDC in fig. 4.20(b) (values in parentheses indicate the numerical error of the last significant digit). The degeneracy of the $\overline{\mathrm{K}}$ point is already accounted for.

Band	$\Delta k_\parallel$ (Å^{-1})	q_F (nm^{-1})	n ($10^{14}\,\mathrm{cm}^{-2}$)	e$^-$ per UC$_{(2\times2)}$
π^*	0.52(2)	2.60(9)	1.6(1)	0.34(3)
IL_1	0.88(1)	4.44(6)	2.36(6)	0.49(1)
IL_2	0.40(8)	2.0(4)	0.5(2)	0.10(4)

The estimated total charge carrier density $n = 4.46(36) \cdot 10^{14}\,\mathrm{cm}^{-2}$ suggests that 0.94(8) electrons are donated per unit cell of the (2×2) superstructure. In fact, this value agrees remarkably well with the value 0.944 calculated via DFT for freestanding K-doped BLG [66], even though potassium is considered between the graphene sheets, solely. The negligible discrepancy between experiment and theory may be somewhat surprising, because in those calculations the Dirac point is located closer to the Fermi level and only one IL state is filled. However, DFT calculations usually underestimate the actual IL pocket size [74]. The observed additional shift might then be caused by the K atoms located between the SiC substrate and the former buffer layer, donating their charge partially to the substrate and to the graphene system. As discussed in sec. 4.1, pristine EMLG and EBLG are slightly doped due to the presence of the SiC substrate (≈ 0.005 electrons per graphene unit cell [43]). Based on this value, 0.02 additional charges are donated in the case of a hypothetical (2×2) unit cell of pristine epitaxial graphene. Compared to the charge donation upon K intercalation, this value is indeed negligible. Thus, the substrate influence on the doping is so small that the properties of the K-intercalated sample can be considered as isolated K-intercalated bilayer graphene.

To gain further insights, point spectroscopy data was acquired at two different sample positions as depicted in fig. 4.21. For the sake of lucidity, only the spectra at position 1 will be discussed

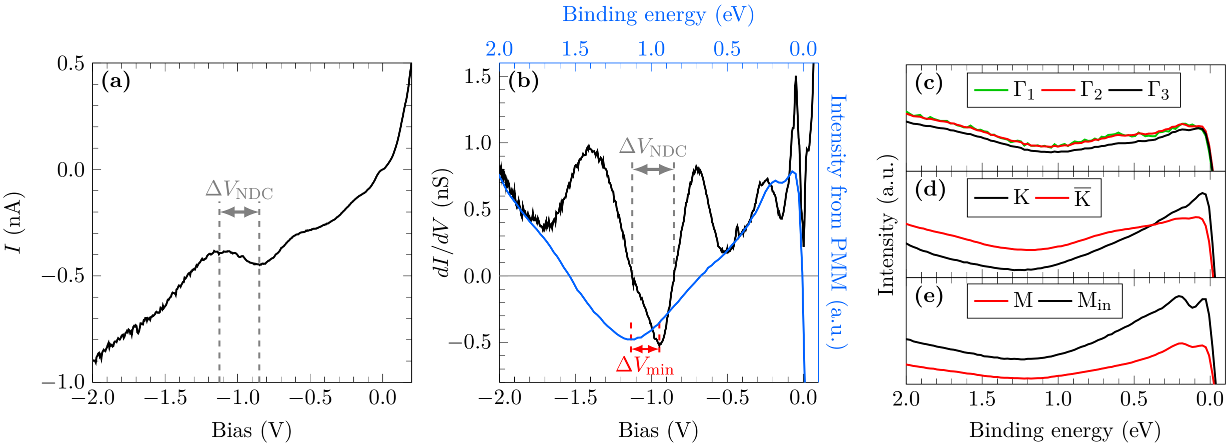

Figure 4.22: (a) Wide-range bias-dependent tunneling current and (b) corresponding dI/dV spectrum (black) acquired using lock-in technique at position 1 ($T = 1.2\,\mathrm{K}$, $I_s = 500\,\mathrm{pA}$ at $V_b = 200\,\mathrm{mV}$, $V_{\mathrm{mod}} = 5\,\mathrm{mV}$, 5 acc.) along with an EDC calculated by angular integration of PMM intensities shown in fig. 4.13 (cos-scaled). (c)-(e) EDCs of slices depicted in fig. 4.13.

in the main text, while those at position 2 are presented in app. A.15 for comparison. The determined wide-range current-voltage characteristic exhibits an unusual behavior in the bias range ΔV_{NDC} as depicted in fig. 4.22(a). For negative bias values, an increasing absolute bias results in a decreasing absolute current in that range. As a result, the respective dI/dV spectrum reveals negative values (fig. 4.22(b)). In eq. 3.12, which is widely used for the interpretation of tunneling spectra, the dI/dV signal is proportional to the DOS that by definition can only exhibit positive values. Nonetheless, this phenomenon has already been observed in several studies [203, 204], even for pristine EBLG [45]. According to ref. [203], a negative differential conductance (NDC)[u] can occur when energetically localized states are present in sample and tip. When the applied bias is appropriate for a coincidence of those states, a maximum in the tunneling current appears that might lead to an NDC. For clarity, fig. 4.23 depicts this process. An energetically localized feature at E_0 in the sample DOS (occupied state) and a feature at $-E_0$ in the tip DOS (unoccupied), result both in a feature at $V_0 = E_0/e$ in the dI/dV spectrum. However, when a second narrow feature is present in the sample DOS at E_1, the tunneling spectrum exhibits negative values in the vicinity of $E_0 + E_1$ (fig. 4.23(b)), which is not the case when it is located in the sample DOS (fig. 4.23(a)). Especially when a high lateral resolution is achieved, as is the case here, the apex of the tunneling tip is atomically sharp. The tip-apex atoms induce a narrow, energetically localized state that can be described by a Lorentzian function near E_F [45, 203]. Accordingly, the observation of an NDC in the tunneling spectra most likely originates from an energetically localized state in the tip DOS.

Tunneling spectroscopy is frequently assumed to be an angle-integrating method [129]. However, the comparison of the dI/dV spectrum with the angle-integrated, energy-dependent intensity of the PMM data stack (blue line in fig. 4.22(b)) reveals a strongly deviating shape. Even the minima of both curves appear shifted by ΔV_{min}. To account for a possible k dependence of the tunneling process, different slices are presented in (c)-(e) that are extracted from the

---

[u] This phenomenon is sometimes also referred to as negative differential resistance (NDR) in the literature [203].

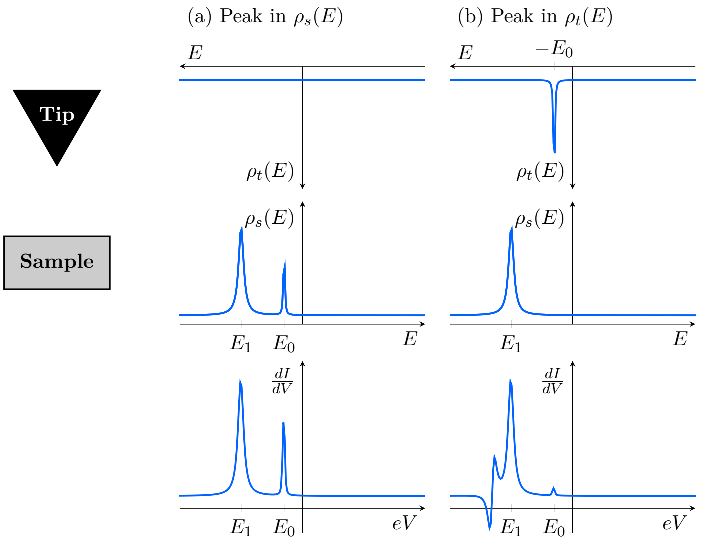

Figure 4.23: Schematic explanation of negative values in dI/dV spectra. While no NDC is present when the sample DOS exhibits two sharp features (a), an NDC is present when one of these features originates from the tip DOS (b). Further explanations are provided in the text.

PMMs around different high symmetry points as depicted in fig. 4.13. Yet, none of the extracted slices exhibits a shape that is comparable to the measured dI/dV spectrum. This apparent contradiction will be resolved later in this section.

The STM measurements of K-intercalated EMLG are capable of mapping the lateral structure (fig. 4.21). Conversely, that implies spatial variations of the DOS at the surface. To monitor those variations, a dI/dV map is acquired in this region by performing an STS experiment at every point of a lateral grid with prior stabilization of the tunneling current at a given bias. The lateral drift during the about 11 hour measurement was less than $< 0.04\,\mathrm{nm}$ as can be seen in the STM images taken before and after the dI/dV map acquisition that are shown in fig. A.16 (app. A.14). The z image, in which the elongation of the z piezo after the stabilization is illustrated and which is comparable to a moderately resolved STM image, explicitly reveals the (2×2) superstructure, which is also clearly visible in the related FT image (fig. 4.24(a)). The respective maps in fig. 4.24(c,d) depict the laterally resolved dI/dV signal at certain biases indicated in fig. 4.24(b). While features related to the (2×2) superstructure are present in the dI/dV maps at negative bias (fig. 4.24(c)), they are suppressed in the maps at positive bias (fig. 4.24(d)), although they are present in the STM and z images acquired with positive bias. This behavior is a direct consequence of the stabilization problem introduced in sec. 3.2.1 that transfers the information about the dominant structure to the z image upon adjustment of the tip height during stabilization at positive bias. Consequently, the absolute height of the dI/dV signal is arbitrary due to the arbitrarily chosen stabilization bias. Nevertheless, the relative height variations can be interpreted, since they result in the emergence of the observed structure in the STM image. Independent of the bias sign, faint QI features are visible in the FT of all drawn dI/dV maps. Figure 4.24(b) depicts arbitrarily chosen spectra from the map. Indeed, those spectra deviate strongly for both bias branches, which originates from additional laterally different contributions on a small energy scale of several meV. Even though it is obvious that the presence of the (2×2) superstructure and QI are responsible for the deviations of the spectra

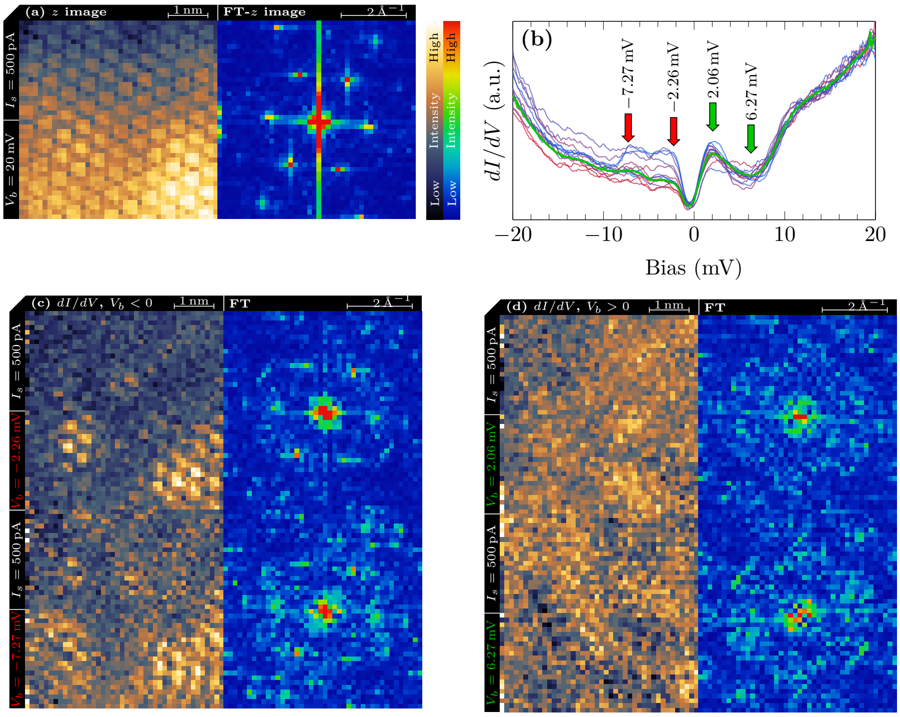

Figure 4.24: dI/dV mapping of the sample area depicted in fig. 4.21 (42×42 spectra ⇒ total 1764, bias resolution 0.1 mV, lock-in: $f_{\mathrm{mod}} = 1612\,\mathrm{Hz}$, $V_{\mathrm{mod}} = 0.1\,\mathrm{mV}$, only one forward sweep, spectra smoothed by a Savitzky-Golay filter over 13 data points). (a) Image of initial z values (left) where the tip is stabilized (similar to the STM image) and corresponding FT image (right). (b) Averaged dI/dV spectrum (green) along with arbitrarily chosen single spectra (blue to red). Arrows depict the negative (red) and positive (green) biases at which the dI/dV maps in (c) and (d) and the corresponding FT images were recorded, respectively.

in this energy region, the origin of the features cannot be assigned to a certain process, due to arbitrary normalization. However, for the following quantitative analysis of the spectroscopic data, it is essential to account for those laterally changing features in the meV range. Similar to the approach in sec. 4.1, the tip-sample distance is estimated to 3 Å at $V_b = 200\,\mathrm{mV}$ (cf. fig. A.8), and the work function of 2.69 eV (cf. sec. A.3) is used for modeling of the transmission coefficient of the tunneling process. The best description of the dI/dV spectrum (fig. 4.25(a)) was achieved with the sample DOS shown in fig. 4.25(c), under the assumption of a parabolic tip DOS[v] with a localized state near E_F (fig. 4.25(b)) and several inelastic contributions originating from phonons ($< 200\,\mathrm{meV}$) and plasmons ($> E_D$) (fig. 4.25(d)). The complete model for the fitting procedure is provided in app. A.8. The interplay of the tip DOS with elastic and inelastic sample contributions is capable of describing the NDC appropriately. This phenomenon is mediated by the relatively sharp drop of the electronic sample DOS at about -0.9 eV[w] that is additionally pronounced by the inelastic contributions *mirrored* at this feature as discussed in sec. 3.2.2.

---

[v] For the measurement here, the same tip as for the tunneling experiments on pristine EMLG was used (cf. sec. 4.1). However, it had been conditioned newly, which might be the reason for the modified DOS.

[w] A similar drop of the sample DOS, though at different energies, leads to the observation of an NDC in dI/dV spectra of pristine EBLG [45].

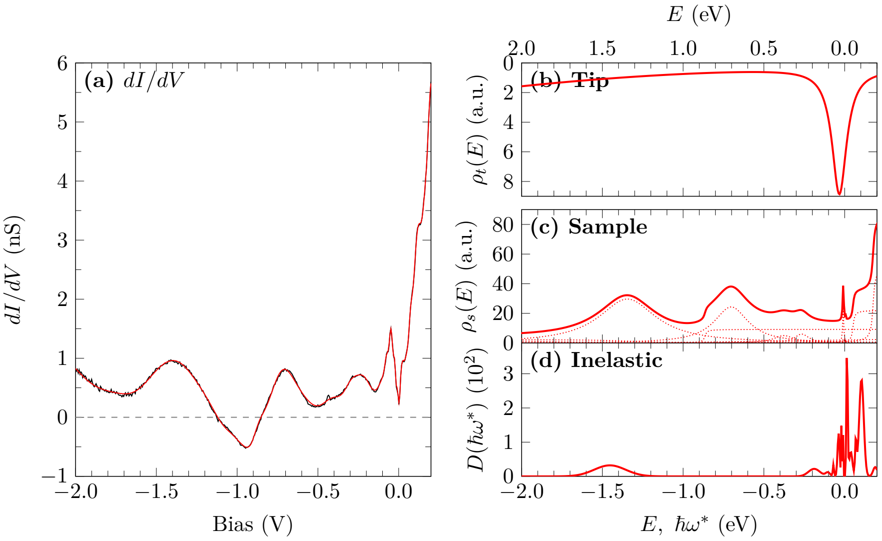

Figure 4.25: (a) Wide-range dI/dV spectrum acquired at position 1 (black solid line) ($T = 1.2\,\mathrm{K}$, $I_s = 500\,\mathrm{pA}$ at $V_b = 200\,\mathrm{mV}$, $V_{\mathrm{mod}} = 5\,\mathrm{mV}$, 5 acc.). Fit result (red solid line) containing contributions of the electronic DOS of (b) tip and (c) sample (individual sample DOS components depicted as red dotted lines) as well as (d) inelastic contributions.

Note that without inelastic contributions, which are assumed to arise from phonon and plasmon excitations of K-intercalated graphene, a sufficient description of the minimum of the NDC was not feasible.

Unfortunately, the extracted electronic sample DOS is still not comparable to any of the angular-integrated PMM slices in fig. 4.22. Since the tunneling process is most effective for low $k_{\|}$ values (cf. sec. 3.2.1), the extracted electronic sample DOS most likely arises from the electronic structure near the Γ point, which is equal to the M point of the graphene SBZ in the present case. Both high-symmetry points exhibit two pronounced parabolic IL bands. Parabolic bands usually manifest as steps in dI/dV spectra (and DOS), as observed, amongst others, for the surface state of Ag(111) [205]. However, when very low $k_{\|}$ values are probed solely, only the vertex of the parabolic band contributes. Consequently, the vertex is overestimated, which results in a peak (rather than a step) at the onset of the parabolic band. Thus, the features in the range between the Fermi level and $-1.0\,\mathrm{eV}$ can be attributed to the IL bands already observed in the ARUPS data. Astonishingly, the weak band at higher binding energies observed in the ARUPS data also contributes to the tunneling DOS of the sample and is – in conjunction with inelastic plasmon contributions – responsible for the pronounced feature at 1.4 eV. Moreover, the fitting procedure suggests the possibility of step-like features in the positive bias branch that most likely arise from unoccupied parabolic bands. Obviously, just a very small volume of the reciprocal space around the Γ point is probed via tunneling experiments. In turn, this result implies that the contribution of the Dirac bands, located at the K and $\overline{\mathrm{K}}$ point of the SBZ, to the total tunneling current is negligible. Further, the tunneling experiments were performed with the tip positioned over the bright features in the STM image (cf. fig. 4.21). Since the K atoms are located below the topmost graphene sheet, the wave function of the interlayer states also partially extends to above the graphene sheet, which is in agreement with the calculations in ref. [66], albeit being

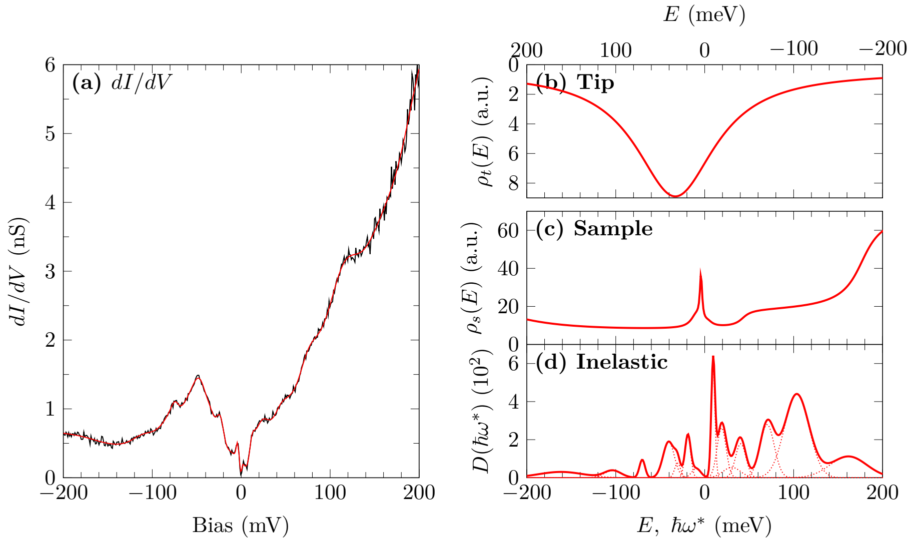

Figure 4.26: (a) dI/dV spectrum covering the phonon range acquired at position 1 (black solid line) ($T = 1.2\,\mathrm{K}$, $I_s = 500\,\mathrm{pA}$ at $V_b = 200\,\mathrm{mV}$, $V_{\mathrm{mod}} = 1\,\mathrm{mV}$, 5 acc.). Fit result (red solid line) containing contributions of electronic DOS of (b) tip and (c) sample as well as (d) inelastic contributions (individual inelastic components depicted as red dotted lines).

carried out for freestanding K-intercalated BLG. At this tip position, the overlap of the tip wave function with the IL bands is dominant, which may explain its predominant contribution to the tunneling data.

Figure 4.26(a) shows a tunneling spectrum acquired with improved resolution of the region, where inelastic phonon contributions of graphene are expected. The fitting model assumes the same electronic sample and tip DOS like in the wider range, but is reduced to relevant contributions (cf. sec. A.8). The deconvolution reveals that the dI/dV spectrum is dominated by inelastic processes in this region that are assumed to originate from phonon excitations in K-intercalated graphene. Further, sharp features around the Fermi level are necessary to describe the measured data. Those features stem from local variations of the sample DOS as discussed above. In fact, those local variations ought to be present in the entire spectral range, but are apparently most relevant close to the Fermi level. Due to the consideration of those features, the presence of peaks caused by inelastic contributions can be described.

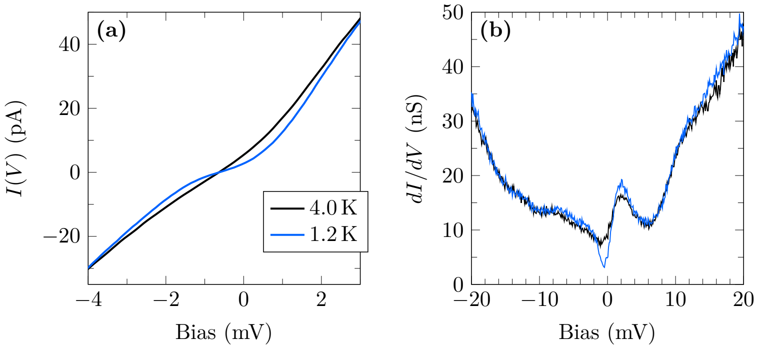

Figure 4.27: Temperature-dependent (a) tunneling current and (b) scaled dI/dV spectra acquired at position 1 ($T = 1.2\,\mathrm{K}$ (blue) and $4.0\,\mathrm{K}$ (black), $I_s = 500\,\mathrm{pA}$ at $V_b = 20\,\mathrm{mV}$, resistance of the tunneling junction $\approx 40\,\mathrm{M\Omega}$, $V_{\mathrm{mod}} = 0.1\,\mathrm{mV}$, 10 acc.).

High-resolution tunneling spectra of the low-bias region further reveal that the tunneling current (fig. 4.27(a)) exhibits a kink in the vicinity of the Fermi level at a sample temperature of 1.2 K. Consequently, the related dI/dV spectrum exhibits a significant dip near the Fermi level (fig. 4.27(b)). At a sample temperature of 4.0 K, however, neither the kink in the tunneling current, nor the narrow dip at the Fermi level of the dI/dV spectrum is present. This observation suggests

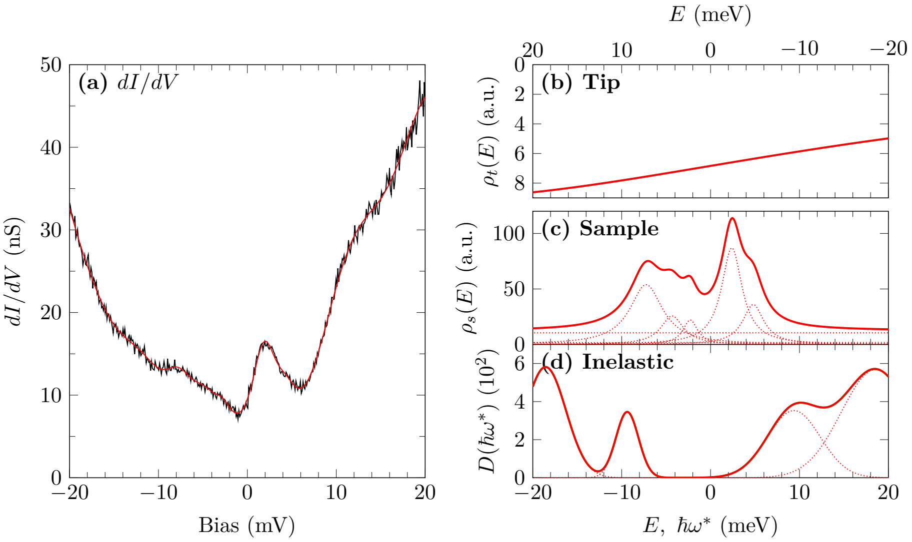

Figure 4.28: (a) dI/dV data from fig. 4.27(b) for $T = 4.0\,\mathrm{K}$ (black solid line). Fit result (red solid line) containing contributions of electronic DOS of (b) tip and (d) sample as well as (c) inelastic contributions from the sample (individual sample DOS and inelastic components depicted as red dotted lines).

the existence of a small, temperature-dependent energy gap that can possibly be attributed to a superconducting state of the sample. This potentially superconducting energy gap will be thoroughly analyzed and discussed in the next section. For the deconvolution of tip and sample contributions to the small-range tunneling data, the spectrum acquired at 4.0 K is preferred because a superconducting gap can be excluded in the fitting model. Nonetheless, the elevated temperature has to be taken into account. Since the spectroscopic data is rescaled and the respective tip-sample distance is included for the stabilization at different biases, it is possible to consider the already determined tip and sample DOS even with similar intensity for the low-setpoint measurement. The best fit of the acquired data (fig. 4.28(a)) was achieved by considering the localized unoccupied tip state whose slope is visible in the narrow energy range here (b), five additional features that result from the locally enhanced DOS besides a nearly constant background in the electronic sample DOS (c), and, in particular, pronounced inelastic features that most likely arise from low-energy phonon modes (d). The determined inelastic contributions are summarized in fig. 4.29. Contrary to EBLG as discussed in sec. 4.1, a clear assignment of the features to specific phonon modes is hardly feasible here. This is most likely a consequence of the variety of possible inelastic processes since, in the vicinity of the Fermi level, electronic bands are available for almost every k value of the SBZ of K-intercalated graphene (cf. PMMs in fig. 4.13). However, DFT calculations of K-intercalated freestanding BLG predict an additional low-energy phonon mode at about $8 - 9\,\mathrm{meV}$ ($70\,\mathrm{cm}^{-1}$) that arises from vibrations of the K atoms located between both graphene sheets [66], which possibly explains the pronounced low-energy feature at about 9 meV in the tunneling data.

The tunneling experiments turned out to be very challenging under certain circumstances. To gain proper spectroscopic results (especially in the region around the Fermi level), relatively high tunneling currents are necessary at low bias voltages. Therefore, the tip-sample distance needs to be very small. The induced electrical field might cause dramatic changes of the sample. For instance, application of a short bias pulse leads to a drastic change of the lateral structure in

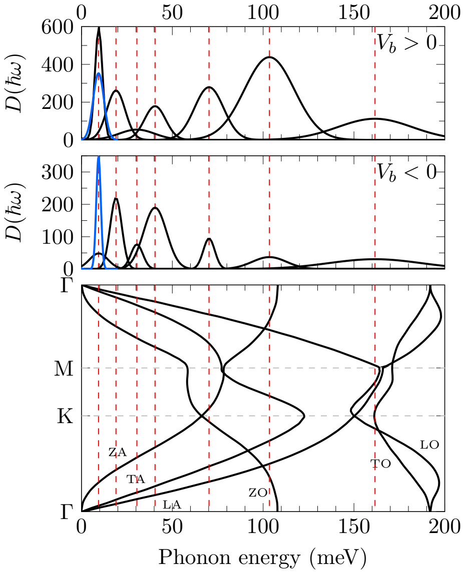

Figure 4.29: Phonon spectra determined from numerical deconvolution at positive (upper panel) and negative bias (mid panel) side of the measurements shown in fig. 4.26 (black) and 4.28 (blue). The calculated phonon dispersion from ref. [105] (black solid lines in lower panel) and the energy positions of the maxima from determined phonon features are depicted (red dashed lines).

the area where it was applied (cf. fig. 4.3(b)). As already discussed in sec. 4.2, these changes are caused either by lifting of the topmost layer or by displacement of the K intercalants. Another challenge of the small tip-sample distance is that the tip is so close to the sample that possible contaminations on the surface cannot be balanced by the feedback loop of the STM system. Accordingly, this might lead to a destruction or strong broadening of the fragile tip, which is only amendable by conditioning of the tip on a different metal sample. The condition of the tunneling tip is the major key to success of the experiments performed here. The tip needs to be sharp enough to obtain an appropriate resolution to distinguish between intercalated and pristine graphene (which itself is a big challenge). However, (atomically) sharp tips tend to be unstable, especially over the longer period of time that was necessary for the temperature dependent measurements. For these reasons, it took many experiments and repeated sample preparations, which in total lasted for about two years, to gain a set of data that is (i) complete and (ii) appropriate for a quantitative analysis.

In summary, the comparison of the FT-STM and ARUPS data reveals that both methods probe the same electronic structure, even if the sample had to be prepared newly by annealing and subsequent K deposition. Yet, this comparison is only possible due to QI effects emerging in the K-intercalated sample. The comparison of ARUPS and tunneling spectroscopy confirms that the latter probes solely electronic bands that are very close to the Γ point, which resolves the apparent contradiction on page 74. However, a temperature dependent energy gap was identified via STS that is analyzed and discussed in the following.

5 Superconductivity of K-Intercalated Epitaxial Graphene

This chapter focuses on the analysis and discussion of spectroscopic data with regard to potential superconductivity of the highly n-doped EMLG on SiC(0001) sample, which most likely behaves like quasi-freestanding EBLG upon K intercalation. In the first part, the energy gap around the Fermi level observed in the tunneling spectroscopy data is analyzed thoroughly. In the second part, ARUPS data is analyzed with regard to a proper estimation of EPC processes that affect and enable a superconducting ground state. Finally, the findings are discussed in the context of possible pairing mechanisms.

5.1 Examination of the Energy Gap

The tunneling spectra taken at a sample temperature of 1.2 K at positions 1 and 2 (fig. 4.27 and A.19, respectively) both show evidence for the existence of a small energy gap at the Fermi level, which was not observed in the spectra acquired on pristine EMLG and EBLG (cf. fig. 4.9). Further, all spectra acquired for the dI/dV map show a similar dip as depicted by the arbitrarily chosen examples in fig. 4.24(b). However, an analysis of the lateral distribution of the energy gap is not reliable, because the depth of the dip and thus the height of the gap edges depend on the spatially varying, non-flat DOS that consequently influences the absolute intensities of the spectra due to the stabilization problem (cf. sec. 3.2.1). For that reason, the energy gap appears differently pronounced in the example spectra in fig. 4.24(b).

Figure 5.1(b) shows the color-coded intensities of dI/dV spectra acquired along the white line in fig. 5.1(a). The energy gap is always discernible and does not significantly change in size and depth. In particular, it is even unaltered in the area, where only the corrugation of pristine graphene is visible. This observation does not contradict the assumption that the energy gap might be related to superconductivity, since Cooper pairs can also penetrate into potentially normal-conducting areas. This is possible on a length scale of several tens to hundreds of nanometers [91], which surely exceeds the extension of the supposedly pristine area here.

Since the energy gap at the Fermi level is no longer detectable at 4.0 K (cf. figs. 4.27 and A.19), its temperature dependence is analyzed as follows. As a first attempt the differential conductance

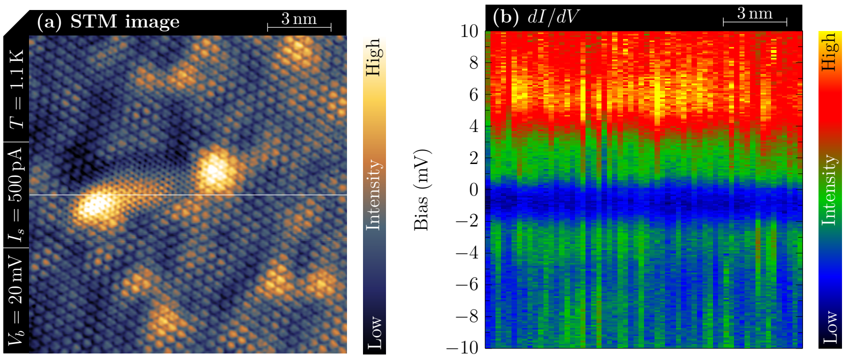

Figure 5.1: (a) STM image reprinted from fig. 4.11(b). (b) Color-coded dI/dV spectra determined along the white line in (a), shown here without further normalization.

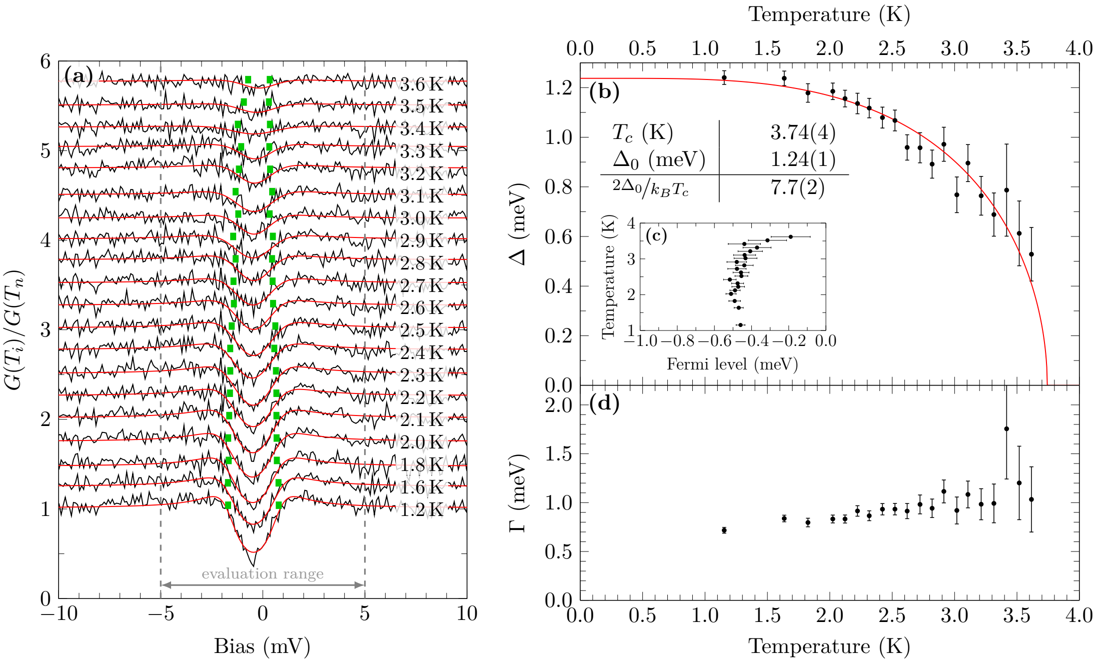

Figure 5.2: (a) Temperature-dependent dI/dV spectra (black, position 1, y-shifted 0.25) normalized by the spectrum at $T_n = 4.0\,\mathrm{K}$ and respective fitted spectra (red). The total gap size $2\Delta(T_i)$ is depicted by green markers. Corresponding parameters determined from the fitting procedure are shown in (b), (c), and (d). $\Delta(T_i)$ is further fitted using eq. (2.5) (red line) to determine T_c, Δ_0, and the gap ratio as indicated in (b). For comparison, a similar analysis of the data acquired at position 2 is provided in fig. A.26.

spectra $G(T_i)$ acquired at various temperatures T_i are normalized by the spectrum $G(T_n)$ at $T_n = 4.0\,\mathrm{K}$. The resulting spectra are shown in fig. 5.2(a). The evolution of the normalized differential conductance reveals that the energy gap at the Fermi level decreases in size with increasing temperature, which is even more easily discernible in the color-coded plot in fig. 5.3(b). This behavior is quantified by using the standard approach for describing normalized spectra provided in sec. 3.2.4. For the data evaluation here, possible broadening caused by the lock-in technique is additionally accounted for according to refs. [159, 160] as depicted in app. A.16.1. Apart from slight deviations at the gap edges, the normalized spectra are well described by the simple fit function (fig. 5.2(a)). The determined values of the energy gap exhibit the expected temperature-dependent development and are describable by the gap equation (2.5) within the error margin (fig. 5.2(b)). However, the gap ratio depicted in fig. 5.2(b), as a result of the

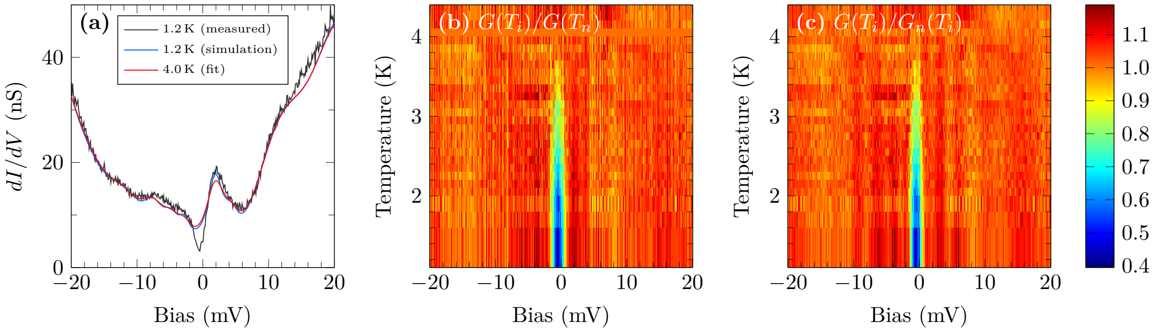

Figure 5.3: (a) Comparison of measured (black) and simulated (blue) spectrum at 1.2 K (position 1) based on the DOS contributions determined at 4.0 K (red) (cf. fig. 4.28). The normalized dI/dV spectra (b) and (c) depict the same data, but they are differently normalized using the standard and modified approach, respectively.

determined T_c and Δ_0, clearly exceeds the expected value of 3.52 for a BCS superconductor (cf. eq. (2.6)). Since the Fermi level is not directly located at $eV_b = 0$ in the employed experimental system (cf. figs. 3.8 and 3.6), E_F was included as an additional fitting parameter. Surprisingly, the fit results for E_F vary with the temperature as shown in fig. 5.2(c) which might have an impact on the determined gap values. Since this behavior seems to be systematic, it is most likely not a consequence of the lower SNR at elevated temperatures where the dip in the spectra becomes less pronounced. Judging from the high gap ratio and the deviations of the shape at the gap edges, the standard approach is probably inappropriate for the analysis of the given data.

In order to verify this behavior, a forward calculation is performed by generating a model data set based on the numerically fitted spectrum in fig. 4.28. From the parameters derived from the measured data at 4.0 K it is possible to calculate the expected spectra for varying temperatures. As shown in fig. 5.3(a), the simulated spectrum at 1.2 K (blue) is capable of describing the general shape of the measured spectrum (black), especially the height of the peak emerging slightly above the Fermi level. As expected, the dip located at the Fermi level is not well reproduced by simply accounting for the temperature changes. On that basis, a model data set (fig. 5.4(a)) is generated in the range from 1.0 to 4.2 K by assuming a temperature-dependent energy gap according to eq. (2.5) that is defined by $\Delta_0 = 1.00\,\text{meV}$ and $T_c = 3.70\,\text{K}$ ($E_F = -0.42\,\text{meV}$, $A = 1$, $\Gamma = \text{const.} = 0.6\,\text{meV}$) and by considering the DOS model that is valid for non-flat densities of states in the normal-conducting state via eq. (3.22). Normalization of the model data set $G(T_i)$ at different temperatures by the model spectrum $G_n(T_n)$ at $T_n = 4.0\,\text{K}$ (i.e., above the critical temperature) results in the spectra depicted in fig. 5.4(b). The normalized spectra exhibit an asymmetry between the coherence peaks above and below the Fermi level. Further, they appear broadened, shifted, and distorted compared to the assumed shape (cf. fig. 3.7). An analysis of this data set with the standard approach, as used before, is depicted in fig. A.21 and reveals (i) a systematic variation of the Fermi level similar to the behavior determined from the assessment of the actual data, (ii) a significant overestimation of the energy gap (and, to a lesser extent, of T_c), and (iii) increased Γ values close to T_c. The key problem

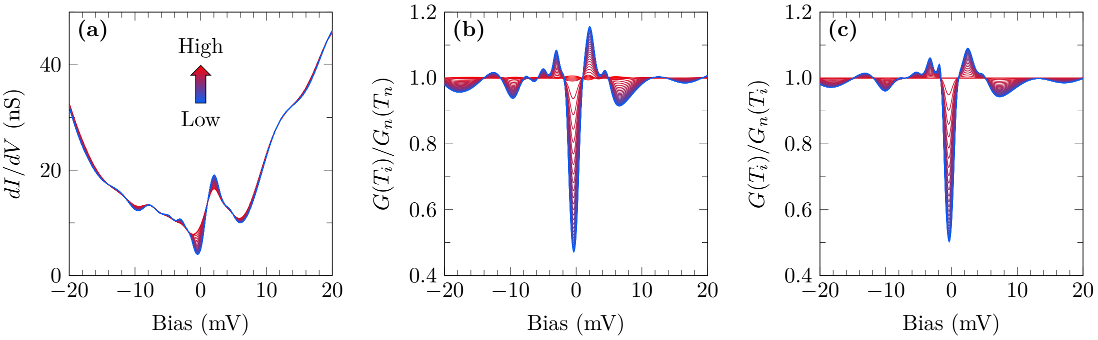

Figure 5.4: (a) Model data set in the temperature range from 1.0 (blue) to 4.2 K (red) in steps of 0.1 K as described in the text. Differently normalized model data (b) using the standard approach ($T_n = 4.0$ K) and (c) using the modified approach.

that emerges from the use of the standard approach is that it is only valid for energetically flat densities of states of the sample and the tip around the Fermi level above T_c (cf. sec. 3.2.4), which is clearly not satisfied here. In particular, the thermal broadening of spectral features that are apparent above T_c is neglected, which leads to distortions of the normalized spectra. Therefore, a modified approach is developed in this work that is also valid for non-flat densities of states. The approach is based on the knowledge of the electronic sample and tip DOS as well as inelastic contributions in the normal-conducting state as determined in fig. 4.28. This allows for a normalization of the measured data by the spectrum that would be expected without the presence of an energy gap at each temperature. A beneficial consequence compared to the standard approach, where the spectra are normalized by a measured, noisy curve, is that the SNR does not decrease, because the normalization is performed with a noise-free curve in the modified approach. Applying this approach to the model data set leads to the spectra shown in fig. 5.4(c) that, however, still deviate strongly from the symmetric line shape expected under consideration of a flat DOS in the normal-conducting state (cf. fig. 3.7). Since the influence of different thermal broadening between a particular spectrum and the normalization spectrum is removed by using this approach, those deviations are a result of the energy shift of $\rho_{s,nc}$ in the calculation of $\rho_{s,sc}$ compared to normal-conducting conditions in case an energy gap exists (cf. eq. (3.22)). The normalized actual data are depicted as color-coded map in fig. 5.3(c) and hardly deviate from the data normalized by the spectrum experimentally acquired at 4.0 K at first glance.

Further, for the fit quantity the entire model of the tunneling current is assumed without approximations using elastic and inelastic contributions to the DOS of tip and sample based on the parameters determined at 4.0 K. The electronic sample DOS under superconducting conditions is considered by the modified Dynes equation for non-flat densities of states (eq. (3.22)). In the fitting procedure, all DOS contributions determined in the normal-conducting state are fixed, but enter energetically shifted into the calculation of the superconducting DOS according to eq. (3.22). The thermal broadening is considered at the temperature T_i of the respective measurement. Like before, the application of the lock-in technique accompanied by

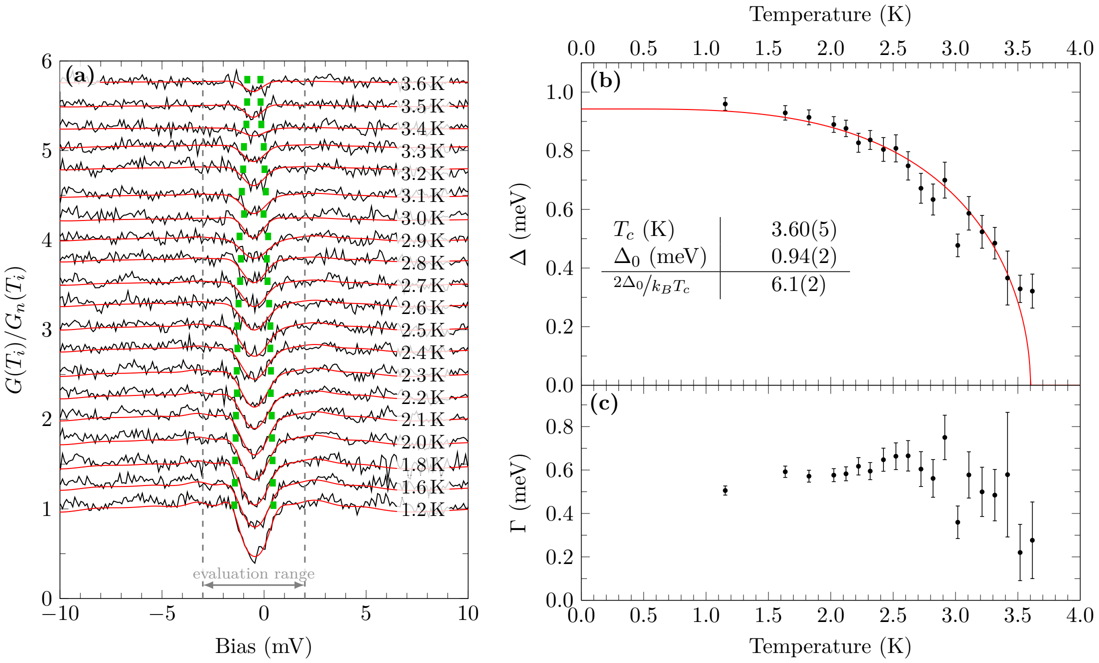

Figure 5.5: (a) Temperature-dependent dI/dV spectra (black, position 1, y-shifted 0.25) normalized using the modified approach (G_n determined at 4.0 K) and corresponding fitted spectrum (red) (both branches, Fermi level fixed to $E_F = -0.52$ meV as shown in fig. A.22). The total gap size $2\Delta(T_i)$ is depicted by green markers. Corresponding parameters determined from the fitting procedure are shown in (b) and (c). $\Delta(T_i)$ is further fitted using eq. (2.5) (red line) to determine T_c, Δ_0, and the gap ratio as indicated in (b). For comparison, a similar analysis of the data acquired at position 2 is provided in fig. A.29.

possible broadening effects is accounted for. The fit quantity also needs to be normalized in the same way as the measured data, considering the thermal broadening at the temperature T_i.[a] The complete fitting model is provided in app. A.16.1. An analysis of the model data set with this approach readily reproduces the prescribed parameters. Although the number of fit parameters is equal to the standard approach, the computational costs are about 20 times higher.

The fitting procedure of the measured data with this modified approach reveals that the determined values of the Fermi level still exhibit variations as shown in fig. A.22. However, those deviations are non-systematic and most likely caused by noise in the measured data, since they are most pronounced at elevated temperatures where the SNR of the normalized data is lower. In the light of these findings (and in order to avoid an unnecessary degree of freedom) it seems reasonable that the Fermi level parameter is fixed to the mean value determined at the spectra recorded at the five lowest temperatures as depicted by the blue solid line in fig. A.22(c). The results of the fitting procedure with with a constant Fermi level parameter are shown in fig. 5.5(a). In the evaluated spectral region the agreement of fitted and measured data is improved compared to the standard approach. As before, the determined gap values exhibit the expected behavior upon temperature variation (fig. 5.5(b)) that is quantified by fitting of the gap equation (2.5).

---

[a] The fitting procedure without using normalization does not result in reliable values due to numerical issues.

The simulation of the non-gapped dI/dV spectrum at 1.2 K based on the spectrum determined at 4.0 K slightly deviates from the measured spectrum outside of the gap region (cf. fig. 5.3(a)), which primarily originates from the energy shift of the normal-state DOS due to the presence of an energy gap (cf. eq. (3.22)). With the used system, however, the lateral tip position with respect to the sample surface can only be fixed visually due to drift effects of the piezo actuators upon temperature variation. Already tiny variations of the lateral tip position above the sample cause changes of the local DOS due to the presence of scattering features as already shown in fig. 4.24. This effect might also have an influence on the deviations outside of the gap region. Since this impact can in principle be different for the occupied and unoccupied branches, the fitting procedure is repeated for the left and right branches of the gap region separately (with fixed E_F) as shown in figs. A.23 and A.24, respectively. All determined values of T_c and Δ_0 as well as the gap ratio are presented in tab. 5.1 and agree well within the error margins. Besides the influence of noise in the measured spectra, the slightly deviating values are most likely caused by tiny variations of the lateral tip position for measurements at different temperatures. This effect is even more pronounced for the evaluation of the data set measured at the second position (cf. sec. A.16.4), where the determined T_c value of the distorted left branch is significantly increased.

Table 5.1: Parameters determined from the fitting procedure based on the modified approach for different fit regions. The respective data are provided in the denoted figures.

	Branch Region	Both -3.0 to $+2.0$ meV	Both[1] -3.0 to $+2.0$ meV	Left[1] -3.0 to $+0.1$ meV	Right[1] -1.0 to $+2.0$ meV
Position 1	T_c(K)	3.59(5)	3.60(5)	3.67(5)	3.69(5)
	Δ_0(meV)	0.95(2)	0.94(2)	0.97(3)	0.92(2)
	$2\Delta_0/k_BT_c$	6.1(2)	6.1(2)	6.2(2)	5.8(2)
	Figure	A.22	5.5	A.23	A.24
Position 2	T_c(K)	3.75(8)	3.76(7)	4.0(2)	3.71(4)
	Δ_0(meV)	0.90(3)	0.90(2)	0.93(2)	0.89(2)
	$2\Delta_0/k_BT_c$	5.6(3)	5.6(3)	5.3(3)	5.6(2)
	Figure	A.28	A.29	A.30	A.31

[1] E_F fixed at -0.52 meV for position 1 (cf. fig. A.22) and at -0.44 meV for position 2 (cf. fig. A.28)

Independent of the fitting range, the determined Δ_0 and T_c values are lowered compared to the results using the standard approach, as expected from the analysis of the model data. Even though also the gap ratio decreased upon applying the modified approach, it is still significantly higher than the value of 3.52 expected from conventional BCS theory. A possible reason for this observation is that the energy gap might not be entirely closed at 4.0 K, even if no longer resolved in the tunneling spectroscopy data. Complete closure of the energy gap at this temperature could be doubted especially in the data acquired at position 2 (cf. fig. A.19).

To exclude this possible systematic error, the impact of false normalization is examined using model data with the parameters given above. At first, a simple flat DOS is assumed for tip and sample. Afterwards, the model spectra are normalized by spectra at different temperatures T_n above and intentionally also below T_c. Obviously, upon normalization with non-gapped spectra above T_c and applying the fitting procedure for the standard approach, the correct critical temperatures are determined. However, if T_n is below T_c, the determined T_c values follow a

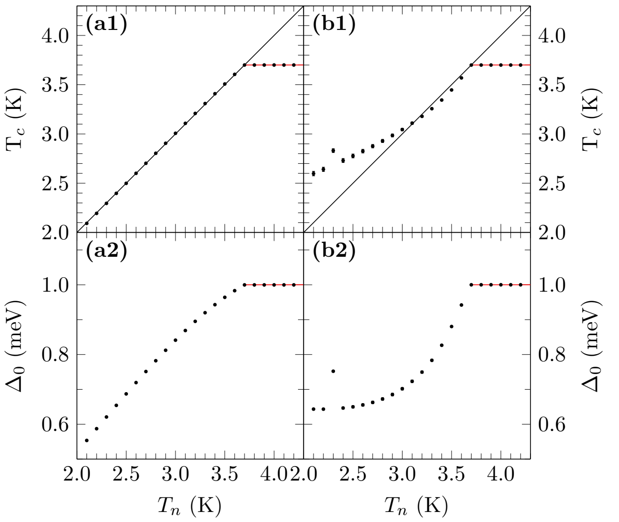

Figure 5.6: Dependency of the determinable T_c and Δ_0 on T_n (temperature of the normalization spectrum) using model data sets assuming (a1,a2) a flat sample DOS and the standard approach as well as (b1,b2) a non-flat sample DOS and the modified approach for the data analysis. Further information is provided in the text.

straight line $T_c = T_n$ (fig. 5.6(a1)). Δ_0 behaves similarly (fig. 5.6(a2)). Secondly, the non-flat DOS acquired at 4.0 K is taken into account for the data modeling. In this case, the normalization spectrum $G_n(T_n)$ has to be determined prior to applying the modified approach. The results in fig. 5.6(b1) depict the same behavior above T_c as for the flat DOS. By choosing T_n values below the critical temperature, however, the determined T_c values deviate strongly from the straight line (especially at low temperatures). This behavior is caused by the fact that the fitting model for the potentially non-gapped spectra is no longer sufficient to describe the gapped spectra. Also Δ_0 is only determined appropriately above T_c (fig. 5.6(b2)).

This approach of intentionally wrong normalization is applied to the actual data by (i) fitting of the potentially non-gapped spectra at different temperatures T_n with the model used in fig. 4.28 and (ii) applying the modified approach for the determination of the temperature dependence of the energy gap. The results of this procedure are depicted in fig. 5.7 for the entire fit region (a) as well as the left (b, occupied) and right (c, unoccupied) branches separately. All data show the expected saturation of the determined T_c values for $T_n \gtrsim 3.7\,\mathrm{K}$, which is most obvious in the data that considers both branches. The remaining deviations are a result of tiny lateral variations as well as noise issues in the normalization spectra, which also cause deviations of the determined Δ_0 values and, in particular, can explain the difference between the different evaluation regions. Nevertheless, these findings demonstrate that the energy gap is closed for $T \gtrsim 3.7\,\mathrm{K}$. Thus, under the assumption of the entire fit region, $T_c = 3.65(2)\,\mathrm{K}$ and $\Delta_0 = 0.97(1)\,\mathrm{meV}$ are estimated by considering the mean value (weighted by error margins) of the results for $T_n \gtrsim 3.7\,\mathrm{K}$. Consequently, a gap ratio of 6.19(7) can be determined that is indeed lowered compared to the analysis using the standard approach, but still exceptionally high in contrast to the BCS value of 3.52 (cf. eq. (2.6)). The occupied branch of the spectra acquired at position 2 deviates strongly, which makes a quantitative analysis almost impossible (cf. sec. A.16.4). However, consideration of the unoccupied branch solely, results in a critical temperature of $T_c = 3.72(3)\,\mathrm{K}$ which is close to the value determined at position 1. The determined value for Δ_0 is considered unreliable though, because the determined Fermi level values are shifted upon distortions in the spectra.

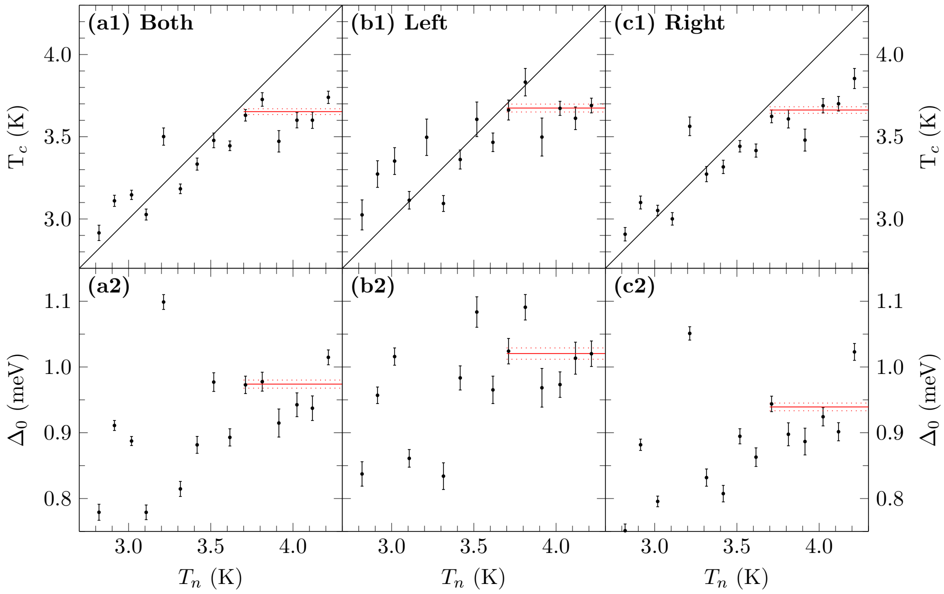

Figure 5.7: T_c and Δ_0 determined for normalization by spectra at different T_n according to the modified approach assuming (a1,a2) the complete gap, (b1,b2) only the left and (c1,c2) only the right branch of the tunneling data (position 1). Red solid lines depict the weighted average values for $T_n \geq 3.7\,\mathrm{K}$ and dotted lines the respective error margins. Further information is provided in the text.

The full analysis, including the modified approach for a non-flat DOS in the normal-conducting state, proves the existence of an energy gap that follows the expected temperature dependence of the gap equation for conventional superconductors (cf. eq. (2.5)). Further, the energy gap is sufficiently described by the modified Dynes equation (3.22) that includes lifetime broadening effects and accounts for non-flat densities of states in the normal-conducting state. Thus, there is no evidence in the spectral shape of the energy gap that would suggest a different mechanism besides conventional s-wave pairing of the Cooper pairs. This finding is in agreement with the spectroscopic data of the Ca-intercalated bulk graphite (CaC_6) [18, 19], which are the only available data for a comparable system.

However, the ratio between $\Gamma \approx 0.6\,\mathrm{meV}$ and $\Delta_0 \approx 0.9\,\mathrm{meV}$, determined from the low-temperature spectra here (cf. fig. 5.5(c)), exceeds the ratio of values reported for CaC_6 severely ($\Gamma = 0.2\,\mathrm{meV}$ and $\Delta_0 = 1.6\,\mathrm{meV}$ [18], $\Gamma = 0.2\,\mathrm{meV}$ and $\Delta_0 = 2.3\,\mathrm{meV}$ [19]). Compared to conventional superconductors all ratios (in this work and in literature reports alike) are drastically enlarged (e.g., Nb: $\Gamma = 0.01\,\mathrm{meV}$ and $\Delta_0 = 0.96\,\mathrm{meV}$ [160,161]). This would suggest an extremely short lifetime of the Cooper pairs in the sample studied in this work. Still, the parameter Γ is influenced by all types of broadening effects besides pure lifetime influence, in particular, also possible experimental issues caused by a limited resolution of the system. Considering the data provided in sec. 3.2.5 (STS of Au(111) with Nb tip), however, experimental issues leading to such high Γ values can be excluded for the setup used here, especially since effects related to the lock-in technique are accounted for in the numerical fitting procedure. Moreover, the determined Γ values exhibit a clear temperature dependency (fig. 5.5(c)). While for temperatures sufficiently far away from the critical temperature the Γ values slightly rise upon temperature increase, a continuous drop is observed when the temperature further approaches T_c. This behavior is completely unexpected, since Γ is assumed to increase exponentially with rising temperature (cf. eq. (3.20)), especially for $T \rightarrow T_c$ (cf. ref. [206] for Pb nanoparticles). In the limiting case of negligible impact of the temperature on the quasiparticle lifetime, a thermally independent Γ value would be expected. Especially at elevated temperatures, where the SNR of the normalized data is low, the determined Γ values might be artificially decreased due to an over-interpretation of noise by the fitting routine. Following ref. [18], this effect should be avoided by assuming a temperature-independent Γ. As shown in fig. A.25, however, the assumption of a constant Γ (weighted mean) does not result in a temperature dependence of the corresponding gap values that follows the gap equation. Thus, under the assumption of a superconducting state of the examined sample, lowered Γ values due to noise artifacts in the data can be excluded.

In general, unusually high Γ values are assigned to averaging over various Δ values [160] in the tunneling data, that might be caused by anisotropy [207] or multiple gaps [208]. The occurrence of an anisotropic energy gap is plausible in the present case, because a strong angular dependence of the EPC on the Dirac cone has already been observed via ARPES for K-intercalated graphite [12], monolayer graphene on Au [16, 59] and also EMLG on SiC(0001) (Dirac point at lower binding energies) [86, 209]. Comparable anisotropic EPC has also been reported for CaC_6 [14]. Indeed, the related tunneling data already discussed above exhibits a relatively high Γ value compared to conventional superconductors [18, 19]. In relation to the corresponding energy gap, this value is, however, significantly smaller than the values determined here, especially at low temperatures, but also close to T_c (ratio approximately doubled). Although anisotropy might have an impact on the elevated Γ, the comparison shows that this effect is not capable of explaining the observations entirely. Especially, the temperature dependence is not present in the tunneling data of CaC_6 [18]. Nonetheless, a comparison of the ARPES data of CaC_6 and the K-intercalated EMLG sample investigated here reveals one significant difference. In the present case two occupied parabolic IL bands are observed while only one is apparent in CaC_6 [17]. Thus, an additional possibility for the formation of Cooper pairs is available that might result in an additional energy gap originating from superconducting states characterized by different parameters. The possibility of two-band superconductivity is also theoretically predicted for highly n-doped graphene [210]. On the one hand, differently sized gaps cannot be resolved and identified in the tunneling data. On the other hand, the superposition of differently sized energy gaps might result in the observation of an effectively broadened gap, due to the limited experimental resolution caused by the thermal broadening stemming from the metallic tip. In particular, if energy gaps with smaller Δ_0 close at lower temperatures compared to the determined T_c, a decrease of the broadening parameter is expectable, since in-gap features disappear. Consequently, only the largest energy gap with the corresponding T_c is estimated appropriately. In conclusion, the existence of multiple gaps closing at different critical temperatures is a plausible explanation of the extraordinarily high Γ value and its temperature dependence observed here.

Despite all of the above, this interpretation does not adequately explain why the determined gap ratio drastically exceeds the expected value of 3.52 for conventional superconductors and even the already larger value reported for CaC_6 (gap ratio 4.6 [19]). High gap ratios are commonly observed for strongly coupled superconductors (cf. sec. 2.4.2), which was also suggested in ref. [19] to be responsible for the elevated gap ratio of Ca-intercalated graphite. Thus, the EPC strength will be determined in the following by a thorough analysis of related ARUPS data.

5.2 Electron-Phonon Coupling Strength

For the determination of the EPC strength, ARPES data were acquired for the same sample already examined via tunneling spectroscopy in the previous section. Due to structural instabilities at RT (cf. sec. 4.2, note that warming up the sample to 300 K is inevitable during sample transfer via UHV shuttle), the specimen was freshly cleaned by annealing prior to re-applied K intercalation. As mentioned in sec. 3.1.3 the lowest sample temperature accessible in the PES setup is about 35 K, which is significantly above the critical temperature determined in the previous section. Thus, a direct analysis of the superconducting gap around the Fermi level is not possible. The data to be analyzed in this section (fig. 5.8(a)) is acquired with the 2D detector subsequent to the measurement depicted in fig. 4.15(a), but with higher resolution and slightly modified azimuth angle. The dotted blue line in fig. 5.8(b) illustrates the section at the Fermi level where the data are collected. It corresponds to a slightly bent section nearly perpendicular to the ΓK direction. The ARUPS data exhibit a kink at about 160 meV in the π^* band accompanied by an increased intensity for low binding energies. Previous studies on alkali-metal-intercalated graphene-based systems attribute this observation to renormalization of the π^* band upon electron-phonon coupling [59, 99]. The magnitude of this renormalization depends on the adatom species [59] and the number of graphene layers, as the comparison of the particular case of K-intercalated graphite [12] and MLG on Au/Ni [16] reveals. However, there is no data available in the literature regarding a similar number of graphene layers and electronic structure compared to the sample investigated here. As already mentioned in sec. 4.2, the visually adjusted band using a 3NN TB model (cf. app. A.6) does not describe the ARUPS data accurately (red line), because this simple approach does not account for many-body effects that can also originate from other interactions besides EPC (cf. sec. 3.1.2).

The ARUPS data are analyzed with a home-built software tool developed by the author, which follows the standard procedure, e.g., used in ref. [99], via (i) fitting of MDCs by spectral functions, (ii) extraction of the complex self-energy by bare band estimation, and (iii) self-energy deconvolution by assessment of $\alpha^2F(\omega)$, from which the EPC constant λ is extractable. In the following, ε denotes the binding energy and thus $E = -\varepsilon$ compared to the tunneling experiments.[b]

---

[b] In the related literature, commonly $\hbar = 1$ is assumed. Accordingly, $\varepsilon = \omega$.

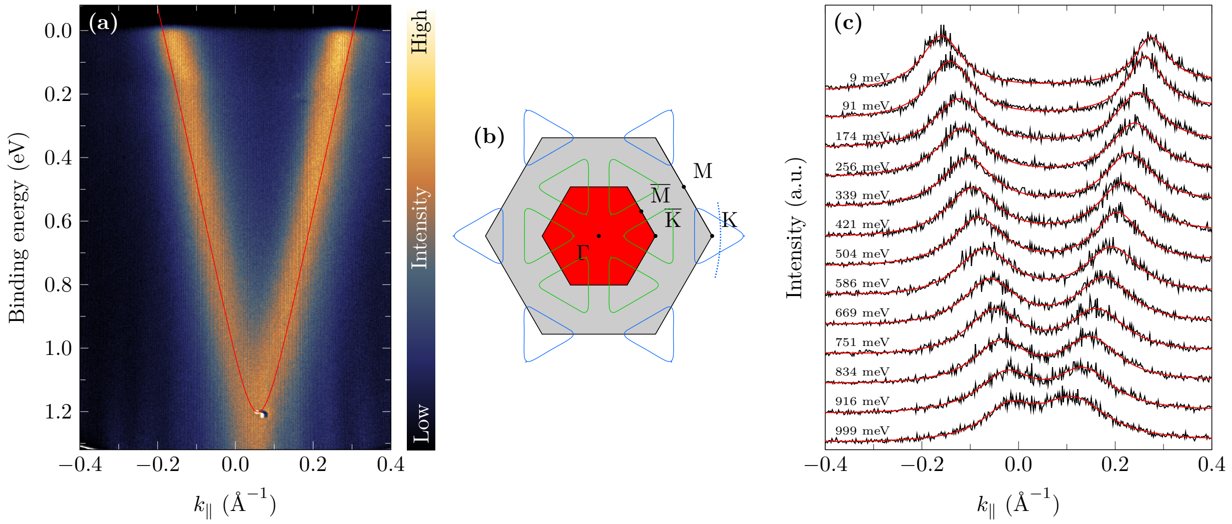

Figure 5.8: ARPES of K-intercalated epitaxial graphene determined with the 2D detector (same preparation as in fig. 4.15) with improved resolution and slightly modified azimuth angle (resolution: 8.36 meV, 0.1° corresponding to $\approx 0.0034\,\text{Å}^{-1}$). Estimated bare band (red) using the same parameters as in fig. 4.15. (b) SBZ of graphene (gray) and the (2×2) superstructure (red) as well as the expected Fermi surfaces modeled with a 3NN TB approach at both K points. The blue dashed line represents the 2D detector cut in k space (at E_F) where the ARPES data in (a) are determined. (c) MDCs (black) of the data in (a) at several binding energies (constant y-shift) and fitted curves (red) with the model provided in the text.

The intensity of the ARUPS data is given by $I(k,\varepsilon) = A(k,\varepsilon)f(\varepsilon)$, where $f(\varepsilon)$ is the Fermi distribution [211]. The spectral function $A(k,\varepsilon)$ (cf. sec. 3.1.2) at a constant energy $\tilde{\varepsilon}$ can be approximated via [212]

$$A_{\tilde{\varepsilon}}(k) \approx \frac{A_0}{\pi}\frac{\Delta k_m}{(k-k_m)^2+(\Delta k_m)^2}, \text{ with } \Delta k_m = \text{HWHM, and } A_0 = \int A_{\tilde{\varepsilon}}(k)dk. \tag{5.1}$$

In the particular case here, two spectral functions are included to account for both branches, and a second-order polynomial background is assumed. As shown in fig. 5.8(c), the intensities of the MDCs are sufficiently described by the fitted spectral functions. Thus, there is no need for considering additional electronic bands that potentially originate from the decoupled former buffer layer or residual amounts of second-layer areas as discussed in secs. 4.1 and 4.2. A visual proof of the fit quality is provided in fig. A.34. The determined energy-dependent maximum positions k_m of the left branch, which is scrutinized in the following, are depicted in fig. 5.9(a).[c] The related half width at half maximum (HWHM) in fig. 5.9(b) is dominated by a step-like feature at the binding energy where the kink is apparent. Provided that the bare band $\varepsilon^b(k)$ (cf. sec. 3.1.2) is known, the complex self-energy can be estimated from both extracted energy-dependent quantities by [212]

$$\Sigma'_{\tilde{\varepsilon}} = \tilde{\varepsilon} - \varepsilon^b_{k_m} \qquad \text{and} \qquad \Sigma''_{\tilde{\varepsilon}} = (-)\hbar\Delta k_m v^b_{k_m}, \tag{5.2}$$

---

[c] A state of the art minimum gradient method [213] was also applied for the determination of k_m and produced the same results (not shown). However, width estimation is not possible with this method.

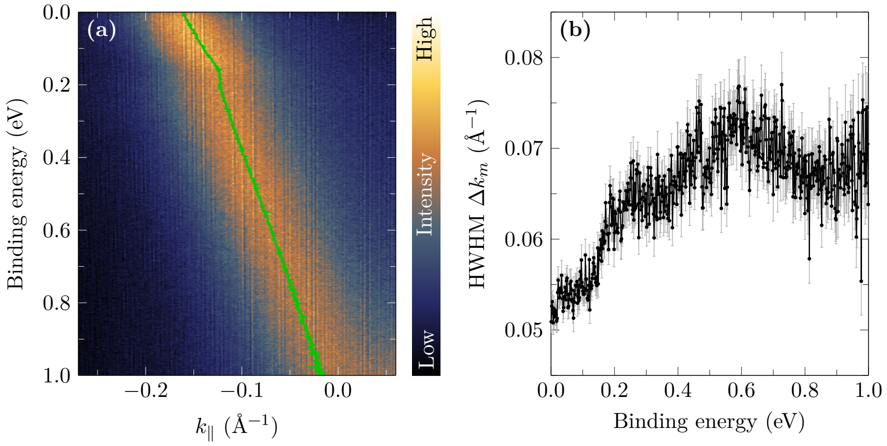

Figure 5.9: Results of the MDC fitting procedure of the left branch of the ARPES data shown in fig. 5.8. The green line in (a) indicates the determined maximum positions k_m and (b) the corresponding half width at half maximum values (Δk_m).

where $\varepsilon^b_{k_m} = \varepsilon^b(k_m)$, and similarly $v^b_{k_m}$ is proportional to the derivative of the bare band dispersion at k_m. In other words, the real part of the self-energy is equal to the energy difference between the measured band and the bare band at the determined k_m [214], while the imaginary part depends on the width of the measured band at $\tilde{\varepsilon}$ and the slope of the bare band at related k_m values. Nonetheless, the original bare band is generally unknown. Since the band estimated via the 3NN TB model is only visually adjusted as mentioned above, it does not provide an appropriate description of the actual bare band. Unfortunately, calculated bare bands based on *ab initio* DFT are not available for this system yet. Nevertheless, an estimation of the bare band is feasible by the requirement for self-consistency of the complex quasiparticle self-energy $\Sigma(\vec{k},\varepsilon) = \Sigma'(\vec{k},\varepsilon) + i\Sigma''(\vec{k},\varepsilon)$ using a Hilbert transformation (HT)[d] [215]:

$$\Sigma^{\prime,\prime\prime}_{\mathrm{HT}}(\vec{k},\varepsilon) = HT(\Sigma^{\prime\prime,\prime}_{\mathrm{MDC}}(\vec{k},\varepsilon)) = \pm\frac{1}{\pi}\ \mathrm{PV}\int_{-\infty}^{\infty} d\xi\, \frac{\Sigma^{\prime\prime,\prime}_{\mathrm{MDC}}(\vec{k},\xi)}{\xi-\varepsilon}, \tag{5.3}$$

where PV indicates a principal value integral.[e] Accordingly, the bare band can be estimated by numerical minimization of $\Sigma'' - HT(\Sigma')$ upon variation of the parameters describing a model bare band. Thereby, a self-consistent description of the complex self-energy and the bare band are determined simultaneously. According to ref. [99], the bare band model can be constrained to a second-order polynomial. Close inspection of the adjusted bare band via the 3NN TB model (cf. fig. 5.8) suggests that the band is curved outwards in the low-binding-energy region, which is accounted for in the model. Further, the bare band estimation procedure is usually constrained by a coincidence with the measured band at the Fermi level, e.g., ref. [99]. However, a thorough examination of the k_m values close to the Fermi level, depicted as inset in fig. 5.10(a), reveals a trend toward higher $k_\parallel$ values (to the right) that is not expected and probably caused by noise in the data. Thus, in order to avoid suppression of possible low-energy features, this constraint is not applied here. Further, the determined HWHM values (Δk_m) exhibit a broad

---

[d] In the literature sometimes also referred to as Kramers-Kronig transformation, e.g., ref. [215].

[e] The principal value integral is numerically calculated by using an approach for a discrete Hilbert transformation provided in ref. [216]. Due to the request of point symmetry, an expansion to negative values is mandatory. An extrapolation on the high-energy side is not necessary, because Σ' is close enough to zero at the upper bound of the fitting region. Various tests showed that the results do not differ significantly.

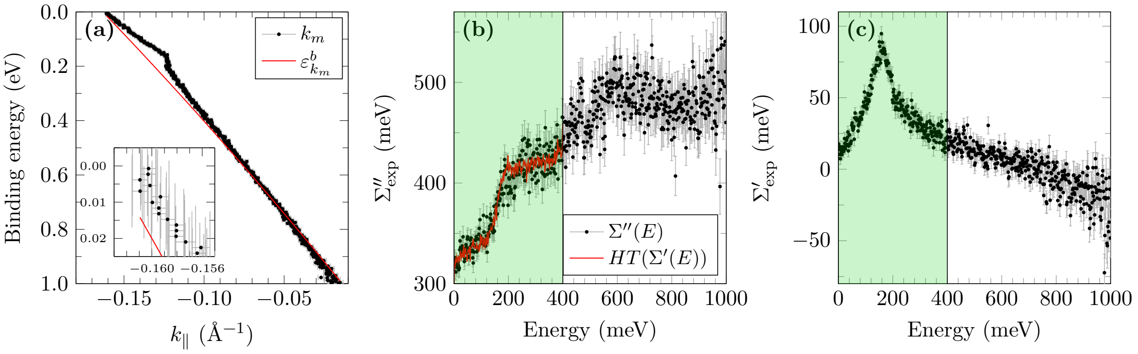

Figure 5.10: (a) Determined k_m values (black dots with gray error bars) for different binding energies and zoom window of the Fermi level region as inset. (b) Coincidence of the imaginary part (black) and the respective Hilbert-transformed real part (red) that is shown in (c) as a result of estimating the bare band in (a) self-consistently in the energy region highlighted in green.

maximum centered at a binding energy of about 0.6 eV (cf. fig. 5.9) that is most likely caused by the additional K 4s core level as discussed in sec. 4.2. Applying the self-consistent bare band estimation procedure to the data in different evaluation regions reveals that this maximum has no counterpart that reflects in the real part of the self-energy as shown in fig. A.35. Accordingly, the K 4s core level does not cause an energy renormalization of the band dispersion that would be expected upon hybridization with the Dirac bands as observed for Yb-intercalated ZLG [84]. Thus, the ARUPS data probes a simple superposition of the K 4s core level of a K atom species that does not interact with the π^* bands of graphene. In accordance to sec. 4.2, this species is most likely located below the former buffer layer and not completely depleted by charge donation to π^* bands contrary to K-intercalated MLG on Au/Ni [16]. Due to this superposition, a reasonable evaluation of the self-consistent bare band estimation procedure is only possible in a limited energy range, where the influence of the K 4s core level on the imaginary part of the self-energy is negligible. A sufficient self-consistency at low binding energies ($<$ 160 meV) could only be achieved in an evaluation range of binding energies $<$ 400 meV as depicted in fig. 5.10(b). Due to the limited range and the deviation of k_m close to the Fermi level, the estimated bare band obviously differs from the actual bare band, since it intersects with the k_m values (fig. 5.10(a)), and an unphysical offset of Σ' at the Fermi level is observed in fig. 5.10(c). Nevertheless, the self-consistency of the experimentally determined self-energy Σ_{exp} is ensured, even if a potentially wrong bare band is estimated. For the qualitative analysis of the self-energy, the deviation between the experimentally determined and the actual bare band is accounted for via $\Sigma(\vec{k},\varepsilon) = \Sigma_{\mathrm{exp}}(\vec{k},\varepsilon) + \Sigma_{\mathrm{corr}}(\vec{k},\varepsilon)$. This correction of the self-energy shall be defined by the assumption of a modified, but still parabolic dispersion of the actual bare band via

$$\begin{aligned} \Sigma'_{\tilde\varepsilon} &= \tilde\varepsilon - \varepsilon^b_{k_m} = \underbrace{\tilde\varepsilon - \varepsilon^b_{k_m,\mathrm{exp}}}_{\Sigma'_{\tilde\varepsilon,\mathrm{exp}}} + \underbrace{\varepsilon^b_{k_m,\mathrm{exp}} - \varepsilon^b_{k_m}}_{\Sigma'_{\tilde\varepsilon,\mathrm{corr}}} \equiv \Sigma'_{\tilde\varepsilon,\mathrm{exp}} + \Sigma'_{\tilde\varepsilon,\mathrm{corr}}, \\ \Sigma''_{\tilde\varepsilon} &= (-)\hbar\Delta k_m v^b_{k_m} = (-)[\underbrace{\hbar\Delta k_m v^b_{k_m,\mathrm{exp}}}_{\Sigma''_{\tilde\varepsilon,\mathrm{exp}}} \underbrace{-\hbar\Delta k_m v^b_{k_m,\mathrm{exp}} + \hbar\Delta k_m v^b_{k_m}}_{\Sigma''_{\tilde\varepsilon,\mathrm{corr}}}] \equiv \Sigma''_{\tilde\varepsilon,\mathrm{exp}} + \Sigma''_{\tilde\varepsilon,\mathrm{corr}}. \end{aligned} \tag{5.4}$$

Herein, $\Sigma'_{\tilde{\varepsilon},\mathrm{corr}}$ is a highly non-trivial function, because it follows the $(k_m, \tilde{\varepsilon})$ relation determined from the actual data. Since different processes contribute to the total self-energy (cf. sec. 3.1.2), the determined $\Sigma_{\mathrm{exp}}(\vec{k}, \varepsilon)$ can be described by

$$\Sigma_{\mathrm{exp}}(\vec{k}, \varepsilon) = \Sigma_{\text{e-ph}}(\vec{k}, \varepsilon) + \Sigma_{\text{e-e}}(\vec{k}, \varepsilon) + \Sigma_{\text{e-def}}(\vec{k}, \varepsilon) - \Sigma_{\mathrm{corr}}(\vec{k}, \varepsilon) \equiv \Sigma_{\text{e-ph}}(\vec{k}, \varepsilon) + \Sigma_{\mathrm{rest}}(\vec{k}, \varepsilon). \tag{5.5}$$

Provided that a self-consistent description of $\Sigma_{\text{e-ph}}(\vec{k}, \varepsilon)$ is possible, the self-consistency of $\Sigma_{\mathrm{rest}}(\vec{k}, \varepsilon)$ that sums up all other contributions is implied, since this property is ensured for $\Sigma_{\mathrm{exp}}(\vec{k}, \varepsilon)$ by the bare band estimation procedure. The analysis here aims at the extraction of EPC contributions. Thus, the actual amount of other processes contributing to the total self-energy are not relevant here, but still have to be considered.

The self-energy contribution originating from electron-phonon interactions is directly connected to the Eliashberg function.[f] The real part [217]

$$\Sigma'_{\text{e-ph}}(\varepsilon, T) = \hbar \int_{-\infty}^{\infty} d\nu \int_0^{\omega_{max}} d\omega' \alpha^2 F(\omega') \frac{2\omega'}{\nu^2 - \omega'^2} f(\hbar\nu + \varepsilon) \tag{5.6}$$

and the imaginary part [61]

$$\Sigma''_{\text{e-ph}}(\varepsilon, T) = \pi\hbar \int_0^{\omega_{max}} d\omega' \alpha^2 F(\omega') [1 - f(\varepsilon - \hbar\omega') + f(\varepsilon + \hbar\omega') + 2b(\hbar\omega')], \tag{5.7}$$

where $b(\varepsilon)$ and $f(\varepsilon)$ are the Bose and Fermi functions, respectively, constitute a self-consistent description. The electron-electron interaction is assumed according to the Fermi liquid theory via $\Sigma_{\text{e-e}}(\varepsilon) = \alpha\varepsilon + i\beta\varepsilon^2$ [219, 220]. Defect scattering solely contributes to the imaginary part by a constant value [16] that also accounts for possible experimental broadening.

The integral inversion problem for the extraction of $\alpha^2 F(\omega)$ from the experimentally determined self-energy is mostly solved by applying the maximum entropy method [218] for the real part. However, this procedure is highly sensitive to noise [99]. To avoid this problem, the Eliashberg function can also be modeled by a sum of Gaussian profiles [99]. Under additional consideration of all other contributions to Σ_{exp} as described above, the least squares of the deviation between Σ_{exp} and the modeled self-energy are minimized by taking both, real and imaginary part of Σ_{exp} into account.[g]

Figure 5.11(a) depicts the determined $\alpha^2 F(\omega)$ (red line) that is capable of describing the real (b) and imaginary part (c) of Σ_{exp} along with Σ_{rest} (light red line). The contributions to Σ_{rest}

---

[f] EPC is based on the Eliashberg function that usually exhibits a dependency on the initial state of the interacting electron [217]. However, if there is no sharp electronic structure near the Fermi level within the energy range of the phonon bandwidth, the dependency on the initial state energy ε_i can be ignored and replaced by the Fermi level [218]. For sufficiently small ranges near the Fermi level it can be approximated via $\alpha^2 F(\omega) \equiv \alpha^2 F(\omega; \varepsilon, \vec{k})$ [218] for a certain direction in k space.

[g] $\chi^2 = \sum_{i=1}^{N_D} \frac{[D'_i - \Sigma'_{\mathrm{exp}}(\varepsilon_i)]^2}{\sigma_i^2} + \sum_{i=1}^{N_D} \frac{[D''_i - \Sigma''_{\mathrm{exp}}(\varepsilon_i)]^2}{\sigma_i^2}$, where $D_i = D'_i + iD''_i$ are the data of the complex self-energy at E_i, N_D total number of data points, and σ_i the error bars of the data.

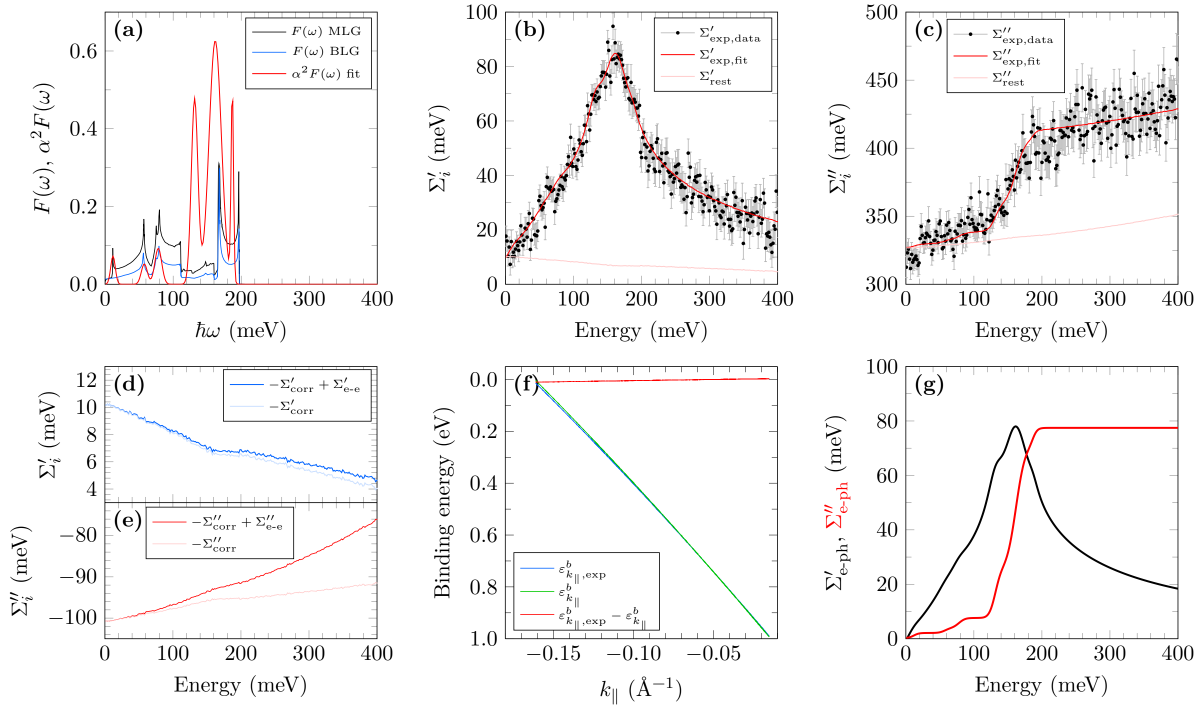

Figure 5.11: (a) Comparison of the determined Eliashberg function $\alpha^2F(\omega)$ and calculated PhDOS $F(\omega)$ (arbitrarily scaled) of MLG and AB-stacked BLG from refs. [106, 107]. (b) and (c) depict the data (black) and fit function (red) of the real and imaginary part of the self-energy, respectively, along with other contributions (light red) upon various included mechanisms presented in (d) and (e). (f) Experimental (blue) and modified (green) bare band and their difference (red). (g) Real (black) and imaginary (red) part of the self-energy originating from electron-phonon coupling exclusively. Further information is provided in the text.

are provided in (d) and (e) for the real and imaginary part, respectively. As depicted in (f), the required modified bare band $\varepsilon^b_{k_\parallel}$ deviates just slightly from the estimated band at low binding energies. $\varepsilon^b_{k_\parallel}$ can still vary from the actual bare band since the electron-electron contributions are not fully included in the limited evaluation range.

The comparison of the determined $\alpha^2F(\omega)$ with the PhDOS $F(\omega)$ (fig. 5.11(a)) suggests that the high-energy peaks centered at about 160 meV and 185 meV relate to in-plane optical phonon modes of graphene (cf. fig. 2.6). However, the highest-energy feature of $\alpha^2F(\omega)$ appears at slightly lower energies compared to the PhDOS, which is probably a result of the modified environment upon K intercalation. The lower-energy features at about 60 meV and 80 meV can be assigned to interactions with out-of-plane optical and acoustic modes. However, the peak centered at about 130 meV does not possess a direct counterpart in $F(\omega)$. Remarkably, a similar feature has also been observed for K-intercalated MLG on Au/Ni [16]. Further, a theoretical study, based on *ab initio* Migdal-Eliashberg theory of heavily n-doped graphene, predicts such a contribution to $\alpha^2F(\omega)$ as a result of renormalization of the phonon dispersion of in-plane optical modes upon n-doping, which is also responsible for the softening of both high-energy modes as observed here [210]. In comparison to this study, the determined contributions to $\alpha^2F(\omega)$ discussed so far are well described by renormalization of the graphene phonon dispersion upon n-doping. On closer inspection, $\alpha^2F(\omega)$ exhibits a low-energy peak centered at about 10 meV that is similar to the low-energy feature suggested from the analysis of the tunneling spectroscopy data (cf. sec. 4.3), but not predicted in the calculations of highly n-doped (single-layer) graphene [210]. The energy position of this feature agrees well with the out-of-plane acoustic mode of AB-stacked BLG [107]. According to sec. 4.2, however, there are K atoms located between the topmost graphene and the former buffer layer so that (i) adjacent layers are most likely arranged by AA stacking and (ii) the interlayer spacing is definitely increased compared to freestanding BLG [66] as it is also apparent in K-intercalated graphite [64]. Therefore, the calculated low-energy mode of AB-stacked BLG is most likely modified and does not explain this low-energy feature here. Thus, it is more likely assignable to a vibrational mode of the metal atoms originating from in-plane displacements that is theoretically predicted for freestanding, K-intercalated, AA-stacked BLG at about $8-9$ meV [66]. Similar low-energy modes are also reported in theoretical studies regarding freestanding K-intercalated MLG [112] and BLG, albeit with lower K content (C_6KC_6) [113]. Those low-energy in-plane modes are known to be essential for the occurrence of superconductivity in GICs [66, 221].

From the determined Eliashberg function, an EPC constant of $\lambda \approx 0.46$ is estimated via eq. (2.7). Its energy dependence (fig. 5.12(a)) reveals that low-energy contributions have a crucial impact on this value due to the $1/\omega$ weighting. As already mentioned, K-intercalated graphene-based systems all exhibit anisotropic EPC strengths, which results in varying λ values for every direction in k space. The ARUPS data of the ΓK direction in fig. 4.20(a) verifies this behavior through differently pronounced kinks of both branches related to the same Dirac cone, since the branch beyond the K point ($k_\parallel \gtrsim 1.7\,\text{Å}^{-1}$) corresponds to the KM direction. The λ values reported for K-intercalated MLG on Au/Ni range from $\lambda \approx 0.1$ in ΓK direction to $\lambda \approx 0.2$ in KM direction [16]. Although extracted from a direction where an even lower value is expected, the EPC constant identified here exceeds the reported maximum value by a factor > 2. This also manifests in the maximum and step height in the real and imaginary part of $\Sigma_{\text{e-ph}}$, respectively (fig. 5.11(g)), which are both about twice as large compared to the data in ref. [16]. Apart from the low-energy mode of the K interlayer, this originates from an increased intensity of the peaks in $\alpha^2F(\omega)$ that can be ascribed to a significantly enhanced intensity of the PhDOS. Similar to the two-fold degeneracy in AB-stacked pristine BLG [107], this can be provided by an additional graphene layer. Since residual amounts of EBLG do not significantly contribute to the area-averaged ARUPS signal here (cf. sec. 4.1), the enhanced intensity must originate from the former buffer layer that is not available in the MLG on Au/Ni sample studied in ref. [16]. In turn, this proves the effective decoupling of the former buffer layer from the SiC substrate, since it acts like freestanding BLG regarding the phonon degeneracy. On the contrary, ref. [86] reports $\lambda \approx 0.3$ for K-intercalated EMLG on SiC, determined in the same direction in k space as the data discussed here. There, the K atoms were deposited at low temperatures [87], which did result in a severely lower doping level ($n = 5.6 \cdot 10^{13}\,\text{cm}^{-2}$) [86, 87] than in this work (cf. sec. 4.3).

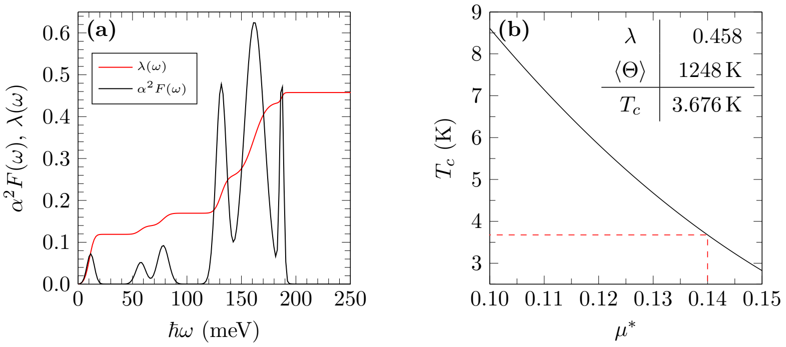

Figure 5.12: (a) Eliashberg function $\alpha^2F(\omega)$ (black) and associated mass enhancement factor $\lambda(\omega)$ (red) as a function of phonon energy $\hbar\omega$. (b) Critical temperature T_c as a function of plausible values for the Coulomb pseudopotential μ^*. The red dashed line assigns the reported value of $\mu^* = 0.14$ [11] to the corresponding T_c.

The comparison to Li intercalation of EMLG further reveals[h] that decoupling of the buffer layer is most likely not possible upon intercalation at low temperatures. Thus, the comparability to the value determined here is limited. K-intercalated graphite (KC_8) also exhibits an anisotropic EPC strength ranging from $\lambda \approx 0.15$ in ΓK direction to $\lambda \approx 0.79$ in KM direction, with an average of $\lambda = 0.45$ determined at the angle bisector between ΓK and KM direction [12]. The reported average value [12] and the EPC constant extracted in this thesis were determined in almost identical directions (cf. fig. 5.8(b)) and agree quantitatively. Thus, the EPC strength determined here is comparable to K-intercalated graphite rather than K-intercalated single-layer graphene as a result of the effective decoupling of the former buffer layer. The comparison to the data reported for KC_8 [12] further reveals that the determined λ value in the given direction here represents a sufficient estimate for the average EPC strength.

From the average $\lambda = 0.46$ and the determined Eliashberg function $\alpha^2F(\omega)$ the critical temperature can be estimated via eqs. (2.8) and (2.9) in dependence of typical values of the Coulomb pseudopotential μ^* as shown in fig. 5.12(b). Taking the theoretically predicted value $\mu^* = 0.14$ [11] into account, a critical temperature of $T_c \approx 3.7\,\mathrm{K}$ can be estimated (red dashed line) for the investigated sample.[i] This value agrees almost perfectly with the value determined via tunneling spectroscopy in the prior section, although an average value for the EPC strength is assumed.

Remark: Bostwick *et al.* suggest $\Sigma_{\text{e-h}}(\varepsilon) = \alpha\varepsilon^{\frac{1}{2}} + i\beta\varepsilon^{\frac{3}{2}}$ for the electron-hole or electron-electron interaction for doped EMLG produced by K intercalation at low temperatures as discussed above [41, 86]. For the sake of completeness, the ARUPS data are reanalyzed on that basis. As shown in sec. A.17.2, the analysis yields comparable results, albeit with a noticeably worsened fit quality compared to the above analysis. The slightly lowered λ is, however, still appropriate to reproduce the T_c determined via STS in a reasonable range of μ^*. Therefore, the assumption in refs. [41, 86] does not permit any further reliable statements.

---

[h] Deposition of Li atoms onto EMLG on SiC at RT results in the observation of two slightly shifted π bands that are expected for a decoupling of the buffer layer [75, 76]. Upon deposition at low temperatures, however, a single π band is observed [99], indicating that Li does not penetrate below the buffer layer.

[i] A stringent determination of the error margin is not feasible, due to the variety of numerical procedures applied for the estimation of the EPC constant. However, from several tests of the numerical algorithm the error margin can be estimated to be at least 0.1 K.

5.3 Discussion of the Superconducting Properties

The determined average Eliashberg function allows an estimation of the logarithmically weighted phonon energy $\hbar\omega_{\ln} = 68\,\mathrm{meV}$ via eq. (2.10). On that basis, the influence of the EPC on the gap ratio can be evaluated via eq. (2.12) in dependence of the critical temperature as provided in fig. 5.13. For the critical temperature determined via STS (and ARUPS), the impact on the gap ratio is negligible as depicted by the red dashed line. Thus, the extraordinarily high gap ratio of 6.19(7) determined from the STS analysis cannot be attributed to strong-coupling effects. Taking EPC into account yields the black curve in fig. 5.13. Not even the maximum of this curve at $2\Delta_0/(k_\mathrm{B}T_\mathrm{c}) \approx 5.6$ (indicated by blue dashed lines) is sufficient to explain the high gap ratio observed here. As already mentioned above, tunneling experiments for CaC_6 also reveal an elevated gap ratio of 4.6, which the authors attribute to strong-coupling effects [19]. Moreover, an average EPC constant of $\lambda = 0.53$ was reported for that system [14]. Since λ is directly related to the gap ratio (cf. sec. 2.4.2), the lower average EPC constant of $\lambda \approx 0.46$ determined here would suggest a gap ratio even lower than 4.6. Nonetheless, the gap ratio determined in the present study exceeds that value by far. This comparison also verifies that a different mechanism, besides strong coupling, must be responsible for the high gap ratio in K-intercalated quasi-freestanding EBLG.

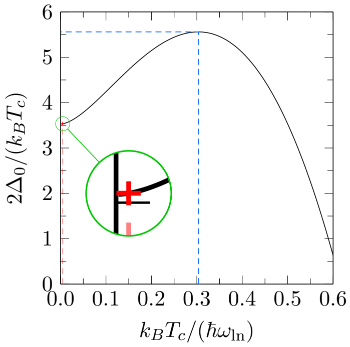

Figure 5.13: Gap ratio in the strong-coupling limit according to eq. (2.12) for $\hbar\omega_{\ln} = 68\,\mathrm{meV}$. For the determined T_c electron-phonon coupling does not modify the gap ratio significantly (marked by red cross and red dashed line close to the left-hand y-axis). Assuming higher critical temperatures explains the occurrence of a maximum of the gap ratio depicted by the blue dashed line.

The quantitative agreement between the critical temperature estimated from the EPC and the (highest) T_c determined via STS suggests that the electron pairing leading to superconductivity takes place at the Dirac cone. Although wide-range tunneling spectroscopy solely probes the local DOS at the Γ point of the SBZ (cf. sec. 4.3), tunneling to bands centered at the K point can also be possible and efficient for a low stabilization bias, due to the reduced tip-sample distance (cf. sec. 4.1). It is conceivable that similar EPC on one (or both) of the IL bands is responsible for the electron pairing and the observation of an energy gap related to superconductivity via STS. As thoroughly discussed in sec. 5.1, also different pairing processes might occur on one (or both) IL band(s) leading to the unusual temperature dependence of the unexpectedly high broadening parameter Γ.

Nevertheless, high Γ values were also reported for nanometer-sized lateral domains of conventional superconductors accompanied with drastically increased gap ratios [206, 222, 223]. In particular, for Pb islands with a diameter of 9 nm an elevated $\Gamma \approx 0.7\,\mathrm{meV}$ and a gap ratio > 6 were determined. Increasing Γ values ($0.1 - 0.6\,\mathrm{meV}$) are also reported for superconducting La films upon decreasing film thickness[j] [160]. Since the thinnest film in ref. [160] was about 10 nm thick, a severe impact on the broadening parameter Γ, but also on the gap ratio of the sample investigated in this work (film thickness $< 1\,\mathrm{nm}$), is expectable. Accordingly, the high Γ value and the extraordinarily high gap ratio of K-intercalated quasi-freestanding EBLG are most likely caused by low dimensional effects due to the limited thickness. However, due to the unusual temperature dependence of Γ, multiple energy gaps from additional pairing on the IL bands are probable, and the value can also be influenced upon anisotropic coupling.

Judging from the decoupling of the buffer layer upon K intercalation, the intercalants are located below the former buffer layer and between the adjacent carbon layers. This configuration can be considered as the thinnest limit of an extended, K-intercalated stage-1 GIC. However, the critical temperature determined here is strongly elevated compared to the highest reported $T_c = 0.55\,\mathrm{K}$ of K-intercalated graphite [9]. Due to the missing bonding partners of the surface graphene layer, the interlayer spacing between adjacent sheets is supposedly larger compared to the GIC counterpart [7]. As a consequence, the IL bands are expected to shift further below the Fermi energy, whereby in the present case even a second band is partially filled. Thus, the Fermi surface on which electron pairing occurs is extended, which possibly causes higher critical temperatures. However, upon increased interlayer distances, the EPC is expected to decrease [7], which is not the case here as determined in the previous section. This can be most likely attributed to higher intensities of the observed low-energy vibrations of the K atom layer due to the enhanced space.

In comparison to K-intercalated few-layer graphene (mainly four sheets), which exhibits a $T_c = 4.5\,\mathrm{K}$ [10], the determined critical temperature here is slightly lower. In this thickness regime, an increased interlayer spacing might still be apparent and affect the superconducting properties. Considering the lower T_c observed in the GIC, there seems to be a non-monotonic dependence of the critical temperature on the number of K-intercalated graphene layers and, thus, an optimal layer thickness for a maximal T_c. Compared to few-layer graphene, however, the lower value determined here most likely arises from low-dimensional effects owing to a pronounced influence of the surface and/or a non-negligible influence of the SiC substrate underneath.

The bottom line of the main findings of this thesis is in agreement with previous studies of comparable systems: the superconducting properties of K-intercalated epitaxial monolayer graphene or, more appropriately, quasi-freestanding epitaxial bilayer graphene are caused by the presence of IL bands in combination with electron pairing mediated by phonons of the K atom interlayer and both graphene layers, i.e., also from the former buffer layer, which itself is electronically decoupled from the substrate upon K intercalation.

---

[j] The temperature dependence of the superconducting energy gap is not investigated in that study. Thus, the evolution of the gap ratio with the film thickness is not known.

6 Conclusions

The primary objective of this study was the proof and thorough investigation of superconductivity among K-intercalated ultra-thin films of epitaxial graphene on SiC(0001). For this purpose, the pristine and K-intercalated EMLG sample was characterized in detail with regard to structural and electronic properties. Superconductivity of K-intercalated (former) EMLG was proven by analyzing the temperature dependence of the energy gap and further verified via determination of the EPC strength.

Investigations of pristine EMLG and EBLG samples, which were clearly distinguished via STM by emerging quasiparticle interference patterns [146], revealed that inelastic effects have a major impact on electron tunneling as already known from the literature. The consideration of elastic and inelastic contributions to the total tunneling current allowed a quantitative analysis of the acquired spectroscopic data. This analysis exposed that, especially for EBLG, the tunneling probability increases strongly when phonons of the graphene lattice can be excited that provide a sufficient momentum transfer for the tunneling electrons to reach electronic bands near the K points of the SBZ of graphene. Even though electron tunneling is most efficient for low $k_{\|}$ values, direct tunneling to the electronic bands of pristine graphene was achieved by lowering the tip-sample distance. This finding verified the $k_{\|}$ dependence of the Tersoff-Hamann model [127, 128] and enabled the examination of the graphene DOS near the Fermi level.

Upon K intercalation of EMLG a rigid shift of the Dirac cones toward higher binding energies was observed with PES and could also be monitored via optical measurements. At the highest doping level achieved, the metal atoms form a (2×2) superstructure with respect to the graphene lattice that could be imaged via STM, which is the first real-space observation of this structure in the thin film limit. Further, two occupied IL bands were identified at the Γ point of the SBZ. Upon folding induced by the superstructure, the electronic bands emerge in the vicinity of different high-symmetry points of the graphene SBZ. A total charge carrier density for the highly doped phase was estimated at about 50 times the value of pristine epitaxial graphene, resulting from a charge transfer of 0.94(8) electrons per unit cell of the (2×2) superstructure to the graphene-based system. Due to the emergence of a quasiparticle interference pattern in the FT-STM images, it was demonstrated that the same electronic structure is probed on a local (STM) and area-averaged (ARPES) scale. It could further be shown that the K atoms not only penetrate below the graphene layer, but also below the buffer layer. As a result, the buffer layer most likely decouples electronically from the underlying substrate, and the sample behaves like K-intercalated bilayer graphene. This is also manifested by the strongly enhanced EPC strength compared to K-intercalated MLG [16]. The wide-range tunneling data of K-intercalated quasi-freestanding EBLG exhibits an NDC that was explained by the existence of a sharp, energetically localized electronic state of the tunneling tip. The quantitative analysis of these data revealed that STS only probes electronic bands of the sample located at the Γ point, whereas inelastic tunneling caused by phonon and plasmon contributions also plays a significant role.

While the highly doped sample was found to be stable at low temperatures for several weeks, its stability at RT is limited to a few minutes. In particular, at RT the K atom concentration between substrate and former buffer layer increases while the interlayer between both adjacent carbon layers is depopulated. Upon this transformation, the topmost layer behaves similarly to pristine EMLG, while the lower layer remains doped.

The data acquired via tunneling spectroscopy further exposed a temperature-dependent energy gap around the Fermi level that is not present in the data of pristine EMLG or EBLG. For the quantitative evaluation of the energy gaps, a modified approach was developed that is also valid for a non-flat DOS of the sample in the normal-conducting state. The detailed analysis of the temperature dependence revealed that K-intercalated quasi-freestanding EBLG actually is a superconductor characterized by the parameters $T_c = 3.65(2)\,\mathrm{K}$ and $\Delta_0 = 0.97(1)\,\mathrm{meV}$. The same critical temperature was estimated from the average EPC strength determined from ARUPS data for the Dirac bands near the K point of the graphene SBZ. Thereby, low-energy phonon modes, which most likely originate from the K atom interlayer, are of particular importance. Consequently, this finding suggests that the superconductivity among K-intercalated quasi-freestanding EBLG is indeed driven by EPC. However, the temperature-dependent tunneling data exhibit evidence of multiple gaps that are possibly enabled by the presence of IL bands or anisotropic coupling. Moreover, an extraordinarily high gap ratio of 6.19(7) was determined for this sample that is most likely not a consequence of strong coupling, but can be attributed to low-dimension effects. Even though the determined critical temperature here is higher than in the bulk counterpart [9], it is, however, smaller than the reported value for K-intercalated few-layer graphene [10].

In particular, this study provides the first observation of the temperature dependence of the energy gap related to superconductivity among metal-intercalated thin films of graphene-based layered systems. For an even better understanding of those findings, future studies should perform tunneling experiments using superconducting tips to gain higher resolution, accompanied with a determination of the EPC strength across the entire SBZ. In combination with future calculations regarding the exact structural geometry determined here, this system is a promising candidate to uncover the mechanisms that are responsible for superconductivity of graphene-based, layered materials and low-dimensional systems.

A Appendix

A.1 2D Detector Relations

The following equations represent the relation of the detector angle D and the sample tilt angle T to the actual polar θ and azimuth angle ϕ in measurements in 2D mode:

$$\theta = \arctan \sqrt{\frac{\sin^2 T + \tan^2 D}{\cos^2 T}} \tag{A.1}$$

and

$$\phi = \arctan \left(\frac{\tan D}{\sin T} \right). \tag{A.2}$$

Upon additional rotation of the sample by an azimuth angle S, the last equation modifies to:

$$\phi = \arctan \left(\frac{\tan D}{\sin T} \right) + S. \tag{A.3}$$

A.2 Lock-In Technique

A.2.1 Lock-In Signal at Different Deconvolution Frequencies

The measured tunneling current is a function of the applied voltage

$$I(V_{\text{appl}}(t)) = f(V_{\text{appl}}(t)) = f(V_b + V_{\text{mod}} \sin(\omega_{\text{mod}} t)) \tag{A.4}$$

that can be expanded as a Taylor series

$$f(x) = \frac{f(a)}{0!} + \frac{f'(a)(x-a)}{1!} + \frac{f''(a)(x-a)^2}{2!} + ... + \frac{f^{(n)}(a)(x-a)^n}{n!} + ... \tag{A.5}$$

A Taylor expansion for small V_{mod} at the point $a = V_b$ (with $x = V_b + V_{\text{mod}} \sin(\omega_{\text{mod}} t)$) leads to the following expression:

$$I(V_{\text{appl}}(t)) = I(V_b) + \left.\frac{dI}{dV}\right|_{V_b} V_{\text{mod}} \sin(\omega_{\text{mod}} t) + \left.\frac{d^2 I}{dV^2}\right|_{V_b} \frac{V_{\text{mod}}^2}{2} \sin^2(\omega_{\text{mod}} t) + O(V_{\text{mod}}^3). \tag{A.6}$$

Upon using the trigonometric identity

$$\sin^2(x) = \frac{1}{2}(1 - \cos(2x)) = \frac{1}{2}(1 - \sin(\frac{\pi}{2} - 2x)) = \frac{1}{2}(1 + \sin(2x - \frac{\pi}{2})) \tag{A.7}$$

the tunneling current can be rewritten in the following way:

$$I(V_{\text{appl}}(t)) = I(V_b) + \left.\frac{dI}{dV}\right|_{V_b} V_{\text{mod}} \sin(\omega_{\text{mod}} t)) + \left.\frac{d^2I}{dV^2}\right|_{V_b} \frac{V_{mod}^2}{4}(1 + \sin(2\omega_{\text{mod}} t - \frac{\pi}{2})) + O(V_{\text{mod}}^3). \tag{A.8}$$

The signal determined by deconvolution of all signals with a frequency of ω_{mod} amounts to

$$S(V_b) = \left.\frac{dI}{dV}\right|_{V_b} V_{\text{mod}}. \tag{A.9}$$

Since lock-in-specific parameters like sensitivity and amplification factors need to be considered, the function $S(V_b)$ is related to the lock-in signal via

$$S(V_b) = B \cdot \text{lock-in signal}(V_b) \tag{A.10}$$

and thus

$$\frac{dI}{dV}(V_b) = \frac{B}{V_{\text{mod}}} \cdot \text{lock-in signal}(V_b). \tag{A.11}$$

Accordingly, signal deconvolution with the doubled frequency leads to a quantity that is proportional to the second derivative of the tunneling current, but phase-shifted by 90° compared to the signal of the first derivative. Due to the factor $\frac{V_{\text{mod}}^2}{4}$ the signal is noticeably smaller than the signal acquired at ω_{mod} and is, thus, in most experiments smaller than the noise signal.

A.2.2 Derivation of the Proportionality Constant for the Lock-In Signal

Under the assumption of a simple linear characteristic $I(V) = aV$, with $a = \text{const.}$, it is obvious that broadening arising from an AC voltage modulation does not play a role and, thus, the differential conductance determined via lock-in technique (left-hand side of eq. (3.24)) can be expressed as:

$$\left(\frac{dI}{dV}\right)_L (V_b) = \frac{dI}{dV}(V_b) = a. \tag{A.12}$$

Accordingly, the right-hand side of eq. (3.24) simplifies to

$$\int_{-\pi/2}^{\pi/2} d\alpha \sin(\alpha) \cdot a \cdot (V_b + V_{\text{mod}} \sin(\alpha)) = \frac{\pi}{2} \cdot V_{\text{mod}} \cdot a. \tag{A.13}$$

Upon simple comparison of both sides, the factors of proportionality can be determined and eq. (3.24) can be rewritten:

$$\left(\frac{dI}{dV}\right)_L (V_b) = \frac{2}{\pi V_{\text{mod}}} \int_{-\pi/2}^{\pi/2} d\alpha \sin(\alpha) \cdot I \left(V_b + V_{\text{mod}} \sin(\alpha)\right). \tag{A.14}$$

As the modulation voltage is very small, the assumption of a (piece wise) linear current-voltage characteristics is sufficiently fulfilled for all measured $I(V)$ curves.

A.3 Determination of the Work Functions

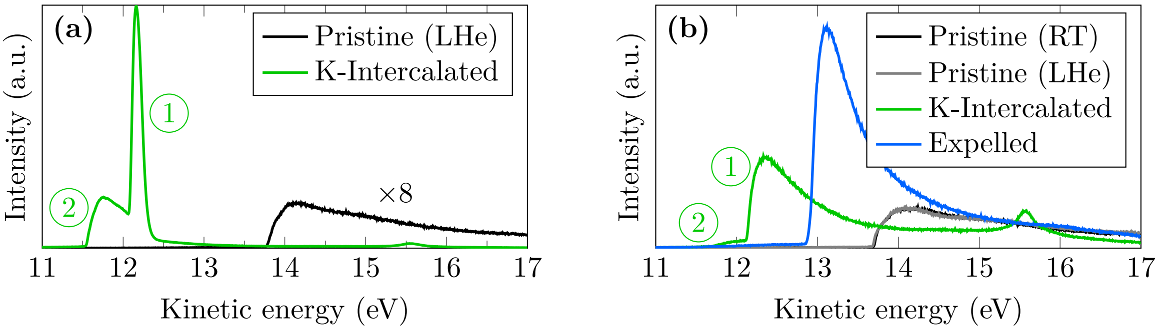

Figure A.1: SECO of two different preparations via K intercalation of the same sample for the work function estimation. (a) refers to ARUPS data in fig. 4.15 (unexpectedly sharp intensity distribution of the feature labeled with (1) caused by a faulty aperture setting of the electron optics, kinetic energy position not influenced) and (b) to data in fig. A.11. (1) and (2) denote the distinct cutoffs of two separate secondary electron backgrounds of the K-intercalated sample.

Table A.1: Work functions determined from the SECOs in fig. A.1 (estimated by using kinetic energy position of Fermi edge, bias ≈ 9.4 V).

	Work function (eV)	
Sample	(a)	(b)
Pristine (RT)	-	4.23(2)
Pristine (LHe)	4.39(4)	4.20(2)
K-Intercalated ①	2.69(4)	2.64(1)
K-Intercalated ②	2.16(4)	2.13(2)
Expelled	-	3.44(3)

A.4 Polarization and Temperature Dependence of ARUPS Data

A.4.1 Pristine Sample

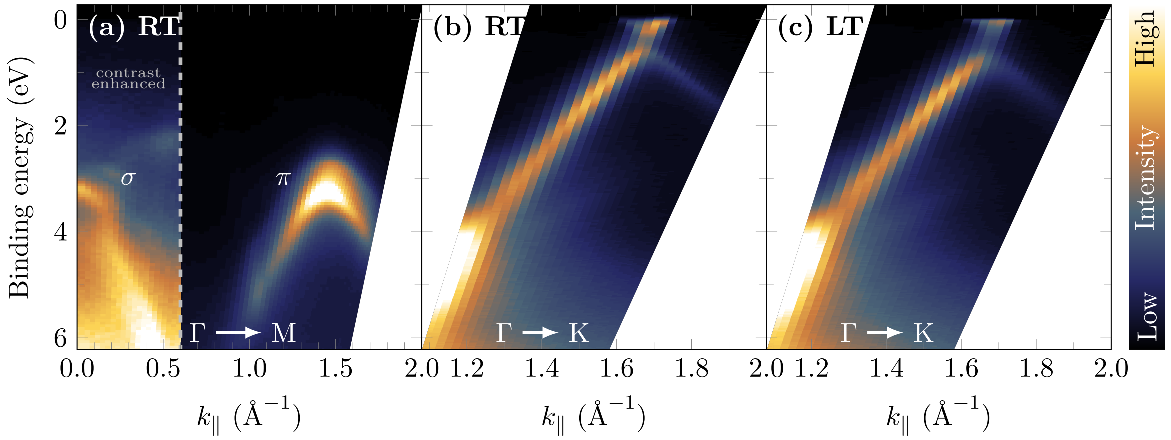

Figure A.2: ARUPS data of the pristine 1.3 ML epitaxial graphene on SiC(0001) sample (a) in ΓM direction at RT, (b) in ΓK direction at RT and (c) in ΓK direction at low temperature (LT) of about 35 K (cf. sec. 3.1.3). (Resolution: $\Delta\theta = 1°$, (a) and (b) $\Delta E = 50\,\text{meV}$, (c) $\Delta E = 20\,\text{meV}$.)

A.4.2 K-Intercalated Sample

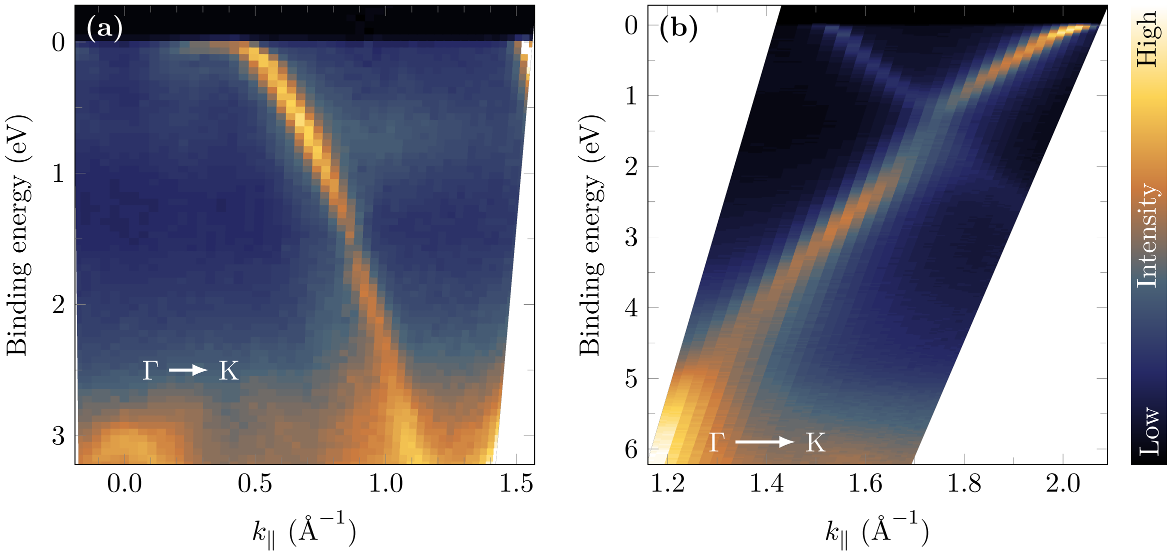

Figure A.3: Polarization dependence of the π bands visible in the ARUPS data of K-intercalated 1.3 ML epitaxial graphene on SiC(0001) in ΓK direction at about 35 K. (a) depicts data acquired at low $k_{\|}$ values in the region of the $\overline{\mathrm{K}}$ point and (b) at higher $k_{\|}$ values in the region of the K point (resolution: $\Delta\theta = 1°$, (a) $\Delta E = 50\,\text{meV}$, (b) $\Delta E = 20\,\text{meV}$).

A.5 ARUPS Data of a Comparable Sample

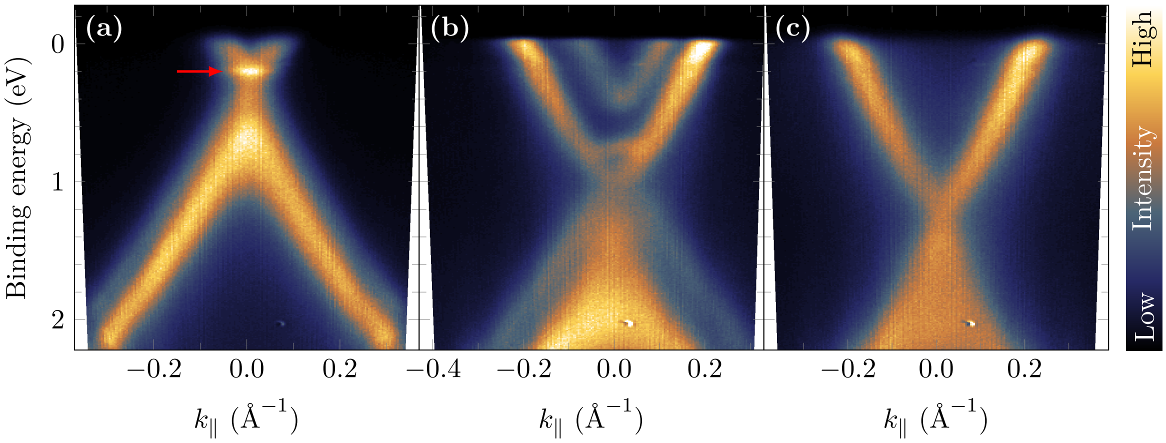

Figure A.4: ARUPS data acquired near the K point of a different sample with a nominal coverage (derived from XPS) of 1.2 ML epitaxial graphene on SiC(0001) by using the 2D detector at low temperatures (resolution: 8.36 meV, 0.1° corresponding to $\approx 0.0034\,\text{Å}^{-1}$). (a) Pristine sample, (b) intercalated sample with low K content, and (c) with higher K content compared to (b). The red arrow in (a) points at the extremely flat band that originates from 2 ML areas.

A.6 Third-Nearest-Neighbor Tight-Binding Model

According to ref. [178] the energy dispersion of electrons in graphene can be described by

$$E^{\pm}(k) = \frac{(2E_0 - E_1) \pm \sqrt{(E_1 - 2E_0)^2 - 4E_2E_3}}{2E_3}, \tag{A.15}$$

where the coefficients are defined by

$$\begin{aligned}
E_0 &= [E_{2p} + \gamma_1 u(k)]\,[1 + s_1 u(k)]\,,\\
E_1 &= 2s_0\gamma_0 g(k) + (s_0\gamma_2 + \gamma_0 s_2)t(k) + 2s_2\gamma_2 g(2k),\\
E_2 &= [E_{2p} + \gamma_1 u(k)]^2 - \left[\gamma_0^2 g(k) + \gamma_0\gamma_2 t(k) + \gamma_2^2 g(2k)\right],\\
E_3 &= [1 + s_1 u(k)]^2 - \left[s_0^2 g(k) + s_0 s_2 t(k) + s_2^2 g(2k)\right],
\end{aligned}$$

with the k-dependent functions using Cartesian coordinates as in ref. [179]

$$\begin{aligned}
u(k) &= 2\cos(k_y a) + 4\cos(k_x a\sqrt{3}/2)\cos(k_y a/2),\\
g(k) &= 1 + 4\cos^2(k_y a/2) + 4\cos(\sqrt{3}k_x a/2)\cos(k_y a/2),\\
t(k) &= 2\cos(k_x a\sqrt{3}) + 4\cos(k_y a) + 4\cos(k_y a/2)\cos(k_x a\sqrt{3}/2)\\
&\quad + 8\cos(k_y a)\cos(k_y a/2)cos(k_x a\sqrt{3}/2),
\end{aligned}$$

where a is the lattice constant of graphite. To match the PMM data, the coordinate system is rotated by 90° upon interchanging k_x and k_y. The parameters for evaluating the ARUPS data are provided in tab. A.2.

Table A.2: Parameters used in the 3NN TB model for the undoped and doped epitaxial graphene samples based on reported parameters from the literature by adjusting E_{2p} and γ_0 to describe the measured data.

Sample	Reference	E_{2p} (eV)	γ_0 (eV)	γ_1 (eV)	γ_2 (eV)	s_0	s_1	s_2
Undoped	Ref. [179]	−0.45	−2.78	−0.15	−0.095	0.117	0.004	0.002
Undoped	This work	−0.815	−3.35	−0.15	−0.095	0.117	0.004	0.002
Doped	Ref. [192]	−1.937	−2.937	−0.286	−0.265	0.025	0.068	0.059
Doped	This work	−2.10	−2.55	−0.286	−0.265	0.025	0.068	0.059

A.7 FT-STM Data Analysis

A.7.1 Pristine EMLG

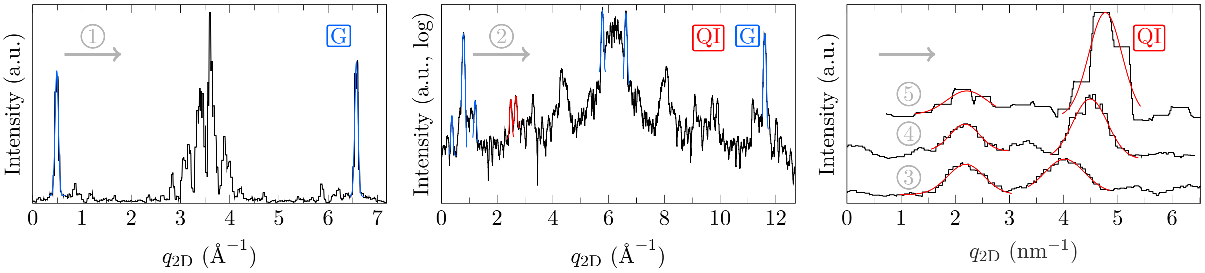

Figure A.5: Line profiles extracted from the FT-STM image acquired on EMLG in directions depicted in fig. 4.4(a) and (b). They are labeled by gray numbers that correspond to the respective directions and are referred to in tabs. A.3 and A.4. Reciprocal distances are provided in 2D scaling in due consideration of the factor $4\pi/\sqrt{3}$. Peaks related to the graphene lattice (G) and QI processes are analyzed by fitting of Voigt profiles that are depicted in blue and red, respectively, to determine their separation in reciprocal space.

Table A.3: Determination of calibration factors CF for the line profiles in fig. A.5 with regard to known quantities in the particular direction by assuming the graphite lattice constant a_G (CF $= a_G/a$) and the (6×6) superstructure $a_{(6\times6)}$ of the buffer layer w.r.t. the SiC substrate (CF $= a_{(6\times6)}/a$ with $a_{(6\times6)} = 6a_{\mathrm{SiC}} = 18.4836$ Å), respectively.

Direction	Structure	Order	a (Å)	CF
1	G	1	2.3847(7)	1.0320(3)
2	G	2	2.3242(2)	1.0588(1)
2	(6×6)	1	17.22(4)	1.073(2)
2	(6×6)	ms	17.40(5)	1.062(3)

Table A.4: Estimated values of the Fermi wave vector q_F from the FT-STM image in fig. 4.4(a) given in 1D and 2D scaling (values in parentheses indicate the numerical error of the last significant digit, calibrated by the respective factors in tab. A.3).

Direction	$q_{\mathrm{F,1D}}$ (nm^{-1})	$q_{\mathrm{F,2D}}$ (nm^{-1})
2	0.369(4)	0.427(4)
3	0.373(2)	0.430(2)
4	0.473(1)	0.547(1)
5	0.522(2)	0.603(2)

A.7.2 Pristine EBLG

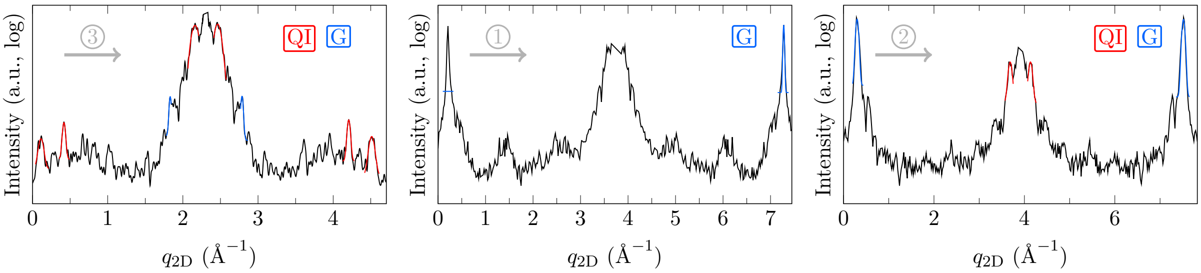

Figure A.6: Line profiles extracted from the FT-STM image acquired on EBLG in directions depicted in fig. 4.4(c). They are labeled by gray numbers that correspond to the respective directions and are referred to in tabs. A.5 and A.6. Reciprocal distances are provided in 2D scaling in due consideration of the factor $4\pi/\sqrt{3}$. Peaks related to the graphene lattice (G) and QI processes are analyzed by fitting of Voigt profiles that are depicted in blue and red, respectively, to determine their separation in reciprocal space.

Table A.5: Determination of calibration factors CF for the line profiles in fig. A.6 with regard to known quantities in the particular direction by assuming the graphite lattice constant a_G (CF $= a_G/a$) and the (6×6) superstructure $a_{(6\times6)}$ of the buffer layer w.r.t. the SiC substrate (CF $= a_{(6\times6)}/a$ with $a_{(6\times6)} = 6a_{\mathrm{SiC}} = 18.4836$ Å), respectively.

Direction	Structure	a (Å)	CF
1	G	2.052 25(5)	1.1991(3)
2	G	2.031(2)	1.2118(8)
3	(6×6)	15.20(1)	1.2163(8)

During the measurement of the 2 ML sample a wrong calibration matrix was used in the STM software, which leads to higher calibration factor values (tab. A.5) compared to the 1.3 ML sample (tab. A.3). Thus, the scale bars in the (FT-)STM images of the 2 ML sample in figs. 4.3(c,d) and 4.4(d-f) slightly deviate from the actual length, but, due to subsequent calibration, the determined q_F values in tab. A.6 are correct.

Table A.6: Estimated values of the Fermi wave vector q_F from the FT-STM image in fig. 4.4(c) given in 1D and 2D scaling (values in parentheses indicate the numerical error of the last significant digit, calibrated by the respective factors in tab. A.5).

Direction	Measurement	$q_{\mathrm{F,1D}}$ (nm^{-1})	$q_{\mathrm{F,2D}}$ (nm^{-1})
3	Intervalley 1	0.544(4)	0.628(4)
3	Intervalley 2	0.544(3)	0.628(4)
3	Intravalley	0.535(4)	0.618(5)

A.7.3 K-Intercalated EMLG

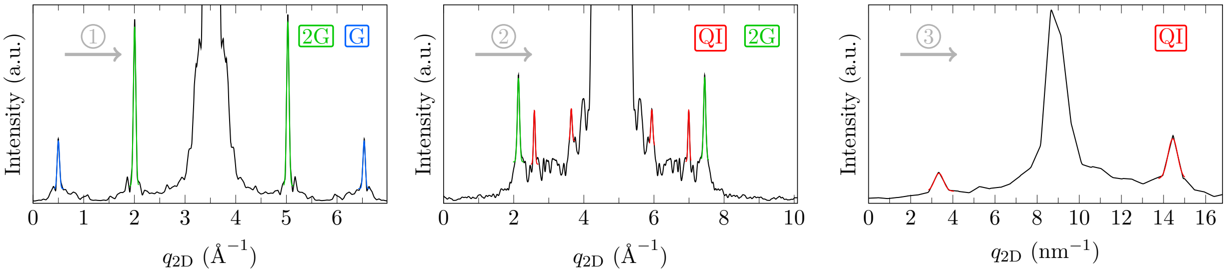

Figure A.7: Line profiles extracted from the FT-STM image acquired on K-intercalated EMLG in directions depicted in fig. 4.19(a). They are labeled by gray numbers that correspond to the respective directions and are referred to in tabs. A.7 and 4.2. Reciprocal distances are provided in 2D scaling in due consideration of the factor $4\pi/\sqrt{3}$. Peaks related to the graphene lattice (G), the (2×2) superstructure (2G), and QI processes are analyzed by fitting of Voigt profiles that are depicted in blue, green and red, respectively, to determine their separation in reciprocal space.

Table A.7: Determination of calibration factors CF for the line profiles in fig. A.6 with regard to known quantities in the particular direction by assuming the graphite lattice constant a_G (CF $= a_G/a$) and the (2×2) superstructure $2a_G$ under consideration of the actual order, respectively.

Direction	Structure	Order	a (Å)	CF $= a_{\mathrm{G}}/a$
1	G	1	2.4047(3)	1.0234(1)
1	2G	1	2.3988(3)	1.0259(2)
2	2G	2	2.3664(4)	1.0340(2)

A.8 DOS Models for the STS Data Analysis

A.8.1 Inelastic Contributions

The inelastic contributions $D(\hbar\omega)$ to the total tunneling current are described by a sum of Gaussian peaks. The only restriction applied is that for phonon features positive and negative bias (energy) positions are assumed to be equal:

$$D(\hbar\omega^*) = \sum_{i=1}^{n} \left[\frac{a_{+,i}}{\sigma_{+,i}\sqrt{2\pi}} \exp\left(-\frac{\hbar^2(\omega^* - \omega_i^*)^2}{2\sigma_{+,i}^2} \right) + \frac{a_{-,i}}{\sigma_{-,i}\sqrt{2\pi}} \exp\left(-\frac{\hbar^2(\omega^* + \omega_i^*)^2}{2\sigma_{-,i}^2} \right) \right] \tag{A.16}$$

where σ is related to the full width at half maximum (FWHM) via

$$\sigma_{\pm,i} = \frac{\mathrm{FWHM}_{\pm,i}}{2\sqrt{2\ln 2}}.$$

The plasmon contribution is described by a single Gaussian peak.

A.8.2 Electronic DOS

Pristine EMLG

In the case of EMLG, the electronic sample DOS is described as simple V-shaped function:

$$\rho_s(E) = |a_1(E - E_D)|, \tag{A.17}$$

and the tip DOS is assumed as a constant.

Pristine EBLG

In the case of EBLG, the electronic sample DOS of graphene is described by a parabolic background, a superposition of peaks and steps at the edges of the small energy gap Δ_s and just steps at the edges of the large energy gap Δ_b in the following way

$$\begin{aligned}\rho_s(E) = {} & a_1(E - E_D)^2 \\ & + S(E; a_2, \Gamma_2, E_D + \Delta_s/2) + (1 - S(E; a_3, \Gamma_3, E_D - \Delta_s/2)) + L(E; a_4, \Gamma_4, E_D + \Delta_s/2)) \\ & + S(E; a_5, \Gamma_5, E_D + \Delta_b/2) \\ & + \sum_{i=6}^{8} L(E; a_i, \Gamma_i, E_{0,i}),\end{aligned} \tag{A.18}$$

to satisfy the site-resolved DOS provided in refs. [45, 183]. In this description, the steps are described similar to the DOS of the 2D electron gas with finite lifetime Γ (taken as broadening parameter here) [205, 224]:

$$S(E; a_i, \Gamma_i, E_{0,i}) = a_i \left(\frac{1}{2} + \frac{1}{\pi} \arctan \left[\frac{2(E - E_{0,i})}{\Gamma_i} \right] \right), \tag{A.19}$$

and the peaks as standard Lorentzian functions (normalized such that the peak height equals a_i):

$$L(E; a_i, \Gamma_i, E_{0,i}) = a_i \frac{(\frac{1}{2}\Gamma_i)^2}{(E - E_{0,i})^2 + (\frac{1}{2}\Gamma_i)^2} \tag{A.20}$$

with Γ =FWHM. Further, a parabolic tip DOS is assumed via

$$\rho_t(E) = a_2 E^2 + a_1. \tag{A.21}$$

K-Intercalated EMLG

In the case of K-intercalated EMLG, the tip DOS is described by a parabolic background and a Lorentzian peak

$$\rho_t(E) = a_2 E^2 + a_1 + L(E; a_3, \Gamma_3, E_{0,3}) \tag{A.22}$$

to account for the energetically localized state near E_F. The electronic sample DOS for the wide-range spectrum (cf. fig. 4.25) is modeled by

$$\begin{aligned} \rho_s(E) = {} & V(E; a_1, E_D) \\ & + S(E; a_2, \Gamma_2, E_{0,2}) + L(E; a_3, \Gamma_3, E_{0,3})) \\ & + (1 - S(E; a_4, \Gamma_4, E_{0,4})) + L(E; a_5, \Gamma_5, E_{0,5}) \\ & + \sum_{i=6}^{7} L(E; a_i, \Gamma_i, E_{0,i}) \\ & + \sum_{i=8}^{9} S(E; a_i, \Gamma_i, E_{0,i}) \\ & + \sum_{i=10}^{12} L(E; a_i, \Gamma_i, E_{0,i}). \end{aligned} \tag{A.23}$$

For the spectrum in fig. 4.26, not all contributions are required. Thus, the model reduces to

$$\begin{aligned}\rho_s(E) = a_1 \\ &+ L(E; a_2, \Gamma_2, E_{0,2}) \\ &+ \sum_{i=3}^{4} S(E; a_i, \Gamma_i, E_{0,i}) \\ &+ \sum_{i=5}^{7} L(E; a_i, \Gamma_i, E_{0,i}).\end{aligned} \tag{A.24}$$

For the analysis of the Fermi level region (cf. fig. 4.28) the model reduces further to

$$\rho_s(E) = a_1 + \sum_{i=2}^{6} L(E; a_i, \Gamma_i, E_{0,i}) \tag{A.25}$$

and, accordingly, only two inelastic contributions have to be considered.

A.9 Estimation of Tip-Sample Distances

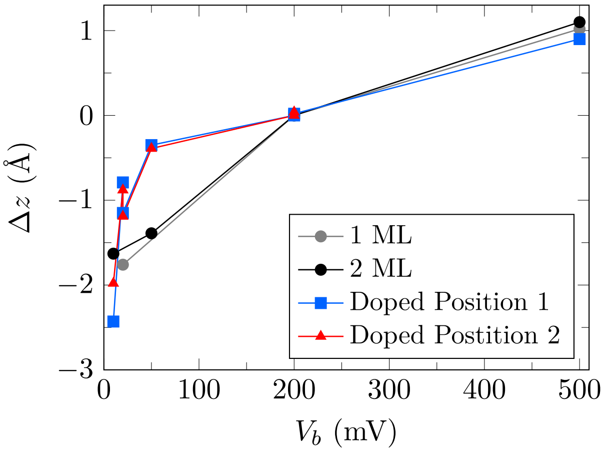

Figure A.8: Tip-sample distance variation in dependence of V_b to achieve an identical stabilization current of $I_s = 500\,\text{pA}$. Given values of different samples are normalized to zero at $V_b = 200\,\text{mV}$. From the V_b dependence the absolute tip-sample distance at $V_{set} = 200\,\text{mV}$ is estimated as 2 Å for pristine graphene samples (1 ML and 2 ML) and 3 Å for the K-intercalated sample.

A.10 PMM Data Set

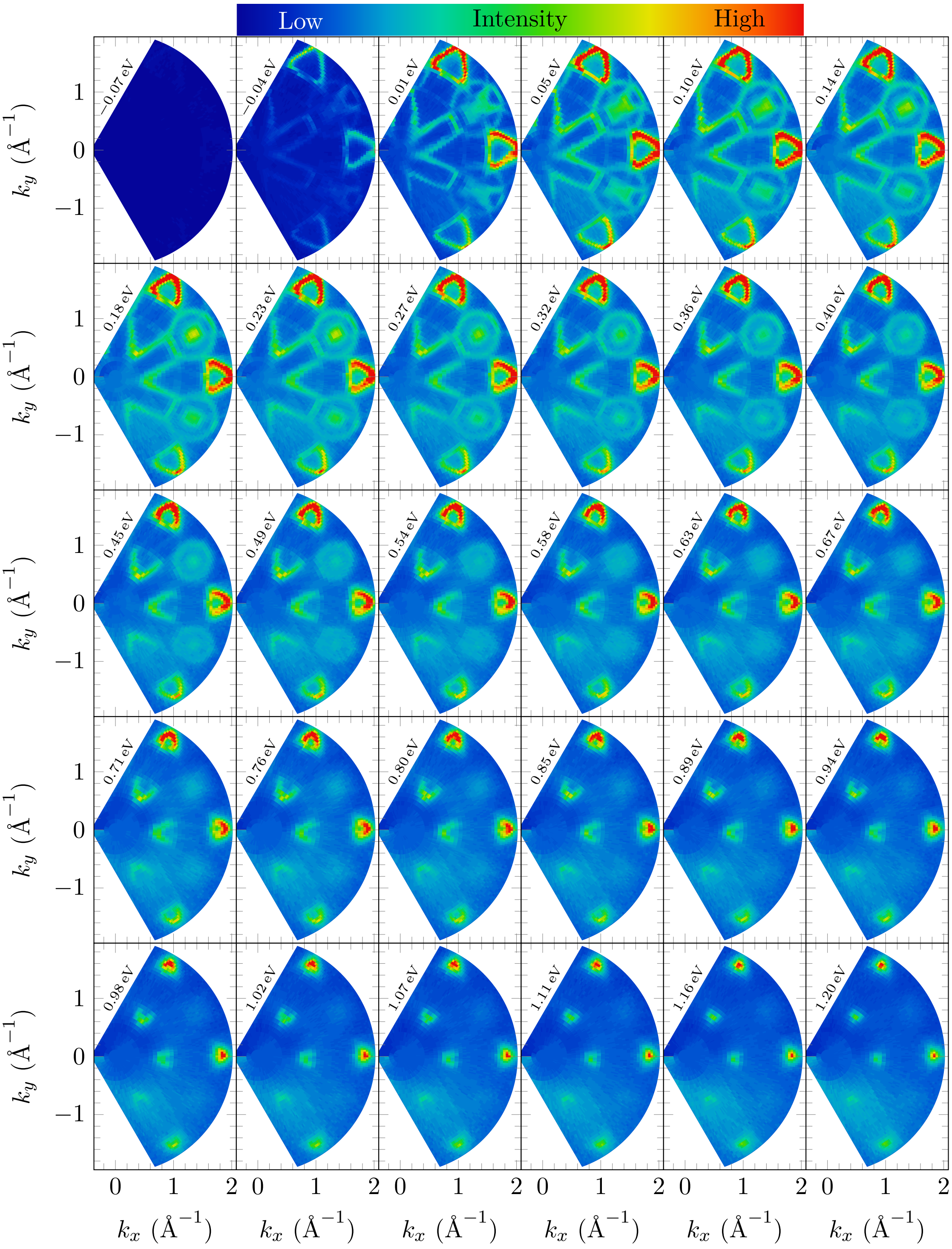

Figure A.9: Full PMM data set of K-intercalated 1.3 ML epitaxial graphene on SiC(0001) at binding energies given in the upper left corners (energy range: ±22 meV, resolution: $\Delta\phi = 1^\circ$, $\Delta\theta = 2^\circ$).

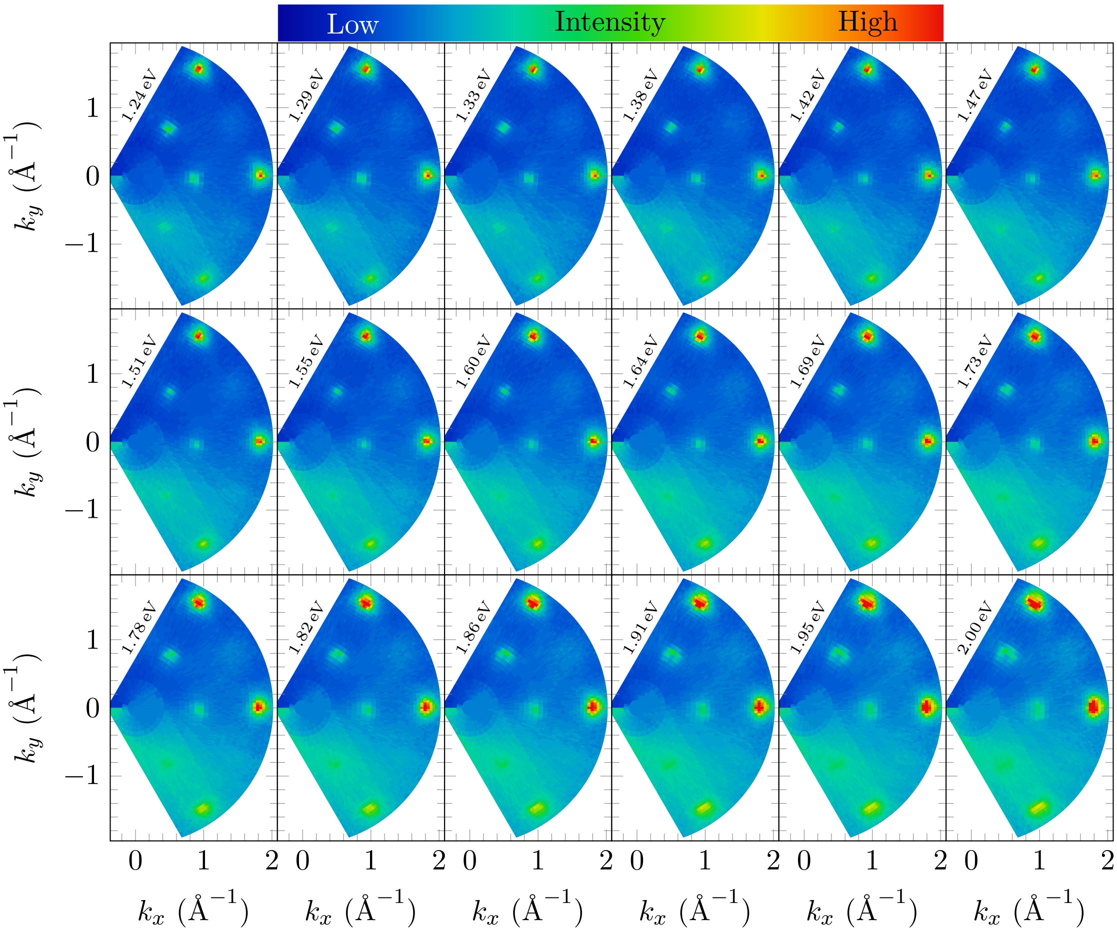

Figure A.10: Continuation of fig. A.10.

A.11 PES Data of a Different Preparation of K-Intercalated EMLG

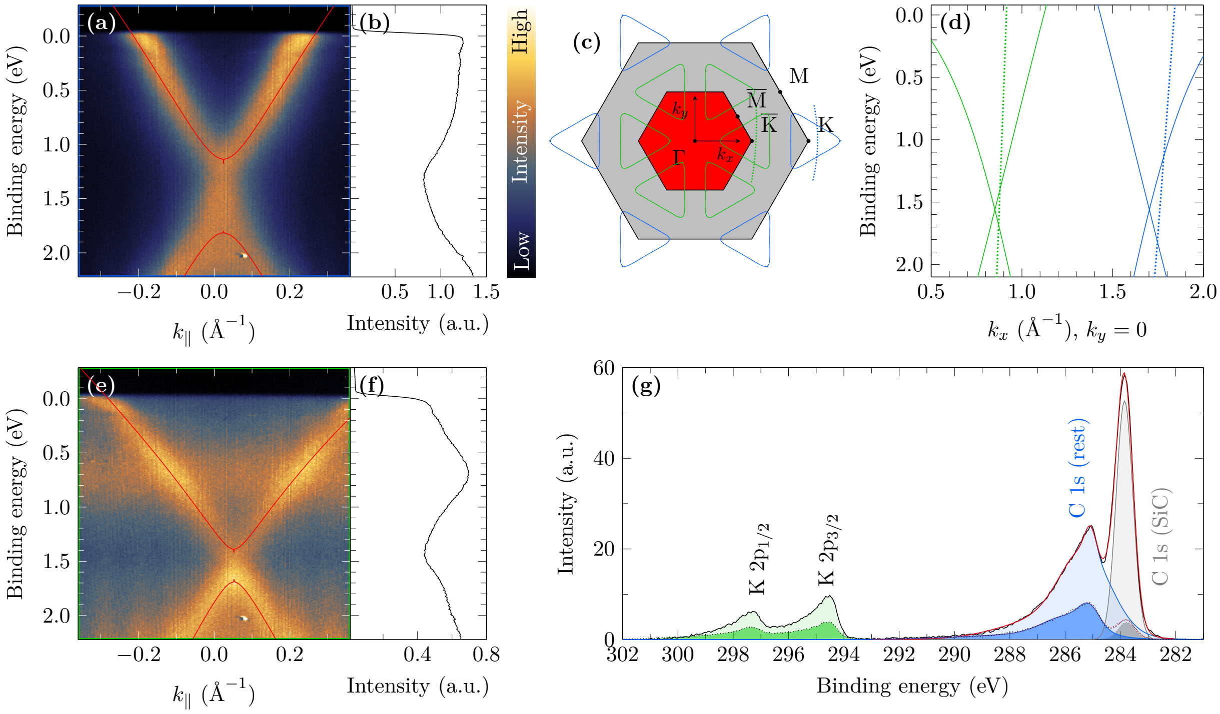

Figure A.11: (a) ARUPS near the K point ($\theta = 56.5°$, $\phi = -0.8°$) and (e) near the $\overline{\text{K}}$ point ($\theta = 24.5°$, $\phi = -3.5°$) of K-intercalated EMLG on SiC(0001) (cooled with liquid helium, resolution: 8.3 meV, 0.1° corresponding to $\approx 0.004\,\text{Å}^{-1}$) and respective sections from a 3NN TB calculation (red lines). Data are acquired from a different preparation cycle with slightly lower K content compared to data in fig. 4.15. (b) and (f) show the EDC of (a) and (e), respectively, integrated over all k values. (c) SBZ of epitaxial graphene (gray) and (2×2) superstructure with constant-energy contours at E_F calculated with a 3NN TB approach. Dotted lines depict the sections where the ARUPS data is acquired. (d) Related energy-dependent band structure and sections in ΓK direction. (g) XPS core level spectra of the C 1s and K 2p energy regions in normal (solid) and grazing (dotted) emission (0° and 70°).

A.12 XPS Data Analysis

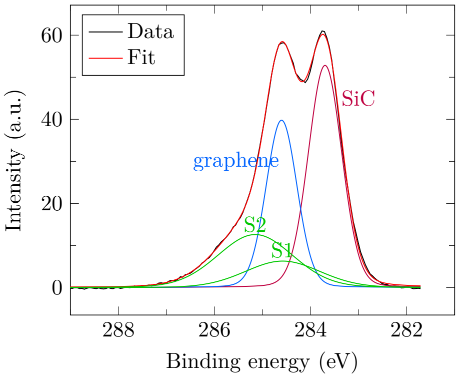

Figure A.12: XPS spectrum of the C 1s core level (black) and respective fit function (red) composed of four components originating from SiC (magenta), graphene (blue), and S1 and S2 (green) from the buffer layer along with a Shirley background (gray). From the ratio between graphene and SiC contributions a nominal graphene layer thickness of 2.0(1) ML above the buffer layer can be estimated.

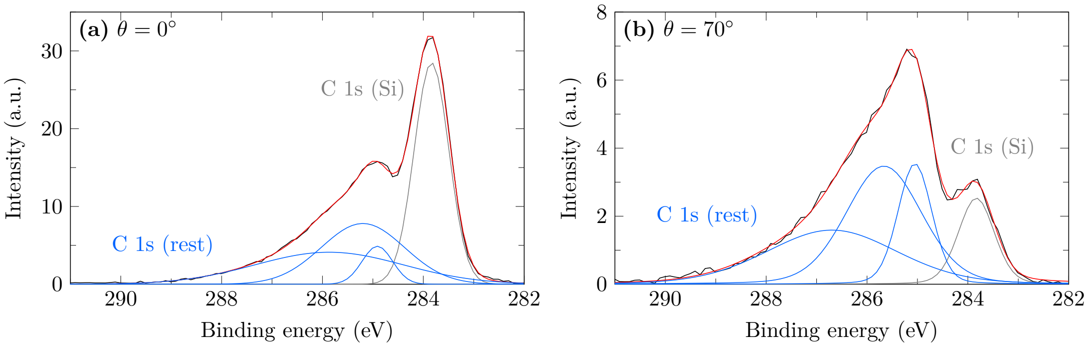

Figure A.13: XPS spectra of the C 1s core level (black) in (a) normal and (b) grazing emission also presented in fig. 4.15. For an accurate estimation of the K/C ratio, the spectrum is evaluated by a fit function (red) composed of four components. One component is precisely assignable to carbon in SiC (gray). The remaining components (blue) can be attributed to K-intercalated graphene, but the exact origin is unknown. Therefore, the components are summed up for the estimation of the K/C ratio.

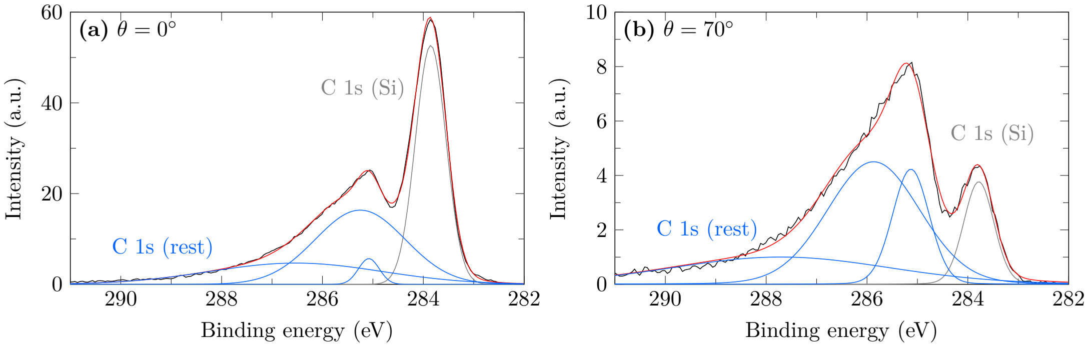

Figure A.14: Same as fig. A.13, but related to data in fig. A.11.

A.13 LEED Data of Different Samples

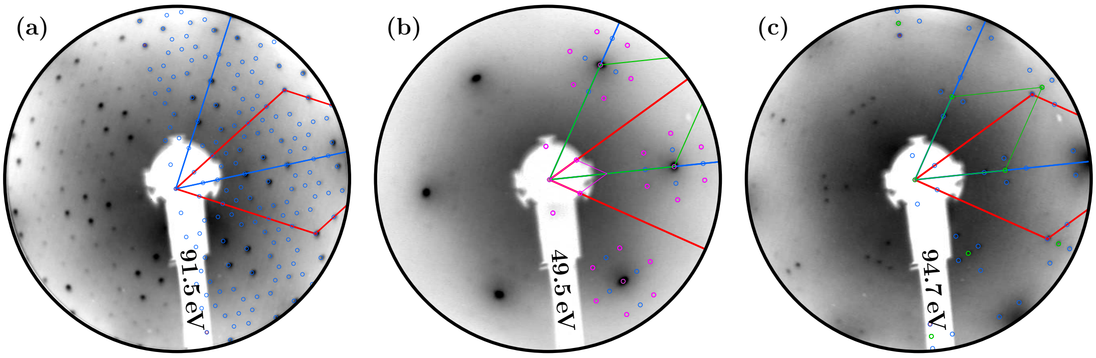

Figure A.15: (a) High-quality LEED image of epitaxial graphene of unknown thickness on SiC(0001). (b) and (c) LEED images of K-intercalated 2.0 ML epitaxial graphene on SiC(0001). Lines depict 2D reciprocal unit cells of SiC (red), graphene lattice (blue), and the (2 × 2) superstructure (green). Blue circles indicate spot positions of graphene and multiple scattering between graphene and SiC lattice. Magenta circles depict spot positions originating from multiple scattering processes between the (2 × 2) superstructure of K intercalants and the (6 × 6) superstructure of the buffer layer. Those features are only present for low K contents shown in (b) and vanish for higher K concentrations shown in (c). All images are plotted with inverted, logarithmically scaled intensities and are corrected for distortions.

A.14 STM Images Related to the dI/dV Map Acquisition

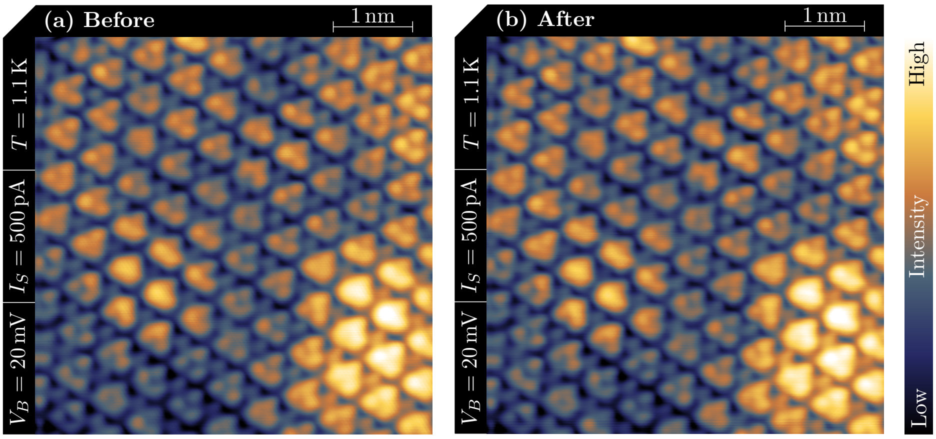

Figure A.16: STM images (a) before and (b) after the dI/dV map acquisition. Note that the spectroscopy measurements in between these two STM scans took about 11 hours.

A.15 Analysis of STS Data Acquired at Position 2

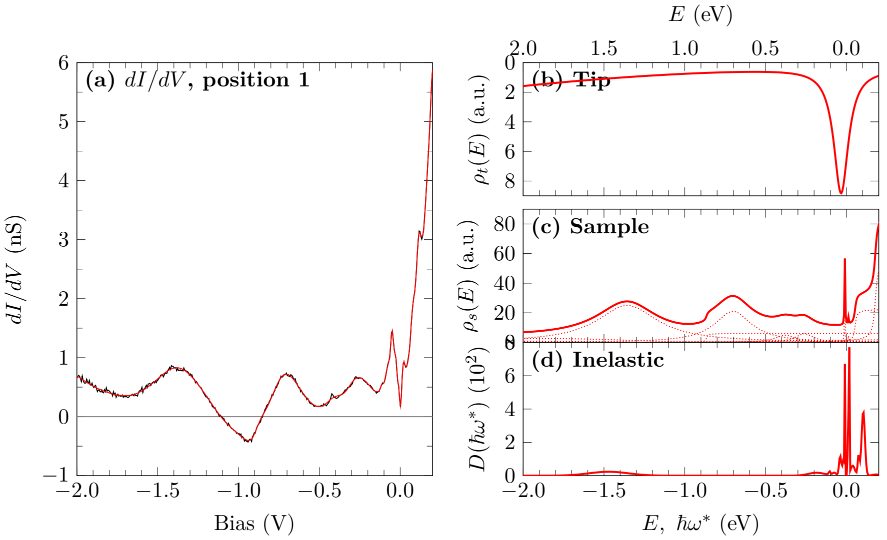

Figure A.17: (a) Wide-range dI/dV spectrum acquired at position 2 (black solid line) ($T = 1.2\,\mathrm{K}$, $I_s = 500\,\mathrm{pA}$ at $V_b = 200\,\mathrm{mV}$, $V_{\mathrm{mod}} = 5\,\mathrm{mV}$, 5 acc.). Fit result (red solid line) containing contributions of electronic DOS of (b) tip and (c) sample (individual sample DOS components depicted as red dotted lines) as well as (d) inelastic contributions.

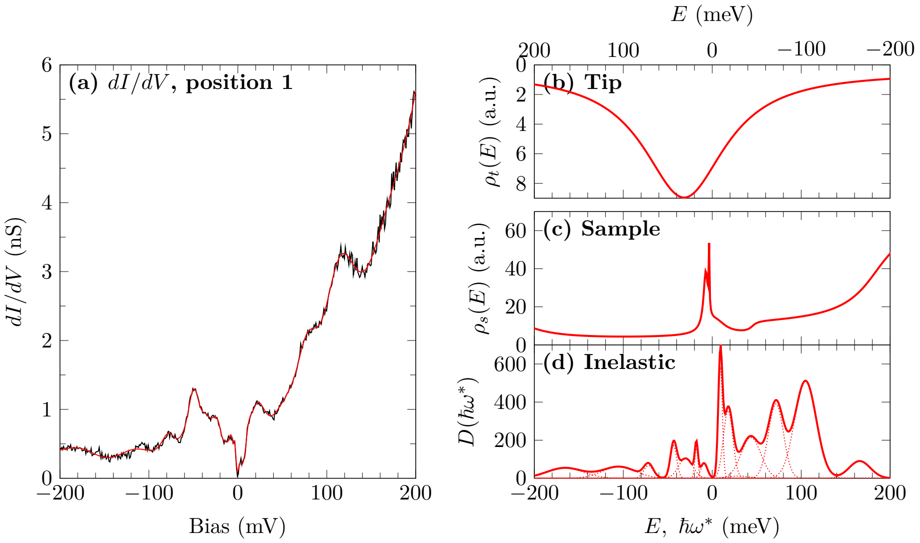

Figure A.18: (a) dI/dV spectrum covering the phonon range acquired at position 2 (black solid line) ($T = 1.2\,\mathrm{K}$, $I_s = 500\,\mathrm{pA}$ at $V_b = 200\,\mathrm{mV}$, $V_{\mathrm{mod}} = 1\,\mathrm{mV}$, 5 acc.). Fit result (red solid line) containing contributions of electronic DOS of (b) tip and (c) sample as well as (d) inelastic contributions (individual inelastic components depicted as red dotted lines).

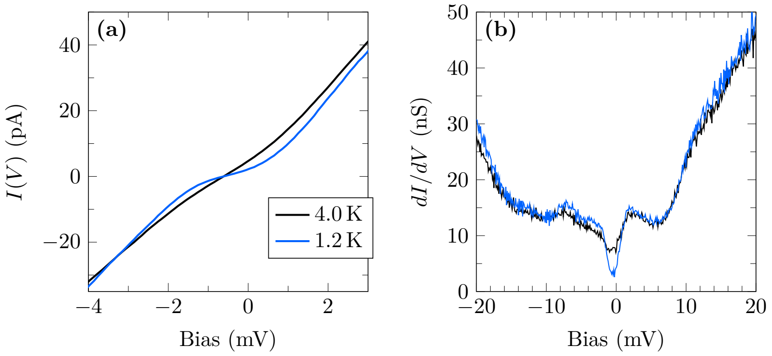

Figure A.19: Temperature-dependent (a) tunneling current and (b) scaled dI/dV spectrum acquired at position 2 ($T = 1.2\,\mathrm{K}$ (blue) and $4.0\,\mathrm{K}$ (black), $I_s = 500\,\mathrm{pA}$ at $V_b = 20\,\mathrm{mV}$, resistance of the tunneling junction $\approx 40\,\mathrm{M\Omega}$, $V_{\mathrm{mod}} = 0.1\,\mathrm{mV}$, 10 acc.).

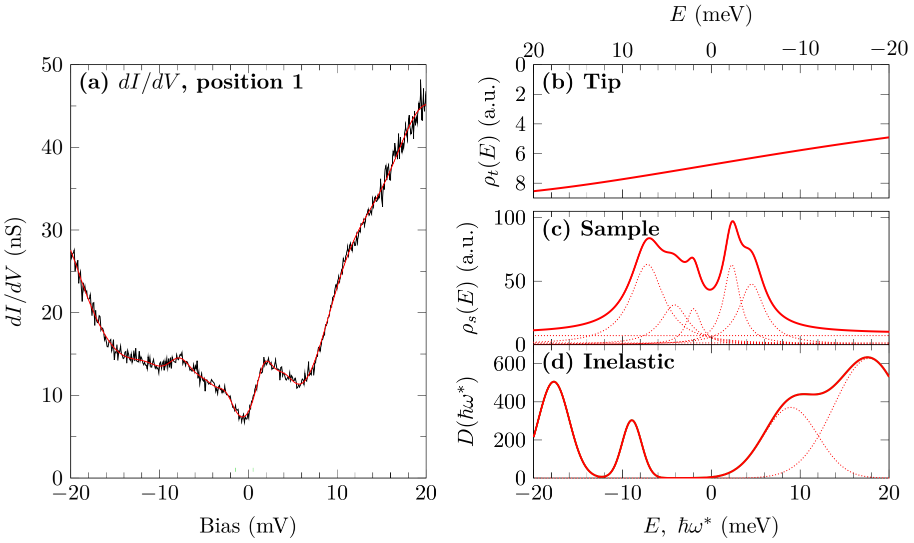

Figure A.20: (a) dI/dV spectrum of Fermi level region acquired at position 2 (black solid line) ($T = 3.9\,\mathrm{K}$, $I_s = 500\,\mathrm{pA}$ at $V_b = 20\,\mathrm{mV}$, Resistance of the tunneling junction $\approx 40\,\mathrm{M\Omega}$, $V_{\mathrm{mod}} = 0.1\,\mathrm{mV}$, 10 acc.). Fit result (red solid line) containing contributions of electronic DOS of (b) tip and (c) sample as well as (d) inelastic contributions (individual sample DOS and inelastic components depicted as red dotted lines).

A.16 Analysis of the Superconducting Energy Gap

A.16.1 Approaches for the Quantitative Analysis

Standard Approach with Lock-In Influence

For the first analysis of the energy gap at the Fermi level, the standard approach shown in eq. (3.21) is modified by accounting for broadening caused by the use of the lock-in technique. In accordance to refs. [160, 161] the normalized differential conductance in due consideration of the lock-in working principle is given by

$$\frac{G(V,T_i)}{G(V,T_n)} = \frac{1}{\rho_{t,nc}(E_{F,i})\rho_{s,nc}(E_{F,i})}\frac{2}{\pi V_{\text{mod}}}\int_{-\pi/2}^{\pi/2} d\alpha \sin(\alpha)\cdot I\left(V + V_{\text{mod}}\sin(\alpha), T_i; \Delta_i, \Gamma_i, E_{F,i}, A_i\right), \tag{A.26}$$

with

$$I\left(V, T_i; \Delta_i, \Gamma_i, E_{F,i}\right) \approx \int_{-\infty}^{\infty} \rho_{t,nc}(E_{F,i})\rho_{s,sc}(E; \Delta_i, \Gamma_i, E_{F,i}, A_i)\left[f(E-eV,T_i) - f(E,T_i)\right]dE, \tag{A.27}$$

where

$$\rho_{s,sc}(E; \Delta_i, \Gamma_i, E_{F,i}, A_i) = A_i\rho_{s,nc}(E_{F,i})\cdot\left|\text{Re}\left[\frac{E - E_{F,i} - i\Gamma_i}{\sqrt{(E - E_{F,i} - i\Gamma_i)^2 - \Delta_i^2}}\right]\right|. \tag{A.28}$$

The scaling factor A_i in the DOS of the superconducting state is introduced as additional fitting parameter that accounts for possible intensity deviations between a particular spectrum and the normalization spectrum that can originate from slight lateral variations of the tip positions during the data acquisition. The standard approach remains valid just for flat densities of states of tip ($\rho_{t,nc}(E) \approx \rho_{t,nc}(E_{F,i}) = \text{const.}$) and sample ($\rho_{s,nc}(E) \approx \rho_{s,nc}(E_{F,i}) = \text{const.}$) as well as a negligible spectral influence of the transmission function.

Modified Approach for Non-Flat Densities of States

In consideration of the non-flat contributions to the sample and tip DOS (cf. fig. 4.28) as well as the working principle of the lock-in technique, the normalized differential conductance is assumed as

$$\frac{G(V,T_i)}{G_n(V,T_i)} = \frac{\int_{-\pi/2}^{\pi/2} d\alpha \sin(\alpha) I_f\left(V_b + V_{\text{mod}}\sin(\alpha), T_i; \Delta_i, \Gamma_i, E_{F,i}, A_i\right)}{\int_{-\pi/2}^{\pi/2} d\alpha \sin(\alpha) I_n\left(V_b + V_{\text{mod}}\sin(\alpha), T_i\right)}, \tag{A.29}$$

with

$$\begin{aligned}
I_{f/n}(V,T_i) &= I_{\text{el.},f/n}(V,T_i) + I_{\text{inel.},+,f/n}(V,T_i) + I_{\text{inel.},-,f/n}(V,T_i)\\
&= \int_{-\infty}^{\infty} T(d,V,E)\rho_t(E-eV)\rho_{s,f/n}(E)\left[f(E-eV,T_i) - f(E,T_i)\right]dE\\
&+ \int_{-\infty}^{0} d\omega^* D(\omega^*)\\
&\int_{-\infty}^{\infty} T(d,V,E)f(E-eV,T_i)[1 - f(E-\hbar\omega^*,T_i)]\rho_t(E-eV)\rho_{s,f/n}(E-\hbar\omega^*)dE\\
&+ \int_{-\infty}^{0} d\omega^* D(\omega^*)\\
&\int_{-\infty}^{\infty} T(d,V,E)[1 - f(E-eV,T_i)]f(E-\hbar\omega^*,T_i)\rho_t(E-eV)\rho_{s,f/n}(E-\hbar\omega^*)dE.
\end{aligned} \tag{A.30}$$

The DOS function $\rho_{s,f}(E;\Delta_i,\Gamma_i,E_{F,i},A_i)$ that is defined by

$$\begin{aligned}\rho_{s,f}(E;\Delta_i,\Gamma_i,E_{F,i},A_i) =&A_i\rho_{s,n}\left(\operatorname{sgn}(E-E_{F,i})\cdot\operatorname{Re}\left[\sqrt{(E-E_{F,i}-i\Gamma_i)^2-\Delta_i^2}\right]+E_{F,i}\right) &\text{(A.31)}\\ &\cdot\left|\operatorname{Re}\left[\frac{E-E_{F,i}-i\Gamma_i}{\sqrt{(E-E_{F,i}-i\Gamma_i)^2-\Delta_i^2}}\right]\right| &\text{(A.32)}\end{aligned}$$

includes all the fitting parameters, and $\rho_{s,n}(E)$ is already known at 4.0 K (cf. fig. 4.28). The scaling factor A_i in the DOS of the superconducting state is already introduced in the standard approach. Note that the standard model normalizes the data measured at T_i by the spectrum $G_n(V,T_n)$ at the temperature T_n via

$$\frac{G(V,T_i)}{G_n(V,T_n)}=\frac{\int_{-\pi/2}^{\pi/2}d\alpha\sin(\alpha)I_f\left(V_b+V_{\text{mod}}\sin(\alpha),T_i;\Delta_i,\Gamma_i,E_{F,i},A_i\right)}{\int_{-\pi/2}^{\pi/2}d\alpha\sin(\alpha)I_n\left(V_b+V_{\text{mod}}\sin(\alpha),T_n\right)},\tag{A.33}$$

while the modified approach normalizes by the spectrum at the very same temperature T_i.

A.16.2 Analysis of Test Data with the Standard Approach

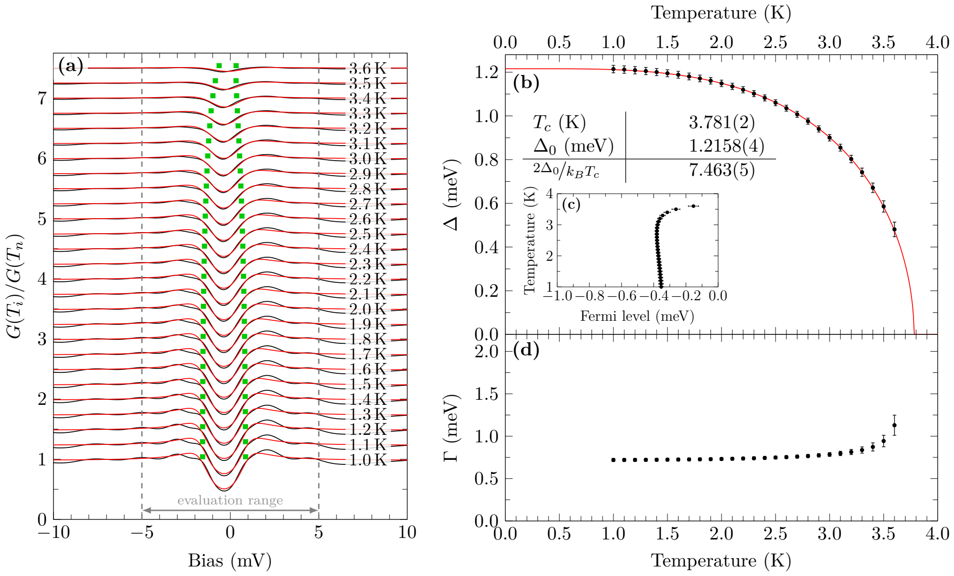

Figure A.21: (a) Temperature-dependent dI/dV spectra (black, y-shifted 0.25) of the model data set (cf. sec. 5.1) normalized by the spectrum at $T_n = 4.0\,\text{K}$ and corresponding fitted spectra using the standard approach (red). The total gap size $2\Delta(T_i)$ is depicted by green markers. Corresponding parameters determined from the fitting procedure are shown in (b), (c), and (d). $\Delta(T_i)$ is further fitted using eq. (2.5) (red line) to determine T_c, Δ_0, and the gap ratio as indicated in (b).

A.16.3 Quantitative Analysis with the Modified Approach

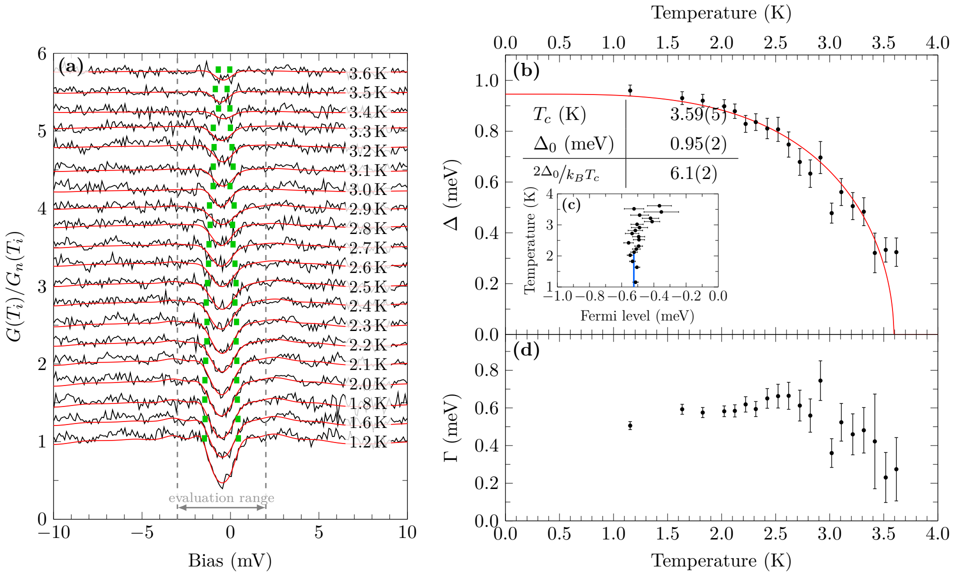

Figure A.22: (a) Temperature-dependent dI/dV spectra (black, position 1, y-shifted 0.25) normalized using the modified approach (G_n determined at 4.0 K) and corresponding fitted spectra (red) (both branches, Fermi level as fit parameter). The total gap size $2\Delta(T_i)$ is depicted by green markers. Corresponding parameters determined from the fitting procedure are shown in (b), (c), and (d). $\Delta(T_i)$ is further fitted using eq. (2.5) (red line) to determine T_c, Δ_0, and the gap ratio as indicated in (b). Blue line in (c) depicts the average Fermi level parameter $E_F = -0.52$ meV considering the values at the five lowest measured temperatures that is used as fixed parameter in further analyses. (Analysis of position 2 in fig. A.31.)

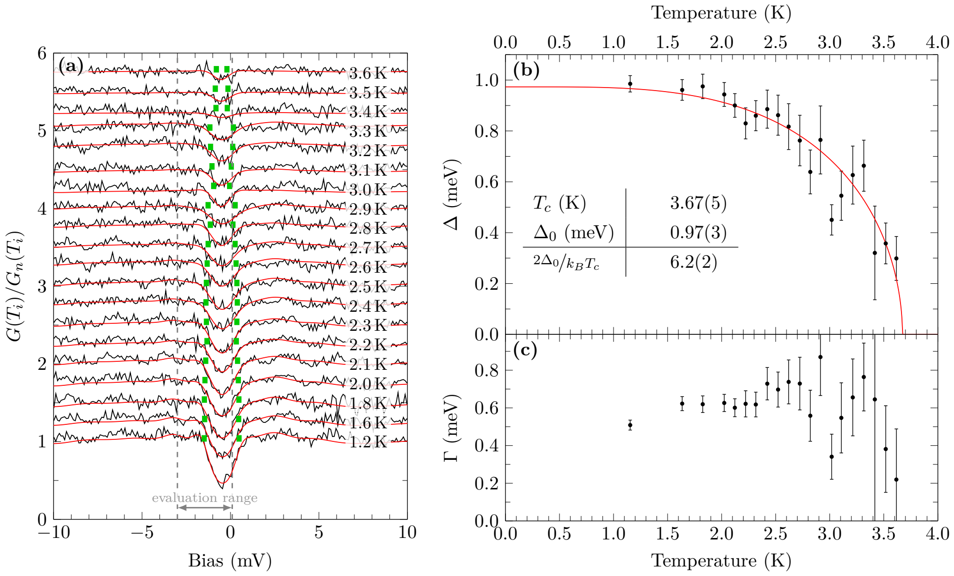

Figure A.23: (a) Temperature-dependent dI/dV spectra (black, position 1, y-shifted 0.25) normalized using the modified approach (G_n determined at 4.0 K) and corresponding fitted spectra (red) (left branch, Fermi level fixed to $E_F = -0.52$ meV as shown in fig. A.22). The total gap size $2\Delta(T_i)$ is depicted by green markers. Corresponding parameters determined from the fitting procedure are shown in (b) and (c). $\Delta(T_i)$ is further fitted using eq. 2.5 (red line) to determine T_c, Δ_0, and the gap ratio as indicated in (b). (Analysis of position 2 in fig. A.31.)

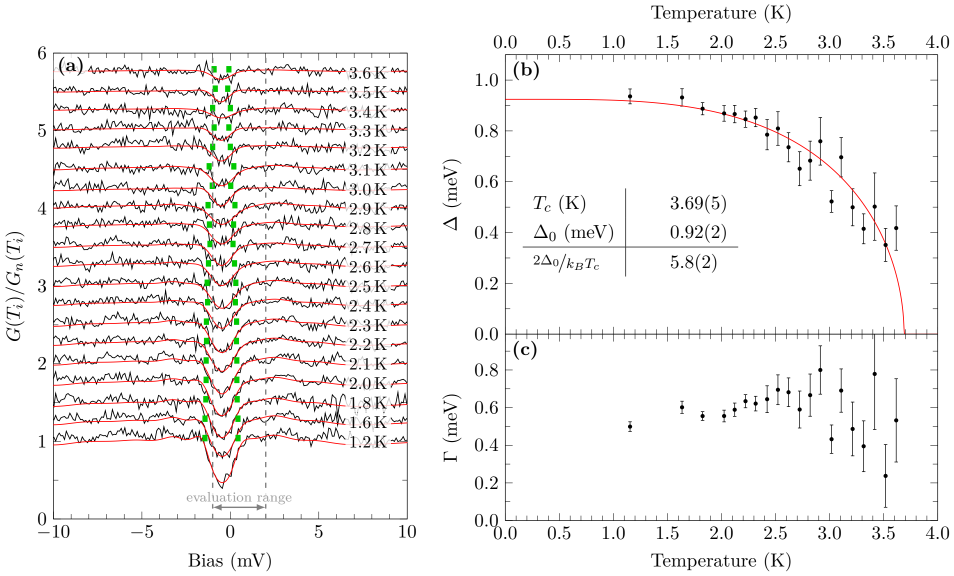

Figure A.24: (a) Temperature-dependent dI/dV spectra (black, position 1, y-shifted 0.25) normalized using modified approach (G_n determined at 4.0 K) and corresponding fitted spectra (red) (right branch, Fermi level fixed to $E_F = -0.52$ meV as shown in fig. A.22). The total gap size $2\Delta(T_i)$ is depicted by green markers. Corresponding parameters determined from the fitting procedure are shown in (b) and (c). $\Delta(T_i)$ is further fitted using eq. (2.5) (red line) to determine T_c, Δ_0, and the gap ratio as indicated in (b). (Analysis of position 2 in fig. A.31.)

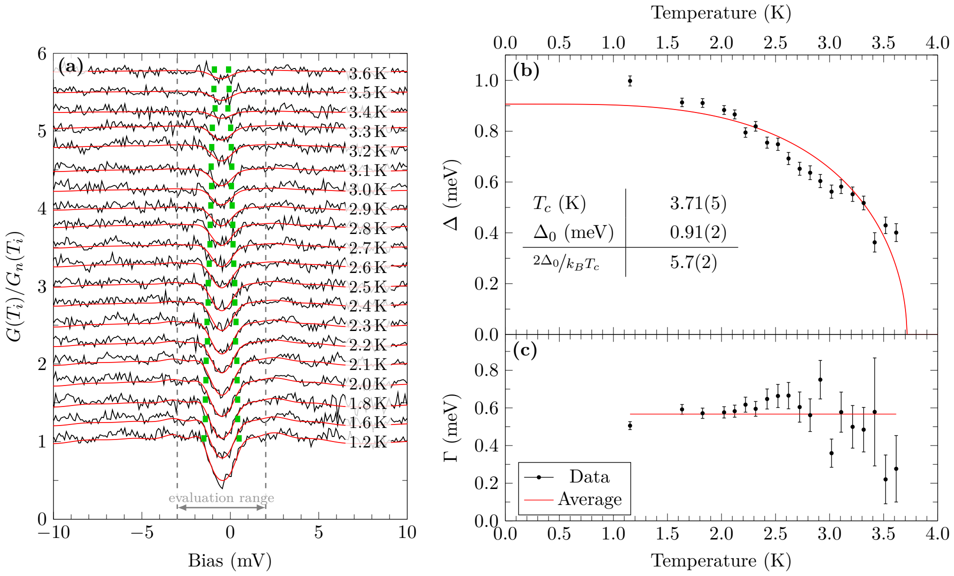

Figure A.25: (a) Temperature-dependent dI/dV spectra (black, position 1, y-shifted 0.25) normalized using the modified approach (G_n determined at 4.0 K) and corresponding fitted spectra (red) considering the average Γ value as fixed parameter as depicted by red line in (c) (both branches, Fermi level fixed to $E_F = -0.52$ meV as shown in fig. A.22). The total gap size $2\Delta(T_i)$ is depicted by green markers. Corresponding parameters determined from the fitting procedure are shown in (b) and (c). $\Delta(T_i)$ is further fitted using eq. (2.5) (red line) to determine T_c, Δ_0, and the gap ratio as indicated in (b). (Analysis of position 2 in fig. A.31.)

A.16.4 Data Acquired at Position 2

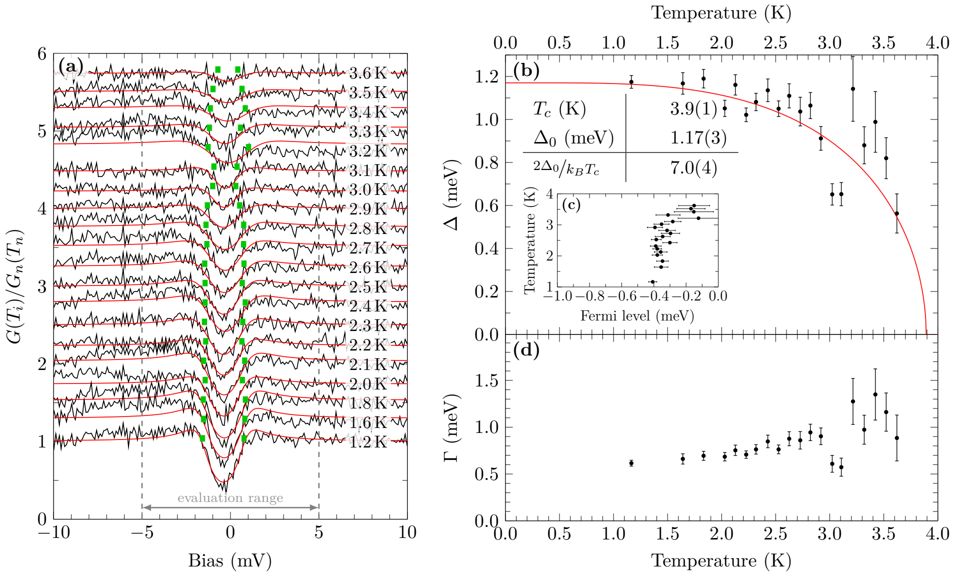

Figure A.26: (a) Temperature-dependent dI/dV spectra (black, position 2, y-shifted 0.25) normalized by the spectrum at $T_n = 4.0\,\mathrm{K}$ and corresponding fitted spectra (red) using the standard approach provided in app. A.16.1. The total gap size $2\Delta(T_i)$ is depicted by green markers. Corresponding parameters determined from the fitting procedure are shown in (b), (c), and (d). $\Delta(T_i)$ is further fitted using eq. (2.5) (red line) to determine T_c, Δ_0, and the gap ratio as indicated in (b).

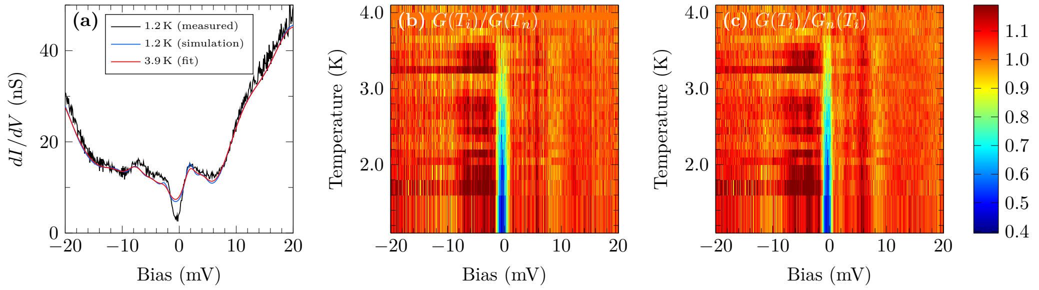

Figure A.27: (a) Comparison of measured (black) and simulated (blue) spectrum at 1.2 K (position 2) based on the DOS contributions determined at 3.9 K (red) (cf. fig. A.20). The normalized dI/dV spectra (b) and (c) depict the same data, but they are differently normalized using the standard and modified approach, respectively.

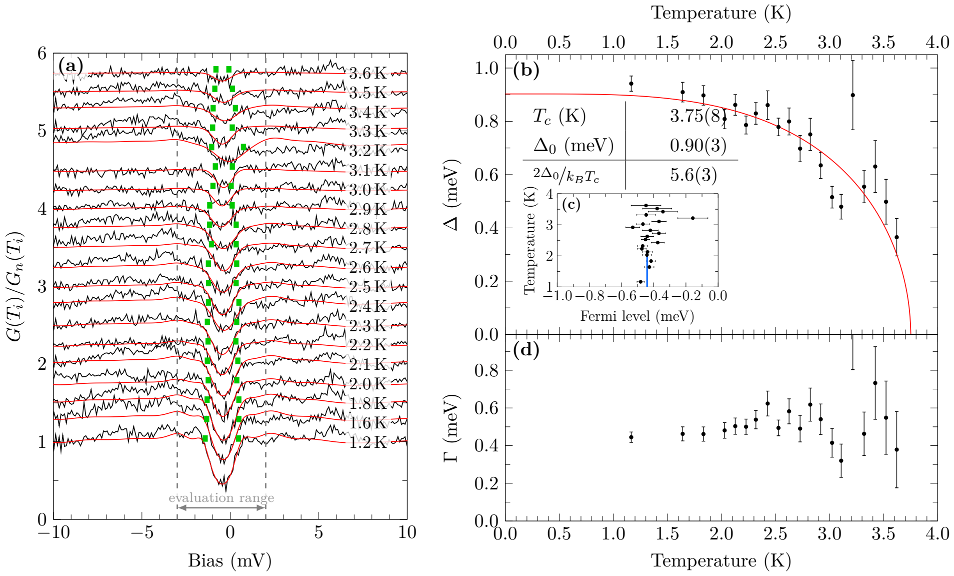

Figure A.28: (a) Temperature-dependent dI/dV spectra (black, position 2, y-shifted 0.25) normalized using the modified approach (G_n determined at 3.9 K) and corresponding fitted spectra (red) (both branches, Fermi level as fit parameter). The total gap size $2\Delta(T_i)$ is depicted by green markers. Corresponding parameters determined from the fitting procedure are shown in (b), (c), and (d). $\Delta(T_i)$ is further fitted using eq. (2.5) (red line) to determine T_c, Δ_0, and the gap ratio as indicated in (b). Blue line in (c) depicts the average Fermi level parameter $E_F = -0.44$ meV considering the values at the five lowest measured temperatures that is used as fixed parameter in further analyses.

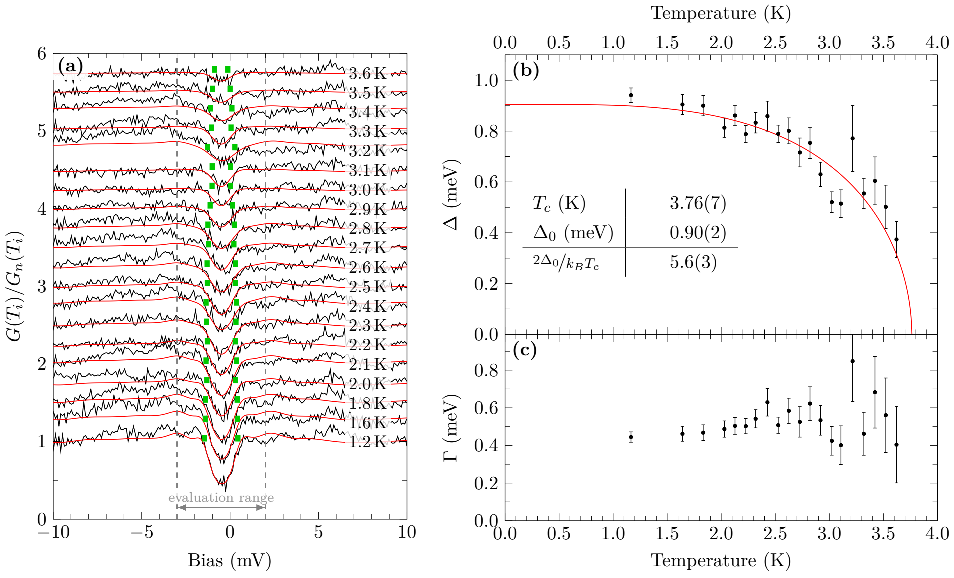

Figure A.29: (a) Temperature-dependent dI/dV spectra (black, position 2, y-shifted 0.25) normalized using the modified approach (G_n determined at 3.9 K) and corresponding fitted spectra (red) (both branches, Fermi level fixed to $E_F = -0.44$ meV as shown in fig. A.22). The total gap size $2\Delta(T_i)$ is depicted by green markers. Corresponding parameters determined from the fitting procedure are shown in (b) and (c). $\Delta(T_i)$ is further fitted using eq. (2.5) (red line) to determine T_c, Δ_0, and the gap ratio as indicated in (b).

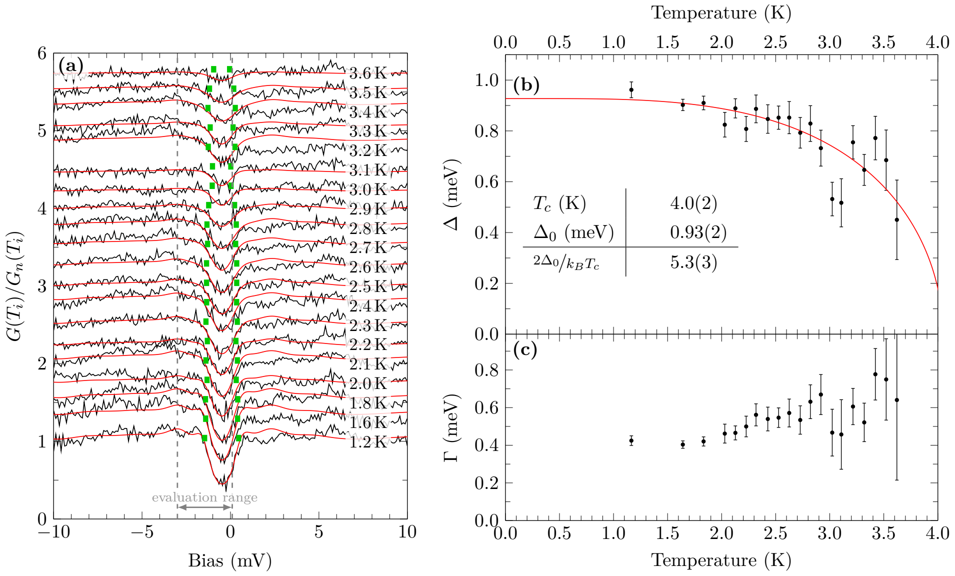

Figure A.30: (a) Temperature-dependent dI/dV spectra (black, position 2, y-shifted 0.25) normalized using the modified approach (G_n determined at 3.9 K) and corresponding fitted spectra (red) (left branch, Fermi level fixed to $E_F = -0.44$ meV as shown in fig. A.22). The total gap size $2\Delta(T_i)$ is depicted by green markers. Corresponding parameters determined from the fitting procedure are shown in (b) and (c). $\Delta(T_i)$ is further fitted using eq. (2.5) (red line) to determine T_c, Δ_0, and the gap ratio as indicated in (b).

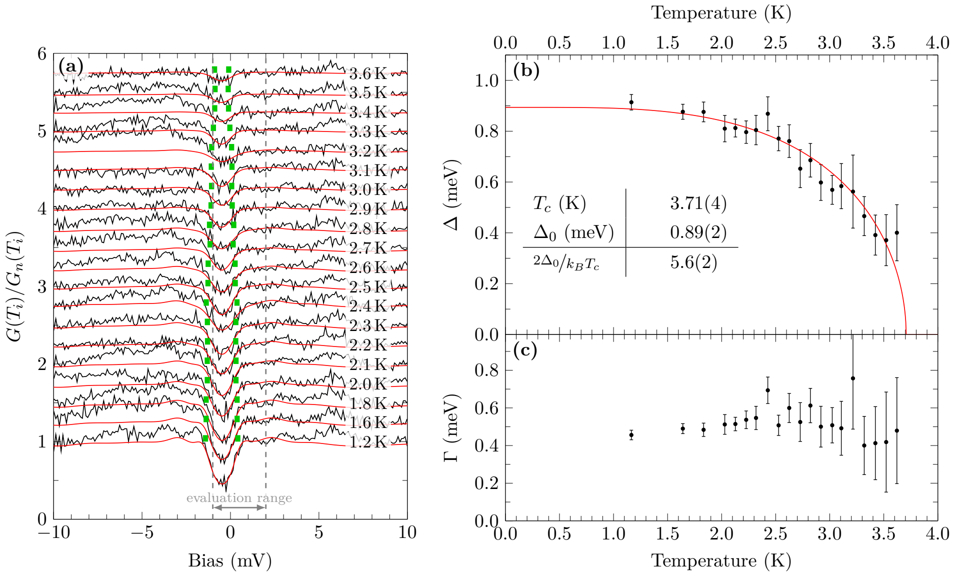

Figure A.31: (a) Temperature-dependent dI/dV spectra (black, position 2, y-shifted 0.25) normalized using the modified approach (G_n determined at 3.9 K) and corresponding fitted spectra (red) (right branch, Fermi level fixed to $E_F = -0.44$ meV as shown in fig. A.22). The total gap size $2\Delta(T_i)$ is depicted by green markers. Corresponding parameters determined from the fitting procedure are shown in (b) and (c). $\Delta(T_i)$ is further fitted using eq. (2.5) (red line) to determine T_c, Δ_0, and the gap ratio as indicated in (b).

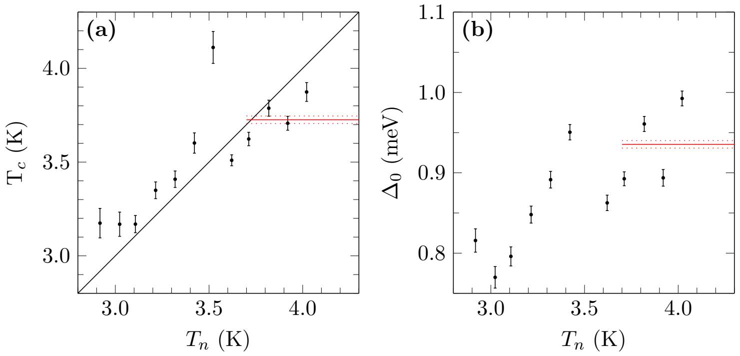

Figure A.32: (a) T_c and (b) Δ_0 determined for normalization by spectra at different T_n according to the modified approach assuming only the right branch of the tunneling data (position 2). Red solid lines depict the weighted average values for $T_n \geq 3.7\,\mathrm{K}$ and dotted lines the respective error margin.

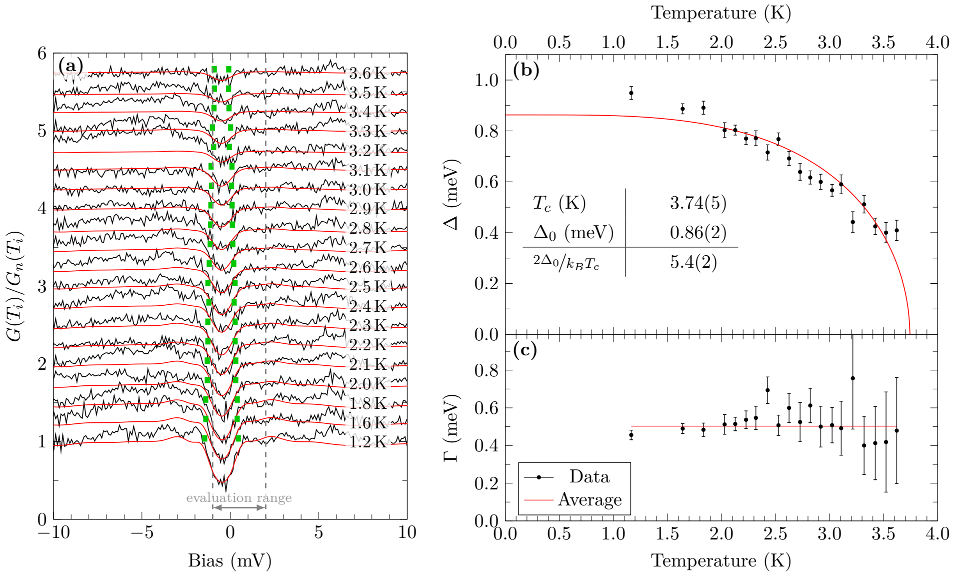

Figure A.33: (a) Temperature-dependent dI/dV spectra (black, position 2, y-shifted 0.25) normalized using the modified approach (G_n determined at 3.9 K) and corresponding fitted spectra (red) considering the average Γ value as fixed parameter as depicted by red line in (c) (both branches, Fermi level fixed to $E_F = -0.44\,\mathrm{meV}$ as shown in fig. A.22). The total gap size $2\Delta(T_i)$ is depicted by green markers. Corresponding parameters determined from the fitting procedure are shown in (b) and (c). $\Delta(T_i)$ is further fitted using eq. (2.5) (red line) to determine T_c, Δ_0, and the gap ratio as indicated in (b).

A.17 Determination of the EPC Strength

A.17.1 Supplementary Data

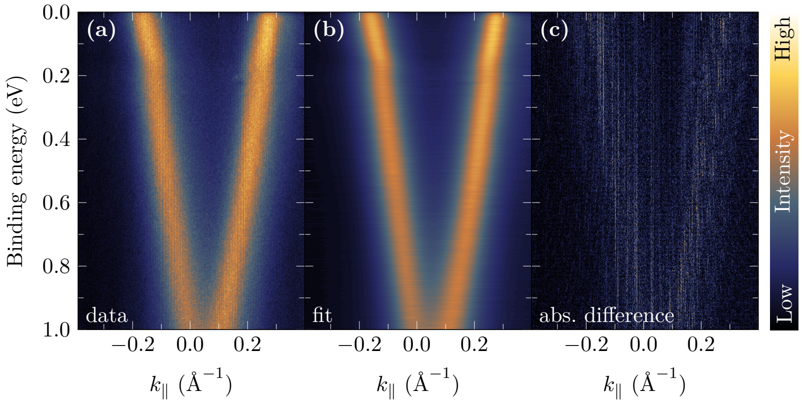

Figure A.34: Visual proof of the MDC fitting procedure. (a) depicts the measured data, (b) the data described by the fitting procedure, and (c) the absolute difference between (a) and (b). The difference is dominated by noise. Thus, the fit describes the measured data appropriately.

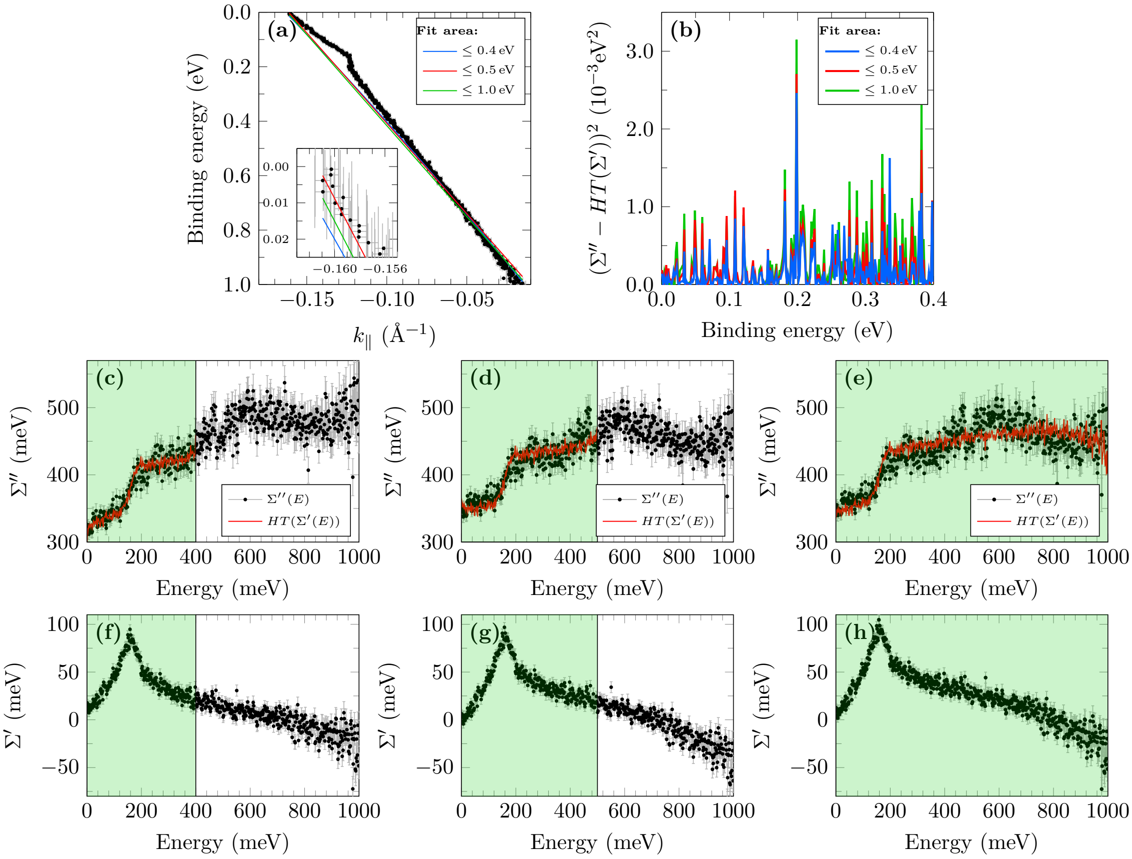

Figure A.35: (a) k_m (black dots with gray error bars) and estimated bare bands for different fit areas. (b) Squared deviation of the fit quantity for different fit areas. Imaginary parts upon self-consistent bare band estimation are given in (c)-(e) for different fitting areas (highlighted in green), based on related real parts in (f)-(h).

A.17.2 Second Method

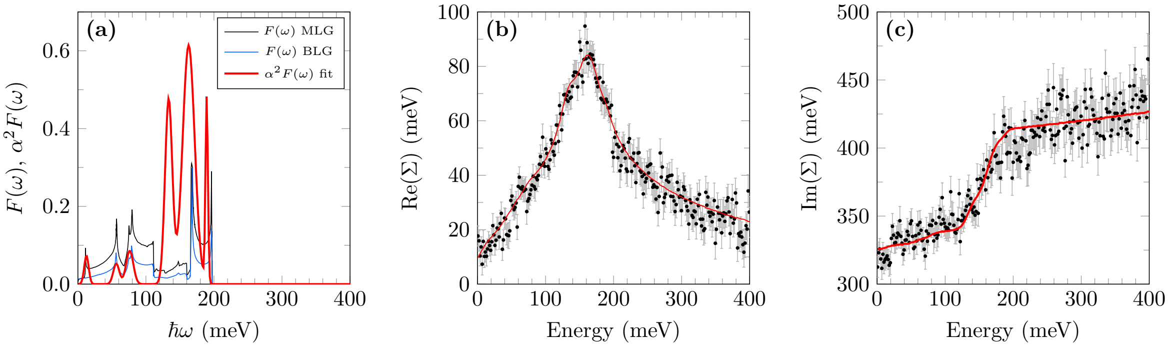

Figure A.36: (a) Eliashberg function $\alpha^2F(\omega)$ determined by using the modified description of the electron-hole interaction of K-intercalated EMLG suggested in ref. [86] compared to the calculated PhDOS $F(\omega)$ (scaled arbitrarily) of MLG and AB-stacked BLG from refs. [106,107]. (b) and (c) depict the data (black) and fit function (red) of the real and imaginary part of the self-energy, respectively. However, the total deviation between data and fit is enlarged compared to the description discussed in sec. 5.2.

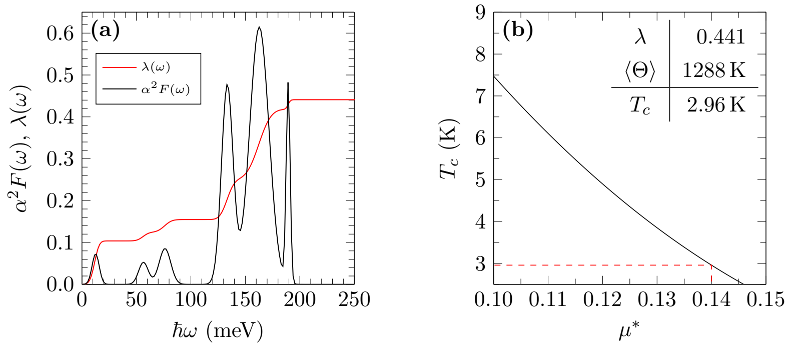

Figure A.37: (a) Eliashberg function $\alpha^2F(\omega)$ (black) and associated mass enhancement factor $\lambda(\omega)$ (red) as a function of phonon energy $\hbar\omega$ from the fitting procedure shown in fig. A.36. (b) Critical temperature T_c as a function of plausible values for the Coulomb pseudopotential μ^*. The red dashed line assigns the reported $\mu^* = 0.14$ value [11] to the corresponding T_c.

Bibliography

[1] Y. Cao, V. Fatemi, S. Fang, K. Watanabe, T. Taniguchi, E. Kaxiras, and P. Jarillo-Herrero: *Unconventional superconductivity in magic-angle graphene superlattices.* Nature **556**, 43 (2018).

[2] M. Yankowitz, S. Chen, H. Polshyn, Y. Zhang, K. Watanabe, T. Taniguchi, D. Graf, A. F. Young, and C. R. Dean: *Tuning superconductivity in twisted bilayer graphene.* Science **363**, 1059 (2019).

[3] T. E. Weller, M. Ellerby, S. S. Saxena, R. P. Smith, and N. T. Skipper: *Superconductivity in the intercalated graphite compounds* C_6Yb *and* C_6Ca. Nat. Phys. **1**, 39–41 (2005).

[4] N. Emery, C. Hérold, M. d'Astuto, V. Garcia, C. Bellin, J. F. Marêché, P. Lagrange, and G. Loupias: *Superconductivity of Bulk* CaC_6. Phys. Rev. Lett. **95**, 087003 (2005).

[5] K. Li, X. Feng, W. Zhang, Y. Ou, L. Chen, K. He, L.-L. Wang, L. Guo, G. Liu, Q.-K. Xue, and X. Ma: *Superconductivity in Ca-intercalated epitaxial graphene on silicon carbide.* Appl. Phys. Lett. **103**, 062601 (2013).

[6] S. Ichinokura, K. Sugawara, A. Takayama, T. Takahashi, and S. Hasegawa: *Superconducting Calcium-Intercalated Bilayer Graphene.* ACS Nano **10**, 2761–2765 (2016).

[7] S. Ichinokura: *Intercalation Compounds of Bilayer Graphene.* In: *Observation of Superconductivity in Epitaxially Grown Atomic Layers: In Situ Electrical Transport Measurements*, 93–113. Springer Singapore, Singapore (2018).

[8] A. P. Tiwari, S. Shin, E. Hwang, S.-G. Jung, T. Park, and H. Lee: *Superconductivity at 7.4 K in few layer graphene by Li-intercalation.* J. Phys.: Condens. Matter **29**, 445701 (2017).

[9] N. B. Hannay, T. H. Geballe, B. T. Matthias, K. Andres, P. Schmidt, and D. MacNair: *Superconductivity in Graphitic Compounds.* Phys. Rev. Lett. **14**, 225–226 (1965).

[10] M. Xue, G. Chen, H. Yang, Y. Zhu, D. Wang, J. He, and T. Cao: *Superconductivity in Potassium-Doped Few-Layer Graphene.* J. Am. Chem. Soc. **134**, 6536–6539 (2012).

[11] M. Calandra and F. Mauri: *Theoretical Explanation of Superconductivity in* $\mathrm{C_6Ca}$. Phys. Rev. Lett. **95**, 237002 (2005).

[12] A. Grüneis, C. Attaccalite, A. Rubio, D. V. Vyalikh, S. L. Molodtsov, J. Fink, R. Follath, W. Eberhardt, B. Büchner, and T. Pichler: *Electronic structure and electron-phonon coupling of doped graphene layers in* KC_8. Phys. Rev. B **79**, 205106 (2009).

[13] I. Mazin: *Intercalant-Driven Superconductivity in* YbC_6 *and* CaC_6. Phys. Rev. Lett. **95**, 227001 (2005).

[14] T. Valla, J. Camacho, Z.-H. Pan, A. V. Fedorov, A. C. Walters, C. A. Howard, and M. Ellerby: *Anisotropic Electron-Phonon Coupling and Dynamical Nesting on the Graphene Sheets in Superconducting* $\mathrm{CaC_6}$ *using Angle-Resolved Photoemission Spectroscopy.* Phys. Rev. Lett. **102**, 107007 (2009).

[15] G. Csányi, P. B. Littlewood, A. H. Nevidomskyy, C. J. Pickard, and B. D. Simons: *The role of the interlayer state in the electronic structure of superconducting graphite intercalated compounds.* Nat. Phys. **1**, 42–45 (2005).

[16] D. Haberer, L. Petaccia, A. V. Fedorov, C. S. Praveen, S. Fabris, S. Piccinin, O. Vilkov, D. V. Vyalikh, A. Preobrajenski, N. I. Verbitskiy, H. Shiozawa, J. Fink, M. Knupfer, B. Büchner, and A. Grüneis: *Anisotropic Eliashberg function and electron-phonon coupling in doped graphene.* Phys. Rev. B **88**, 081401 (2013).

[17] K. Sugawara, T. Sato, and T. Takahashi: *Fermi-surface-dependent superconducting gap in* C_6Ca. Nat. Phys. **5**, 40–43 (2009).

[18] N. Bergeal, V. Dubost, Y. Noat, W. Sacks, D. Roditchev, N. Emery, C. Herold, J.-F. Mareche, P. Lagrange, and G. Loupias: *Scanning Tunneling Spectroscopy on the Novel Superconductor* $\mathrm{CaC_6}$. Phys. Rev. Lett. **97**, 077003 (2006).

[19] C. Kurter, L. Ozyuzer, D. Mazur, J. F. Zasadzinski, D. Rosenmann, H. Claus, D. G. Hinks, and K. E. Gray: *Large energy gaps in* CaC_6 *from tunneling spectroscopy: Possible evidence of strong-coupling superconductivity.* Phys. Rev. B **76** (2007).

[20] R. W. Lynch and H. G. Drickamer: *Effect of High Pressure on the Lattice Parameters of Diamond, Graphite, and Hexagonal Boron Nitride.* J. Chem. Phys. **44**, 181–184 (1966).

[21] A. H. Castro Neto, F. Guinea, N. M. R. Peres, K. S. Novoselov, and A. K. Geim: *The electronic properties of graphene.* Rev. Mod. Phys. **81**, 109–162 (2009).

[22] C. Riedl, C. Coletti, and U. Starke: *Structural and electronic properties of epitaxial graphene on SiC(0001): a review of growth, characterization, transfer doping and hydrogen intercalation.* J. Phys. D: Appl. Phys. **43**, 374009 (2010).

[23] T. Ohta, A. Bostwick, T. Seyller, K. Horn, and E. Rotenberg: *Controlling the Electronic Structure of Bilayer Graphene.* Science **313**, 951–954 (2006).

[24] P. R. Wallace: *The Band Theory of Graphite.* Phys. Rev. **71**, 622–634 (1947).

[25] E. McCann and V. I. Fal'ko: *Landau-Level Degeneracy and Quantum Hall Effect in a Graphite Bilayer.* Phys. Rev. Lett. **96**, 086805 (2006).

[26] J. D. Bernal and W. L. Bragg: *The structure of graphite.* Proc. R. Soc. A **106**, 749–773 (1924).

[27] R. Peierls: *Bemerkungen über Umwandlungstemperaturen.* Helv. Phys. Acta **7**, 81–83 (1934).

[28] R. Peierls: *Quelques proprietes typiques des corpses solides.* Ann. I. H. Poincare **5**, 177–222 (1935).

[29] K. S. Novoselov, D. Jiang, F. Schedin, T. J. Booth, V. V. Khotkevich, S. V. Morozov, and A. K. Geim: *Two-dimensional atomic crystals.* Proc. Natl. Acad. Sci. U. S. A. **102**, 10451–10453 (2005).

[30] H. C. Lee, W.-W. Liu, S.-P. Chai, A. R. Mohamed, A. Aziz, C.-S. Khe, N. S. Hidayah, and U. Hashim: *Review of the synthesis, transfer, characterization and growth mechanisms of single and multilayer graphene.* RSC Adv. **7**, 15644–15693 (2017).

[31] C. Riedl, C. Coletti, T. Iwasaki, A. A. Zakharov, and U. Starke: *Quasi-Free-Standing Epitaxial Graphene on SiC Obtained by Hydrogen Intercalation.* Phys. Rev. Lett. **103**, 246804 (2009).

[32] K. V. Emtsev, A. Bostwick, K. Horn, J. Jobst, G. L. Kellogg, L. Ley, J. L. McChesney, T. Ohta, S. A. Reshanov, J. Röhrl, E. Rotenberg, A. K. Schmid, D. Waldmann, H. B. Weber, and T. Seyller: *Towards wafer-size graphene layers by atmospheric pressure graphitization of silicon carbide.* Nat. Mater. **8**, 203–207 (2009).

[33] S. Schreiber: *Untersuchungen zum epitaktischen Wachstum von 3C-SiC bei Verwendung einer C60-Kohlenstoffquelle.* Dissertation, Universität Augsburg (2006).

[34] A. Taylor and R. M. Jones: *Silicon Carbide - A High Temperature Semiconductor.* Pergamon Press, New York (1960).

[35] I. Forbeaux, J.-M. Themlin, and J.-M. Debever: *Heteroepitaxial graphite on 6H-SiC(0001): Interface formation through conduction-band electronic structure.* Phys. Rev. B **58**, 16396–16406 (1998).

[36] K. V. Emtsev, F. Speck, T. Seyller, L. Ley, and J. D. Riley: *Interaction, growth, and ordering of epitaxial graphene on SiC*{0001} *surfaces: A comparative photoelectron spectroscopy study.* Phys. Rev. B **77**, 155303 (2008).

[37] S. Kim, J. Ihm, H. J. Choi, and Y.-W. Son: *Origin of Anomalous Electronic Structures of Epitaxial Graphene on Silicon Carbide.* Phys. Rev. Lett. **100**, 176802 (2008).

[38] F. Varchon, P. Mallet, J.-Y. Veuillen, and L. Magaud: *Ripples in epitaxial graphene on the Si-terminated SiC(0001) surface.* Phys. Rev. B **77**, 235412 (2008).

[39] C. Riedl, U. Starke, J. Bernhardt, M. Franke, and K. Heinz: *Structural properties of the graphene-SiC(0001) interface as a key for the preparation of homogeneous large-terrace graphene surfaces.* Phys. Rev. B **76**, 245406 (2007).

[40] W. Chen, H. Xu, L. Liu, X. Gao, D. Qi, G. Peng, S. C. Tan, Y. Feng, K. P. Loh, and A. T. S. Wee: *Atomic structure of the 6H–SiC(0001) nanomesh.* Surf. Sci. **596**, 176–186 (2005).

[41] A. Bostwick, T. Ohta, J. L. McChesney, K. V. Emtsev, T. Seyller, K. Horn, and E. Rotenberg: *Symmetry breaking in few layer graphene films.* New J. Phys. **9**, 385 (2007).

[42] D. Marchenko, D. V. Evtushinsky, E. Golias, A. Varykhalov, T. Seyller, and O. Rader: *Extremely flat band in bilayer graphene.* Sci. Adv. **4**, eaau0059 (2018).

[43] A. Bostwick, K. Emtsev, K. Horn, E. Huwald, L. Ley, J. McChesney, T. Ohta, J. Riley, E. Rotenberg, F. Speck, and T. Seyller: *Photoemission Studies of Graphene on SiC: Growth, Interface, and Electronic Structure.* Adv. Solid State Phys. **47**, 159–170 (2008).

[44] I. Razado-Colambo, J. Avila, D. Vignaud, S. Godey, X. Wallart, D. P. Woodruff, and M. C. Asensio: *Structural determination of bilayer graphene on SiC(0001) using synchrotron radiation photoelectron diffraction.* Sci. Rep. **8**, 10190 (2018).

[45] K. S. Kim, T.-H. Kim, A. L. Walter, T. Seyller, H. W. Yeom, E. Rotenberg, and A. Bostwick: *Visualizing Atomic-Scale Negative Differential Resistance in Bilayer Graphene.* Phys. Rev. Lett. **110**, 036804 (2013).

[46] M. Kim, H. C. Choi, J. H. Shim, and B. I. Min: *Correlated electronic structures and the phase diagram of hydrocarbon-based superconductors.* New J. Phys. **15**, 113030 (2013).

[47] F. Guinea: *Charge distribution and screening in layered graphene systems.* Phys. Rev. B **75**, 235433 (2007).

[48] C. Haberstroh, R. Helbig, and R. A. Stein: *Some new features of the photoluminescence of SiC(6H), SiC(4H), and SiC(15R)c.* J. Appl. Phys. **76**, 509–513 (1994).

[49] J. B. Casady and R. W. Johnson: *Status of silicon carbide (SiC) as a wide-bandgap semiconductor for high-temperature applications: A review.* Solid-State Electron. **39**, 1409–1422 (1996).

[50] T. Seyller, K. V. Emtsev, F. Speck, K.-Y. Gao, and L. Ley: *Schottky barrier between 6H-SiC and graphite: Implications for metal/SiC contact formation.* Appl. Phys. Lett. **88**, 242103 (2006).

[51] Y. Zhang, T.-T. Tang, C. Girit, Z. Hao, M. C. Martin, A. Zettl, M. F. Crommie, Y. R. Shen, and F. Wang: *Direct observation of a widely tunable bandgap in bilayer graphene.* Nature **459**, 820–823 (2009).

[52] C. Coletti, C. Riedl, D. S. Lee, B. Krauss, L. Patthey, K. von Klitzing, J. H. Smet, and U. Starke: *Charge neutrality and band-gap tuning of epitaxial graphene on SiC by molecular doping.* Phys. Rev. B **81**, 235401 (2010).

[53] C. Coletti, C. Riedl, D. S. Lee, B. Krauss, L. Patthey, K. von Klitzing, J. H. Smet, and U. Starke: *Charge neutrality and band-gap tuning of epitaxial graphene on SiC by molecular doping.* Physical Review B **81** (2010).

[54] N. Briggs, Z. M. Gebeyehu, A. Vera, T. Zhao, K. Wang, A. De La Fuente Duran, B. Bersch, T. Bowen, K. L. Knappenberger, and J. A. Robinson: *Epitaxial graphene/silicon carbide intercalation: a minireview on graphene modulation and unique 2D materials.* Nanoscale **11**, 15440–15447 (2019).

[55] Y. Li, Y. Lu, P. Adelhelm, M.-M. Titirici, and Y.-S. Hu: *Intercalation chemistry of graphite: alkali metal ions and beyond.* Chem. Soc. Rev. **48**, 4655–4687 (2019).

[56] J. Algdal, T. Balasubramanian, M. Breitholtz, T. Kihlgren, and L. Walldén: *Thin graphite overlayers: Graphene and alkali metal intercalation.* Surf. Sci. **601**, 1167–1175 (2007).

[57] J. Kleeman, K. Sugawara, T. Sato, and T. Takahashi: *Direct evidence for a metallic interlayer band in Rb-intercalated bilayer graphene.* Phys. Rev. B **87**, 195401 (2013).

[58] K. Kanetani, K. Sugawara, T. Sato, R. Shimizu, K. Iwaya, T. Hitosugi, and T. Takahashi: *Ca intercalated bilayer graphene as a thinnest limit of superconducting* C_6Ca*.* Proc. Nat. Acad. Sci. **109**, 19610–19613 (2012).

[59] A. V. Fedorov, N. I. Verbitskiy, D. Haberer, C. Struzzi, L. Petaccia, D. Usachov, O. Y. Vilkov, D. V. Vyalikh, J. Fink, M. Knupfer, B. Büchner, and A. Grüneis: *Observation of a universal donor-dependent vibrational mode in graphene.* Nat. Commun. **5**, 3257 (2014).

[60] T. Haber, R. Resel, A. Thierry, M. Campione, A. Sassella, and M. Moret: *Epitaxially grown sexiphenyl nanocrystals on the organic KAP(010) surface.* Physica E **41**, 133–137 (2008).

[61] M. Bianchi, E. D. L. Rienks, S. Lizzit, A. Baraldi, R. Balog, L. Hornekaer, and P. Hofmann: *Electron-phonon coupling in potassium-doped graphene: Angle-resolved photoemission spectroscopy.* Phys. Rev. B **81**, 041403 (2010).

[62] W. J. Shin, S. W. Jung, Y. Sohn, S. H. Ryu, M. Huh, and K. S. Kim: *Electron-phonon coupling in the ordered phase of Rb on monolayer graphene.* Curr. Appl Phys. **20**, 484–488 (2020).

[63] Y. Guo, Y. Wei, H. Li, and T. Zhai: *Layer Structured Materials for Advanced Energy Storage and Conversion.* Small **13**, 1701649 (2017).

[64] Y. Koike, S.-i. Tanuma, H. Suematsu, and K. Higuchi: *Superconductivity in the graphite-potassium intercalation compound* C_8K. Journal of Physics and Chemistry of Solids **41**, 1111–1118 (1980).

[65] N. Emery, C. Herold, J.-F. Mareche, and P. Lagrange: *Synthesis and superconducting properties of* CaC_6. Science and Technology of Advanced Materials **9**, 044102 (2008).

[66] T. Kaneko and R. Saito: *First-principles study on interlayer state in alkali and alkaline earth metal atoms intercalated bilayer graphene.* Surf. Sci. **665**, 1–9 (2017).

[67] T. P. Kaloni, M. U. Kahaly, Y. C. Cheng, and U. Schwingenschlögl: *K-intercalated carbon systems: Effects of dimensionality and substrate.* Europhys. Lett. **98**, 67003 (2012).

[68] K. Ji, J. Han, A. Hirata, T. Fujita, Y. Shen, S. Ning, P. Liu, H. Kashani, Y. Tian, Y. Ito, J.-i. Fujita, and Y. Oyama: *Lithium intercalation into bilayer graphene.* Nat. Commun. **10**, 275 (2019).

[69] K. Sugawara, K. Kanetani, T. Sato, and T. Takahashi: *Fabrication of Li-intercalated bilayer graphene.* AIP Adv. **1**, 022103 (2011).

[70] Y. Endo, Y. Fukaya, I. Mochizuki, A. Takayama, T. Hyodo, and S. Hasegawa: *Structure of superconducting Ca-intercalated bilayer Graphene/SiC studied using total-reflection high-energy positron diffraction.* Carbon **157**, 857–862 (2020).

[71] T. A. de Jong, E. E. Krasovskii, C. Ott, R. M. Tromp, S. J. van der Molen, and J. Jobst: *Intrinsic stacking domains in graphene on silicon carbide: A pathway for intercalation.* Phys. Rev. Materials **2**, 104005 (2018).

[72] Z.-H. Pan, J. Camacho, M. H. Upton, A. V. Fedorov, C. A. Howard, M. Ellerby, and T. Valla: *Electronic Structure of Superconducting* $\mathrm{KC_8}$ *and Nonsuperconducting* $\mathrm{LiC_6}$ *Graphite Intercalation Compounds: Evidence for a Graphene-Sheet-Driven Superconducting State.* Phys. Rev. Lett. **106**, 187002 (2011).

[73] J. Kleeman, K. Sugawara, T. Sato, and T. Takahashi: *Anisotropic Electron-Phonon Coupling in Rb-Intercalated Bilayer Graphene.* J. Phys. Soc. Jpn. **83**, 124715 (2014).

[74] S.-L. Yang, J. A. Sobota, C. A. Howard, C. J. Pickard, M. Hashimoto, D. H. Lu, S.-K. Mo, P. S. Kirchmann, and Z.-X. Shen: *Superconducting graphene sheets in* CaC_6 *enabled by phonon-mediated interband interactions.* Nat. Commun. **5**, 3493 (2014).

[75] C. Virojanadara, S. Watcharinyanon, A. A. Zakharov, and L. I. Johansson: *Epitaxial graphene on* 6*H-SiC and Li intercalation.* Phys. Rev. B **82** (2010).

[76] N. M. Caffrey, L. I. Johansson, C. Xia, R. Armiento, I. A. Abrikosov, and C. Jacobi: *Structural and electronic properties of Li-intercalated graphene on SiC(0001).* Phys. Rev. B **93** (2016).

[77] S. Watcharinyanon, C. Virojanadara, and L. Johansson: *Rb and Cs deposition on epitaxial graphene grown on 6H-SiC(0001).* Surf. Sci. **605**, 1918–1922 (2011).

[78] S. Watcharinyanon, L. I. Johansson, C. Xia, and C. Virojanadara: *Changes in structural and electronic properties of graphene grown on 6H-SiC(0001) induced by Na deposition.* J. Appl. Phys. **111**, 083711 (2012).

[79] S. Sung, S. Kim, P. Lee, J. Kim, M. Ryu, H. Park, K. Kim, B. I. Min, and J. Chung: *Observation of variable hybridized-band gaps in Eu-intercalated graphene.* Nanotechnology **28**, 205201 (2017).

[80] C. Xia, L. I. Johansson, A. A. Zakharov, L. Hultman, and C. Virojanadara: *Effects of Al on epitaxial graphene grown on 6H-SiC(0001).* Mater. Res. Express **1**, 015606 (2014).

[81] S. Watcharinyanon, L. I. Johansson, C. Xia, J. I. Flege, A. Meyer, J. Falta, and C. Virojanadara: *Ytterbium Intercalation of Epitaxial Graphene Grown on Si-Face SiC.* Graphene **02**, 66–73 (2013).

[82] L. Daukiya, M. N. Nair, S. Hajjar-Garreau, F. Vonau, D. Aubel, J. L. Bubendorff, M. Cranney, E. Denys, A. Florentin, G. Reiter, and L. Simon: *Highly n-doped graphene generated through intercalated terbium atoms.* Phys. Rev. B **97**, 035309 (2018).

[83] I. Gierz, J. Henk, H. Höchst, C. R. Ast, and K. Kern: *Illuminating the dark corridor in graphene: Polarization dependence of angle-resolved photoemission spectroscopy on graphene.* Phys. Rev. B **83**, 121408 (2011).

[84] P. Rosenzweig, H. Karakachian, S. Link, K. Küster, and U. Starke: *Tuning the doping level of graphene in the vicinity of the Van Hove singularity via ytterbium intercalation.* Phys. Rev. B **100**, 035445 (2019).

[85] M. Kim, M. C. Tringides, M. T. Hershberger, S. Chen, M. Hupalo, P. A. Thiel, C.-Z. Wang, and K.-M. Ho: *Manipulation of Dirac cones in intercalated epitaxial graphene.* Carbon **123**, 93–98 (2017).

[86] A. Bostwick, T. Ohta, T. Seyller, K. Horn, and E. Rotenberg: *Quasiparticle dynamics in graphene.* Nat. Phys. **3**, 36–40 (2007).

[87] A. Bostwick, T. Ohta, J. L. McChesney, T. Seyller, K. Horn, and E. Rotenberg: *Band structure and many body effects in graphene.* Eur. Phys. J. Spec. Top. **148**, 5–13 (2007).

[88] H. Kamerlingh Onnes: Leiden Comm. **122b**, 124 (1911).

[89] V. V. Schmidt: *The Physics of Superconductors.* Springer-Verlag Berlin Heidelberg (1997).

[90] W. Meissner and R. Ochsenfeld: *Ein neuer Effekt bei Eintritt der Supraleitfähigkeit.* Naturwissenschaften **21**, 787–788 (1933).

[91] R. Gross and A. Marx: *Festkörperphysik.* De Gruyter Oldenbourg, Berlin (2014).

[92] J. Bardeen, L. N. Cooper, and J. R. Schrieffer: *Microscopic Theory of Superconductivity.* Phys. Rev. **106**, 162–164 (1957).

[93] J. Bardeen, L. N. Cooper, and J. R. Schrieffer: *Theory of Superconductivity.* Phys. Rev. **108**, 1175–1204 (1957).

[94] A. Carrington and F. Manzano: *Magnetic penetration depth of MgB2.* Physica C **385**, 205–214 (2003).

[95] H. Won and K. Maki: *d-wave superconductor as a model of high-*T_C *superconductors.* Phys. Rev. B **49**, 1397–1402 (1994).

[96] B. Dóra and A. Virosztek: *Thermodynamics and optical conductivity of unconventional spin density waves.* Eur. Phys. J. B **22**, 167–178 (2001).

[97] R. Akis: *Some Applications of Eliashberg Theory.* Ph.D. thesis, McMaster University (1991).

[98] G. M. Eliashberg: *Interactions between electrons and lattice vibrations in a superconductor.* Sov. Phys. (JETP) **11**, 696 (1960).

[99] B. M. Ludbrook, G. Levy, P. Nigge, M. Zonno, M. Schneider, D. J. Dvorak, C. N. Veenstra, S. Zhdanovich, D. Wong, P. Dosanjh, C. Straŝer, A. Stöhr, S. Forti, C. R. Ast, U. Starke, and A. Damascelli: *Evidence for superconductivity in Li-decorated monolayer graphene.* Proc. Natl. Acad. Sci. U. S. A. **112**, 11795–11799 (2015).

[100] W. L. McMillan: *Transition Temperature of Strong-Coupled Superconductors.* Phys. Rev. **167**, 331–344 (1968).

[101] P. B. Allen: *The electron-phonon coupling constant.* In: C. P. Poole (Ed.), *Handbook of Superconductivity*, 478–483. Academic Press, San Diego (2000).

[102] P. B. Allen and R. C. Dynes: *Transition temperature of strong-coupled superconductors reanalyzed.* Phys. Rev. B **12**, 905–922 (1975).

[103] J. P. Carbotte: *Properties of boson-exchange superconductors.* Rev. Mod. Phys. **62**, 1027–1157 (1990).

[104] B. Mitrović, H. G. Zarate, and J. P. Carbotte: *The ratio* $\frac{2\Delta_0}{k_B T_c}$ *within Eliashberg theory.* Phys. Rev. B **29**, 184–190 (1984).

[105] T. Susi, C. Hofer, G. Argentero, G. T. Leuthner, T. J. Pennycook, C. Mangler, J. C. Meyer, and J. Kotakoski: *Isotope analysis in the transmission electron microscope.* Nat. Commun. **7**, 13040 (2016).

[106] A. I. Cocemasov, D. L. Nika, and A. A. Balandin: *Engineering of the thermodynamic properties of bilayer graphene by atomic plane rotations: the role of the out-of-plane phonons.* Nanoscale **7**, 12851–12859 (2015).

[107] D. L. Nika and A. A. Balandin: *Phonons and thermal transport in graphene and graphene-based materials.* Rep. Prog. Phys. **80**, 036502 (2017).

[108] F. D. Natterer, J. Ha, H. Baek, D. Zhang, W. G. Cullen, N. B. Zhitenev, Y. Kuk, and J. A. Stroscio: *Scanning tunneling spectroscopy of proximity superconductivity in epitaxial multilayer graphene.* Phys. Rev. B **93**, 045406 (2016).

[109] B. D. Chapman, A. Checco, R. Pindak, T. Siegrist, and C. Kloc: *Dislocations and grain boundaries in semiconducting rubrene single-crystals.* J. Cryst. Growth **290**, 479–484 (2006).

[110] G. Profeta, M. Calandra, and F. Mauri: *Phonon-mediated superconductivity in graphene by lithium deposition.* Nat. Phys. **8**, 131–134 (2012).

[111] E. R. Margine, H. Lambert, and F. Giustino: *Electron-phonon interaction and pairing mechanism in superconducting Ca-intercalated bilayer graphene.* Sci. Rep. **6**, 21414 (2016).

[112] A. P. Durajski, K. M. Skoczylas, and R. Szczęśniak: *Adatom-dependent superconducting transition temperature in monolayer graphene.* Supercond. Sci. Technol. **32**, 125005 (2019).

[113] A. P. Durajski, K. M. Skoczylas, and R. Szczęśniak: *Superconductivity in bilayer graphene intercalated with alkali and alkaline earth metals.* Phys. Chem. Chem. Phys. **21**, 5925–5931 (2019).

[114] B. Uchoa and A. H. Castro Neto: *Superconducting States of Pure and Doped Graphene.* Phys. Rev. Lett. **98**, 146801 (2007).

[115] A. M. Black-Schaffer and C. Honerkamp: *Chiral d-wave superconductivity in doped graphene.* J. Phys.: Condens. Matter **26**, 423201 (2014).

[116] M. L. Kiesel, C. Platt, W. Hanke, D. A. Abanin, and R. Thomale: *Competing many-body instabilities and unconventional superconductivity in graphene.* Phys. Rev. B **86**, 020507 (2012).

[117] A. Einstein: *Über einen die Erzeugung und Verwandlung des Lichtes betreffenden heuristischen Gesichtspunkt.* Ann. Phys. **322**, 132–148 (1905).

[118] N. Ueno and S. Kera: *Electron spectroscopy of functional organic thin films: Deep insights into valence electronic structure in relation to charge transport property.* Prog. Surf. Sci. **83**, 490–557 (2008).

[119] A. Damascelli: *Probing the Electronic Structure of Complex Systems by ARPES.* Phys. Scr. **2004**, 61–74 (2004).

[120] M. P. Seah and W. A. Dench: *Quantitative electron spectroscopy of surfaces: A standard data base for electron inelastic mean free paths in solids.* Surf. Interface Anal. **1**, 2–11 (1979).

[121] T. Koopmans: *Über die Zuordnung von Wellenfunktionen und Eigenwerten zu den Einzelnen Elektronen Eines Atoms.* Physica **1**, 104–113 (1934).

[122] K. Wandelt (Ed.): *Photoelectron Spectroscopy and Diffraction.* Wiley-VCH Verlag GmbH (2012).

[123] J. Picker: *Untersuchung der elektronischen Eigenschaften von Kalium-interkalierten 1,2;8,9-Dibenzopentacen-Dünnschichten.* Bachelor thesis, Friedrich-Schiller-Universität Jena (2018).

[124] G. Binnig and H. Rohrer: *Scanning tunneling microscopy.* Helv. Phys. Acta **55**, 726–735 (1982).

[125] G. Binnig, H. Rohrer, C. Gerber, and E. Weibel: *Surface Studies by Scanning Tunneling Microscopy.* Phys. Rev. Lett. **49**, 57–61 (1982).

[126] J. Bardeen: *Tunneling from a many-particle point of view.* Phys. Rev. Lett. **6**, 57–59 (1961).

[127] J. Tersoff and D. R. Hamann: *Theory and Application for the Scanning Tunneling Microscope.* Phys. Rev. Lett. **50**, 1998–2001 (1983).

[128] J. Tersoff and D. R. Hamann: *Theory of the scanning tunneling microscope.* Phys. Rev. B **31**, 805–813 (1985).

[129] R. M. Tromp: *Spectroscopy with the scanning tunnelling microscope: a critical review.* J. Phys.: Condens. Matter **1**, 10211–10228 (1989).

[130] H. Raza: *Graphene Nanoelectronics: Metrology, Synthesis, Properties and Applications.* Springer-Verlag Berlin Heidelberg (2012).

[131] T. O. Wehling, I. Grigorenko, A. I. Lichtenstein, and A. V. Balatsky: *Phonon-Mediated Tunneling into Graphene.* Phys. Rev. Lett. **101**, 216803 (2008).

[132] R. Wiesendanger: *Scanning Probe Microscopy and Spectroscopy: Methods and Applications.* Cambridge University Press (1994).

[133] C. Wagner, R. Franke, and T. Fritz: *Evaluation of I(V) curves in scanning tunneling spectroscopy of organic nanolayers.* Phys. Rev. B **75**, 235432 (2007).

[134] C. J. Adkins and W. A. Phillips: *Inelastic electron tunnelling spectroscopy.* J. Phys. C: Solid State Phys. **18**, 1313–1346 (1985).

[135] W. Phillips: *Inelastic electron tunnelling spectroscopy in glasses.* Physica B+C **127**, 112 – 116 (1984). Proceedings of the 4th General Conference of the Condensed Matter Division of the EPS.

[136] D. P. E. Smith, M. D. Kirk, and C. F. Quate: *Molecular images and vibrational spectroscopy of sorbic acid with the scanning tunneling microscope.* J. Chem. Phys. **86**, 6034–6038 (2019).

[137] J. Lambe and R. C. Jaklevic: *Molecular Vibration Spectra by Inelastic Electron Tunneling.* Phys. Rev. **165**, 821–832 (1968).

[138] J. Klein, A. Leger, M. Belin, D. Defourneau, and M. J. L. Sangster: *Inelastic-Electron-Tunneling Spectroscopy of Metal-Insulator-Metal Junctions.* Phys. Rev. B **7**, 2336–2348 (1973).

[139] J. Kirtley and P. K. Hansma: *Vibrational-mode shifts in inelastic electron tunneling spectroscopy: Effects due to superconductivity and surface interactions.* Phys. Rev. B **13**, 2910–2917 (1976).

[140] K. Morgenstern, N. Lorente, and K.-H. Rieder: *Controlled manipulation of single atoms and small molecules using the scanning tunnelling microscope.* Phys. Status Solidi B **250**, 1671–1751 (2013).

[141] L. Vitali, M. A. Schneider, K. Kern, L. Wirtz, and A. Rubio: *Phonon and plasmon excitation in inelastic electron tunneling spectroscopy of graphite.* Phys. Rev. B **69**, 121414(R) (2004).

[142] J. Friedel: *Metallic alloys.* Il Nuovo Cimento (1955-1965) **7**, 287–311 (1958).

[143] L. Petersen, P. Laitenberger, E. Lægsgaard, and F. Besenbacher: *Screening waves from steps and defects on Cu(111) and Au(111) imaged with STM: Contribution from bulk electrons.* Phys. Rev. B **58**, 7361–7366 (1998).

[144] L. Petersen, P. T. Sprunger, P. Hofmann, E. Lægsgaard, B. G. Briner, M. Doering, H.-P. Rust, A. M. Bradshaw, F. Besenbacher, and E. W. Plummer: *Direct imaging of the two-dimensional Fermi contour: Fourier-transform STM.* Phys. Rev. B **57**, R6858–R6861 (1998).

[145] I. Brihuega, P. Mallet, C. Bena, S. Bose, C. Michaelis, L. Vitali, F. Varchon, L. Magaud, K. Kern, and J. Y. Veuillen: *Quasiparticle Chirality in Epitaxial Graphene Probed at the Nanometer Scale.* Phys. Rev. Lett. **101**, 206802 (2008).

[146] P. Mallet, I. Brihuega, S. Bose, M. M. Ugeda, J. M. Gomez-Rodriguez, K. Kern, and J. Y. Veuillen: *Role of pseudospin in quasiparticle interferences in epitaxial graphene probed by high-resolution scanning tunneling microscopy.* Phys. Rev. B **86**, 045444 (2012).

[147] P. Mallet, F. Varchon, C. Naud, L. Magaud, C. Berger, and J.-Y. Veuillen: *Electron states of mono- and bilayer graphene on SiC probed by scanning-tunneling microscopy.* Phys. Rev. B **76**, 041403 (2007).

[148] G. M. Rutter, J. N. Crain, N. P. Guisinger, T. Li, P. N. First, and J. A. Stroscio: *Scattering and Interference in Epitaxial Graphene.* Science **317**, 219–222 (2007).

[149] R. C. Tatar and S. Rabii: *Electronic properties of graphite: A unified theoretical study.* Phys. Rev. B **25**, 4126–4141 (1982).

[150] L. Simon, C. Bena, F. Vonau, M. Cranney, and D. Aubel: *Fourier-transform scanning tunnelling spectroscopy: the possibility to obtain constant-energy maps and band dispersion using a local measurement.* J. Phys. D: Appl. Phys. **44**, 464010 (2011).

[151] S. Das Sarma, S. Adam, E. H. Hwang, and E. Rossi: *Electronic transport in two-dimensional graphene.* Rev. Mod. Phys. **83**, 407–470 (2011).

[152] D. Nečas and P. Klapetek: *Gwyddion: an open-source software for SPM data analysis.* Cent. Eur. J. Phys. **10**, 181–188 (2012).

[153] I. Horcas, R. Fernández, J. M. Gómez-Rodríguez, J. Colchero, J. Gómez-Herrero, and A. M. Baro: *WSXM: A software for scanning probe microscopy and a tool for nanotechnology.* Rev. Sci. Instrum. **78**, 013705 (2007).

[154] C. Kittel: *Introduction to Solid State Physics.* John Wiley & Sons, Inc., New York, 8th edn. (2005).

[155] R. C. Dynes, V. Narayanamurti, and J. P. Garno: *Direct measurement of quasiparticle-lifetime broadening in a strong-coupled superconductor.* Phys. Rev. Lett. **41**, 1509–1512 (1978).

[156] S. B. Kaplan, C. C. Chi, D. N. Langenberg, J. J. Chang, S. Jafarey, and D. J. Scalapino: *Quasiparticle and phonon lifetimes in superconductors.* Phys. Rev. B **14**, 4854–4873 (1976).

[157] M. Tinkham: *Introduction to Superconductivity: Second Edition.* Dover Publications (2004).

[158] H. B. Michaelson: *The work function of the elements and its periodicity.* J. Appl. Phys. **48**, 4729–4733 (1977).

[159] J. Wiebe, A. Wachowiak, F. Meier, D. Haude, T. Foster, M. Morgenstern, and R. Wiesendanger: *A 300 mK ultra-high vacuum scanning tunneling microscope for spin-resolved spectroscopy at high energy resolution.* Rev. Sci. Instrum. **75**, 4871–4879 (2004).

[160] P. Löptien, L. Zhou, A. A. Khajetoorians, J. Wiebe, and R. Wiesendanger: *Tunneling into thin superconducting films: Interface-induced quasiparticle lifetime reduction.* Surf. Sci. **643**, 6–9 (2016).

[161] P. Löptien, L. Zhou, A. A. Khajetoorians, J. Wiebe, and R. Wiesendanger: *Superconductivity of lanthanum revisited: enhanced critical temperature in the clean limit.* J. Phys.: Condens. Matter **26**, 425703 (2014).

[162] J. Kröger, L. Limot, H. Jensen, R. Berndt, S. Crampin, and E. Pehlke: *Surface state electron dynamics of clean and adsorbate-covered metal surfaces studied with the scanning tunnelling microscope.* Prog. Surf. Sci. **80**, 26–48 (2005).

[163] R. Forker and T. Fritz: *Optical differential reflectance spectroscopy of ultrathin epitaxial organic films.* Phys. Chem. Chem. Phys. **11**, 2142–2155 (2009).

[164] R. Forker, M. Gruenewald, and T. Fritz: *Optical differential reflectance spectroscopy on thin molecular films.* Annu. Rep. Prog. Chem., Sect. C: Phys. Chem. **108**, 34–68 (2012).

[165] M. A. Van Hove, W. H. Weinberg, and C.-M. Chan: *Low-Energy Electron Diffraction: Experiment, Theory and Surface Structure Determination.* No. 6 in Springer Series in Surface Sciences. Springer, Berlin (1986).

[166] LEEDCal 2013, version 4.0, Falko Sojka and Torsten Fritz, Fritz & Sojka GbR, Apolda Germany (2018).

[167] F. Sojka, M. Meissner, C. Zwick, R. Forker, and T. Fritz: *Determination and correction of distortions and systematic errors in low-energy electron diffraction.* Rev. Sci. Instrum. **84**, 015111 (2013).

[168] K. Takayanagi, Y. Tanishiro, S. Takahashi, and M. Takahashi: *Structure analysis of Si(111)-*7×7 *reconstructed surface by transmission electron diffraction.* Surf. Sci. **164**, 367–392 (1985).

[169] LEEDLab 2018, version 1.0, Falko Sojka and Torsten Fritz, Fritz & Sojka GbR, Apolda Germany (2018).

[170] J. C. Kotsakidis, A. Grubišić-Čabo, Y. Yin, A. Tadich, R. L. Myers-Ward, M. DeJarld, S. P. Pavunny, M. Currie, K. M. Daniels, C. Liu, M. T. Edmonds, N. V. Medhekar, D. K. Gaskill, A. L. V. de Parga, and M. S. Fuhrer: *Freestanding n-Doped Graphene via Intercalation of Calcium and Magnesium into the Buffer Layer–SiC(0001) Interface.* Chem. Mater **32**, 6464–6482 (2020).

[171] M. Meissner, M. Gruenewald, F. Sojka, C. Udhardt, R. Forker, and T. Fritz: *Highly ordered growth of PTCDA on epitaxial bilayer graphene.* Surf. Sci. **606**, 1709–1715 (2012).

[172] M. Meissner: *Organische Moleküle auf epitaktischem Graphen.* Diplomarbeit, Friedrich-Schiller-Universität Jena (2010).

[173] F. Otto: *Untersuchung der Kalium-Dotierung von Tetraphenyldibenzoperiflanthen (DBP) mittels Photoelektronenspektroskopie.* Master's thesis, Friedrich-Schiller-Universität Jena (2015).

[174] T. Ohta, F. E. Gabaly, A. Bostwick, J. L. McChesney, K. V. Emtsev, A. K. Schmid, T. Seyller, K. Horn, and E. Rotenberg: *Morphology of graphene thin film growth on SiC(0001).* New J. Phys. **10**, 023034 (2008).

[175] L. N. Srivastava, G. He, R. M. Feenstra, and P. J. Fisher: *Comparison of graphene formation on C-face and Si-face SiC {0001} surfaces.* Phys. Rev. B **82** (2010).

[176] C. Virojanadara, M. Syväjarvi, R. Yakimova, L. I. Johansson, A. A. Zakharov, and T. Balasubramanian: *Homogeneous large-area graphene layer growth on6H-SiC(0001).* Phys. Rev. B **78** (2008).

[177] Z. Torbatian and R. Asgari: *Plasmonic Physics of 2D Crystalline Materials.* Appl. Sci. 238 (2018).

[178] S. Reich, J. Maultzsch, C. Thomsen, and P. Ordejón: *Tight-binding description of graphene.* Phys. Rev. B **66**, 035412 (2002).

[179] R. Kundu: *Tight-binding parameters for graphene.* Mod. Phys. Lett. B **25**, 163–173 (2011).

[180] P. Ruffieux, M. Melle-Franco, O. Gröning, M. Bielmann, F. Zerbetto, and P. Gröning: *Charge-density oscillation on graphite induced by the interference of electron waves.* Phys. Rev. B **71**, 153403 (2005).

[181] V. W. Brar, Y. Zhang, Y. Yayon, T. Ohta, J. L. McChesney, A. Bostwick, E. Rotenberg, K. Horn, and M. F. Crommie: *Scanning tunneling spectroscopy of inhomogeneous electronic structure in monolayer and bilayer graphene on SiC.* Appl. Phys. Lett. **91**, 122102 (2007).

[182] Y. Zhang, V. W. Brar, F. Wang, C. Girit, Y. Yayon, M. Panlasigui, A. Zettl, and M. F. Crommie: *Giant phonon-induced conductance in scanning tunnelling spectroscopy of gate-tunable graphene.* Nat. Phys. **4**, 627–630 (2008).

[183] A. Ramasubramaniam, D. Naveh, and E. Towe: *Tunable band gaps in bilayer transition-metal dichalcogenides.* Phys. Rev. B **84**, 205325 (2011).

[184] F. D. Natterer, Y. Zhao, J. Wyrick, Y.-H. Chan, W.-Y. Ruan, M.-Y. Chou, K. Watanabe, T. Taniguchi, N. B. Zhitenev, and J. A. Stroscio: *Strong Asymmetric Charge Carrier Dependence in Inelastic Electron Tunneling Spectroscopy of Graphene Phonons.* Phys. Rev. Lett. **114**, 245502 (2015).

[185] J. Chapman, Y. Su, C. A. Howard, D. Kundys, A. N. Grigorenko, F. Guinea, A. K. Geim, I. V. Grigorieva, and R. R. Nair: *Superconductivity in Ca-doped graphene laminates.* Sci. Rep. **6**, 23254 (2016).

[186] N. Jung, B. Kim, A. C. Crowther, N. Kim, C. Nuckolls, and L. Brus: *Optical Reflectivity and Raman Scattering in Few-Layer-Thick Graphene Highly Doped by K and Rb.* ACS Nano **5**, 5708–5716 (2011).

[187] S. P. Kelty and C. M. Lieber: *Scanning Tunneling Microscopy Investigations of the Electronic Structure of Potassium-Graphite Intercalation Compounds.* J. Phys. Chem **93**, 5983–5985 (1989).

[188] S. Fiori, Y. Murata, S. Veronesi, A. Rossi, C. Coletti, and S. Heun: *Li-intercalated graphene on SiC(0001): An STM study.* Phys. Rev. B **96**, 125429 (2017).

[189] S. Goler, C. Coletti, V. Piazza, P. Pingue, F. Colangelo, V. Pellegrini, K. V. Emtsev, S. Forti, U. Starke, F. Beltram, and S. Heun: *Revealing the atomic structure of the buffer layer between SiC(0001) and epitaxial graphene.* Carbon **51**, 249–254 (2013).

[190] R. D. Shannon: *Revised effective ionic radii and systematic studies of interatomic distances in halides and chalcogenides.* Acta Cryst. A **32**, 751–767 (1976).

[191] K. Xu, P. Cao, and J. R. Heath: *Scanning Tunneling Microscopy Characterization of the Electrical Properties of Wrinkles in Exfoliated Graphene Monolayers.* Nano Lett. **9**, 4446–4451 (2009).

[192] A. Grüneis, C. Attaccalite, A. Rubio, D. V. Vyalikh, S. L. Molodtsov, J. Fink, R. Follath, W. Eberhardt, B. Büchner, and T. Pichler: *Angle-resolved photoemission study of the graphite intercalation compound* KC_8*: A key to graphene.* Phys. Rev. B **80**, 075431 (2009).

[193] A. Caballero, J. P. Espinós, A. Fernández, L. Soriano, and A. R. González-Elipe: *Adsorption and oxidation of K deposited on graphite.* Surf. Sci. **364**, 253–265 (1996).

[194] M. A. Brisk and A. D. Baker: *Shake-up satellites in X-ray photoelectron spectroscopy.* J. Electron Spectrosc. Relat. Phenom. **7**, 197–213 (1975).

[195] I. Gierz, T. Suzuki, R. T. Weitz, D. S. Lee, B. Krauss, C. Riedl, U. Starke, H. Höchst, J. H. Smet, C. R. Ast, and K. Kern: *Electronic decoupling of an epitaxial graphene monolayer by gold intercalation.* Phys. Rev. B **81** (2010).

[196] J. F. Moudler, W. F. Stickle, P. E. Sobol, and K. D. Bomben: *Handbook of X-ray photoelectron spectroscopy.* Physical Electronics, Inc. (1995).

[197] J. J. Yeh and I. Lindau: *Atomic subshell photoionization cross sections and asymmetry parameters:* $1 \leq Z \leq 103$. At. Data Nucl. Data Tables **32**, 1–155 (1985).

[198] L.-G. Petersson and S.-E. Karlsson: *Clean and Oxygen Exposed Potassium Studied by Photoelectron Spectroscopy.* Phys. Scr. **16**, 425 (1977).

[199] J. Pireaux, N. Mårtensson, R. Didriksson, K. Siegbahn, J. Riga, and J. Verbist: *High resolution esca study of uranium fluorides: UF4 and K2UF6.* Chem. Phys. Lett. **46**, 215–219 (1977).

[200] K. Kishi and S. Ikeda: *X-Ray Photoelectron Spectroscopic Study for the Reaction of Evaporated Iron with O2and H2O.* Bull. Chem. Soc. Jpn. **46**, 341–345 (1973).

[201] C. Bena: *Effect of a Single Localized Impurity on the Local Density of States in Monolayer and Bilayer Graphene.* Phys. Rev. Lett. **100**, 076601 (2008).

[202] N. M. R. Peres, L. Yang, and S.-W. Tsai: *Local density of states and scanning tunneling currents in graphene.* New J. Phys. **11**, 095007 (2009).

[203] I.-W. Lyo and P. Avouris: *Negative Differential Resistance on the Atomic Scale: Implications for Atomic Scale Devices.* Science **245**, 1369–1371 (1989).

[204] P. Bedrossian, D. M. Chen, K. Mortensen, and J. A. Golovchenko: *Demonstration of the tunnel-diode effect on an atomic scale.* Nature **342**, 258–260 (1989).

[205] J. Li, W.-D. Schneider, R. Berndt, O. R. Bryant, and S. Crampin: *Surface-State Lifetime Measured by Scanning Tunneling Spectroscopy.* Phys. Rev. Lett. **81**, 4464–4467 (1998).

[206] I. Brihuega, A. M. García-García, P. Ribeiro, M. M. Ugeda, C. H. Michaelis, S. Bose, and K. Kern: *Experimental observation of thermal fluctuations in single superconducting Pb nanoparticles through tunneling measurements.* Phys. Rev. B **84**, 104525 (2011).

[207] B. L. Blackford and R. H. March: *Tunneling Investigation of Energy-Gap Anisotropy in Superconducting Bulk Pb.* Phys. Rev. **186**, 397–399 (1969).

[208] J. Rodrigo and S. Vieira: *STM study of multiband superconductivity in NbSe2 using a superconducting tip.* Physica C **404**, 306–310 (2004).

[209] J. L. McChesney, A. Bostwick, T. Ohta, T. Seyller, K. Horn, J. Gonzlez, and E. Rotenberg: *Extended van Hove Singularity and Superconducting Instability in Doped Graphene.* Phys. Rev. Lett. **104**, 136803 (2010).

[210] E. R. Margine and F. Giustino: *Two-gap superconductivity in heavily n-doped graphene: Ab initio Migdal-Eliashberg theory.* Phys. Rev. B **90** (2014).

[211] A. Kaminski and H. M. Fretwell: *On the extraction of the self-energy from angle-resolved photoemission spectroscopy.* New J. Phys. **7**, 98 (2005).

[212] C. N. Veenstra, G. L. Goodvin, M. Berciu, and A. Damascelli: *Spectral function tour of electron-phonon coupling outside the Migdal limit.* Phys. Rev. B **84**, 085126 (2011).

[213] Y. He, Y. Wang, and Z.-X. Shen: *Visualizing dispersive features in 2D image via minimum gradient method.* Rev. Sci. Instrum. **88**, 073903 (2017).

[214] A. A. Kordyuk, S. V. Borisenko, A. Koitzsch, J. Fink, M. Knupfer, and H. Berger: *Bare electron dispersion from experiment: Self-consistent self-energy analysis of photoemission data.* Phys. Rev. B **71**, 214513 (2005).

[215] C. N. Veenstra, G. L. Goodvin, M. Berciu, and A. Damascelli: *Elusive electron-phonon coupling in quantitative analyses of the spectral function.* Phys. Rev. B **82**, 012504 (2010).

[216] S. C. Kak: *The discrete Hilbert transform.* Proc. IEEE **58**, 585–586 (1970).

[217] P. Hofmann, I. Y. Sklyadneva, E. D. L. Rienks, and E. V. Chulkov: *Electron-phonon coupling at surfaces and interfaces.* New J. Phys. **11**, 125005 (2009).

[218] J. Shi, S.-J. Tang, B. Wu, P. T. Sprunger, W. L. Yang, V. Brouet, X. J. Zhou, Z. Hussain, Z.-X. Shen, Z. Zhang, and E. W. Plummer: *Direct Extraction of the Eliashberg Function for Electron-Phonon Coupling: A Case Study of* $\mathrm{Be}(10\bar{1}0)$. Phys. Rev. Lett. **92**, 186401 (2004).

[219] S. Harm, R. Dürig, R. Manzke, M. Skibowski, R. Claessen, and J. W. Allen: *Fermi-liquid-type spectral function and angle resolved photoelectron spectra of the Ti-3dz2-band of TiTe2.* J. Electron Spectrosc. Relat. Phenom. **68**, 111–119 (1994).

[220] L. Hedin, S. Lundqvist, F. Seitz, D. Turnbull, and H. Ehrenreich: *Effects of Electron-Electron and Electron-Phonon Interactions on the One-Electron States of Solids.* In: *Solid State Physics*, vol. 23, 1–181. Academic Press (1970).

[221] I. Mazin and A. Balatsky: *Superconductivity in Ca-intercalated bilayer graphene.* Philos. Mag. Lett. **90**, 731–738 (2010).

[222] S. Bose, C. Galande, S. P. Chockalingam, R. Banerjee, P. Raychaudhuri, and P. Ayyub: *Competing effects of surface phonon softening and quantum size effects on the superconducting properties of nanostructured Pb.* J. Phys.: Condens. Matter **21**, 205702 (2009).

[223] T. Nishio, M. Ono, T. Eguchi, H. Sakata, and Y. Hasegawa: *Superconductivity of nanometer-size Pb islands studied by low-temperature scanning tunneling microscopy.* Appl. Phys. Lett. **88**, 113115 (2006).

[224] M. Ziegler, N. Néel, A. Sperl, J. Kröger, and R. Berndt: *Local density of states from constant-current tunneling spectra.* Phys. Rev. B **80**, 125402 (2009).

Publications

Articles

[A1] T. Huempfner, F. Sojka, R. Forker, and T. Fritz: *Growth of coronene on (100)- and (111)-surfaces of fcc-crystals.* Surf. Sci. **639**, 80–88 (2015).

[A2] T. Huempfner, M. Hafermann, C. Udhardt, F. Otto, R. Forker, and T. Fritz: *Insight into the unit cell: Structure of picene thin films on Ag(100) revealed with complementary methods.* J. Chem. Phys. **145**, 174706 (2016).

[A3] C. Udhardt, F. Otto, C. Kern, D. Lüftner, T. Huempfner, T. Kirchhuebel, F. Sojka, M. Meissner, B. Schröter, R. Forker, P. Puschnig, and T. Fritz: *Influence of Film and Substrate Structure on Photoelectron Momentum Maps of Coronene Thin Films on Ag(111).* J. Phys. Chem. C **121**, 12285–12293 (2017).

[A4] F. Otto, T. Huempfner, M. Schaal, C. Udhardt, L. Vorbrink, B. Schroeter, R. Forker, and T. Fritz: *Ordered Growth and Electronic Properties of 1,2:8,9-Dibenzopentacene (trans-DBPen) on Ag(111).* J. Phys. Chem. C **122**, 8348–8355 (2018).

[A5] C. Udhardt, F. Otto, T. Huempfner, B. Schröter, R. Forker, and T. Fritz: *π-Like band structure observed for coronene monolayers deposited on Ag(111).* J. Electron Spectrosc. Relat. Phenom. **227**, 40–43 (2018).

[A6] R. Forker, M. Gruenewald, F. Sojka, J. Peuker, P. Mueller, C. Zwick, T. Huempfner, M. Meissner, and T. Fritz: *Fraternal twins: distinction between PbPc and SnPc by their switching behaviour in a scanning tunnelling microscope.* J. Phys.: Condens. Matter **31**, 134004 (2019).

[A7] T. Kirchhuebel, S. Kera, T. Munakata, N. Ueno, F. F. Bussolotti, J. Yang, T. Yamada, R. Mori, S. Kunieda, T. Huempfner, M. Gruenewald, R. Forker, and T. Fritz: *The Role of Initial and Final States in Molecular Spectroscopies - the Example of Tetraphenyldibenzoperiflanthene (DBP) on Graphite.* J. Phys. Chem. C **124**, 19622–19638 (2020).

Talks

[T1] F. Sojka, J. Peuker, T. Huempfner, M. Meissner, R. Forker, and T. Fritz: *High-precision LEED measurements of organic monolayers.* DPG Frühjahrstagung, 30 March - 4 April 2014 in Dresden, Germany.

[T2] T. Huempfner, F. Sojka, R. Forker, and T. Fritz: *Potassium doping of ultrathin layers of coronene on Ag(111).* DPG Frühjahrstagung, 15-20 March 2015 in Berlin,Germany.

[T3] T. Huempfner, T. Kirchhuebel, R. Forker, and T. Fritz: *Growth of Ultrathin DBP-Layers on Ag(111) and Graphene.* Talk given at the group seminar of the Surface Chemistry Lab, Department of Chemistry, Graduate School of Science, Osaka University, 6 October 2015 in Osaka, Japan.

[T4] T. Huempfner, R. Forker, and T. Fritz: *Organic Superconductivity.* Talk given at the group seminar of the Surface Chemistry Lab, Department of Chemistry, Graduate School of Science, Osaka University, 20 October 2015 in Osaka, Japan.

[T5] T. Huempfner, T. Kirchhuebel, R. Forker, N. Kawakita, T. Yamada, T. Munakata, and T. Fritz: *Coverage dependent evolution of electronic states of tetraphenyldibenzoperiflanthene (DBP) on HOPG and graphite.* DPG Frühjahrstagung, 6-11 March 2016 in Regensburg, Germany.

[T6] F. Otto, M. Schaal, C. Udhardt, T. Huempfner, L. Vorbrink, B. Schroeter, R. Forker, and T. Fritz:: *Electronic Properties of the Potential Organic Superconductor 1,2;8,9-Dibenzopentacene on Ag(111).* DPG Frühjahrstagung, 19-24 March 2017 in Dresden, Germany.

[T7] T. Huempfner, M. Hafermann, C. Udhardt, F. Otto, R. Forker, and T. Fritz: *Insight into the unit cell: Structure of picene thin films on Ag(100) revealed with complementary methods.* DPG Frühjahrstagung, 11-16 March 2018 in Berlin, Germany.

Posters

[P1] T. Huempfner, F. Sojka, M. Gruenewald, R. Forker, and T. Fritz: *Growth of coronene-layers on reactive and inert substrates.* DPG Frühjahrstagung, 30 March - 4 April 2014 in Dresden, Germany.

[P2] F. Sojka, M. Meissner, T. Huempfner, R. Forker, and T. Fritz: *Ordered growth of hexagonal molecules on hexagonal surfaces: a new type of epitaxy?* DPG Frühjahrstagung, 15-20 March 2015 in Berlin, Germany.

[P3] F. Sojka, T. Huempfner, C. Zwick, R. Forker, and T. Fritz: *First steps on the way to a superconductive organic layer.* DPG Frühjahrstagung, 15-20 March 2015 in Berlin, Germany.

[P4] M. Hafermann, T. Huempfner, R. Forker, and T. Fritz: *Growth and potassium doping of ultrathin layers of picene on Ag(100).* DPG Frühjahrstagung, 6-11 March 2016 in Regensburg, Germany.

[P5] C. Udhardt, F. Otto, T. Kirchhuebel, F. Sojka, T. Huempfner, B. Schroeter, R. Forker, and T. Fritz: *Investigation of Coronene Thin-Films on Ag(111) Using Photoelectron Spectroscopy.* DPG Frühjahrstagung, 6-11 March 2016 in Regensburg, Germany.

[P6] T. Huempfner, L. Vorbrink, F. Otto, M. Schaal, B. Schroeter, R. Forker, and T. Fritz: *On the Thin Film Growth of Two Isomers of Dibenzopentacene on Ag(111).* DPG Frühjahrstagung, 19-24 March 2017 in Dresden, Germany.

[P7] F. Sojka, M. Meissner, T. Huempfner, L. Matthes, R. Forker, and T. Fritz: *Continuously changing incommensurate adlayer: Coronene on Graphene.* DPG Frühjahrstagung, 19-24 March 2017 in Dresden, Germany.

[P8] C. Udhardt, F. Otto, T. Kirchhuebel, F. Sojka, T. Huempfner, M. Meissner, C. Kern, D. Lueftner, P. Puschnig, B. Schroeter, R. Forker, and T. Fritz: *Influence of the Surface Structure on Photoelectron Momentum Maps Measured for Coronene Monolayers on Ag(111).* DPG Frühjahrstagung, 19-24 March 2017 in Dresden, Germany.

[P9] T. Kirchhuebel, F. Bussolotti, J. Yang, K. Yonezawa, R. Shiraishi, T. Yamaguchi, T. Ueba, R. Mori, S. Kunieda, T. Yamada, T. Huempfner, R. Forker, T. Munakata, S. Kera, and T. Fritz: *Synthesis of Different Experimental Techniques in Surface Science.* DPG Frühjahrstagung, 11-16 March 2018 in Berlin, Germany.

Abbrevations

3NN	third-nearest-neighbor
acc.	accumulations
ARPES	angle-resolved photoelectron spectroscopy
ARUPS	angle-resolved ultra-violet photoelectron spectroscopy
BLG	bilayer graphene
BZ	Brillouin zone
DFT	density functional theory
DOS	density of states
DRS	differential reflectance spectroscopy
EBLG	epitaxial bilayer graphene
EDC	energy distribution curve
EMLG	epitaxial monolayer graphene
EPC	electron-phonon coupling
FT	Fourier transform
FT-STM	Fourier-transform scanning tunneling microscopy
FWHM	full width at half maximum
GIC	graphite intercalation compound
HOPG	highly oriented pyrolytic graphite
HWHM	half width at half maximum
IL	interlayer
LDOS	local density of states
LEED	low-energy electron diffraction
MDC	momentum distribution curve
ML	monolayer
MLG	monolayer graphene
NDC	negative differential conductance
PES	photoelectron spectroscopy
PhDOS	phonon density of states
PMM	photoelectron momentum map
QI	quasiparticle interference
RT	room temperature
SBZ	surface Brillouin zone
SECO	secondary electron cut off
SNR	signal-to-noise ratio
STM	scanning tunneling microscopy
STS	scanning tunneling spectroscopy
TB	tight-binding
UHV	ultra-high vacuum
UPS	ultra-violet photoelectron spectroscopy
XPS	x-ray photoelectron spectroscopy
ZLG	zero-layer graphene

Danksagung

An dieser Stelle möchte ich mich bei all jenen Personen bedanken, die zum erfolgreichen Abschluss dieser Arbeit beigetragen haben. Allen voran möchte ich mich bei Prof. Dr. Torsten Fritz für die Betreuung dieser Arbeit und die Möglichkeit bedanken, in diesem spannenden Themengebiet arbeiten zu dürfen. Außerdem bin ich ihm sehr dankbar für die tolle Unterstützung bei Problemen jeglicher Art und sein Vertrauen in mich und meine Arbeit. Weiterhin möchte ich mich bei der Studienstiftung des deutschen Volkes für die finanzielle Unterstützung meines Promotionsprojektes bedanken. Mein besonderer Dank gilt auch Prof. Dr. Paul Müller, der mir mit seiner Expertise im Bereich der Supraleitung stets mit Rat und Tat zu Seite stand.

Für sein stets offenes Ohr und gute Ratschläge bei Angelegenheiten jeglicher Art bedanke ich mich bei Dr. Roman Forker. Besonderes bedanken möchte ich mich bei Felix Otto, der zum einen die PES Messungen durchgeführt hat, zum anderen jedoch vor allem, dank seiner Expertise im Bereich der Photoelektronenspektroskopie, immer ein perfekter Ansprechpartner für hilfreiche Diskussionen war. Weiterhin gilt mein dank Dr. Falko Sojka für die Entwicklung des Softwaretools zur „richtigen“ Darstellung der winkelabhängigen PES Daten und für viele hilfreiche Diskussionen und Denkanstöße. Außerdem möchte ich mich bei meinen Mitstreitern und Bürokollegen Christian Zwick, Tino Kirchhübel, Jari Domke und Dr. Marco Grünewald bedanken für viele schöne Stunden in und außerhalb der Uni sowie ihre Bereitschaft sich auch in mein Themengebiet mit einzudenken. Außerdem danke ich den technischen Mitarbeitern für ihre Unterstützung im Labor, allen voran Holger Mühlig, mit dessen Hilfe die langwierigen Tieftemperaturmessungen überhaupt erst möglich wurden und für viele schöne Unterhaltungen über Gott und die Welt.

Abseits der Fachwelt möchte ich mich insbesondere bei meiner Frau Sophia für ihre unendliche Geduld, ihre Unterstützung und ihre aufbauenden Worte bedanken, vor allem wenn die Dinge mal nicht so gut gelaufen sind wie erhofft. Außerdem bedanke ich mich bei meiner Familie, besonders meinen Eltern, auf deren bedingungslose Unterstützung ich immer zählen konnte.

DANKE!

Erklärung

Ich erkläre hiermit ehrenwörtlich, dass ich die vorliegende Arbeit selbständig, ohne unzulässige Hilfe Dritter und ohne Benutzung anderer als der angegebenen Hilfsmittel und Literatur angefertigt habe. Die aus anderen Quellen direkt oder indirekt übernommenen Daten und Konzepte sind unter Angabe der Quelle gekennzeichnet.

Bei der Auswahl und Auswertung folgenden Materials haben mir die nachstehend aufgeführten Personen in der jeweils beschriebenen Weise unentgeltlich geholfen:

1. M.Sc. Felix Otto hat alle gezeigten PES-Daten aufgenommen und für die weiterführende Auswertung aufbereitet,
2. Dr. Falko Sojka hat ein Softwaretool zur richtigen Darstellung von ARUPS und PMM Daten entwickelt, das hier verwendet wurde,
3. Prof. Dr. Paul Müller hat viele Literaturhinweise zur klassischen Supraleitungstheorie gegeben, die bei der Auswertung und Interpretation der STS-Spektren im Bereich der superaleitenden Energielücke geholfen haben,
4. Prof. Dr. Torsten Fritz als betreuender Hochschullehrer.

Weitere Personen waren an der inhaltlich-materiellen Erstellung der vorliegenden Arbeit nicht beteiligt. Insbesondere habe ich hierfür nicht die entgeltliche Hilfe von Vermittlungs- bzw. Beratungsdiensten (Promotionsberater oder andere Personen) in Anspruch genommen. Niemand hat von mir unmittelbar oder mittelbar geldwerte Leistungen für Arbeiten erhalten, die im Zusammenhang mit dem Inhalt der vorgelegten Dissertation stehen.

Die Arbeit wurde bisher weder im In- noch im Ausland in gleicher oder ähnlicher Form einer anderen Prüfungsbehörde vorgelegt.

Die geltende Promotionsordnung der Physikalisch-Astronomischen Fakultät ist mir bekannt.

Ich versichere ehrenwörtlich, dass ich nach bestem Wissen die reine Wahrheit gesagt und nichts verschwiegen habe.

Jena, den 12. März 2021 ....